NTNU
Det skapende universitet

Simulering av strømning i en diffusor med ruhet på en vegg

Magnus Nytun

Master i energi og miljø
Innlevert: juni 2014
Hovedveileder: Per-Åge Krogstad, EPT

Norges teknisk-naturvitenskapelige universitet
Institutt for energi- og prosessteknikk

NTNU

Norges teknisk-
naturvitenskapelige universitet

Institutt for energi- og prosessteknikk

EPT-M-2014-79

MASTEROPPGAVE

for

Student Magnus Nytun

Våren 2014

Simulering av strømning i en diffusor med ruhet på en vegg

Simulation of flow in a diffusor with one rough wall

Bakgrunn og målsetting

Diffusorer brukes i stor grad i prosessindustrien og i vannkraftverk hvor poenget er å gjenvinne så mye som mulig av hastighetsenergien uten tap. Derved kan trykkgjenvinningen maksimeres.

Ved instituttet er det gjort detaljerte målinger på en spesiell difussor-geometri med glatte vegger som produserer såkalt likevekts-strømning. Dette er den raskeste måten energien kan gjenvinnes og som derfor gir det minste tapet.

For industrielle anvendelser vil det være vanskelig å produsere en diffusor med helt glatte overflater. I modell-diffusoren er derfor den ene veggen nå belagt med ruhetselementer for å se hvordan diffusoren nå oppfører seg. Det er gjort målinger som viser at dette forårsaker massiv separasjon i strømningen. Geometrien har derfor gått fra å produsere tilnærmet tapsfri strømning til å generere store tap. Derved vil geometrien være uegnet for bruk industrielt.

Det er ønskelig å studere hvilken mekanisme som forårsaker separasjonen for derigjennom å få informasjon om hvordan geometrien kan endres, slik at dette blir en optimal difussor også med ru overflate.

Oppgaven bearbeides ut fra følgende punkter

1. Studenten skal sett seg inn i hvilken effekt overflateruhet har på en strømning
2. Strømningen i instituttets diffusor skal beregnes, både for glatt og ru overflate
3. Ved å sammenligne de to sett med beregninger skal mekanismen som forårsaket separasjon i den rue kanalen forklares.

" - "

Senest 14 dager etter utlevering av oppgaven skal kandidaten levere/sende instituttet en detaljert fremdrift- og eventuelt forsøksplan for oppgaven til evaluering og eventuelt diskusjon med faglig

ansvarlig/veiledere. Detaljer ved eventuell utførelse av dataprogrammer skal avtales nærmere i samråd med faglig ansvarlig.

Besvarelsen redigeres mest mulig som en forskningsrapport med et sammendrag både på norsk og engelsk, konklusjon, litteraturliste, innholdsfortegnelse etc. Ved utarbeidelsen av teksten skal kandidaten legge vekt på å gjøre teksten oversiktlig og velskrevet. Med henblikk på lesning av besvarelsen er det viktig at de nødvendige henvisninger for korresponderende steder i tekst, tabeller og figurer anføres på begge steder. Ved bedømmelsen legges det stor vekt på at resultatene er grundig bearbeidet, at de oppstilles tabellarisk og/eller grafisk på en oversiktlig måte, og at de er diskutert utførlig.

Alle benyttede kilder, også muntlige opplysninger, skal oppgis på fullstendig måte. For tidsskrifter og bøker oppgis forfatter, tittel, årgang, sidetall og eventuelt figurnummer.

Det forutsettes at kandidaten tar initiativ til og holder nødvendig kontakt med faglærer og veileder(e). Kandidaten skal rette seg etter de reglementer og retningslinjer som gjelder ved alle (andre) fagmiljøer som kandidaten har kontakt med gjennom sin utførelse av oppgaven, samt etter eventuelle pålegg fra Institutt for energi- og prosessteknikk.

Risikovurdering av kandidatens arbeid skal gjennomføres i henhold til instituttets prosedyrer. Risikovurderingen skal dokumenteres og inngå som del av besvarelsen. Hendelser relatert til kandidatens arbeid med uheldig innvirkning på helse, miljø eller sikkerhet, skal dokumenteres og inngå som en del av besvarelsen. Hvis dokumentasjonen på risikovurderingen utgjør veldig mange sider, leveres den fulle versjonen elektronisk til veileder og et utdrag inkluderes i besvarelsen.

I henhold til "Utfyllende regler til studieforskriften for teknologistudiet/sivilingeniørstudiet" ved NTNU § 20, forbeholder instituttet seg retten til å benytte alle resultater og data til undervisnings- og forskningsformål, samt til fremtidige publikasjoner.

Besvarelsen leveres digitalt i DAIM. Et faglig sammendrag med oppgavens tittel, kandidatens navn, veileders navn, årstall, instituttnavn, og NTNUs logo og navn, leveres til instituttet som en separat pdf-fil. Etter avtale leveres besvarelse og evt. annet materiale til veileder i digitalt format.

☐ Arbeid i laboratorium (vannkraftlaboratoriet, strømningsteknisk, varmeteknisk)
☐ Feltarbeid

NTNU, Institutt for energi- og prosessteknikk, 14. januar 2014

Olav Bolland
Instituttleder

Per-Åge Krogstad
Faglig ansvarlig/veileder

Sammendrag

Denne masteroppgaven har tatt for seg beregninger av en spesiell diffusor geometri som er utviklet ved institutt for energi og prosessteknikk ved Norges teknisk-naturvitenskaplige universitet. Denne diffusor geometrien produserer likevekts-strømning som er den raskeste måten energien kan gjennvinnes på og som derfor gir de minste tapene. Beregningene er utført ved hjelp av kommersielt numerisk beregningsverktøy ANSYS Fluent 14.5. Diffusoren har blitt beregnet i orginal likevekts form med glatte vegger, og for industrielle applikasjoner noe som i dette tilfelle betyr at den ene veggen har blitt tilført k-type ruhetselementer. Resultatene av beregningene av den orginale likevekts diffusoren har blitt validert mot de fysiske målingene utført i [17]. Resultatene av beregningene når diffusoren har blitt tilført k-type ruhetselementer har blitt validert mot de fysiske målingene utført i [43]. Etter beregningene har blitt validert, er de sammenlignet for å forklare hvilken mekanisme som forårsakt separasjon i diffusoren med k-type ruhets elementer.

Beregningene på den orginale likevekts diffusoren har blitt utført ved hjelp av k-ω SST, k-ε RNG of Spalart-Allmaras turbulens modeller. Modellene viste god overensstemmelse med målingene i [17], dog påviser ingen av modellene tilsvarende likevekts-strømning som målt i [17]. Spalart-Allmaras modellen ble vurdert som den modellen som produserte best resultater på bakgrunn av at den viste størst tendenser til konstante likevektsparametre i det aktuelle likevektsområdet i [17]

Beregningene på den orginale likevekts diffusoren har blitt utført ved hjelp av k-ω SST, Standard k-ω, k-ε RNG, k-ε Realizable, RSM og Spalart-Allmaras turbulens modeller. Når diffusoren var dekket av k-type ruhetselementer var spredningen relative stor i de produserte resultatene for de forskjellige turbulens modellene. Det ble funnet at turbulens modellen som gav de beste resultatene for den massive grensesjiktseparasjonen i diffusoren dekket av ruhetselementer var Spalart-Allmaras modellen.

Sammenligningen av de to beregningene viser at k-type ruhetselementene gir en betydelig økning av fortregnings og bevegelsesmengdetykkelsen. Bidraget fra de økte fortregnings og bevegelsesmengdetykkelsene er mye kraftigere enn bidraget fra den økte turbulente miksingen som ruhetslementene også skaper. Dette fører til at grensesjiktet ikke klarer å overvinne den ugunstige trykkgradienten i diffusoren og dermed separerer grensesjiktet.

Abstract

In this thesis the flow through the special equilibrium diffuser geometry developed by the department of Energy and Process Engineering at the Norwegian University of Science and Technology has been simulated. The simulations have been performed utilizing the commercial computational fluid dynamics tool ANSYS Fluent 14.5. The diffuser flow has been simulated in original form when the walls were smooth, and for industrial applications meaning that the floor of the diffuser were covered with k-type roughness elements. The results of the simulations for the original equilibrium diffuser have been validated against the measurements performed in [17]. The results of the simulations on the diffuser when covered with k-type roughness have been validated against the measurements in [42]. Thereafter the simulations have been compared to investigate the mechanism causing the boundary layer to separate in the diffuser covered with the roughness elements.

The simulations performed on the smooth equilibrium diffuser have been executed with the k-ω SST, k-ε RNG and the Spalart-Allmaras turbulence models. These models displays good resemblance with the measurements in [17] but unfortunately none of the applied models shows complete equilibrium flow as in [17]. Nevertheless it was found that the Spalart-Allmaras model produced the best results, since this models showed the best tendencies of constant values of the equilibrium parameters in the specific equilibrium area in [17].

The simulations performed on the diffuser covered with roughness elements have been executed with the k-ω SST, Standard k-ω, k-ε RNG, k-ε Realizable, RSM and Spalart-Allmaras models. For the rough diffuser the deviation of the results produced by the different turbulence models were significantly larger than for the smooth diffuser. It was found that the turbulence model producing the best results for the massively separated flow over k-type roughness were the Spalart-Allmaras model.

The comparison of the two simulations shows that the k-type roughness elements causes a substantially increase of the displacement and momentum thicknesses which far overwhelms the enlarged turbulent mixing also produced by the roughness elements. Thereby the boundary layer separates.

Acknowledgments

I would like to thank my supervisor Professor Per-Åge Krogstad for all his support throughout this thesis.

I would also like to thank senior technical consultant in EDRMedeso Love Håkansson for help concerning ANSYS fluent.

In addition I would like to thank co-student Mikkel Bakli for general inputs regarding computational fluid dynamics and turbulence.

Table of Contents

Introduction

A diffusor is a common device used in fluid mechanical systems to convert kinetic energy, into static pressure by decelerating the flow by means of expanding the geometrical area. It has many applications, and is used extensively in compressors, pumps, water turbines, inlet to incineration chambers and in general everywhere you need to decrease the velocity and increase the pressure of the flow. In an ideal diffuser any kinetic energy losses will be converted into a pressure gain, this is because the total energy of the fluid is conserved since the fluid does not experience any frictional losses or other non-isentropic processes. However all real fluid experience losses in the form of energy dissipation, and for the diffuser, the dissipation of kinetic energy takes place inside the boundary layer. The boundary layer is the region next to the wall where the velocity increases from zero to the free stream, and therefore viscous effects becomes important. For the diffuser to operate at its peak performance it must be able to use the total geometrical area that is available for flow expanding, and to minimize the energy losses due to friction. Because of the increasing area of the diffuser, the flow is subjected to an adverse pressure gradient which it has to overcome. However the flow in the boundary layer may not be as energetic as the free stream due to frictional energy dissipation based on the surface texture. As a result the flow can be forced away from the wall and separated areas with recirculating flow can occur, severely affecting the diffuser performance. To predict separation the turbulent boundary layer growth must be calculated, however this is not a simple process mainly because the phenomenon of turbulence is not well understood.

At the department of Energy and Process Engineering at the Norwegian University of Science and Technology a diffuser with smooth walls producing equilibrium flow has been developed. Equilibrium flow is the fastest way for pressure recovery and thereby this type of diffuser flow gives the smallest losses. However, for industrial applications it will be difficult to produce a diffuser with completely smooth walls, meaning that the surface texture will always have some degree of roughness. Therefore, k-type roughness elements has been placed along the lower wall of the diffuser to study how the diffuser reacts. Unfortunately measurements carried out, shows that the diffuser flow now separates massively and therefore will be unsuited for industrial applications.

In this thesis the mechanism causing the separation is to be studied. Understanding this mechanism will be fundamental for improving the geometry of the diffuser, and thereby making it operate at peak performance.

Method and approach

In order to study the effects of surface roughness and thereby the mechanism causing the separation, the thesis will divided into six main chapters in the interest of achieving a comprehensive investigation of the problem. These chapter are as follows:

Chapter 1 – Theory:

Fundamental theory regarding turbulent flows and corresponding governing equations are presented. Thereafter follows sections where surface roughness and adverse pressure gradient effects are outlined. The chapter is concluded with a presentation of computational fluid dynamics (CFD) and turbulence modeling.

Chapter 2 – Model description:

In this chapter the model used to simulate the flow through the original equilibrium diffuser and the diffuser covered with roughness elements is presented. The chapter is concluded with a presentation of the physical measurements for the original equilibrium diffuser obtained in [17], and for the diffuser when covered with roughness elements obtained in [43].

Chapter 3 – Results:

In this chapter the results from the simulations are presented. First the simulations on the original equilibrium diffuser are presented, and validated against the physical measurements obtained in [17]. Secondly the results from the simulations on the diffuser when covered with roughness elements are presented and validated against the measurements in [43]

Chapter 4 – Discussion of CFD results:

In this chapter the results from the simulations are discussed. First the results from the original equilibrium diffuser are discussed, secondly the results from the diffuser when covered with roughness elements are discussed.

Chapter 5 – Smooth versus rough diffuser

In this chapter the simulations on the original equilibrium diffuser and the diffuser when covered with roughness elements are compared and discussed.

Chapter 6 – Conclusion

In this chapter the conclusion and thereby the reason behind the boundary layer separation is outlined.

Chapter 1 - Theory

1.1 Fluid Flow

1.1.1 Laminar flow

To describe fluid flow it is useful to create the concept of a streamline, this is an imaginary line which is defined as: A line drawn through the flow field in such a manner that the local velocity vector is always tangent to the streamline at every point.

In laminar flow the streamlines are parallel, the flow is well ordered and there is no mixing going on between adjacent layers. Laminar flow is also characterized as having a relative low Reynolds number, i.e. the ratio of inertial forces to viscous forces. Given the characteristic velocity U and length scale L of a system, the Reynolds number (Re) is defined as Re= UL/ν, where ν is the kinematic viscosity. As the velocity increases the shear between the adjacent laminar layers grows and at sufficiently high Re, the fluid starts to rotate and rapidly becomes turbulent. The existence of any given laminar flow situation is therefore governed by its poor resistance to high Re numbers.

1.1.2 Turbulent Flow

The turbulent flow regime is characterized as chaotic and therefore if you look at a point in the flow e.g. points (A) in you will observe velocity fluctuations in the form of swirls. The velocity fluctuations are denoted u', v' and w' for velocity fluctuations in respectively x, v and z direction. Most flows of practical interest are turbulent. Turbulence can be generalized to include the following statements as in [1, p.3].

- Irregularity: The flow is irregular and random which require statistical methods.

- Diffusivity: Rapid mixing of heat, momentum and mass. This is considered one of the most important properties of turbulence.

- Large Re: Turbulence occurs at high Re where the inertial effects are much more significant than the viscous forces.

- Three dimensional vorticity fluctuations: Turbulence is 3D and rotational. In 2D an important aspect of turbulence known as vortex stretching would not be possible

- Dissipation: Turbulent flows dissipate energy because of the viscous shear stress perform deformation work. This increases the internal energy of the fluid at the expense of the kinetic energy of the turbulence. Therefor turbulent flows always need a constant supply of energy or the turbulence will decay rapidly.

- Continuum: Turbulence is governed by the equations of fluid mechanics. The smallest scale of turbulence happens at the Kolmogorov scale and these are far larger than any molecular length scale.

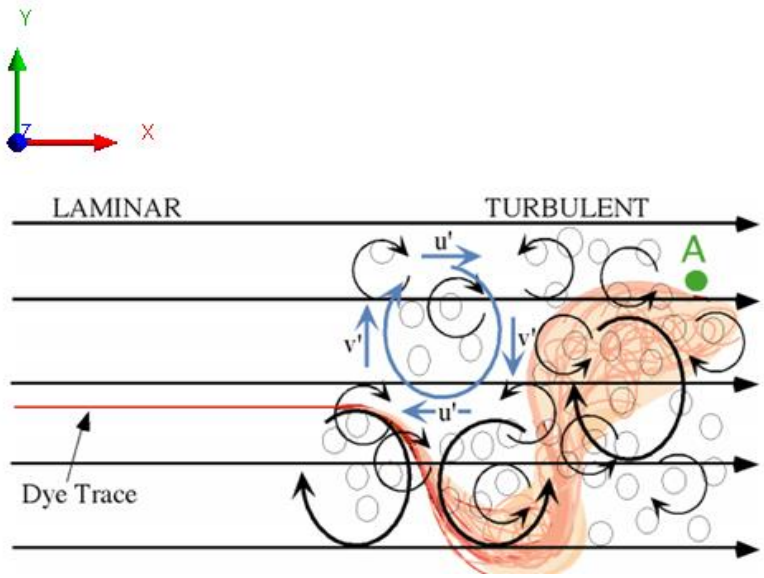

Figure 1: Laminar and turbulent flow visualization [2, p.1]

1.2 Governing equations

The governing equations of fluid dynamics can be derived by considering these fundamental physical laws:

- Conservation of mass
- Conservation of momentum
- Conservation of energy

In this thesis the flow is assumed to have a negligible temperature difference and therefore the governing equations are reduced to conservation of mass and momentum.

1.2.1 Reynolds Transport theorem

In an Eulerian representation of an incompressible fluid, the variables x, y, z, t are independent i.e. the coordinate axis is independent to the flowing fluid particles. The symbol ∂ denotes a partial derivative in an Eulerian reference frame. In a Lagrangian reference frame x, y, z, t are **not** independent i.e. the coordinate frame is fixed to a volume or a particle. The symbol D denotes a partial derivative in a Lagrangian reference frame [3, p.17].

Reynolds transport theorem gives us an relation between the Lagrangian and Eulerian description, of the temporal rate of change of a fluid at every point (x,y,z,t) in a flow field with Eulerian reference frame velocity u(x,y,z,t). Reynolds transport theorem can be derived by considering the rate of change of an extensive property (property that depends on mass) of a system as it passes through a control volume. For derivational details see [3, p.141].

$$\frac{\mathrm{D}\varphi}{\mathrm{D}t} = \frac{\partial\varphi}{\partial t} + \frac{\partial}{\partial x}(\varphi u) + \frac{\partial}{\partial y}(\varphi v) + \frac{\partial}{\partial z}(\varphi w) \tag{1}$$

Where u, v and w is speed in x, y and z direction and φ is an extensive property i.e. mass, momentum or energy. By substituting mass = $\int_V \rho dV$ in for φ, the continuity or conservation of mass equation is derived, yielding:

$$\frac{\partial\rho}{\partial t} = \frac{\partial\rho u}{\partial x} + \frac{\partial\rho v}{\partial y} + \frac{\partial\rho w}{\partial z} \tag{2}$$

This means that in an incompressible two dimensional flow, a decrease in the stream wise velocity u, must be compensated for by an increase in the wall normal velocity v, by the relation:

$$\mathrm{v} = -\frac{\partial}{\partial \mathrm{x}} \int_0^{\mathrm{y}} \mathrm{u}\,\mathrm{dy} \tag{3}$$

1.2.2 Navier-Stokes Equation (conservation of momentum)

The Navier-Stokes equation is derived by considering Newton's second law $\sum \boldsymbol{F} = m\boldsymbol{a}$ where bold letters denote a vector quantity. The sum of forces can be divided into:

- Surface forces: Pressure and viscous
- Body forces: Gravity. Also Coriolis and electromagnetic but these are not of influence in this project.

Newton's second law is defined in a Lagrangian reference frame, so it can be written

$$\sum \boldsymbol{F} = m\frac{D\boldsymbol{V}}{Dt} = \frac{D}{Dt}\int_{V(t)} \rho \boldsymbol{u} dV \tag{4}$$

By considering the x direction (similar for y and z direction) ρ**u** becomes ρu_x and is a scalar quantity. Setting $\varphi = \rho u_x$ and applying Reynolds transport theorem:

$$\frac{D}{Dt}\int_{V(t)} \rho u_{\boldsymbol{x}} dV = \int_{V(t)} \left[\frac{\partial \rho u_x}{\partial t} + \nabla \cdot (\rho u_x \boldsymbol{u})\right] \mathrm{dV} = \sum F_x \tag{5}$$

When considering the right hand side of equation (5), the sum of forces acting on the fluid volume will be; pressure, viscosity and gravity. The Navier-Stokes equations for incompressible viscous fluid in strong form can therefore be written in x, y and z direction as:

$$\frac{\mathrm{D}(\rho \mathrm{u_x})}{\mathrm{Dt}} = -\frac{\partial \mathrm{p}}{\partial \mathrm{x}} + \nabla \cdot (\mu \nabla \mathrm{u_x}) + \rho \mathrm{g_x} \tag{6}$$

$$\frac{\mathrm{D}(\rho \mathrm{u_x})}{\mathrm{Dt}} = -\frac{\partial \mathrm{p}}{\partial \mathrm{x}} + \nabla \cdot (\mu \nabla \mathrm{u_x}) + \rho \mathrm{g_x} \tag{7}$$

$$\frac{\mathrm{D}(\rho \mathrm{u_z})}{\mathrm{Dt}} = -\frac{\partial \mathrm{p}}{\partial \mathrm{z}} + \nabla \cdot (\mu \nabla \mathrm{u_z}) + \rho \mathrm{g_z} \tag{8}$$

1.2.3 Reynolds Average Navier-Stokes equation (RANS)

Because of the fluctuations in turbulent flow, the velocities and pressures are changing rapidly in time and space. This makes a full solution of the N-S equations very difficult to obtain. Also for engineering purpose one is much more interested in averaged values for velocity, pressure and shear stress. Therefor Osborne Reynolds decomposed the velocity and pressure terms in N-S into a mean part and a fluctuating part, written in Einstein tensor notation as.

$$u_i = U_i + u_i' \tag{9}$$

$$p_i = P_i + p_i' \tag{10}$$

Where capital letter denote mean values. Inserting these into the N-S and taking the average of the different terms will yield the Reynolds average Navier-Stokes equation written in Einstein summation tensor notation and with the Kronecker delta $\delta_{ij} = \begin{vmatrix} 1 & 0 & 0 \\ 0 & 1 & 0 \\ 0 & 0 & 1 \end{vmatrix}$

$$\frac{\partial \mathrm{U_i}}{\partial \mathrm{t}} + \mathrm{U_j}\frac{\partial \mathrm{U_i}}{\partial \mathrm{x_j}} = -\frac{1}{\rho}\frac{\partial}{\partial \mathrm{x_j}}\left[-\mathrm{P}\delta_{\mathrm{ij}} + \mu\frac{\partial \mathrm{U_i}}{\partial \mathrm{x_j}} - \overline{\mathrm{u_i' u_j'}}\right] \tag{11}$$

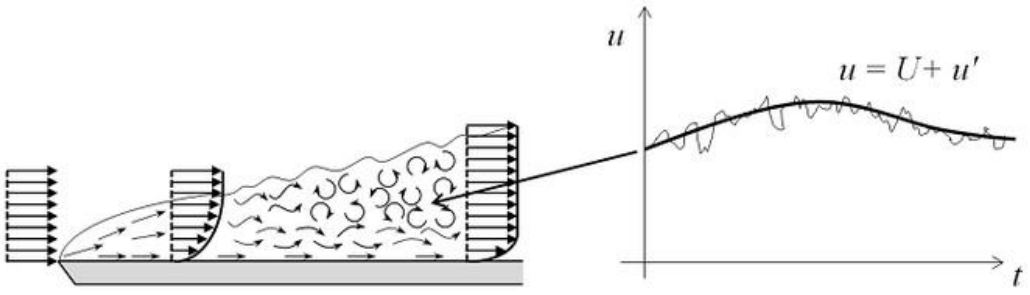

Figure 2 RANS principle [4]

1.2.4 Reynolds stresses

If one compares equation (11) to the conventional N-S equations, one see that the RANS equation has one extra term included. This is the Reynolds stresses $\overline{u_i' u_j'}$ which is a second order tensor and arises from the convective term in the Navier-Stokes equation and represent the effect of turbulent fluctuations. Turbulent fluctuations transport momentum (and other properties) across the flow field and thereby increases the mixing and transport in the flow. Turbulent fluctuations means that small masses of fluid are swept around in the fluid flow. If a small mass of fluid from a high velocity zone is swept into a low velocity zone, it will have an accelerating effect on the fluid in the lower velocity zone. If a small mass of fluid is swept from a low velocity zone into a high velocity zone, it will have a retarding effect on the fluid in the high velocity zone. Even though turbulent fluctuations are called stresses, they actually represent average momentum flux. However as far as the mean flow is concerned this extra flux of momentum per unit area has the same effect as an additional stress. Therefore the total effective stress in a turbulent flow consist of the turbulent Reynolds stresses and the viscous stress [5, p.77]

$$\tau_{ij} = \mu \frac{\partial U_i}{\partial x_j} - \rho \overline{u_i' u_j'} \tag{12}$$

The turbulent contribution to the transport of momentum is substantially higher than the viscous component. In this way, the turbulence can be viewed as an additional viscosity. As a result, in turbulent flows one will have one effective stress and one effective viscosity.

$$\boldsymbol{\tau_{eff} = \tau + \tau_{turb} \quad ; \quad \mu_{eff} = \mu + \mu_{turb}}$$

The turbulent viscosity or eddy viscosity is not a thermodynamic property like the molecular viscosity but it has the same units Pa·s, and varies instead with flow conditions and geometry.

1.2.5 Turbulent kinetic energy

In the same way the RANS equations where derived, the kinetic energy of the turbulent motions per unit mas can be derived by subtracting the mean kinetic energy from the instantaneous kinetic energy of the flow, and then average the remaining part:

$$\frac{1}{2}[\,\overline{u_i u_i - \overline{u_i}\,\overline{u_i}}\,] = \frac{1}{2}\overline{u_i' u_i'} = k \tag{13}$$

The mean turbulent kinetic energy refereed to from now on as turbulent kinetic energy (TKE), is a measurable quantity and its transport equation can be derived by introducing Reynolds decomposition into the instantaneous Navier-Stokes equations. By multiplying the entire equation by the fluctuating velocity u_i' and average the final expression, we arrive at the exact transport equation for k:

$$\frac{\partial k}{\partial t} + U_j \frac{\partial k}{\partial x_j} = D_k + P_k - \varepsilon \tag{14}$$

The two first terms on the left hand side are respectively the rate of change of k plus the transport of k by convection. The terms on the right hand is as follows:

$$D_k = -\frac{\partial}{\partial x_j}\left[\frac{1}{\rho}\overline{u_j' p'} + \frac{1}{2}\rho\overline{u_i' u_i' u_j'} - 2\frac{\mu}{\rho}\overline{u_i' s_{ij}'}\right] \tag{15}$$

Equation (15) represent diffusion of TKE due to turbulent and molecular transport. The name diffusion is somewhat misleading since it actually refers to advection of TKE. This advection is caused by fluxes of TKE from areas of high concentration of TKE to areas of low concentration of TKE and thereby the analogy to diffusion.

The first term inside the bracket represent the transport of k by pressure, the second represent the transport of k by Reynolds stresses, and finally the third one represent the transport of k by viscous stresses. The latter term is negligible for high Reynolds numbers, and are therefore neglected except near the walls where viscous effects are important.

$$P_{k=} - \overline{u_i' u_j'} \frac{\partial U_i}{\partial x_j} \tag{16}$$

Equation (16) represent production of TKE by interaction of the mean flow and the turbulent stresses. More exactly it describes the rate of energy transfer from the mean motion to the turbulence and is always positive. One can see that without mean velocity gradients there is no production of turbulence and hence it will decay. Velocity gradients are strongest near solid boundaries and therefore it is in this region where most of the turbulent production takes place before it get diffused towards the axis.

$$\varepsilon = 2\nu \overline{s_{iJ}' s_{iJ}'} \tag{17}$$

Equation (17) represent the average turbulent dissipation rate and it is this term that converts mechanical energy into thermal energy. It is always positive which consequently means that energy is extracted from the turbulence by the action of the viscous stresses. The dissipation term is of the same order as the production term and consequently never negligible.

1.2.6 Turbulent scales

Turbulent flow transfer its energy from large swirls (eddies) to smaller swirls at the dissipation rate $\varepsilon \sim u^3/l$. Here l and u are the largest scale of motion, and in a pipe these will be typically of the order of the pipe diameter. At these scales the viscosity is not enough to dissipate the eddies, and in order to avoid energy accumulation the large eddies must transfer their energy to smaller and smaller eddies until the length scale of the eddies is such that viscosity becomes important and hence will dampen them out i.e. dissipating them into heat. This transfer of energy from the largest scale down to the smallest scale is known as the energy cascade. The scale where the dissipations take place is called the Kolmogorov scale, which consists of the smallest turbulent scales.

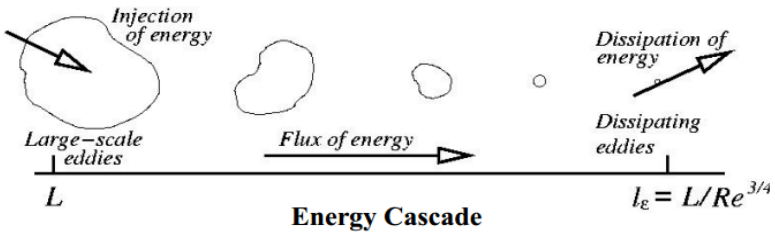

Figure 3: Energy cascade [6]

The molecular viscosity is a product of one velocity scale and one length scale.

$$\mu = \rho l v \tag{18}$$

Where l is the molecular mean free path, and v is the mean molecular velocity. In like manner the eddy viscosity can be interpreted as the product of one characteristic length and velocity scale.

$$\mu_t = \rho l' v' \tag{19}$$

The eddy viscosity is a function of the flow and varies with geometrical flow area and flow conditions. Therefore an adequate scale for the velocity is $\sqrt{k}$ since $v' \sim \sqrt{k}$. By dimensional analysis a scale for the characteristics length of the largest eddies with physical meaning, can be derived by:

$$l \approx \frac{k^{3/2}}{\varepsilon} \tag{20}$$

Where the quantity k/ε is a measure of eddy turnover time indicating how fast turbulence is dissipated by viscosity. Using these quantities, one can derive a viable expression for the kinematic eddy viscosity:

$$\nu_t \approx \frac{k^2}{\varepsilon} \tag{21}$$

1.2.6 Bernoulli's equation

For constant viscosity and density i.e. thermally uncoupled, the Navier-Stokes equation yields

$$\rho \frac{D\boldsymbol{V}}{Dt} = -\frac{\partial p}{\partial x} + \nabla \cdot (\mu \nabla \boldsymbol{V}) + \rho \boldsymbol{g} \tag{22}$$

If one assumes that the viscous terms are negligible and that the flow is steady, then by integrating the remaining part along a streamline between any points 1 and 2, Bernoulli's equation will reveal itself.

$$(p_1 + \frac{1}{2}\rho V_1^2 + \rho g z_1) = (p_2 + \frac{1}{2}\rho V_2^2 + \rho g z_2)$$

$$\mathrm{p} + \frac{1}{2}\rho V^2 = constant \tag{23}$$

Bernoulli's equation states that for an incompressible (within Mach 0.3 compressibility effects are negligible), inviscid and steady flow along a streamline, the sum of static (p) and dynamic ($\frac{1}{2}\rho V^2$) pressures are constant. In equation (23) the gravity term is neglected and this is realistic in gas dynamics.

1.3 The Boundary layer

Boundary layers appear on the surface of bodies because of the no-slip condition. The no slip condition states that because of viscosity, the velocity at the surface must be zero in all directions, meaning that the presence of a wall will have a retarding effect on the flow. The distance needed for the fluid to reach 99.5% of the free stream velocity is defined as the boundary layer, denoted δ. The boundary layer therefore represents the distance from the wall at which viscous effects becomes negligible, which again implies by mass conservation, that when the flow is subjected to the retarding effect of wall friction the free stream velocity increases. The layers above the surface are moving, consequently there will be shear stress between the different layers of fluid [7, p.2]. The shear stress between the surface and the layer immediately above is called wall shear stress or τ_0. In a laminar boundary layer the viscous forces are capable of dampening out disturbances in the flow. As the laminar layer grows the inertial forces gets stronger and at one point will surpass the viscous forces, the disturbances in the flow will amplify and transition to turbulence will occur.

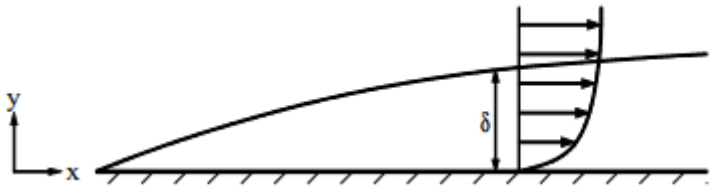

Figure 4 Typical boundary layer profile [8, p.8]

The shear stress is directly related to the rate of deformation of a volume of fluid. The wall shear stress was discovered by Newton to follow the relation:

$$\tau_0 = \mu \frac{du}{dy}\Big|_{y=0} \tag{24}$$

Here μ is the dynamic viscosity, $\frac{du}{dy}$ is the velocity gradient and τ_0 is the wall shear stress. This definition implies that the shear stress is not constant over, e.g. the total length (L) of a plate with width (B), and hence one must integrate over the entire surface to obtain total surface resistance [9, p.436]

$$F_s = \int_0^L \tau_0 B dx \tag{25}$$

The drag experienced by the flow consists however not only by the surface friction drag, but also of a form or pressure drag related to pressure differences experienced by the flow. The form drag is by far the dominant term in bluff bodies, whilst for streamline bodies the skin friction drag is the major contributor.

$$Drag = \oiint \overrightarrow{\tau_0} \cdot \hat{e}_\infty dS - \oiint p\hat{n} \cdot \hat{e}_\infty dS \tag{26}$$

In equation 23, $\hat{e}_\infty$ is a unit vector parallel to the free stream and integration takes place over the entire wetted area [10, p.237]. The second integral represent the form drag.

1.3.1 Boundary layer parameters

In order to describe the boundary layer it is useful to employ different tools. The most important boundary layer parameters are therefore explained in this section.

- The boundary layer thickness

The boundary layer thickness is defined as the distance from the surface to a point vertical to the surface where the velocity has reached 99.5% of the free stream velocity i.e:

$$\delta = y(0.995U_e \tag{27}$$

- Displacement thickness

The displacement thickness $\delta^*$is defined as: "The displacement of the streamlines from the wall compared to the inviscid solution in order to obtain the same mass flow rate as in the real case" I.e.

$$\int_0^\infty u dy = \int_{\delta^*}^\infty U_e dy \rightarrow \quad \delta^* = \int_0^\infty \left(1 - \frac{u}{U_e}\right) dy \tag{28}$$

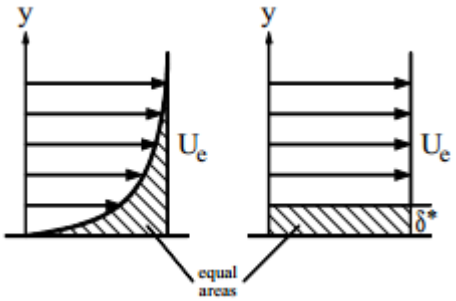

Figure 5: Displacement thickness visualization [11, p.1]

- Momentum Thickness

In the same way the momentum thickness θ is defined as the distance the wall would have to be displaced parallel to itself in an inviscid solution to give the same momentum as in the real case I.e.

$$\theta = \int_0^\infty \frac{u}{U_e}\left(1 - \frac{u}{U_e}\right) dy \tag{29}$$

- Von Kármans integral relation

In Von Kármans integral relation the displacement and momentum thickness is related to the friction coefficient. The relation states that the rate of change of momentum in the boundary layer at any value of x, is equal to the force produced by the shear stress at that location.

$$\frac{1}{2} C_f = \frac{d\theta}{dx} + (2 + H)\frac{\theta}{U_e}\frac{dU_e}{dx} \tag{30}$$

Where the friction coefficient C_f is defined as:

$$C_f = \frac{\tau_0}{0.5\rho U_e^2} \tag{31}$$

- Re_θ

Re_θ is the momentum thickness Reynolds number defined as:

$$Re_\theta = \frac{\rho U_e \theta}{\mu} \tag{32}$$

- Shape factor (H)

The shape factor is defined as the ratio of displacement to momentum thickness, and gives an indication of the fullness of the boundary layer profile. In figure (7) the turbulent boundary layer profile is fuller than the laminar one. High shape factors signifies that the boundary layer is near separation. For turbulent flows a shape factor of around 3 would indicate that the flow is on the verge of separation or has in fact separated.

$$H = \frac{\delta^*}{\theta} \tag{33}$$

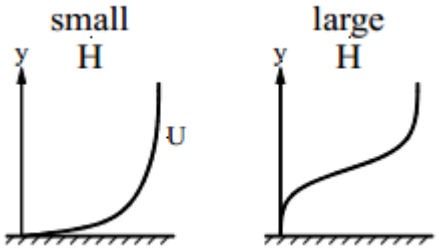

Figure 6 : Boundary layer profile during large and small Shape factor values [11, p.2]

1.3.1 Turbulent boundary layer

Most flows of interest are turbulent and so are the boundary layers. The boundary layer is important because it is here that the surface shear force takes place and hence it is vital for flow rates, drag, flow separation and heat transfer. The turbulence causes much more rapid diffusion of momentum from the wall and hence the turbulent boundary layer grows faster than the laminar one. Also since the velocity gradients are much steeper, due to velocity fluctuations in turbulent boundary layers, the wall shear stress in turbulent boundary layers are higher. The turbulent boundary layer has three different zones that need different equations for the velocity distribution.

Prandtl [12] showed that for the boundary layer, the Navier-Stokes equations can be reduced to a simpler form. By doing an order of magnitude analysis of the N-S and applying Reynolds decomposition one can derive these. For details [10, p149] Where p_E is the external pressure, impinged on the boundary layer, therefor the external pressure dictates the boundary layer pressure. The turbulent boundary layer equation in the x-direction yields:

$$U\frac{\partial U}{\partial x}+V\frac{\partial U}{\partial y}=-\frac{1}{\rho}\frac{\partial p_e}{\partial x}+\frac{\partial}{\partial y}\left(\nu\frac{\partial U}{\partial y}-\overline{u'v'}\right) \tag{34}$$

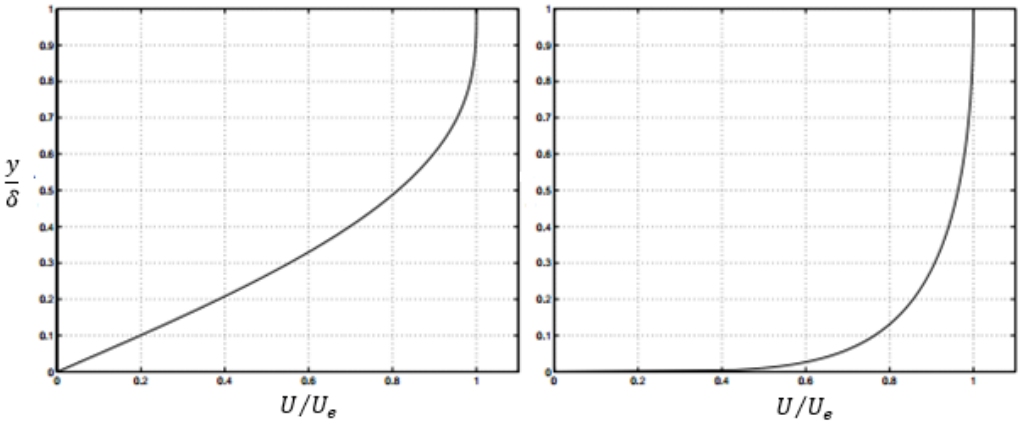

Figure 7: Laminar boundary layer to the left and turbulent boundary layer to the right plotted in non-dimensional profiles [13].

1.3.2 Viscous sub-layer

This is the region very close to the wall, and here the wall dampens out the cross stream mixing. Therefor in this region, viscosity is responsible for the vertical transport of momentum. In the viscous sub-layer is very close to the wall and τ is equal to τ_0, thus equation (34) yields:

$$\mu\frac{dU}{dy} = \tau_0 \tag{35}$$

Which after some integration and rearranging can be written:

$$\frac{u}{\sqrt{\tau_0/\rho}} = \frac{\sqrt{\tau_0/\rho}}{\nu} y \tag{36}$$

The expression $\sqrt{\frac{\tau_0}{\rho}}$ is an important term in boundary layer theory, it has the dimensions of velocity and has been given the name "friction velocity" with the symbol u_τ. Equation (35) can now be written in non-dimensional form:

$$\frac{u}{u_\tau} = \frac{u_\tau y}{\nu} \rightarrow u^+ = y^+ \tag{37}$$

Where y^+ is the local Reynolds number, and measures the ratio of viscous to inertial forces at different distances from the wall.

1.3.3 The logarithmic velocity profile

The region just outside the viscous sub-layer is turbulent and therefor one has to include the Reynolds stresses. Prandtl developed a theory to relate the Reynolds stresses to the mean velocity distribution known as; Prandtl's mixing length theory. The mixing length l is defined by Prandtl as: "The mixing length may be considered as the diameter of the masses of fluid moving as a whole in each individual case; or again, as the distance traversed by a mass of this type before it becomes blended in with neighbouring masses". Prandtl also made the assumption that the mixing length was proportional to the distance from the wall i.e. $l = \kappa y$. The Reynold stresses can be approximated using the mixing length theory to yield [14, p.128]

$$-\rho\overline{u'v'} = \rho\kappa^2 y^2 \left|\frac{du}{dy}\right| \frac{du}{dy} \tag{38}$$

Taking the square root of the above and integrating yields the logarithmic velocity distribution for the turbulent zone next to the viscous sub-layer:

$$u^+ = \frac{1}{\kappa}\ln y^+ + B \tag{39}$$

The logarithmic velocity profile is valid in a region from approximately; $y^+ = 30$ until $y^+ = 500$. The constants κ and B are determined experimentally and are most often respectively 0.41 and 5.2. The logarithmic and viscous sub-layer belongs to the turbulent boundary layers, inner layer. In the case of turbulent flow over rough surfaces, the log law must be modified with a roughness function ΔU^+which main effect is to give the log law a vertical down shift. The log law corrected for roughness yields:

$$u^+ = \frac{1}{\kappa}\ln y^+ + B - \Delta U^+ \tag{40}$$

1.3.4 Velocity defect layer and Coles law of the wake

The velocity defect region is in the outer layer of the boundary layer. In this region momentum transport by turbulence is far greater than by viscosity, hence the velocity profile should depend on u, y, τ_0, ρ and δ but not ν. Using dimensional analysis one can obtain two dimensionless numbers, and by setting those equal to each other one obtains the velocity defect law:

$$\frac{U_e - u}{u_\tau} = \frac{y}{\delta} \rightarrow \frac{U_e - u}{u_\tau} = f(\eta) \tag{41}$$

Here U_e is the flow at the edge of the boundary layer. The velocity defect law contains as much as 80 to 90 % of the turbulent boundary layer.

Particularly in non-equilibrium boundary layers with an adverse pressure gradient APG (see chapter 5) the log law deviates from the velocity profile. Coles found that this deviation had a wake like shape and could be represented by adding an extra term to the log law namely:

$$\frac{2\Pi}{\kappa} w\left(\frac{y}{\delta}\right) \tag{42}$$

The term $w(\frac{y}{\delta})$ is often given an s shaped function in the form of; $\sin^2(\frac{\pi y}{2\delta})$ where Π is the wake strength and depends on the pressure gradient, it has a typical value of 0.45 for zero pressure gradients. The turbulent boundary layer equation corrected for roughness and pressure gradient can therefore be adequately represented by the function:

$$u^+ = \frac{1}{\kappa}\ln y^+ + B + \Delta U^+ + \frac{2\pi}{\kappa}\sin^2(\frac{\pi y}{2\delta}) \tag{43}$$

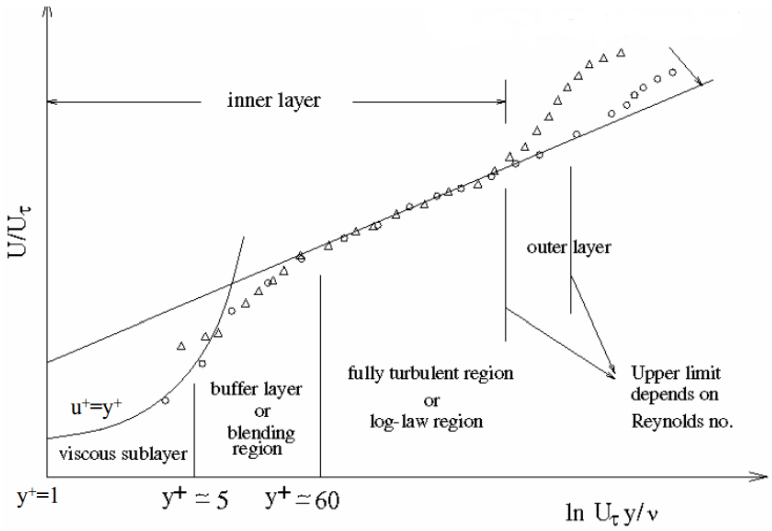

Figure 8: Turbulent boundary layer structure [15]

1.3.5 Equilibrium boundary layers

The concept of an equilibrium turbulent boundary layer was first laid out by the most renowned aerodynamicist Francis H. Clauser in the year 1954. Clauser found that if the mainstream velocity distribution can be classified by a constant value of the Clauser parameter:

$$\beta = \frac{\delta^*}{\tau_w}\left(\frac{\partial P_e}{\partial x}\right) \tag{44}$$

Then the flow is self-similar also known as equilibrium flow. The Clauser parameter represent the ratio of shear forces to pressure forces in a section of the boundary layer. The

pressure gradient controls the growth rate of the boundary layer, and a constant Clauser parameter gives a streamwise pressure distribution which provides a boundary layer growth characterized by similarity of the velocity defects profiles. The origin of equilibrium flow is observed in the logarithmic region, where during equilibrium flows the amount of production and dissipation of TKE is equal [16, p.73]. This leads to boundary layer velocity profiles that are independent of the stream wise direction when plotted using the velocity defect law.

An important implications of a constant Clauser parameter is that the freestream velocity distribution in the streamwise direction can be expressed using a power law formulation [9, p.420]:

$$U_e = U_{ref}(x_0 - x)^{-m} \tag{45}$$

Where the different variables are:

- U_e is the freestream velocity in the specific crossection
- U_{ref} is a theoretical reference velocity
- To have equilibrium flow it is required that the momentum, displacement and boundary layer thickness grow linearly. x_0 is the virtual origin from where these parameters in the equilibrium part of the boundary layer have a common origin [17, p.325].

This constitute that the strength of the APG can be controlled by adjusting the value of m. For zero pressure gradient m equals zero, whilst for strong APG the value of m can be as high as 0.23 for non-separating APG flows.

The last parameter defined by Clauser that must be constant in equilibrium boundary layer flow is the Clauser shape factor:

$$G = \frac{(H-1)}{\left(H\sqrt{0.5C_f}\right)} \tag{46}$$

Where H is the shapefactor and $C_f$is the skin friction coefficient. The Clauser shape factor gives an indication of the fullness of the boundary layer related to the friction.

1.3 Surface roughness

As mentioned in section (1.3) the presence of a wall will have a retarding effect on the flow caused by an imposed drag force from the wall. The magnitude of this drag force is highly dependent on the surface texture. In the case of flow over a smooth surface the drag force consist mainly of skin friction, whilst in flow over a rough surface, the roughness elements will protrude into the flow, thereby giving rise to pressure forces acting on the roughness elements. Consequently, a pressure difference over each roughness element will appear, leading to increased drag since the fluid particles will impinge more of their momentum to the wall. The momentum loss experienced by the flow, will thus consist of both a skin friction drag and the form drag. The latter is however, often significantly higher especially during flow separation. Roughness will also by its nature stimulate turbulence, giving rise to steeper velocity gradients near the surface, and thereby bringing more momentum into the boundary layer.

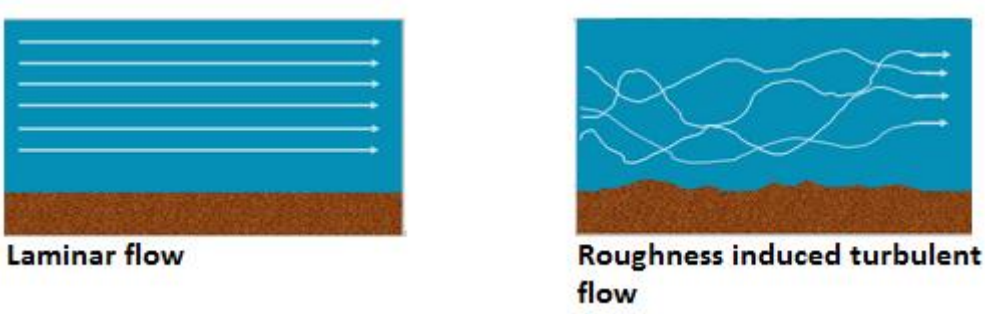

Figure 9: Laminar flow left figure, turbulent flow induced by roughness right figure

Roughness can also have a substantial effect on the log law in figure (8). Prandtl's student Nikuradse found that surface roughness will tend to shift the log law down by an amount ΔU^+. The amount of downshift will be determined by the type of roughness and the roughness distribution, the slope of the log law will however remain the same at $1/k$ [3, p.362]. However, one situation that can occur in turbulent boundary layers with rough walls, is that the logarithmic layer might not survive. If this happens or not is influenced by the ratio δ/k which is the ratio of the boundary layer thickness to the roughness height. In [18, p.192] the author suggest that this ratio has to be larger the 40 before similarity laws can be expected. In a study performed by [45, p.1] the authors found that the roughness significantly changed the secondary flow pattern in rectangular ducts with one rough wall.

Nikuradse simulated roughness by gluing sand grains with approximately the same size at the walls of pipes. He found that the influence of roughness is determined by $k_s^+ = \frac{u_\tau k_s}{\nu}$ where k_s is sand grain size. He managed to determine the following regimes:

Hydraulically smooth: $k_s^+ < 5$. In this regime roughness has no effect on the friction factor or the velocity profile.

Transitional roughness: $5 < k_s^+ < 70$. In this regime both roughness and viscous effects operate.

Fully rough: $k_s^+ > 70$. Transfer of momentum to the wall is predominantly by pressure drag on surface elements. Wall friction becomes independent of Reynolds number.

1.4.1 The Moody chart

Nikuradse did experiments with pipe flow of constant cross section and found that the surface resistance increased with increasing roughness ratio (k/d) where d is the diameter of the pipe. Moody [19] managed to make a chart now known as the Moody chart. This is a non-dimensional chart that relates the Darcy-Weisbach friction factor, Reynolds number and relative roughness (ε/d in Moody chart) for a pipe with fully developed flow. It is used to calculate pressure drops and flow rates down pipes and is valid for both liquid and gas in circular or non-circular pipe flows [3, p.363]. From the Moody chart we can deduct that increased relative roughness gives higher friction factors, and also that when the Reynolds number gets sufficiently large the relative roughness curves are basically horizontal and the friction factor is thereby independent of the Reynolds number. Similarly at higher relative roughness the Reynolds number has less impact on the friction factor. The pressure drop ΔP can be estimated as follows:

$$\Delta P = \rho \frac{f L V^2}{2D} \tag{47}$$

Where $\rho, V, L \; and \; D$ are respectively the density of the fluid, the average velocity in the pipe, the length of the pipe and the diameter of the pipe. From equation (47) one can see that increased roughness in the form of higher friction factor f gives a larger pressure drop and thereby increased energy losses in the pipe.

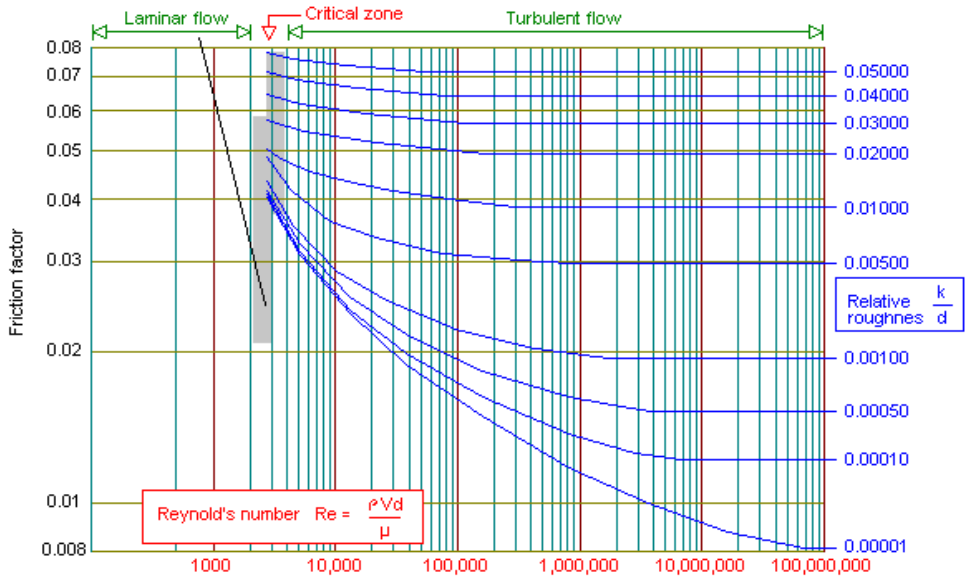

Figure 10: Moody diagram [20]

1.4.2 Roughness types

At the scale of the roughness elements, the flow is no longer parallel to the ground plane and will depend on the geometry of the roughness elements. For roughness elements resembling e.g. bluff bodies, the flow structure is dominated by the wake created by the roughness elements and is therefore non homogenous above the crest of the roughness elements [21, p.2]. According to the wall similarity hypothesis the turbulent motion, outside the roughness sub layer (a region stretching out approximately five roughness heights k) is at a sufficiently high Reynolds number, unaffected by the surface roughness [22, p.600]. However Krogstad et al [22, p.615] suggest that the roughness effect spreads throughout the boundary layer.

It has been made a distinction between so called k-type and d-type roughness. If the roughness height (k) is smaller than the distance (s) between the roughness elements, then one has k-type roughness. If the density of the roughness elements i.e. the spacing between the elements is less than the height (k) then one has d-type roughness. [23, p.1]. The roughness function ΔU^+ for flows over k-type roughness depends on the roughness height k, but for d-type roughness where the distance between the roughness elements are small, the roughness function depends on an outer scale e.g. the pipe diameter. More roughly a distinction between d and k-type roughness is also often determined using the pitch to height ratio defined in figure (11). With a P/k$\geq$ 3 one has k-type roughness if the ratio is less one has d-type roughness.

Figure 11: Pitch (P) to height (k) [24]

In [23, p.2] the authors suggest that for a k-type roughness eddies with length scales of order (k) are shed into the flow above the crests of the elements. Further away from the crests, these eddies diffuse into the flow. The same authors suggest that for d-type roughness stable vortices form within the grooves, and there is essentially no eddy shedding into the flow above the elements. The flow in the recirculation zone will however experience friction against all sides in the cavity. K-type roughness will therefore be the roughness type responsible for the biggest downshift in ΔU^+ and is also the one giving the greatest C_f values. This is because in the d-type roughness a recirculation zone as seen in figure (12) isolates the outer flow from the roughness cavities, and therefore shelters the flow from the roughness. Whilst in k-type roughness two recirculation zones exist and the streamlines curve inward. Consequently the interaction between the overlying flow and the roughness elements becomes stronger with k-type roughness

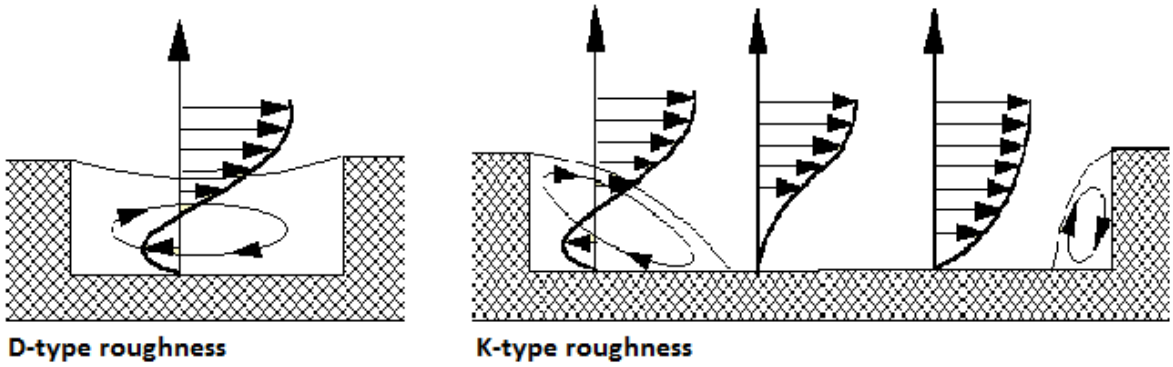

Figure 12 : D-type and K-type roughness [26]

1.5 Adverse pressure gradient

A favourable pressure gradient is one in which the static pressure decreases in the stream wise direction i.e. $\frac{\partial p}{\partial x} < 0$. An adverse pressure gradient (APG) is one in which the static pressure increase in the stream wise direction i.e. $\frac{\partial p}{\partial x} > 0$. APG occurs whenever the flow experiences an enlargement in flow area. This is in accordance with the continuity and Bernoulli equations. The continuity equation yields: $V_2 = \frac{A_1}{A_2} V_1$, and since A_2 is bigger then A_1 the velocity V_2 must be less then V_1. The Bernoulli equation states that the sum of dynamic and static pressure is constant, within the limitations already mentioned. This implies that if the velocity goes down the static pressure must go up. Therefor an enlargement in flow area will decelerate the fluid particles. Also if one takes the derivative of the Bernoulli equation along the x direction, on will obtain:

$$U \frac{dU}{dx} = -\frac{1}{\rho} \frac{dp_0}{dx} \tag{48}$$

Showing that a negative pressure gradient gives acceleration to the flow and a positive gradient will decelerate the flow.

The main effect of an APG on the turbulent boundary layer is to shift the outer layer in figure (8) upwards and to the left. Meaning that the APG increases the wake region which in turn reduces the section where the logarithmic law of the wall is applicable. In flows near separation the wall shear stress and therefore the friction velocity becomes vanishingly small, causing U^+ to become very large, hence y^+ is reduced. Consequently there will be an increase in the wake region to the extent that the log law representation may not survive. Nikuradse did experiments with converging-diverging water flow, he found that in the diverging channel the boundary layer grows fast, and that at a certain angle the flow becomes unstable.

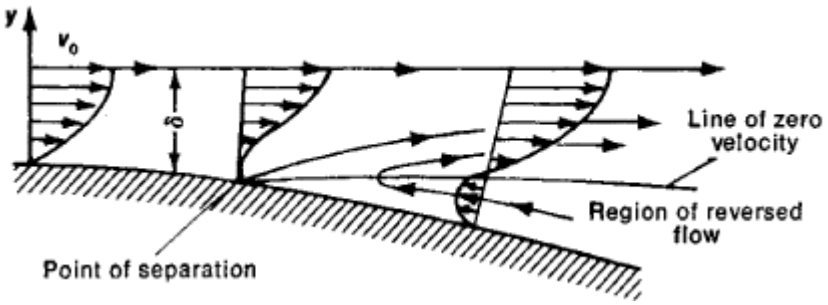

Figure 13 Flow separation [27]

1.5.1 Boundary layer separation

Boundary layer separation is the process of breakdown and departure of the boundary layer flow. This leads to a rapid thickening of the rotational flow region close to the wall. When the pressure increases in the direction of the flow as in a diffuser, the pressure rise is trying to push the flow backwards. Because the frictional losses in the boundary layer are greater than in the rest of the flow, the boundary layer suffers from a momentum deficit compared to the free stream. The momentum in the boundary layer might not be enough to overcome the backwards pushing force the APG creates. The velocity in the boundary layer will slow down and hence the boundary layer will grow until $\frac{du}{dy}\Big|_{y=0} = 0$. This position is known as the separation point, at this point the shear stress must be according to equation (24) also zero. After this point the flow near the walls will flow in the opposite direction of the mean flow. As seen in figure (14), boundary layer separation will cause an increase in the turbulence because vortices are generated by the fluid which is moving in both directions. The result is higher energy losses in the flow [25]. Regardless if the boundary layer separates or not an APG will give rise to an inflection point in the boundary layer, which coincides with the maximum shear in the boundary layer.

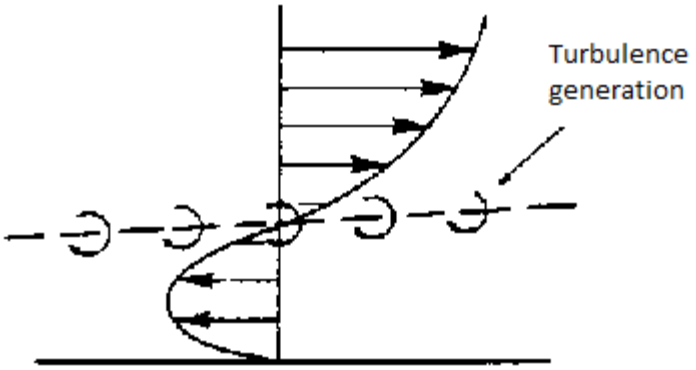

Figure 14 Boundary layer separation and turbulence increasement [25]

Prandtl explained separation in this manner: “On an increase of pressure while the free fluid transforms parts of its kinetic energy into potential energy, the transition layer instead having lost a part of their kinetic energy, have no longer a sufficient quantity to enable them to enter a field of higher pressure, and therefor turn aside from it”.

The pressure distribution after the separation point will determine if the flow reattaches to the surface or not. If the APG continues then the wake of backflow will endure and grow. If the APG vanishes then a separation bubble will form, the reattachment point can however move up and down.

1.5.2 Separation dynamics

Even though separation reduces skin friction drag on the surface, it tends to decrease the pressure coefficient which expresses how much of the static pressure the diffuser recovers from the incoming dynamic head at the reference location and is defined as:

$$C_p = \frac{P - P_{ref}}{Pdynamic_{ref}} \tag{49}$$

The pressure coefficient, or pressure recovery coefficient decreases because the effective expansion of the flow is not as large as the geometry would indicate. The separated zone consist of large eddies unable to convert their rotational kinetic energy into pressure. Consequently the separating zone will produce a blockage effect making the actual flow area less. Therefore according to Bernoulli, the freestream will increase and consequently the pressure recovery is reduced. Since the separation causes the pressure rise to be less than the geometry would indicate, the APG in the case of separation will also be less than it was initially. This means that when the separation has grown to a specific size, the flow will have enough momentum to overcome the APG and the separation zone will shrink or disappear completely. After this the APG will build up again and the cycle repeats itself.

One way of delaying flow separation is to increase the amount of turbulence in the flow. The turbulent fluctuations and mixing capabilities causes much higher drag, but puts more momentum into the boundary layer and thus prevents or delays flow separation. Conventional methods for doing this consist of increasing the surface roughness or applying a turbulence tripping tool to the flow.

1.6 The diffuser

As mentioned in the introduction the diffuser is a device intended to reduce the kinetic energy and thereby increase the potential energy of a flow by means of expanding the flow area. The diffuser utilizes the Bernoulli and continuity equation in order to achieve as high pressure recovery as possible. Poor diffuser design is a major cause of pressure loss. If the Bernoulli and one dimensional continuity equation are manipulated one can write the diffuser efficiency i.e. the pressure recovery coefficient: $C_p = 1 - \left(\frac{V_2}{V_1}\right)^2 = 1 - \left(\frac{A_2}{A_1}\right)^{-2}$. This formula is based on frictionless estimates, therefor phenomena's like flow separation will not occur, resulting in an overestimation of the diffuser performance. Dimensional analysis done on a flat walled conical diffuser shows that to have an adequate pressure recovery one must take these factors into consideration [3, p.400]

- Area ratio A_2/A_1
- Divergence angle
- Inlet Reynolds and Mach number
- Slenderness: Length/Diameter
- Blockage factor A_{bl}=Wall area displaced by retarded boundary layer

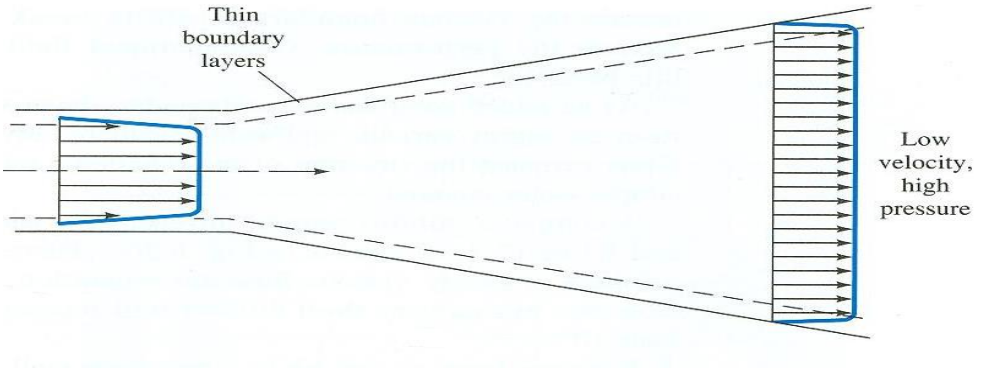

Figure 15: Diffuser with ideal flow pattern and accordingly excellent pressure recovery [3, .399]

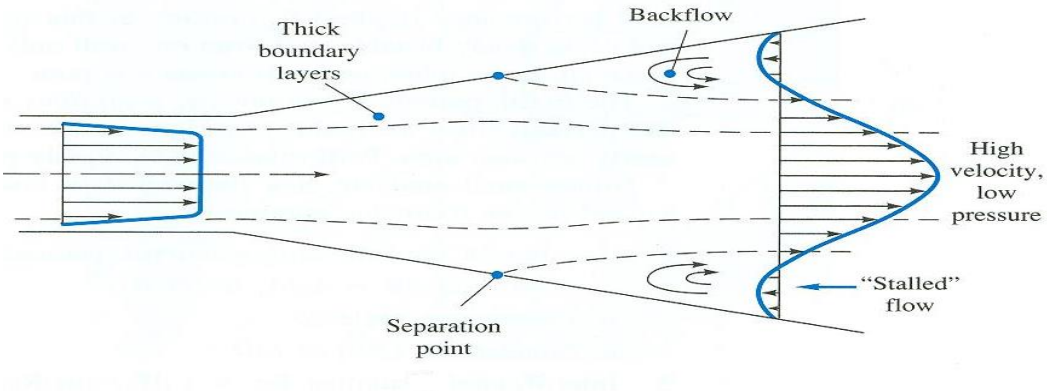

Figure 16 Diffusor with flow separation giving poor pressure recovery [3, p.399]

1.6.1 Diffuser stability map

Fox and Kline published in 1962 a flat diffuser stability map which can be used to determine a design with a minimum pressure loss coefficient, seen in figure (17) as the dotted $C_{p,max}$ line. In the no stall region the flow is steady, viscous and the performance is moderately good. In the Transitory stall region the flow is unsteady but it is here that the maximum efficiency occurs. In the bistable region there is a steady stall, but from one side only, the stall side may however flip flop back and forth from the two sides and performance is poor.

In the jet region the flow has separated almost completely from the wall and flows through the diffuser at nearly constant cross section making the pressure recovery very poor.

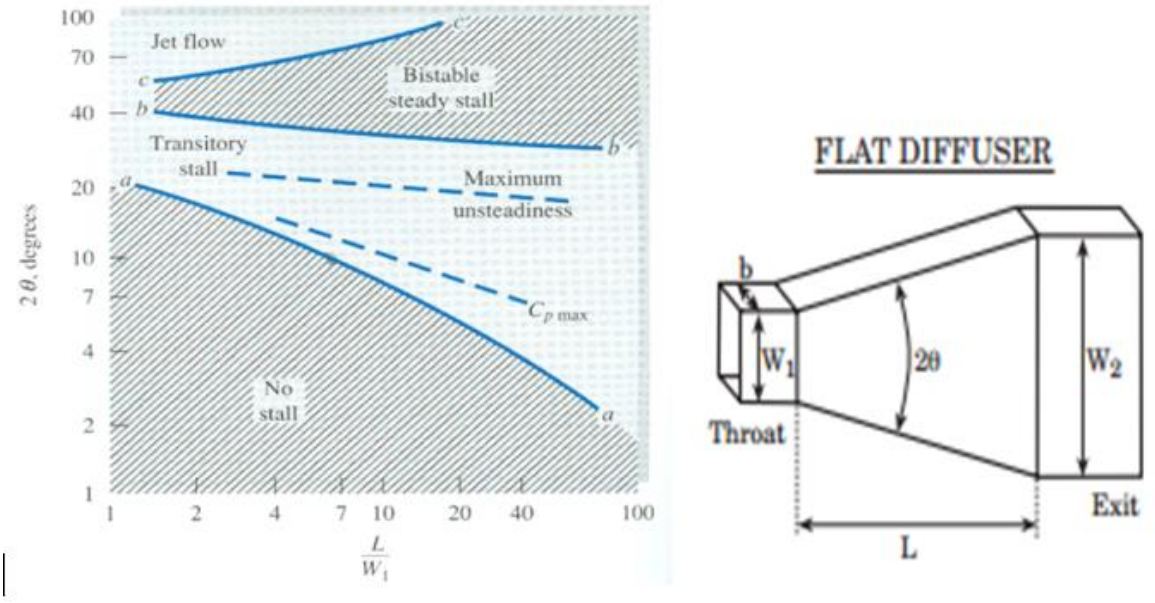

Figure 17 Diffusor stability map [3, p.398]

1.7 Computational fluid dynamics

Computational fluid dynamics or CFD is a tool used by scientist and engineers to solve heat and fluid flow problems. Because of the complexity of the governing equations, most practical problems does not have an analytical solution. CFD replaces the governing partial differential equations with a system of algebraic equations which can be solved by a computer, usually in an iterative way based on the boundary conditions. In this way an approximate numerical solution to the governing equations are obtained.

The most reliable information regarding heat and fluid flow challenges are obtained from measurements. However to build full scale models and conduct measurements can be very expensive and in some cases not possible. Another approach would be to build small scale models and extrapolate the information to full scale. Extrapolating is in itself an uncertain procedure and it is also likely that the small scale model cannot simulate all the mechanisms of the full scale model.

CFD is therefore a cost effective tool to use for simulating heat and fluid flow, especially in the studies of new designs and detailed product development. Nevertheless, CFD uses approximate numerical models and algorithms to solve the governing equations. It is

consequently of vital importance that these models are validated against trustworthy experimental data before they are utilized in the industry or elsewhere.

Computational fluid dynamics consist basically of four components which all people that are going to use a commercial or self-made CFD program have to think through.

- Discretization of the governing equations and solver
- Mesh
- Validation

In this thesis the commercial CFD program ANSYS Fluent 14.5 is to be utilized to study the effects of surface roughness.

1.7.1 Discretization of governing equations

To solve the governing continuous partial differential equations numerically it is necessary to convert the derivatives to discrete expressions. Much as when a physical quantity is measured in a laboratory at discrete points in the region of interest, the discrete expressions are solved at discrete points in space. By connecting the measurement points, a picture of the flow can be produced. The flow quantities between the measurement points are obtained by some interpolation technique which quality depends on how far the measurement points are from each other and the accuracy required.

The most widely used discretization techniques are:

- Finite difference method (FDM)
- Finite volume method (FVM)
- Finite element method (FEM)

ANSYS Fluent 14.5 uses the Finite Volume Method to discretize the governing equations. The fundamental flow equations are derived in FVM using integral approach. The FVM subdivides the spatial domain of the physical problem into non-overlapping cells known as control volumes. A single node is put in the geometrical center of the control volume. The numerical approximations are then obtained at the node by integrating the governing equations over the control volume. The increase of some quantity inside the control volume is equal to flux of quantity into CV minus flux of quantity out of CV plus a source term i.e:

Rate of increase of quantity inside CV = Flux of quantity in – Flux of quantity out + source

The quantity can be either a mass, momentum or energy component. This concept leads to the conservative equations in integral form with its general arrangement:

$$\frac{\partial}{\partial t}\oint_v \rho\varphi dV = -\oint_s \rho\varphi\vec{V}\cdot d\vec{S} + \oint_s \Gamma\nabla\varphi\cdot d\vec{S} + \int_v S_\varphi dV \tag{50}$$

- V=Volume
- S=Surface
- φ=Flow quantity
- F=Flux of θ
- S_φ=Source of θ
- Γ= Diffusion coefficient

Figure (18) shows a typical control volume with a node P in it is center. In the figure W, E, N and S represent respectively nodes west, east, north and south of node P. Likewise cell faces or surfaces are denoted $x_{e,w}$ and $y_{n,s}$.

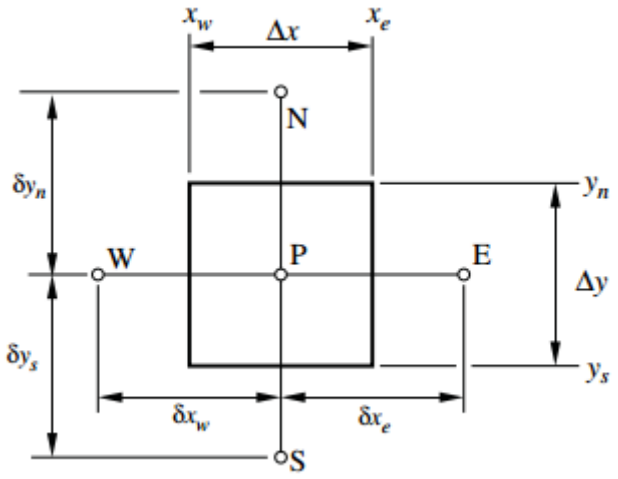

Figure 18: Control volume FVM [26]

As an example the one dimensional steady state convection equation without source term and constant velocity and surface area, is to be integrated around the control volume surrounding node P.

$$\int_V \frac{\partial(u_x\varphi)}{\partial x} dV = 0 \tag{51}$$

This will produce the discretized version of the equation by the finite volume method. The flow travels from left to right and by applying the Divergence theorem, we can replace the volume integral with surface integral:

$$\int_V \frac{\partial(u_x\varphi)}{\partial x} dV = \oint_A u_x\varphi n_x dA = (u_x\varphi A)_e - (u_x\varphi A)_w = 0 \tag{52}$$

The problem now is to obtain discrete expressions for the face fluxes. This process requires interpolation techniques, which vary in complexity and accuracy. The most known interpolation technique is the central difference scheme.

Central difference interpolation scheme:

In the central difference scheme the value of φ at the faces are approximated by assuming that the value at the faces is the average of the nodes in the immediately vicinity of the faces. I.e.

$$\varphi_e = (\varphi_P + \varphi_E)/2 \tag{53}$$

$$\varphi_w = (\varphi_W + \varphi_P)/2 \tag{54}$$

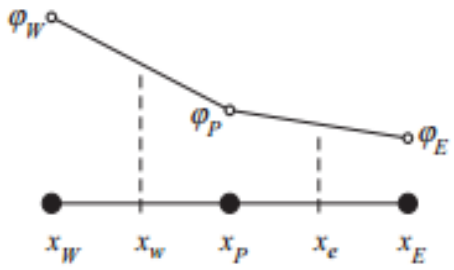

Figure 19: Central differencing scheme [26]

This method is very simple but unfortunately unstable, and also unable to identify flow directions. This means that in a strong convective flow, central differencing is unfitting because a certain flow direction would have almost all the influence. Therefore Fluent 14.5 offers to use another approach called upwinding.

First order upwinding interpolation scheme:

The upwind interpolation scheme employs the node "upstream" relative to u_x and in this way recognizes flow direction. Hence face values are approximated as:

$$\varphi_w = \varphi_W \tag{55}$$

$$\varphi_e = \varphi_P \tag{56}$$

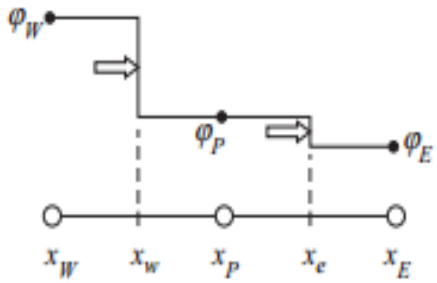

Figure 20: First order upwind scheme [26]

The first order upwind scheme has problems with numerical or false diffusion if the grid lines are not aligned. Therefore second order upwind scheme has been developed which employs two nodes upstream to determine the face values. This scheme is very popular because of its increased accuracy and high stability. Fluent 14.5 offers to use both first order and second order upwinding.

The first order upwind, one dimensional, steady state, incompressible convection equation, without source terms and constant velocity and area therefore yields:

$$\int_V \frac{\partial(u_x\varphi)}{\partial x} dV = u_x(\varphi_P - \varphi_W)A + error \tag{57}$$

Higher order schemes:

The Quadratic upwind interpolation for convective kinetics or QUICK scheme is similar to the second order upwind scheme, but instead fits a quadratic curve to the two nodes upstream and one node downstream of the faces to determine their values. This discretization technique has superb accuracy, but is more prone to instability problems during the calculations. The QUICK scheme has third order accuracy which will be explained later.

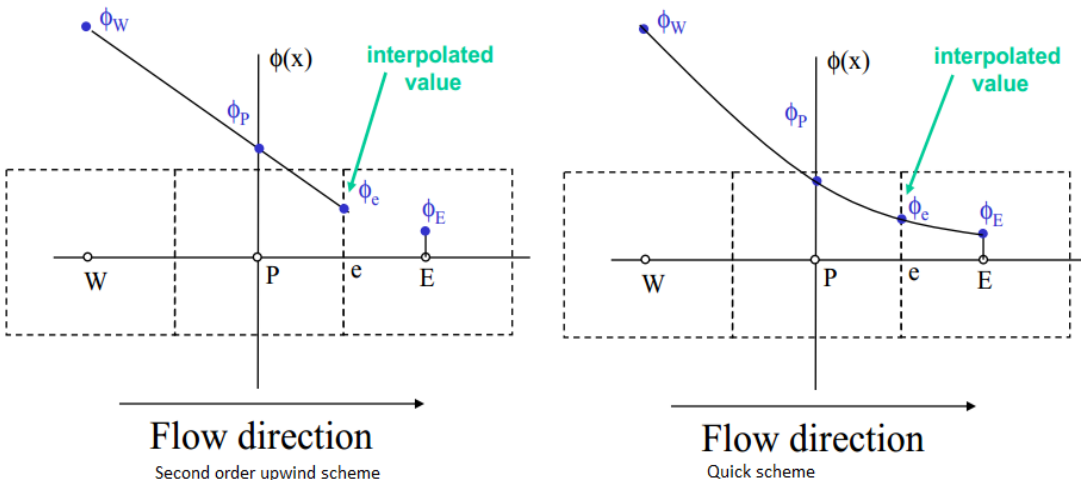

Figure 21: Second order upwind scheme to the left and QUICK scheme to the right [27]

Temporal discretization:

Steady state settings are favored in CFD analysis because they are easy to post process and have a lower computational cost. However, often the flow conditions are unsteady and the solution at a given point will therefore vary in time. The unsteadiness within the fluid happens due to the development of instabilities such as generation of eddies, shock waves, time dependent boundary condition and many more. Fluent 14.5 offers implicit temporal discretization. Implicit temporal discretization is often referred to as backward difference

method i.e. temporal terms are evaluated a t+Δt. The transient one dimensional incompressible convection equation with constant velocity and area yields:

$$\frac{\varphi^{t+\Delta t} - \varphi^{t}}{\Delta t} + \frac{\partial(u_x \varphi^{t+\Delta t})}{\partial x} = 0 \tag{58}$$

The transient discretization with a first order upwind method would result in the following expression:

$$\frac{\varphi^{t+\Delta t} - \varphi^{t}}{\Delta t} + u_x \frac{\left(\varphi_P^{t+\Delta t} - \varphi_W^{t+\Delta t}\right)}{\Delta x} = 0 + error(spatial, temporal) \tag{59}$$

In a transient simulation the solution to the flow field is obtained by iterating through discrete points in time, typically from the inlet boundary. The solution at time $t + \Delta t$ is then reached when the residuals are within a certain limit when compared with the solution at time=t. The chosen time step is of major importance when doing a transient analysis, because if the time step is too large the transient effects may not be resolved and consequently the results obtained will not lie on the correct solution curve.

By using the Courant number, one can be assured that the time step used is satisfactory. The Courant number gives the typical number of control volumes that a fluid parcel passes through in one time step. Having a Courant number less than or equal to one means that the fluid parcel does not pass a typical control volume in one time step, and that reassures that the solution field found is adequate. The two dimensional Courant number yields:

$$C = \frac{u_x \Delta t}{\Delta x} + \frac{u_y \Delta t}{\Delta y} \tag{60}$$

Where u_x and $u_y$are respectively typical speed in x and y direction and Δx and Δy denotes the typical size of the control volume (mesh size) in x and y direction.

1.7.2 Meshing

The mesh is the discrete representation of the geometry of the physical domain. The domain is divided into cells where the discretized partial differential equations are solved at each cell center. Since the accuracy of the solution is dependent on cell center distances, it is important that areas of strong gradients or high interest are divided into smaller control volumes. This is particularly important for boundary layer flow where the transverse gradient is by far the dominant gradient and hence needs to be resolved better. Dividing the geometrical area of interest into finer and finer cells devotes more computer capacity and

therefore it is necessary to have a coarser mesh in areas of less interest or little change in order to make the CFD analysis feasible.

The mesh is often characterized as structured or unstructured. Structured meshes have a regular connectivity which means that each point has the same number of neighboring points, whilst this may not be true in an unstructured mesh.

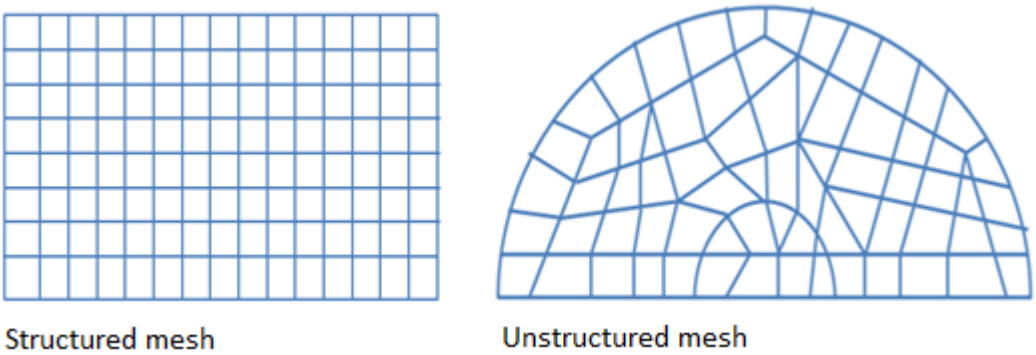

Figure 22: Structured mesh left versus unstructured mesh right [28]

A structured mesh is more computational efficient and may also be more accurate, but unfortunately not applicable to all geometrical shapes. Some complex geometries however have areas with regular curves which can be modeled using a structured grid, these grids are referred to as hybrid mesh.

Mesh quality

The quality of the mesh can be measured by several parameters, which together decides how appropriate the mesh is to produce good CFD results. In general a good quality mesh means that the solution is grid independent i.e. refining or altering the grid does not change the CFD results. Is also means that the studied physics are captured well and that the geometrical details of the flow problem are thoroughly incorporated. If the mesh is of poor quality there can be problems with convergence, numerical diffusion and the physics can also be treated in an incorrect way.

The three most common parameters for mesh quality testing are:

- Mesh aspect ratio
- Mesh smoothness
- Mesh skewness

Mesh aspect ratio

The mesh aspect ratio is the ratio of the longest edge length to the shortest edge length. A large aspect ratio means that a change in one direction will propagate much faster in one direction than the other, resulting in over or underestimating flow properties.

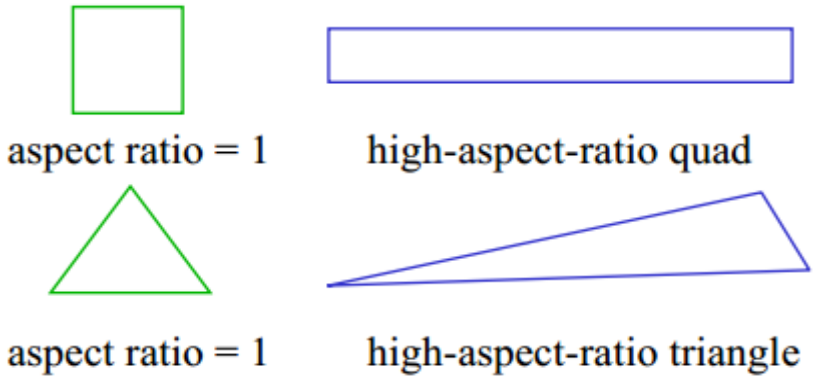

Figure 23 : Aspect ratio for quadratic and triangular cells [32]

However in boundary layer flow, large aspect ratios are accepted as the gradient in the transverse direction is much stronger than in the axial direction and to capture it is a vital part of resolving the boundary layer.

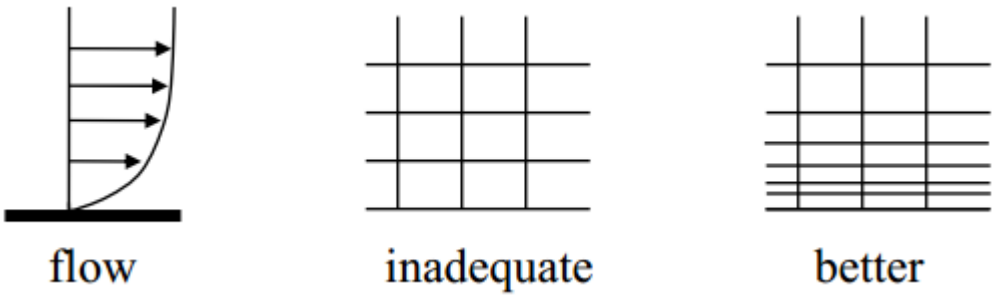

Figure 24: Boundary layer meshing [33]

Mesh smoothness

Because of the computational cost and the effectiveness of the CFD program, it is not feasible to have the same density of control volumes as in the near the wall regions throughout the flow domain. Therefore the ratio of the size of the control volumes have to increase as the flow enters areas of the flow domain with smaller gradients and less interest. The transition of cell sizes should not be higher than 20% in order to adequately capture the

flow properties. Abruptly change in cell size can like cells with high aspect ratio, cause errors in calculating face fluxes.

Mesh skewness

The mesh skewness is a measure of how much the cells differs from ideal geometry. In 2D the ideal shape would be triangles and squares. The skewness factor is defined in different ways for different shapes in 2D and 3D but in general a skewness factor of 0 is the best possible and a skewness of 1 is unsuitable. A large skewness is unfortunate for the accuracy of the interpolation techniques utilized by the numerical solvers.

To summarize the mesh quality parameters the following can be stated:

- Change in cell volumes should be smooth and not increase or decrease by a ratio of more than 1.2.
- More cells gives higher accuracy but is more computationally demanding.
- The aspect ratio should be close to one in multidimensional flows, but can be high in boundary layer flow.
- Areas of high interest must be resolved using a non-uniform mesh with variable mesh concentration.

1.7.3 Validation

For the numerical solvers to be effective in obtaining numerical results they need to be verified. There are three different rules that govern numerical schemes:

- Convergence
- Stability
- Consistency

Convergence:

Convergence can have several meanings. One definitions is that the finite volume solution approaches the true solution to the partial differential equations as the increments $\Delta x, y, z$ and Δt goes to zero. This implies that the solution should improve as the time step and cell

sizes are refined. In most cases the true solution is not known and hence it can be problematic to prove factual convergence. [31, p.50]

In steady state simulations another definition of convergence is to monitor the residuals or the difference in a particular iteration compared with the next iteration. If this approaches zero the solution is tending to converge, and when it reaches a certain value close to zero it has converge i.e. the solution is good enough. However if the residuals are still decreasing when the residual criterion is reached, then the solution may not be properly converged. Also if the residuals are no longer decreasing but have not reached the residual criterion, the solution is considered converged. Higher order discretization schemes are more accurate, but typically have higher residuals then lower order discretization schemes. [27, p.18]

In a transient simulation, the simulation is said to be converged when the time derivative for each time step reaches close to zero, this signifies that the solution has reached a steady state condition and is said to be converged.

Grid convergence or independency is also by many used as a convergence criterion. The solutions are obtained on finer and finer meshes until the results stop changing or reaches an acceptable limit. The result is then assumed to be the exact solution.

In all the cases above, one can however only conclude that a solution to the discretized domain and equations has been reached. This does unfortunately not mean that the physical correct solution has been obtained.

Stability:

Due to final precision of computers an error known as round off error is introduced. How this error perturbed as the computation is advancing can severely affect the solution. The numerical scheme is stable if the round off error does not accumulates or are negligible and can be dampen out. If the error builds up gradually and is mounting up, then the scheme is unstable, and the solutions given by the CFD program will typically be very oscillating.

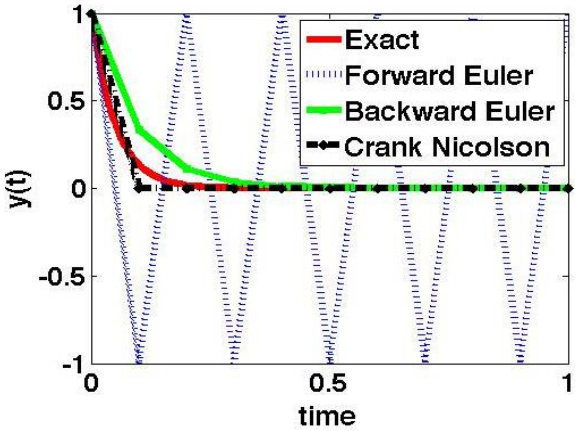

Figure 25: Demonstrating the instability of the Forward Euler method and the stability of the Backward Euler and Crank Nicolson methods [32]

Consistency:

Consistency implies that the discretization of the partial differential equations becomes the equation which it is related to when $\Delta x, y, z$ and Δt tends to zero. This means that the truncation error should disappear. The order of the truncation error can be quantified by doing a Taylor series expansion of equation (57) around node P in figure (18)

$$\int_V \frac{\partial(u_x\varphi)}{\partial x} dV = u_x(\varphi_P - \varphi_W)A + error \tag{61}$$

$$\varphi_W = \varphi_P - \Delta x \frac{\partial\varphi}{\partial x}\bigg|_P + \frac{\Delta x^2}{2}\frac{\partial^2\varphi}{\partial x^2}\bigg|_P - \frac{\Delta x^3}{6}\frac{\partial^3\varphi}{\partial x^3}\bigg|_P + \frac{\Delta x^4}{6}\frac{\partial^4\varphi}{\partial x^4}\bigg|_P - \cdots$$

Where dV=dA/dx. The first order upwind approximation may be obtained from the above by re-arranging the equation and multiplying by u_x as:

$$\frac{\partial(u_x\varphi)}{\partial x}\bigg|_P = u_x\frac{(\varphi_P - \varphi_W)}{\Delta x} + u_x\frac{\Delta x}{2}\frac{\partial^2\varphi}{\partial x^2}\bigg|_P - u_x\frac{\Delta x^2}{2}\frac{\partial^3\varphi}{\partial x^3}\bigg|_P + \cdots$$

$$\frac{\partial(u_x\varphi)}{\partial x}\bigg|_P = u_x\frac{(\varphi_P - \varphi_W)}{\Delta x} + O(\Delta x) \tag{62}$$

Proving first order accuracy for equation (57) and also shows that the discretized equation is consistent as Δx goes to zero.

1.7.4 Numerical diffusion

When examining equation (62), we can see that the error associated with the discretization by the FVM first order upwind scheme is of first order. This means that the first order upwind scheme will introduce some error into the solution of the flow field. The error will make the simulated system behave differently than the real physical system and can make the solution more diffusive. Since the discretization are approximations of the governing equations, and solved discrete in time and space, some of the flow properties must be convected from one cell into the neighboring one whether this is physical true or not. This is because of the interpolation techniques utilized to set the face values of the cells. To cope with this problem one can include more terms from the Taylor series expansion above into

the discrete equation and give it higher order accuracy. With a similar procedure as above one can show that the QUICK scheme is of third order accuracy $O(\Delta x^3)$, meaning that it takes the second order derivative from the Taylor expansion into account.

1.7.5 Relaxation factors

To improve the numerical stability of the different solution schemes one can apply relaxation factors. Meaning that the new value of some variable φ will be "relaxed" in comparison of the predicted value. This will slow down convergence, but will suppress oscillations resulting from numerical errors. Fluent uses relaxation factors by default.

$$\varphi_P^{new,used} = \varphi_P^{old} + U(\varphi_P^{new,predicted} - \varphi_P^{old}) \tag{63}$$

Where U is the relaxation factor.

- U<1 gives underrelaxation, will slow down convergence but increase stability
- U=1 means no relaxation, the predicted value of the variable is used
- U>1 gives overrelaxation, is used to speed up convergence but decreases stability

1.8 Turbulence modelling

Essentially all flows of engineering interest are turbulent and consequently the important effects of turbulence must be included in flow simulations. There are currently three numerical methods for capturing the turbulent effects:

- **Reynolds-averaged Navier-Stokes equations (RANS**)

  As discussed in section (1.2.3) for most engineering purposes one are not interested in resolving the full scale turbulent fluctuations, but rather in the mean properties of the flow. Therefore the Navier-Stokes equations are time averaged, and this process results in an extra term i.e. the Reynolds stresses which needs to be modeled in order to close the system of mean flow equations. There are many models developed for the Reynolds stresses which will be outlined later. However these models are based on the assumption that there exist a limited number of universal

features of turbulence, which when identified properly can lay the foundation for the full or adequately representation of the flow variables of importance to users of CFD. The computational cost for modeling the Reynolds stresses are relative low, as a result this approach has been and most likely will be, the favored method utilized by the industry.

- **Large eddy simulations (LES)**

  In large eddy simulations the large scale eddies are resolved and the small scale eddies are modeled. The effects of the small scale eddies on the large eddies and mean flow are included through a sub-grid system. LES is implicitly based on Kolmogorov's self-similarity theory, where large eddies are dependent upon the geometry surrounding the flow, whilst small eddies are universal. LES has been more successful in areas where RANS fail to meet, for example; flow around bluff bodies, combustion, mixing flow and flow separation [33, p.7]. In terms of computational resources, LES are much more costly then RANS but more accurate in some applications.

- **Direct numerical simulations (DNS)**

  In direct numerical simulations all scales of the turbulence have to be resolved, no modeling should be included. This implies that the full Navier-Stokes equations are solved on a spatial and temporal grid fine enough to resolve the Kolmogorov length scale up to the integral scale associated with the eddies containing most of the turbulent kinetic energy. It must also capture the fastest turbulent fluctuations, this means that in order to be accurate the time step must be appropriately small such that a fluid parcel only moves a fraction of the mesh size for each time step. DNS is the most accurate but costly method in terms of computer resources and is currently not utilized commercially by the industry.

1.8.1 Reynolds averaged Navier-Stokes turbulence models

The preferred method used to capture the effects of turbulence in this thesis is the Reynolds averaged Navier-Stokes equations. This means that a turbulence model for the Reynolds stresses must be incorporated. Since to this day, there is no classical model based on the time average equations, which represent a complete and general multi-purpose turbulence

depiction suitable for all flows, the development and optimization of turbulence models for a limited number of flows has been necessary. There are many models design for this task, all with its own strengths and weaknesses but in general they have to be economical, accurate to run and have a wide range of applicability. Some of the more well-known models includes:

- Zero equation model: Mixing length model
- One equation model: Spalart-Allmaras model
- Two equation model: K-ε models
- Two equation model: K-ω models
- Seven equation model: Reynolds stress model (RSM)

Where the number of equations denote how many extra PDE's needed to solve the model. All of the above except the RSM are based on the assumption that there exist an analogy between the action of the viscous stresses and the Reynolds stresses on the flow. This lays the foundation for Boussinesq eddy viscosity hypothesis. Boussinesq suggested that the Reynolds stresses can be modeled adequately through use of the mean velocity gradients and the eddy viscosity. The idea behind this is the observation that turbulence increases as the mean rate of deformation increases, likewise turbulence decays if there is no shear in isothermal incompressible flow [34, p.67]. In this way the transfer of momentum by turbulent fluctuations, can be modeled in the same way as the momentum transfer caused by molecular diffusion. The incompressible Boussinesq eddy viscosity hypothesis states that:

$$-\rho\overline{u_i'u_j'} = \mu_t\left(\frac{\partial U_i}{\partial x_j}+\frac{\partial U_j}{\partial x_i}\right)-\frac{2}{3}\rho k\delta_{ij} \tag{64}$$

The last term on the right hand side is there to ensure that the normal Reynolds stresses sum to the mean turbulent kinetic energy.

The Boussinesq approximations corresponds with the observations in [34, p.67], where turbulence increases as the mean rate of deformation increases and decays in the absence of shear. The deformation rates are because of viscosity, high near solid surfaces and decreases towards the free stream velocity, where the inertial forces are dominant and the effects of wall shear is shrinking. Accordingly towards the free stream, the turbulence should also decline. In the Boussinesq approximation one can see that the turbulent fluctuations drops as the mean rate of deformation decreases.

Another implication of Boussinesq is the assumption of isotropic eddy viscosity. This suggests that the ratio of the velocity gradients and the Reynolds stresses are independent

of directions. However many complex flows has several velocity gradients and the assumption that one single eddy viscosity should represents an accurate relationship between all the velocity gradients and the Reynolds tresses is doubtful. Therefore when using the Boussinesq assumption one need to be considerate especially towards these effects [16, p.59]:

- Flows with strong curvature (diffuser, bends)
- Flows with strong anisotropy
- Flows where directional forces affects the turbulence
- Flows where turbulent production and dissipation are uncorrelated.
- Flows involving separation

I more complex flows because of the isotropic eddy viscosity assumption in equation (64), the Boussinesq approximation can easily predict to small or to large Reynolds stresses. In these circumstances it is better to use transport equations for the Reynolds stresses themselves.

1.8.2 Mixing length model (zero equation)

The mixing length model is also referred to as a zero equation model because no extra equations are needed in order to close the RANS equations. The mixing length concept was developed by Prandtl which proposed that each turbulent fluctuation could be related to a length scale and a velocity scale. The mixing length is defined analogous to the molecular mean free path, as the distance a fluid parcel will conserve its properties before blending in with the surroundings.

The mixing length models can be used to some extent where there is only one dominant velocity gradient as for example in a thin shear layer. In this case, the relevant components of X can be expressed as:

$$-\overline{u'v'} = \mu_t \frac{\partial U}{\partial y} \tag{65}$$

Then Prandtl assumed that $\mu_t \sim u l_m$ and that $u \sim l_m \left|\frac{\partial U}{\partial y}\right|$ where l_m is the mixing length and u is a turbulent velocity scale.

Consequently the Reynolds stresses could be modeled as:

$$-\overline{u'v'} = l_m^2 \left|\frac{\partial U}{\partial y}\right| \frac{\partial U}{\partial y} \tag{66}$$

One quite considerable disadvantage of this model is that the mixing length is dependent on the nature of the flow, and hence empirical correlations are needed. This makes the model not suited for complex flows and separation. The mixing length model also only calculates mean flow properties and Reynolds shear stresses.

1.8.3 Spalart-Allmaras (one equation)

The Spalart-Allmaras model is a one equation model that solves a modeled transport equation for turbulent viscosity[34, p.89]. The model is especially is designed for aerodynamic and turbo machinery applications where it is necessary to resolve the boundary layer and effectively handle pressure gradients, both favorable and adverse.

The Reynolds stresses are modeled using the Boussinesq approach, but without the mean turbulent kinetic energy term and therefore yields:

$$-\rho\overline{u_i'u_j'} = \mu_t \left(\frac{\partial U_i}{\partial x_j} + \frac{\partial U_j}{\partial x_i}\right) \tag{67}$$

The transport equation for kinematic eddy viscosity:

$$\frac{\partial \rho\tilde{\nu}}{\partial t} + \frac{\partial}{\partial x_i}(\rho\tilde{\nu}U_i) = \frac{1}{\sigma_\nu} div\left[(\mu + \rho\tilde{\nu})grad(\tilde{\nu}) + C_{b2}\rho\left(\frac{\partial\tilde{\nu}}{\partial x_k}\right)^2\right] + C_{b1}\rho\tilde{\nu}\tilde{\Omega} - C_{w1}\rho\left(\frac{\tilde{\nu}}{ky}\right)^2 f_w \tag{68}$$

Where the different terms are as follows:

Rate of change of kinematic eddy parameter $\tilde{\nu}$:

$$\frac{\partial \rho \tilde{\nu}}{\partial t} \tag{69}$$

Transport of $\tilde{\nu}$ by convection

$$div(\rho \tilde{\nu} \boldsymbol{U}) \tag{70}$$

Transport of $\tilde{\nu}$ by turbulent diffusion

$$\frac{1}{\sigma_\nu} div\left[(\mu + \rho\tilde{\nu}) grad(\tilde{\nu}) + C_{b2}\rho \frac{\partial \tilde{\nu}}{\partial x_k}\frac{\partial \tilde{\nu}}{\partial x_k}\right]: \tag{71}$$

Rate of production of $\tilde{\nu}$

$$C_{b1}\rho\tilde{\nu}\tilde{\Omega} \tag{72}$$

Rate of dissipation of $\tilde{\nu}$

$$C_{w1}\rho\left(\frac{\tilde{\nu}}{ky}\right)^2 f_w: \tag{73}$$

The eddy viscosity is linked to the kinematic eddy parameter by the relation

$$\mu_t = \rho\tilde{\nu} f_{\nu 1} \tag{74}$$

Where $f_{\nu 1}$ is a wall dampening function which goes to zero at the wall and towards one at high Re numbers. In this way Newtonian viscosity dominates at the wall and likewise the eddy viscosity is the principal viscosity at high Re numbers?

$$\tilde{\Omega} = \Omega + \frac{\tilde{\nu}}{(ky)^2} f_{v2} \tag{75}$$

Where Ω is the mean vorticity defined as:

$$\Omega = \sqrt{2\Omega_{ij}\Omega_{ij}} \tag{76}$$

And Ω_{ij} is the mean vorticity tensor defined as:

$$\Omega_{ij} = \frac{1}{2}\left(\frac{\partial U_i}{\partial x_j} - \frac{\partial U_j}{\partial x_i}\right) \tag{77}$$

f_{v2} and f_{w2} are additional wall damping functions and ky is an algebraic expression for the length scale with the wall distance y and the Von Karman constant 0.41. The constants C_{b1}, C_{b2} and C_{w1} are models parameters which has been tuned for external aerodynamic flows.

As mentioned the Spalart-Allmaras model is developed for aerodynamic and turbo machinery applications which implies that it is especially suited for wall bounded flows. In its original form the model is effectively a low Reynolds number model, meaning that for the model to perform at its best the boundary layer must be properly resolved. If the mesh is found fitting the model will utilize equation (37) to obtain the wall shear stress. Fluent will however utilize wall functions if the resolution of the boundary layer is not found suitable [42].

Pro and cons Spalar-Allmaras model

The Spalart-Allmaras model is especially designed to handle pressure gradients and has also proven economical and accurate for flows with mild separation and recirculation. However, because the model does not include transport effects for turbulent length scales it is considered weak for internal, complex and massively separated flows [33, p.32].

The Spalart-Allmaras model has not yet been extensively validated to all type of complex engineering flows and cannot be relied on to predict the decay of homogeneous, isotropic turbulence [33, p.12]. Moreover, the model might encounter problems with flows subjected to rapidly changes in length scales.

1.8.4 K-ε two equation model

The standard two equation k-ε model represent the eddy viscosity in terms of transport equations for the mean turbulent kinetic energy and for the turbulent dissipation rate. These transport equation contains several new unknowns which themselves are needed to be modeled. The Reynolds stresses are represented by the Boussinesq approximation, and thereby closes the equations. Since the k-ε model uses transport equation for the TKE and the dissipation rate, it follows from equation (20) that the model explicitly also calculates characteristic turbulent velocity and length scales, hence the model includes historical effects related to the flow. When considering the transport equation of TKE i.e. equation (14), there are three terms in addition to the Reynolds stresses that needs modeling. The

triple correlation $\overline{u_i' u_i' u_j'}$ and the pressure-velocity correlation $\overline{p' u_j'}$ in the diffusive term D_k are unknown, whilst the viscous part of the diffusive term is neglected. The k-ε model therefore only applies to fully turbulent flows and consequently the use of wall functions near solid boundaries are vital. The dissipative term of the TKE equation are modeled by another transport equation to make the model complete.

The production term P_k contains only known quantities provided we use the Boussinesq assumption, and therefore can be modeled in this manner:

$$P_k = \left(2\nu_t S_{ij} - \frac{2}{3}\rho k \delta_{ij}\right)\frac{\partial U_i}{\partial x_j} \tag{78}$$

Where S_{ij} is the rate of strain tensor defined as:

$$S_{ij} = \frac{1}{2}\left(\frac{\partial U_i}{\partial x_j} + \frac{\partial U_j}{\partial x_i}\right) \tag{79}$$

Therefor in incompressible and more compact form, the modeled production term can be written:

$$P_k = 2\nu_t S_{ij} S_{ij} \tag{80}$$

In flows with high Reynolds number the diffusive transport of k due to viscous stresses are very small compared with the turbulent diffusion and is therefore neglected. The remaining part can be modeled using an analog to Fick law of mass flux, which states that flux goes from regions of high concentration to regions of low concentration, with a magnitude that is proportional to the concentration gradient. Fick law yields:

$$J = -D\nabla\varphi \tag{81}$$

Here J is the diffusion flux, or amount of substance per unit area per unit time. D is the diffusion constant with dimensions (length^2)/time, and φ is the concentration in substance per volume. Using this analogy the turbulent diffusion term can be modeled accordingly:

$$D_k = \frac{\partial}{\partial x_j}\left(\frac{\mu_t}{\sigma_k}\frac{\partial k}{\partial x_j}\right) \tag{82}$$

Where σ_k is the turbulent Prandtl number, which is the ratio of the eddy viscosity to the eddy diffusivity.

To make the model complete, the dissipative term is modeled through a separate transport equation. The transport equation for the dissipative term is derived from the Navier-Stokes and continuity equation. The form of the modeled equation for the dissipative term has similar structure as the one for TKE and yields:

$$\frac{\partial \varepsilon}{\partial t} + U_j \frac{\partial \varepsilon}{\partial x_j} = \frac{\partial}{\partial x_j}(D_\varepsilon) + \frac{\varepsilon}{k} c_{\varepsilon 1} P_{\varepsilon k} - Q \tag{83}$$

Where the terms on the left hand side is respectively the rate of increase, plus the convective transport of ε. The first term on the right-hand side is the diffusive transport of ε followed by the rate of production and destruction of ε.

For the diffusive term in the dissipation equation a gradient model is used analogous to the one used in the TKE equation:

$$D_\varepsilon = \frac{\nu_t}{\sigma_\varepsilon} \frac{\partial \varepsilon}{\partial x_j} \tag{84}$$

The production and destruction of ε is put proportional to production and destruction of TKE.

$$P_\varepsilon = C_{\varepsilon 1} \frac{\varepsilon}{k} P_k \tag{85}$$

$$Q_\varepsilon = C_{\varepsilon 2} \frac{\varepsilon}{k} \varepsilon \tag{86}$$

These two terms are closely linked, as a greater production of TKE should be followed by an increase in the dissipation rate to avoid energy accumulation. Likewise should the destruction of turbulence be less if the production is decreasing [16, p.54]

The famous general k-ε epsilon equations are presented [34, p.75]:

$$\frac{\partial(k)}{\partial t} + U_j \frac{\partial k}{\partial x_j} = \frac{\partial}{\partial x_j}\left[\frac{\nu_t}{\sigma_k}\frac{\partial k}{\partial x_j}\right] + 2\nu_t S_{ij} \cdot S_{ij} - \varepsilon \tag{87}$$

$$\frac{\partial(\varepsilon)}{\partial t} + U_j \frac{\partial \varepsilon}{\partial x_j} = \frac{\partial}{\partial x_j}\left[\frac{\nu_t}{\sigma_\varepsilon}\frac{\partial \varepsilon}{\partial x_j}\right] + C_{1\varepsilon}\frac{\varepsilon}{k} 2\nu_t S_{ij} \cdot S_{ij} - C_{2\varepsilon}\varepsilon \tag{88}$$

The kinematic eddy viscosity in the k-ε model is specified analogous to equation (21), but with an extra proportionality term.

$$\nu_t = C_\mu \frac{k^2}{\varepsilon} \tag{89}$$

From equation (19), the eddy viscosity was defined as a function proportional to a length and velocity scale related to the largest eddy structures. Therefore the use of the small eddy variable ε to define the large eddy scale l could be dubious. But since the extraction of energy from the mean flow by the large eddies is matched by the energy cascade ending up at the smallest dissipating eddies, this is acceptable.

The k-ε model thus has five empirical constants:

$$C_\mu = 0.09 \qquad \sigma_k = 1 \qquad C_{1\varepsilon} = 1.44 \qquad C_{2\varepsilon} = 1.92 \qquad \sigma_k = 1.3$$

These parameters are derived by systematic data fitting for a comprehensive range of turbulent flows. They are constants in the equations, since they are not altered during calculations. Still, the constants are not universal but are expected to change little between different flow scenarios. Modifications of the constants can however be imposed to account for effects such as rotation, curvature or swirl.

Since the Newtonian viscosity is neglected in the k-ε model, wall functions are needed to resolve the boundary layer.

To account for the k-ε models lack of accuracy in the near wall region, different variants of the model has been developed to challenge these difficulties. These variants includes the k-ε RNG (renormalization group theory) and the k-ε Realizable model. The main improvements for these models are as follows:

K-ε RNG

- Rather than standard wall functions, the RNG model uses an analytically derived differential formula for the effective viscosity that accounts for low-Reynolds number effects. [35]

- The RNG models is modified with an additional term in the epsilon equation to improve accuracy for rapidly strained flows.

- The effect of swirl is included in the RNG model.

K-ε Realizable

- In the k-ε Realizable model, a new transport equation for the dissipation rate has been derived from the exact equation for the transport of the mean square velocity fluctuation.[36]

- The C_μ parameter is not constant in the Realizable model but a function of the mean strain rotation rates, angular velocity of the system and the turbulent fields (k and ε) [36].

Pro and cons k-ε model

The k-ε model is one of the most widely used turbulence models because of its reasonably well predictions of a wide range of industrial flows. The model is simple to implement, relatively affordable in terms of computational costs, it incorporate history effects and only initial or boundary conditions are needed to be supplied.

The model is however developed for high Reynolds number flow, and consequently it is not accurate close to the wall where TKE and ε have large peaks. This especially true for flows with adverse pressure gradients [37, p.120], which is because the k-ε model tends to produce too large turbulent length scales in the near wall region and other areas with large strain rates. Thereby the TKE gets amplified and in this way, phenomenon's such as separation gets suppressed or delayed [37, p.121]. The k-ε model also performs poorly for flows where large streamlined curvature is present [33, p.14].

Models like the k-ε RNG and k-ε Realizable are often preferred to the standard k-ε model since these models includes terms which improves results for rapidly strained flows, strong streamline curvature and low Reynolds number effects. These correction terms have shown

to improve the results for the k-ε based models in some areas, e.g. the RNG model shows better results towards expanding ducts flow, relative to the standard k-ε model, however it performs worse for contracting duct flow of the same area ratio [34, p.88]. According to [36] studies have shown that the k-ε realizable model gives the most accurate results towards complex and separated flows when compared with the standard k-ε and RNG model.

Attempts to improve the results for k-ε based equations by including terms for low Reynolds effects is according to [37, p.142] a popular misconception since observations show that the k-ε model is inconsistent with the defect layer, and therefore it is not reasonable that viscous correction will be a remedy for the problems with the k-ε towards for example flow separation.

1.8.5 K-ω two equation model

The k-ω model is analogous to k-ε in the way that it utilizes the Boussinesq assumption, but employs the specific dissipation rate of TKE i.e. omega rather than epsilon. The specific dissipation rate of TKE is defined as ω = ε / k which is the reciprocal of the eddy turnover time, and accordingly it is related to the frequency of the largest eddies.

When using this equation the length scale compared to k-ε has to change because of dimensional requirements to yield:

$$l = \frac{\sqrt{k}}{\omega} \tag{90}$$

And naturally the eddy kinematic viscosity becomes:

$$\nu_t = \frac{k}{\omega} \tag{91}$$

Consequently the k-ω model also account for history effects related to the flow. It was Kolmogorov that first postulated the k-ω equations, but this first version has been found unfitting [37, p.86] therefore Fluent utilizes the k-ω model which is based on Wilcox improved model and incorporates modifications for low-Reynolds number effects, compressibility and shear flow spreading [44] and yields:

$$\frac{\partial(k)}{\partial t} + U_j \frac{\partial k}{\partial x_j} = \frac{\partial}{\partial x_j}\left[\left(\nu + \frac{\nu_t}{\sigma_k}\right)\frac{\partial k}{\partial x_j}\right] + P_k - \beta^* f_\beta k\omega \tag{92}$$

$$\frac{\partial(\omega)}{\partial t} + U_j \frac{\partial \omega}{\partial x_j} = \frac{\partial}{\partial x_j}\left[\left(\nu + \frac{\nu_t}{\sigma_\omega}\right)\frac{\partial \omega}{\partial x_j}\right] + \alpha \frac{\omega}{k} P_k - \beta f_\beta \omega^2 \quad (93)$$

The first two terms on the left hand side represent respectively the rate of change, and the transport of k or ω by convection. The first term on the right hand side is the diffusive transport of k or ω and the two last terms represent respectively the rate of production and rate of dissipation of k or ω.

Fluent uses a modified eddy viscosity for the k-ω model to account for low Reynolds number effects. Therefore the operational eddy viscosity in Fluent yields:

$$\nu_t = a^* \frac{k}{\omega} \quad (94)$$

$$a^* = a^*_\infty \left(\frac{a^*_0 + \frac{Re_t}{R_k}}{1 + \frac{Re_t}{R_k}} \right) \quad (95)$$

Where the a^* is a dampening function implemented to damp the turbulent viscosity in order to make sure that viscous stresses takes over from turbulent stresses at low Reynolds numbers and in the viscous sub-layer next to the walls. Consequently a^*=1 in the outer area of the boundary layer where to flow is fully turbulent and a^*=0 near the surface in the viscous region. The production of ω has a similar damping function in α, whilst the dissipative terms for TKE and ω have more complex correction terms in the form of β^*, β and f_β.

The model constants are as follows:

$Re_t = \frac{\rho k}{\mu \omega}$ $\quad R_k = 6$ $\quad \sigma_k = 2$ $\quad \sigma_\omega = 2$ $\quad \alpha^*_0 = \frac{\beta_i}{3}$ $\quad \beta_i = 0.072$

Pro and cons k-ω model

The k-ω equations inhabits several advantages over the more popular k-ε model. The greatest difference is seen in the way the k-ω model handles boundary layers with adverse pressure gradients in a quite accurate manner, whilst k-ε model almost completely fails under such flow conditions [37, p.165] This is especially true when the wake strength parameter is more than [37, p.120] which is not particularly high. The model can also easily be integrated to the wall without any viscous damping, and with viscous damping the model predicts TKE boundary layer features in a relatively correct way. There is also evidence that the model effectively engage problems with recirculating [37, p.165]. Accordingly to [9, p.462] the k-ω model has proven to be superior to the k-ε model with regards to APG boundary layer flow

The k-ω model is however not as effective in free shear flows as the k-ε model, and the boundary layer computations can be sensitive to the values of ω in the free stream [37, p.165]

1.8.6 Menter K-ω SST (Shear stress transport)

Menter [46] noted the superior achievement of the k-ω model over the k-ε in the near wall region and under adverse pressure gradients. He also understood that Wilcox's original k-ω model is overly sensitive to the free stream value of ω, while the k-ε model is not prone to such problems. Therefore Menter developed a hybrid model to effectively blend the robust and accuracy of the k-ω model in the near wall region with the free stream independence of the k-ε model in the fully turbulent region far from the wall [34, p.91].

By converting the k-ε equations into a ω formulation using the relation ε=kω, Menter successfully established the SST k-ω model which is quite similar to the k-ω model but with the following modifications:

- The eddy viscosity is modified to account for the transport of turbulent shear stress.
- The k-ω and k-ε model are both multiplied with a blending function and added together. The blending function is modified to be one near the wall to activate the standard k-ω model, and zero away from the surface which activates the transformed k-ε model.
- The k-ω SST model incorporates a damped cross diffusion term in the ω formulation.
- The modeling constants are different.

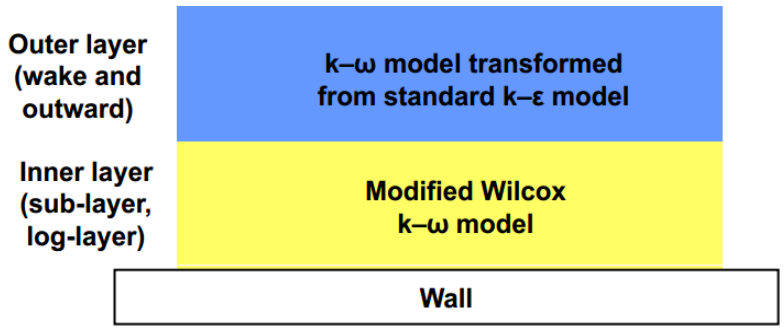

Figure 26: k-ω SST model wall transformation from k-ε to k-ω model [33, p.19]

The k-ω SST transport equations for respectively TKE and specific turbulent dissipation rate are presented as in the fluent user guide:

$$\frac{\partial(\rho k)}{\partial t}+\frac{\partial(\rho k u_i)}{\partial x_i}=\frac{\partial}{\partial x_j}\left[\left(\mu+\frac{\mu_t}{\sigma_k}\right)\frac{\partial k}{\partial x_j}\right]+\tilde{P}_k-Y_k \tag{96}$$

$$\frac{\partial(\rho\omega)}{\partial t}+\frac{\partial(\rho k\omega)}{\partial x_i}=\frac{\partial}{\partial x_j}\left[\left(\mu+\frac{\mu_t}{\sigma_\omega}\right)\frac{\partial \omega}{\partial x_j}\right]+\frac{\alpha}{\nu_t}\tilde{P}_k-Y_\omega+D_\omega \tag{97}$$

Where the two first terms on the left hand side are respectively rate of change of k or ω and the transport of k or ω due to convection. The first term on the right hand side is the diffusive transport of k or ω. The capital letter $\tilde{P}_k$ represent production of k and ω, whilst Y represent dissipation of k and ω.

When comparing equation (84) with (88) we can see that equation (88) has an extra term D_ω included at the right hand side. When the standard k-ε model is transformed into a k-ω formulation by the substitution ε=kω, the cross diffusion term is introduced and in this way couples the k-ε and k-ω models. The cross diffusion term stems from the k-ε formulation and is therefore only active in the far field remote from the wall and tends to zero when approaching the wall.

$$D_\omega=2(1-F_1)\rho\sigma_{\omega,2}\frac{1}{\omega}\frac{\partial k}{\partial x_j}\frac{\partial \omega}{\partial x_j} \tag{98}$$

Where F_1 is a blending function, which purpose is to switch the SST model between the k-ω and k-ε formulations by changing smoothly from 1 close to the wall so as to make the cross diffusion term zero, and one far from the wall giving the k-ε formulation in the far field.

The constants used in the cross diffusion term are also blended between the two formulations.

The eddy viscosity is defined as:

$$\nu_t = \frac{k}{\omega}\frac{1}{max\left[\frac{1}{\alpha^*}, \frac{SF_2}{\alpha_1 \omega}\right]} \tag{99}$$

Where S is the strain rate magnitude, $\alpha^*$is defined above and and F_2 is another blending function which ensures that the eddy viscosity model accounts for turbulent shear stress transport in regions of adverse pressure gradients.

The production term $\tilde{P}_k$ is modified to limit the buildup of turbulent kinetic energy in stagnation areas, and therefor yields:

$$\tilde{P}_k = min(P_k, 10\rho\beta^* k\omega) \tag{100}$$

Where P_k is the same as in the standard k-ω model and β^* is in this case a correction term based on compressibility and low Reynolds numbers.

For more details see fluents user guide

Pro and cons k-ω SST

By combining the k-ω and k-ε models it is possible to utilize the individual strengths of the two models and thereby get the best of each model. The sensitivity of the k-ω model towards free stream values of ω are avoided by utilizing the k-ε model which has no such sensitivity. The low Reynolds number difficulties of the k-ε model are encountered by switching to the k-ω model which shows great accuracy in boundary layer flows.

Additionally the k-ω SST model has been fitted with stress limiters in the viscosity and production term respectively in order to ensure that the turbulent stress does not become too large in regions of adverse pressure gradients and to avoid buildup of turbulent kinetic energy in stagnation areas.

1.8.7 Reynolds stress models (RSM)

By subtracting the mean values from the instantaneous Naver-Stokes equations the differential transport equations governing the behavior of the individual stresses can be derived. The Boussinesq assumption and thereby the eddy viscosity are discarded and the Reynolds stresses are computed directly together with an equation for the dissipation rate. The transport equations for the Reynolds stresses are very complex and thus need modeling. The solution to these modeled form of the stresses are often referred to as second order closure [9, p.452].

The RSM model is the most sophisticated turbulence model that Fluent provides

The RSM differential equations can be expressed as follows [34, p.81]:

$$\frac{D}{Dt}(R_{ij}) = D_{ij} + P_{ij} + \Pi_{ij} - \varepsilon_{ij} + \Omega_{ij} \tag{101}$$

Where $R_{ij} = \overline{u_i' u_j'}$ and the first term on the left hand side represent respectively rate of change, and transport of R_{ij} by convection. The terms on the right hand side are as follows:

$D_{ij} =$ Transport of R_{ij} by turbulent diffusion plus

$P_{ij} =$ Rate of production of R_{ij} plus

$\Pi_{ij} =$ Transport of R_{ij} due to turbulent pressure strain interactions minus

$\varepsilon_{ij} =$ Rate of dissipation

$\Omega_{ij} =$ Transport of R_{ij} due to rotation

Where the exact different terms are as follows:

$$D_{ij} = -\frac{\partial}{\partial x}\left(\overline{u_i' u_j' u_k'} + \frac{\overline{p' u_i'}}{\rho}\delta_{ki}\right) \qquad P_{ij} = -\overline{u_i' u_k'}\frac{\partial \overline{u}_j}{\partial x_k} - \overline{u_j' u_k'}\frac{\partial \overline{u}_i}{\partial x_k}$$

$$\Pi_{ij} = \overline{\frac{p'}{\rho}\left(\frac{\partial u_i'}{\partial x_j} + \frac{\partial u_j'}{\partial x_i}\right)} \qquad \varepsilon_{ij} = 2\nu\overline{\frac{\partial u_i'}{\partial x_j}\frac{\partial u_j'}{\partial x_i}} \qquad \Omega_{ij} = \nu\nabla^2\left(\overline{u_i' u_j'}\right)$$

The terms related to convection, molecular diffusion and production of R_{ij} are all exact. To obtain a solvable form of equation (101) the terms governing the turbulent diffusion, dissipation and pressure strain correlation have to be modeled.

The diffusion term can be modeled by a gradient assumption similar to what is done in the two equation models. Therefore the transport of Reynolds stresses by diffusion is assumed proportional to the gradients of Reynolds stresses

$$D_{ij} = div\left(\frac{\nu_t}{\sigma_k} grad(R_{ij})\right) \tag{102}$$

Where the kinematic eddy viscosity is defined by equation (89) and the value of $\sigma_k$is set to 0.82

The pressure strain term is the one that is the most difficult to model accurately, and is regarded as the term bringing the highest amount of uncertainty into the model. That the term is unmeasurable is not making the process of producing improved models any easier either. The general effect of the pressure strain term is to redistribute energy between the normal stresses and in this way make them more isotropic. This process will then implicitly reduce the Reynolds shear stresses. When approaching the wall however the anisotropy of the normal stresses increases due to the dampening of fluctuations normal to the wall. It is therefore necessary to add a wall reflection term in the model to include these effects [34, p.82].

The dissipative rate term is modeled similar to the one used in the k-ε equation. The smaller eddies are assumed to dissipate their energy isotropic by relating the dissipation of the normal Reynolds stresses to the dissipation of TKE. This is achieved by the relation:

$$\varepsilon_{ij} = \frac{2}{3}\delta_{ij}(\rho\varepsilon + Y_M) \tag{103}$$

Where δ_{ij} is the Dirac function and $Y_M$is related to dilation of dissipation through compressibility effects.

Pro and cons RSM

The RSM model is the most complete turbulence model available in Fluent in the sense that history effect, transport and anisotropy of turbulent stresses are all accounted for. Hence flows that are not adequately represented by the Boussinesq eddy viscosity model can be better predicted by the RSM. However the models requires substantially higher CPU time, and can in many circumstances be computationally too expensive to run.

1.8.8 Near Wall treatment

Accurate calculations in the near wall region is of highest importance in achieving good simulation results. The near wall region can inhabit very large velocity gradients, therefore incorporation of these effects are related to how the boundary layer is resolved. This can be achieved using wall functions or resolving the boundary layer itself by near wall modeling.

Wall functions

This approach is based on the law of the wall formulations from section (1.3) and tries to correctly incorporate the effects of the boundary layer, without having modify the turbulence models to account for the presence of a wall and thereby build a mesh fine enough to resolve the boundary layer behavior explicitly. This can be done because the near wall conditions are often predictable. The first grid cell is be placed in the region $30 < y^+ < 300$ and then the inner laws are patched [9, p.451] into the calculations. This makes the use of wall functions very economical and robust. However, this method is based on empirical observations of simple high Reynolds number flows and is not usable for flow separation or low Reynolds number flow. Also the distance of the first grid cell from the wall is essential in obtaining good results, because if it is placed to near the wall the model becomes invalid, too far and the boundary layer is not properly resolved. ANSYS /Fluent recommends this approach if one is more interested in the mixing in the middle of the domain, rather than the forces on the wall [33, p.20].

Near wall modelling

The other method commonly in use to calculate the boundary layer flow is by utilizing a concept called enhanced wall treatment. In this model, molecular viscosity and dampening terms are added to the model and the boundary layer is resolved right up to the wall by using an adequately fine mesh disregarding empirical correlations. The first grid cell should be placed at $y^+ = 1$ for high accuracy demands, and consequently the computational cost is

significantly increased. When using enhanced wall treatment the boundary layer is divided into two parts:

- The inner and overlapping region in the boundary layer is assumed to be affected by both Newtonian and turbulent viscosity.
- The outer region is regarded as fully turbulent and thereby only dependent on turbulent viscosity.

The two regions are separated by a wall distance Reynolds number defined by:

$$Re_y \equiv \frac{\rho y \sqrt{k}}{\mu} \tag{104}$$

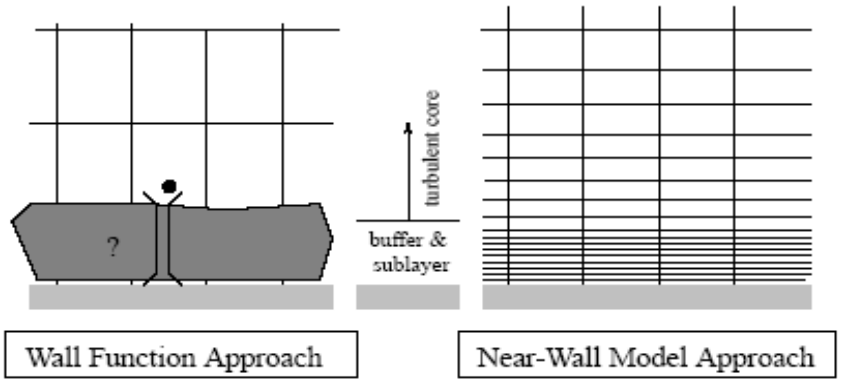

Figure 27: Wall function vs near wall model approach [30]

Considerations in boundary layer modelling

For best predictions ANSYS fluent recommends the use of enhanced wall treatment as it can handle complex flows, pressure gradients, low Reynolds number applications and it does not rely on the empirical law of the wall formulation. The enhanced wall treatment also gives the most consistent wall shear stress and is the least sensitive to y^+values. To allow the grid to capture the features of the boundary layer it is highly recommended to have a structured grid in the wall normal direction. The structured grid should extend beyond the boundary layer to ensure that the boundary layer growth is not restricted, and at the same time the most important shear layers should be covered by at least 10 cells normal to the wall [38, p.687].

It should also be noted that in ANSYS Fluent all ω based models uses the enhanced wall treatment as default. Therefore it is generally not recommended to include low Reynolds number effects when utilizing this turbulence model, since low Reynolds number correction is not needed to integrate the equation through the viscous sub layer. The low Reynolds number correction is not widely calibrated and the main influence is to mimic laminar-turbulent transition. [38, p.686].

1.8.9 Modeling complex flows

The 1981 Stanford Conference on Complex Turbulent Flows was assembled to investigate different computer methods to predict complex flows. By complex flow one means in this context “a complex turbulent flow is simply one that is more complicated than the steady, incompressible, two-dimensional attached thin shear layers”. [9, p.469].

Parameters that contribute to complexity are:

- Wall effects such as irregular geometry, suction, blowing and roughness
- Strain interactions
- Fluid effects e.g. multiple phases, compressibility, chemical reactions
- Turbulent fluctuations

At the conference a total of 35 computer groups were put together for comprehensive testing of different methods for flow predicting. Their findings were that no single method could handle adequately the full spectrum of flow scenarios that were tested, but different methods worked in different cases. Further findings made by the committee were:

- Differential methods that integrate right down to the wall give better results than wall functions
- There were no general correlation between the complexity of the models used and their actual predictive capability
- Prediction of separated flows, were significantly worse than for the corresponding attached flows.
- The weakest part of the two equation models is the ε relation.

Chapter 2 - Model description

2.1 Geometry and mesh

When it is decided to use CFD as a tool for obtaining detailed information of a flow, the approach within CFD communities follows basically the same recipe. The steps are as follows:

1. Real life physical problem is decided to be addressed using CFD.
2. The actual geometry of interest is evaluated and discretized
3. The mathematical model with suitable governing equations, numerical solvers and boundary conditions are applied.
4. The solution is obtained and evaluated.

I this thesis the problems of interest are presented in the introduction. The discretized geometry, mathematical model and evaluation of results are presented in the next sections. For CFD ANSYS has developed a software tool called Workbench. In Workbench the steps above are followed in a firm way, where it is necessary to finish one section before you can continue to the next. You can however import geometry, mesh or solution files directly into workbench without creating them yourself.

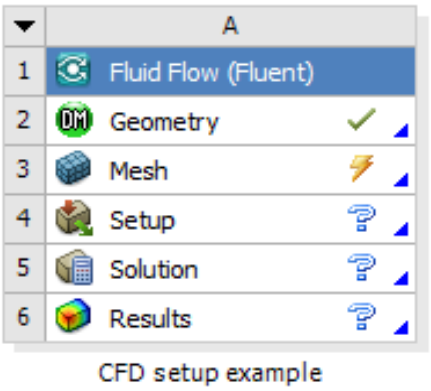

Figure 28: ANSYS Fluent workbench system

As can be seen from figure (28), ANSYS uses different software programs for the different parts of the CFD analysis. In this thesis the geometry is created in Design modeler, which is ANSYS CFD geometry designer. The geometry is then imported into the mesh section, where the mesh is applied. The mesh is then imported into Fluent which is ANSYS CFD setup and solver program. In Fluent the mesh is refined using mesh adaption tools available in Fluent. The geometry, meshing and setup are done on a Dell Inspiron 5520 computer, with a memory of 4.00 GB RAM and a Intel® Core™ 2.50GHz processor.

The CFD setup is then sent to NTNU super computer Kongull [39] for solving, from there the solution is imported back for post processing.

2.1.1 The geometry

As stated in the introduction, the flow through the diffuser is to be simulated, both when the floor is smooth and when the floor is covered with k-type roughness elements. The dimensions of the diffuser and roughness elements are given in appendix (E). Due to limited computer resources available only two-dimensional simulations have been performed. In figure (29), the geometry off the diffuser when it is smooth, and when the floor is covered with k-type roughness elements is depicted. From now on the former will be denoted the "smooth diffuser" whilst the latter will be denoted "the rough diffuser". To give the boundary layer some time to develop, an entrance length of 0.3 meter have been added. Likewise an outlet length of 0.3 meter have also been added, to prevent any unwanted backflow taking place. The roughness elements in figure (29), are only meant to illustrate the scenario and are not scaled correctly.

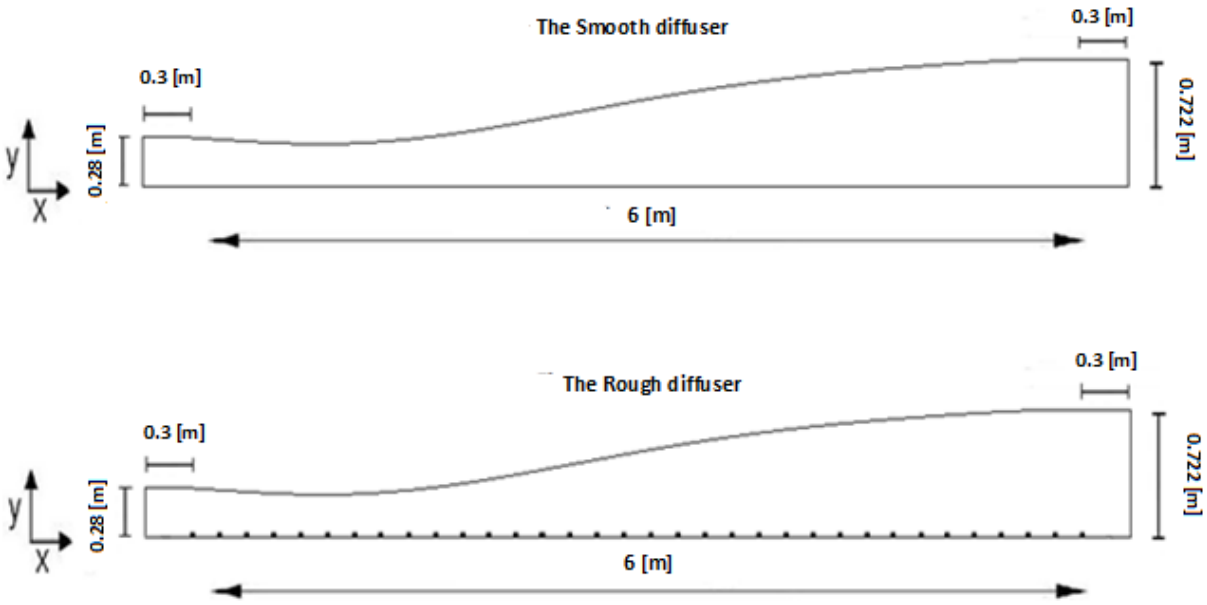

Figure 29: Smooth and rough diffuser depiction.

In Design modeler the geometry is constructed according to the coordinates given in appendix (E). For every ten centimeter there is given a corresponding height, therefore the diffuser is built by drawing sets of horizontal lines (representing the floor) with lengths of 10 cm and at the end of each horizontal line, a vertical line with the correct dimension is placed to represent the diffuser height at the specific cross section. This process is copied and

pasted throughout the design of the diffuser. Finally straight lines are drawn between the end points of the vertical lines in order to generate the rough of the diffuser.

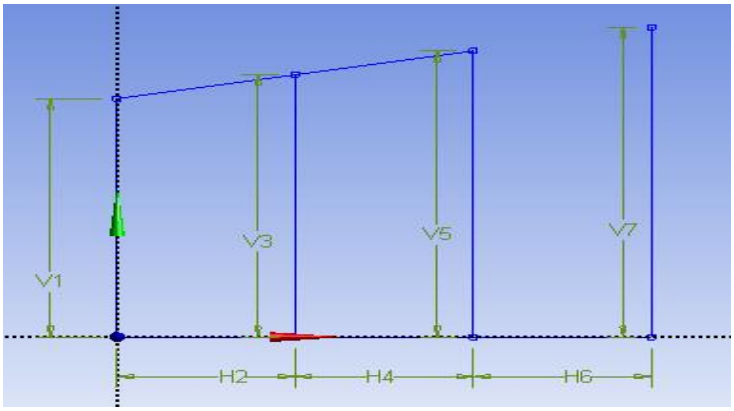

Figure 30: Diffuser geometry building principle

In figure (30), the letters H and V are respectively horizontal and vertical dimensions which must be given to design modeler, each horizontal line is 10 cm long. It is also possible to import the geometry directly into design modeler using a coordinate file. This process did however cause some difficulties in the creation of the rough diffuser, and therefore it was decided to produce the rough diffuser in the same manner as the smooth diffuser. When the rough diffuser was created, roughness elements replaced the floor.

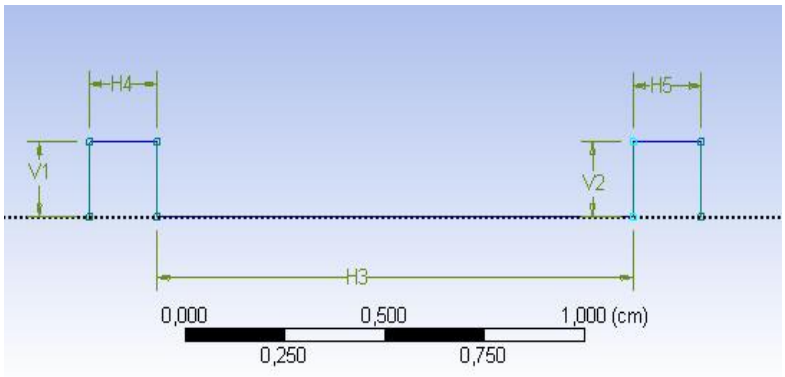

Figure 31: Roughness element construction

The roughness elements are squares with sides of 1.7mm. They have all an equally spacing of 1.19cm between them which means that this is k-type roughness with a pitch to height ratio of 8. The roughness elements are created in design modeler by first drawing a square and give it the right dimension i.e. define H4 and V1 in figure (31). Then the line H3 is drawn and dimensioned, for thereafter to utilize the copy and paste function in design modeler to cover the entire floor of the diffuser with the roughness elements

2.1.2 The mesh

After the geometry of the rough and smooth diffusers are created, the mesh is to be applied. For the purpose of this thesis two meshes for the smooth diffuser, and four meshes for the rough diffuser have been generated. The smooth diffuser meshes are denoted 1.1 and 1.2 whilst the rough diffuser meshes are denoted 2.1, 2.2, 2.3 and 2.4.

As discussed in section (1.7.2), in order to generate the most accurate solutions, a grid should be as fine as possible. However this is not always computational feasible. Therefore it is better to create a mesh where the regions of interest are meshed very fine, whilst the lesser important regions have a coarser mesh. How this is achieved in this thesis is will be outlined in the following section, but first it is important to understand the following concepts:

Mesh adaption:

Mesh adaption means that the cells are refined in a particular way. In this thesis mesh adaption functions are utilized in Fluent after the base mesh is designed in Workbench.

Region adapt: In this function you choose the specific area you would like to refine and how many times you want to refine it. By refining a cell one time, the cell is divided into four new cells. This means that if your mesh consist of one cell and it is refined two times the number of cells in the mesh is now 16. Carefulness must therefore be employed, so as to not generate a mesh which is to computational expensive.

Boundary adapt: In this function you choose a boundary and then the number of cells normal to the boundary you would like to refine.

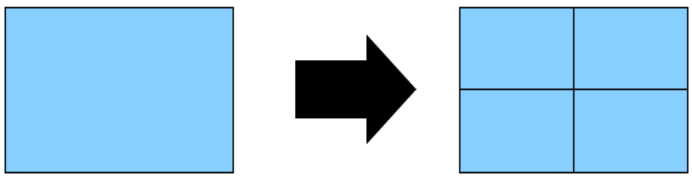

Figure 32: Mesh adaption

Mesh inflation:

Mesh inflation is another tool for designing as computational feasible and at the same time efficient mesh. Inflation is utilized at the boundaries by adding layers of mesh normal to the boundary. This means that the mesh is only refined in one direction. The number of inflation layers and a growth rate between each layer must be specified. Inflation is especially suited for capturing high velocity gradients in the normal direction to the boundaries, and the process can be seen in figure 24.

2.1.3 Smooth diffuser mesh

Mesh 1.1

This mesh is only produced in workbench using the mesh software and is without any mesh adaption in Fluent. By applying the sizing function and choosing a region, the dimensions of the cells in that specific region can be set. The scale that was found most fitting was to give every cell throughout the diffuser the dimension of $1\ cm^2$. The boundary layer belonging to the upper and lower walls are then covered using the inflation function. Twenty layers of inflation with a growth rate of 1.2 and first layer thickness set to 0.00001 meters are employed for this purpose. Using values from [17] $y^+ = 1$ was found to be 0.00003 meter. The boundary layer should therefore be properly resolved.

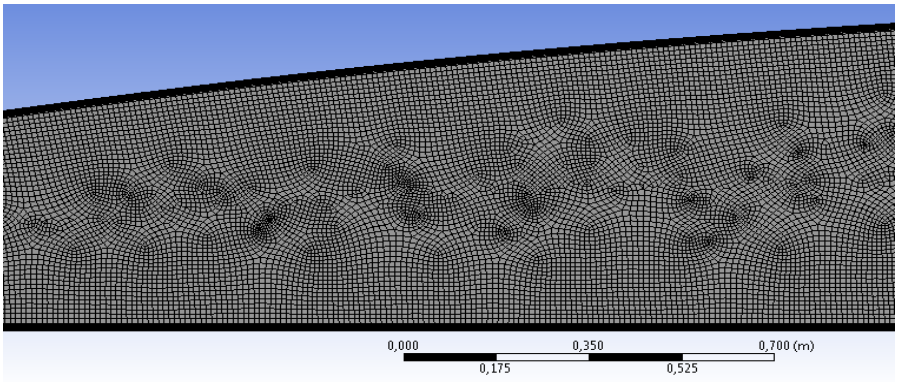

Figure 33: Smooth diffuser mesh overlook

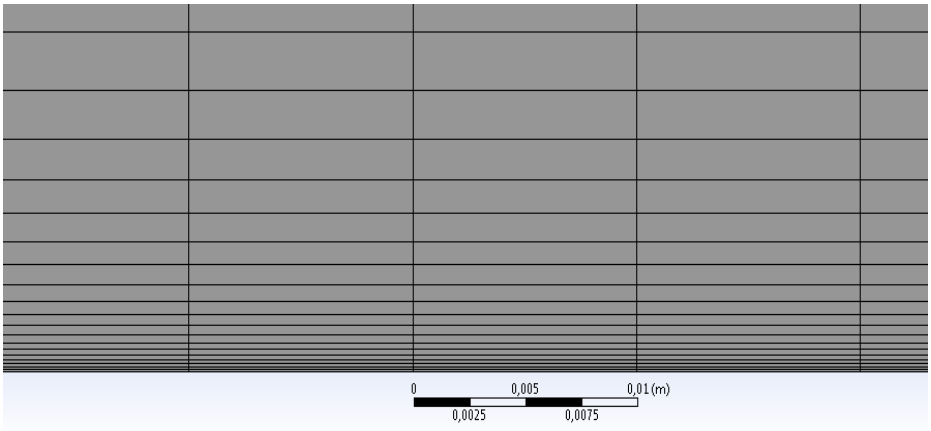

Figure 34: Mesh 1.1 near wall structure

Mesh 1.2

This mesh has the same foundation as mesh 1.1, but the first centimeter up from the floor have been refined one time, meaning that every cell in that region including the inflation layers have been divided in four new cells.

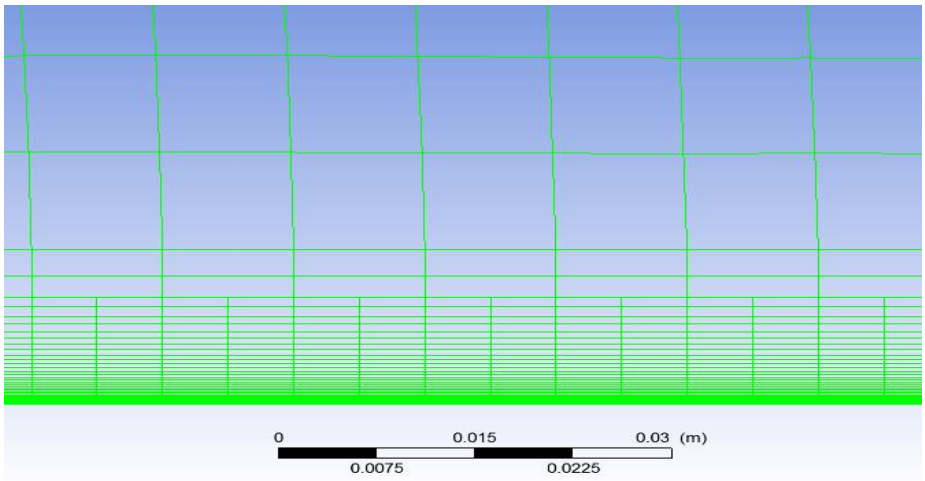

Figure 35: Mesh 1.2 near wall structure

2.1.4 Rough diffuser mesh

There have been constructed four grids for the rough diffuser in the attempt to acheive mesh independence. In common for mesh 2.1 and 2.2 is that they both share the same starting point i.e. they use the same mesh created from the meshing software in Workbench, but they are refined different later in Fluent. The base mesh used for mesh 2.1 and 2.2 is constructed as follows:

- The diffuser is divided into two separate areas, where the first or lower section stretches from the floor out to 20 roughness heights i.e. 34 mm. I this region a structured mesh with cells of size $(0.85 * 0.85)mm^2$ are created. This mesh gives two cells on the top and at the sides of each roughness element, and a total of 14 cells between the roughness elements.

- The second or upper region stretches from the roof of the diffuser down to the first section. In this region a structured mesh with cells of size $1cm^2$ are created. To resolve the boundary layer at the roof of the diffuser inflation is used. Since main attention is given to the boundary layer along the floor, only 10 layers of inflation with a growth rate of 1.2 are utilized at the roof.

- To obtain a smooth transition between the two regions, the lower edge of the upper region is set to have cells of size $(0.85 * 0.85)mm^2$. This is done to make the merging process of the two regions as effective as possible, it also increases the region of fine meshing close to the floor. However one side effect of the merging process is that more heaps of cell structures have emerged relative to the smooth diffuser.

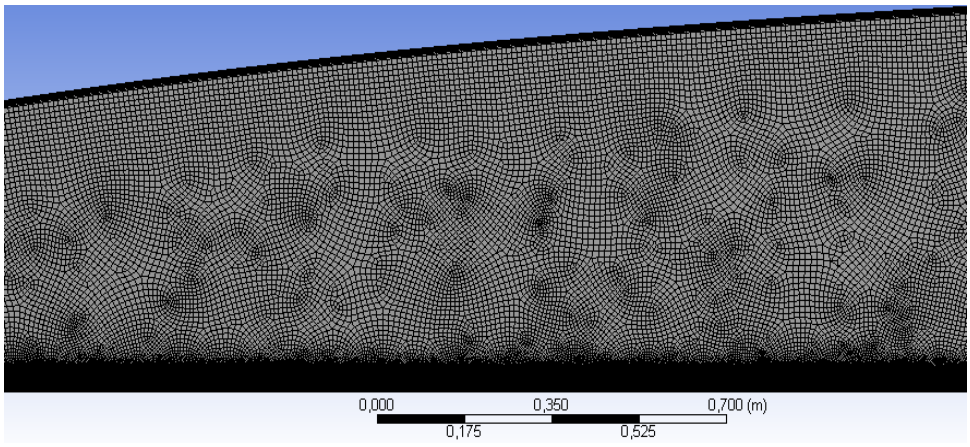

Figure 36: Rough diffuser overlook

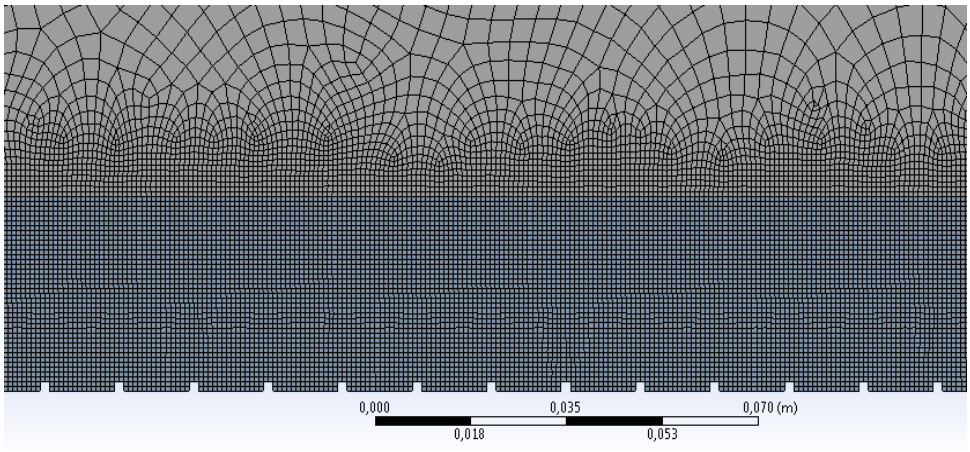

Figure 37: Rough diffuser mesh transition

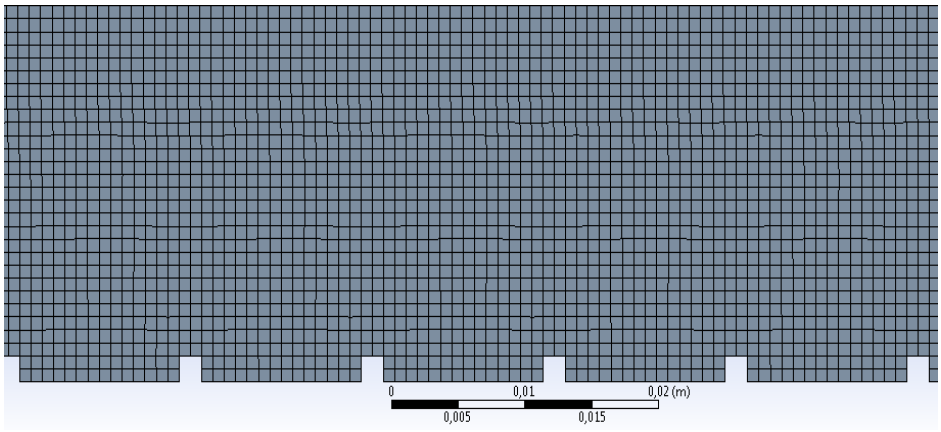

Figure 38: Rough diffuser near wall base structure

Mesh 2.1

Mesh 2.1 is constructed as mentioned with the previous structure as a base. Further it is refined in Fluent using the adapt function according to the following procedure:

1. The region from the floor and stretching out two roughness heights i.e. 3.4mm is refined one time using region adapt function in Fluent.

2. Then using boundary adapt function, the six cells closest to the floor are refined one time.

3. Last, using boundary adapt the two cells closest to the floor are then refined.

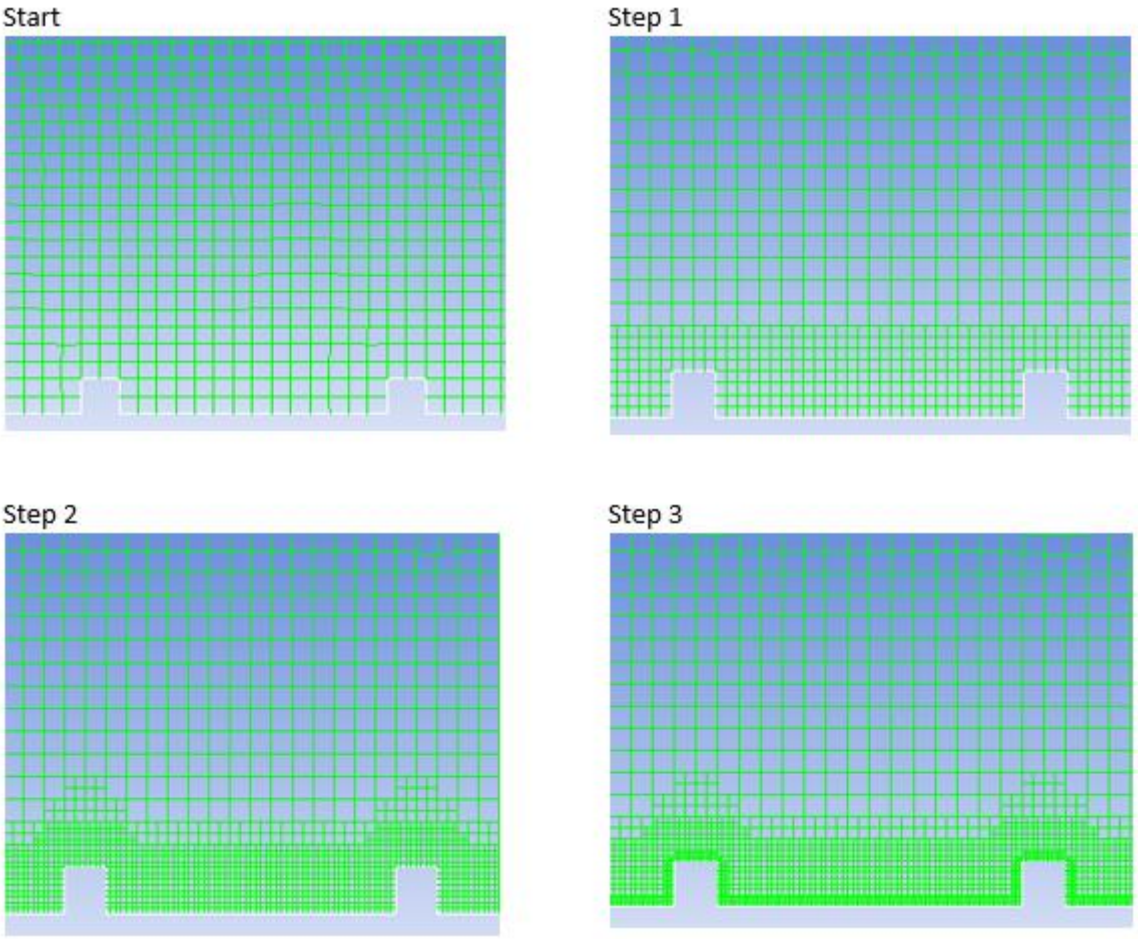

Figure 39: Steps used to build mesh 2.1

In mesh 2.1 the roughness elements are therefore surrounded by 16 cells on each side.

Mesh 2.2

This mesh has been further refined in Fluent compared to mesh 2.1 in order to detect any mesh dependent solutions. By refinening finer close to the roughness elements and also extend the region of refinement out to three roughness elements, the hope is that more of the near wall dynamics shall be advected out from the wall and into a larger part of the boundary layer. Mesh 2.2 is constructed as follows:

1. The region from the floor stretching out three roughness heights i.e. 0.51 cm is refined one time using region adapt function in Fluent.

2. The six cells closest to the floor are then refined one time using boundary adapt.

3. The three cells closest to the floor are the refined one time using boundary adapt.

4. Finely the three cells closest to the wall are refined one time, using boundary adapt

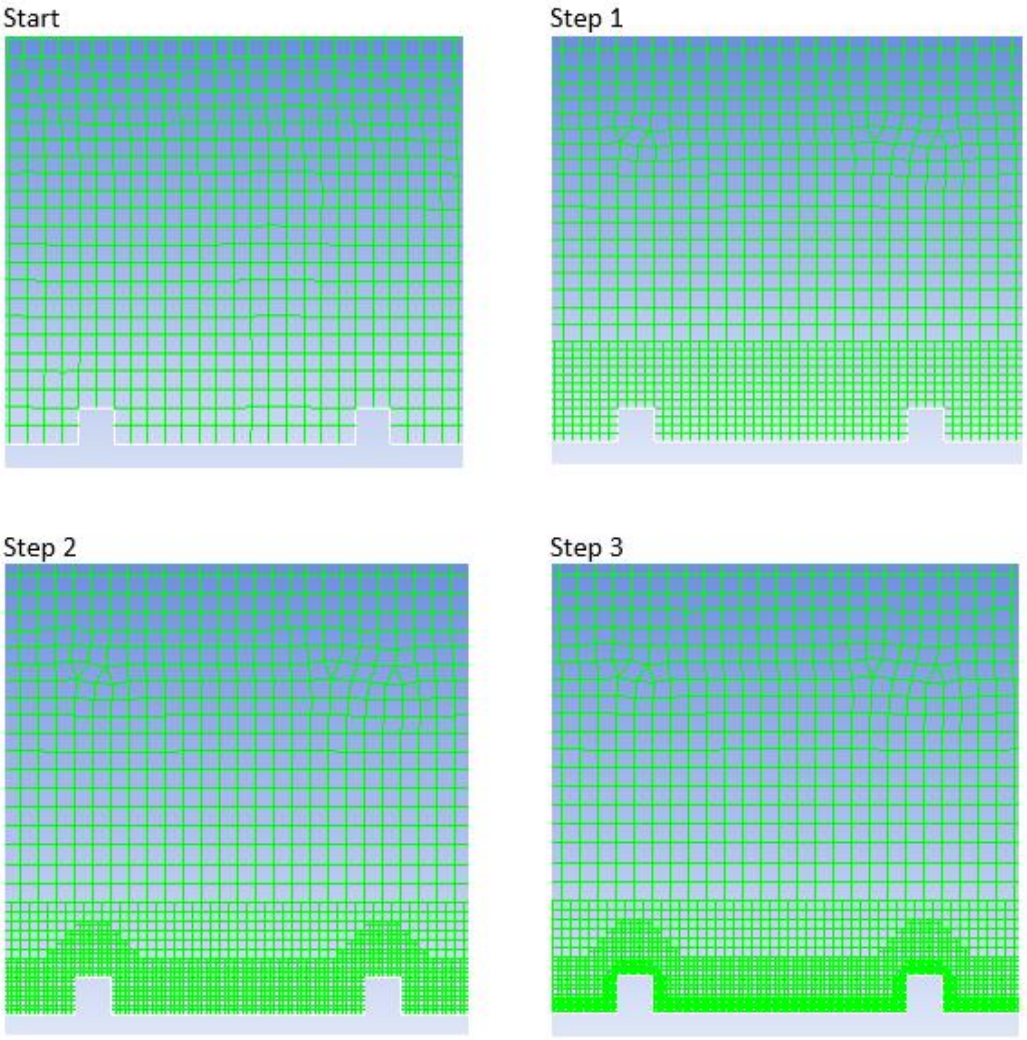

Figure 40: Steps used to build mesh 2.2

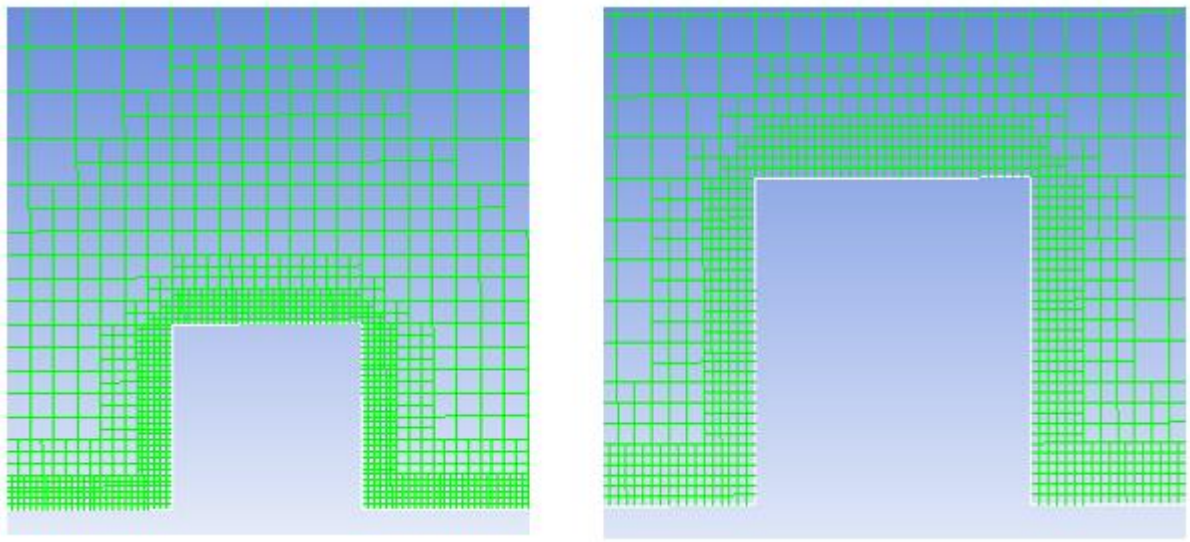

Figure 41: Mesh 2.2 detailed view of mesh 2.2 at roughness elements

In mesh 2.2 the roughness elements are therefore surrounded by 32 cells on each side.

Mesh 2.3

It was recommended by [40] not to divide the diffuser geometry into two parts as done in mesh 2.1 and 2.2, but rather mesh the hole geometry as one body and then utelize inflation to capture the important velocity gradients along the boundaries. This is therfore the baseline for mesh 2.3 and 2.4.

1. The mesh is created from same principle as the smooth diffuser by setting the cell size in the entire diffuser to $1\ \mathrm{cm}^2$, and putting 20 layers of inflation with first layer thickness of 0.00001 meter at the roof of the diffuser.

2. The lower edge or the floor of the diffuser is then set to have cells of size $(0.425 * 0.425)mm^2$. Since the height of the roughness elemets are 1.7mm, this will place four cells along the sides of the roughness element.

3. Five layers of inflation with first layer thickness of 0.00001 meter and a growth rate of 1.2 are then placed at the floor of the diffuser.

4. Using Region adapt in Fluent the mesh is further refined from the floor and stretching out five roughness elements i.e. 8.5mm.

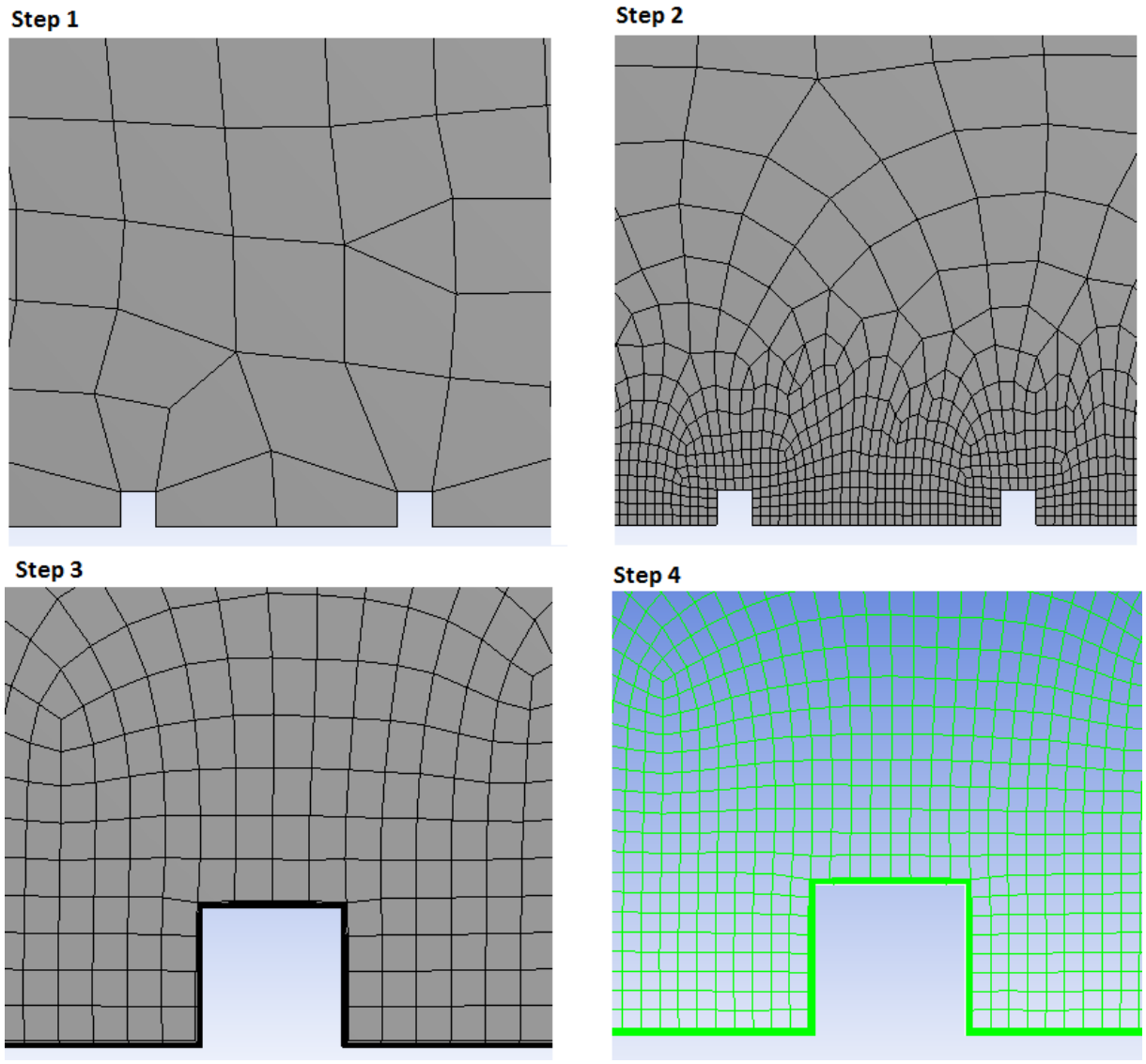

Figure 42: Steps used to build mesh 2.3. Notice the thick black and green line following the geometry of the roughness elements at respectively step 3 and 4. This line represent the inflation layers

In mesh 2.3 the roughness elemets are therefore surronded by 8 cells on each side and also, 10 layers of inflation with first layer thickness of 0.000005 meter and a growth rate of 1.2 have been placed along the floor.

Mesh 2.4

The start point for mesh 2.4 is step 3, in mesh 2.3. Using Region adapt in Fluent mesh 2.4 is refined one time from the floor and extending out ten roughnesss heights i.e 17mm. In addition the region from the floor and extending out one and a half roughness heights i.e. 2.55 mm have been further refined one time. By refineing deeper close to the roughness elements and also extendnig the region of refinement, the hope is that some of the near wall dynamics will be advected out into the boundary layer.

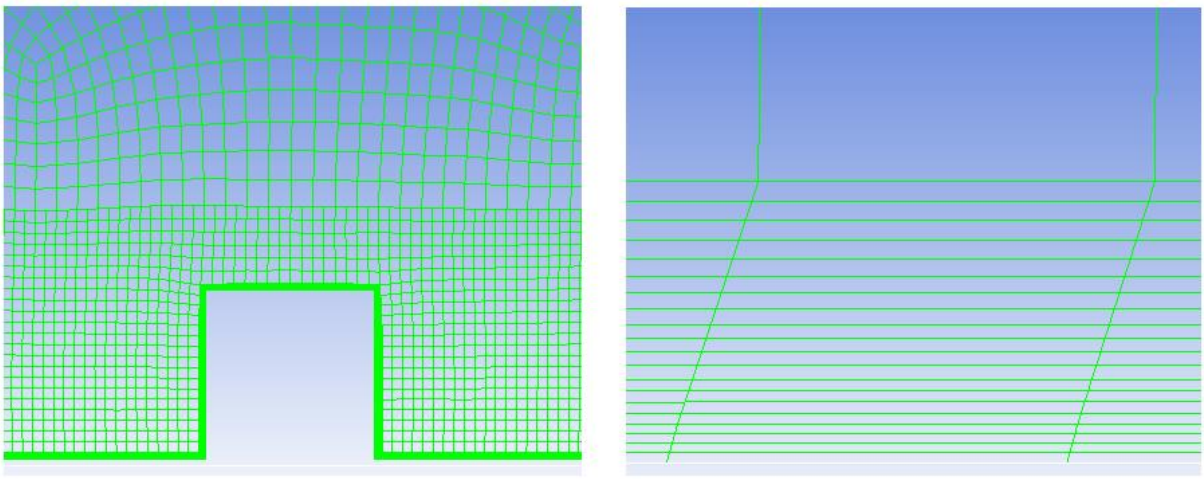

Figure 43: Detailed view of mesh 2.4 at roughness element

In mesh 2.4 the roughness elements are therefore surronded by 16 cells on each side and also 20 layers of inflation with first layer thickness of 0.0000025 meter and a growth rate of 1.2 have been placed along the floor.

In table (1) information regarding number of cells and first cell height in the different meshes are given.

Mesh	Number of cells initially	Number of cells after refinement	Increasement factor	First cell height [m]
1.1	58951	58951	1	0.00001
1.2	58951	94591	1.6	0.000005
2.1	456912	1056825	2.3	0.00010625
2.2	456912	1881876	4.1	0.000053125
2.3	356918	1202600	3.4	0.000005
2.4	356918	3139001	8.8	0.0000025

Table 1: Information of number of cells and first cell height in the different meshes.

2.2 Fluent settings

When the geometry and the proceeding mesh is built, the next step is to load these into Fluent for solving. To start the iteration process a number of parameters needs to be set, these are crucial to the overall result. In this thesis the following input parameters have been chosen:

1. Solver:

For pressure velocity coupling the pressure based solver has been favored over the density based solver. The pressure based approach was chosen because this is the standard for low speed incompressible and mildly compressible flows. With regards to time, the steady state solver has primarily been utilized. To check for any time dependency, transient simulations have been carried out on some of the turbulence models. The results from the transient simulations are presented in appendix (G).

2. Turbulence models:

A number of turbulence models are available in Fluent included the models outlined in section (1.8). In addition, other less relevant models related to the particular scenario in this thesis are offered. Each turbulence model utilized have been adjusted with the modification functions given in Fluent for optimal performance.

- K-ω SST model, with the following modifications:
    - Low Re correction
    - Curvature correction

The Curvature correction suppresses or enhances turbulence based on the flow curvature. As already mentioned the low-Re number correction application is generally not recommended with the k-ω models. However, best results were obtained when this modification were applied.

- Standard K-ω model, with the following modifications:
    - Low Re correction
    - Shear flow correction
    - Curvature correction

- K-ε RNG model, with the following modifications:
    - Differential viscosity model
    - Enhanced wall treatment
    - Pressure gradient effects
    - Curvature correction

- K-ε Realizable model, with the following modifications:
    - Enhanced wall treatment
    - Pressure gradient effects
    - Curvature correction

- RSM model, with the following modifications:
    - Linear pressure strain
    - Wall boundary condition from k equation
    - Wall reflection effects
    - Enhanced wall treatment
    - Pressure gradient effects

- Spalart-Allmaras model, with the following modifications:
    - Vorticity based
    - Curvature correction

3. Material

In this unit the specific fluid and material of the diffuser is to be defined. The fluid is set to air and the material is set to aluminum. These are also the default terms in Fluent.

4. Boundary conditions:

The boundary conditions for the diffuser is then to be specified. These will be the same for all the simulations and are also the basis for the initialization values of the turbulence models.

- Inlet: The inlet conditions has been set as a velocity-inlet meaning that the solver needs a velocity input to start the iteration process. The velocity magnitude was given from the measurements in [17] and yields 31 m/s.

- Turbulent intensity: The turbulence models needs an input for the intensity at the inlet for the models to start. This value has been set to 0.5% of the inlet velocity [41].

$$I = \frac{\sqrt{(2/3)k}}{U_e} \tag{105}$$

- Turbulent length scale: The characteristic length of the largest eddies needs initialization for the turbulence models to start. The size of the largest eddies at the inlet was found by the correlation [34, p.70].

$$l_0 = 0.07L \tag{106}$$

  Where L has been chosen as the vertical height of the diffuser throat giving l_0 a value of 0.0168 meter.

- Outlet: The outlet condition is set to pressure-outlet meaning that a pressure input must be given for the iteration process to start. This was set to atmospheric or equivalently zero gauge pressure.

- The walls: The walls are set to impermeable stationary walls with no slip.

5. Reference values:

Reference values are used in ANSYS Fluent as a basis for the post processing. For example are computed values for the friction coefficient based on the reference velocity and not on the free stream velocity. The Reference values are based on the default values computed from inlet yielding:

- Air density equal to 1.225 kg/m^3
- Temperature equal to 288.16 k
- Dynamic viscosity equal to 1.7894*10^{-5} Ns/m^2
- Atmospheric operating conditions

6. Solution methods:

In solution methods the type of pressure velocity coupling and spatial discretization method are specified. For the steady state solver the Simple (Semi-Implicit Method for Pressure-Linked Equations) algorithm is utilized. This is a pressure based solver, and is based on the principle that fluid flows from regions of high pressure low to low pressure. In this solver the pressure is found by manipulating the momentum and continuity equations. If more mass is flowing into a cell then out of the cell, indicates that the pressure in that cell compared to the neighboring cell must be too low. The correct value of the pressure is then established by an iterative process to satisfy the continuity equation. For the transient simulation the PISO (Pressure Implicit with Splitting of Operators) scheme is used. For spatial discretization the QUICK scheme has been chosen.

7. Solution controls:

The default relaxation coefficients are used, except for the RSM simulation where the relaxation coefficient where adjusted for the solution to converge.

8. Monitors:

The iterations needs a residual criterion for the solution to converge. This criterion has been set to 10^{-7}. The residuals in some of the simulations showed a tendency to drop even after the residual criterion was reached, new residual criterions were therefore put in for these simulations. Also some of the simulations converged before the residual criterion was reached (meaning that the residuals stop changing).

9. Solution initialization:

The iterations starts by initializing from inlet. Meaning that the entire domain has been given the values of the inlet.

10. Run calculation:

In this section the number of iterations in steady state or equivalently time step and number of time steps in transient simulation are given. When these parameters are chosen Fluent will starts the calculation process until the solution diverges, converges or the number of iterations has been reached.

2.2.1 Fluent simulations

As stated in the problem description, the flow through both the smooth and rough diffuser is to be simulated. Measurements for both geometries are available and accordingly the simulations will be compared with the relevant measurements for validation. Different meshes have been used in order to detect any mesh dependencies, consequently only the results from the meshes that gave the best answers will be presented. If the output from the meshes were identical then the least computational expensive mesh where chosen. The results from all of the simulations are found appendix (F) and (G). The focus of the simulations have been on the rough diffuser, therefore more meshes and turbulence models have been applied to the rough diffuser than to the smooth diffuser.

The turbulence models that have been applied to the smooth diffuser are respectively:

1. K-ω SST
2. K-ε RNG
3. Spalart-Allmaras

The turbulence model that have been applied to the rough diffuser are respectively:

1. K- ω SST
2. Standard k- ω
3. K-ε RNG
4. K-ε Realizable
5. RSM
6. Spalart-Allmaras

2.3 Measured values

Physical measurements have been conducted for the smooth diffuser in [17[and for the rough diffuser in [43]. Therefore the simulations on the smooth diffuser will be compared with and validated against the data available from [17]. Likewise the simulations on the rough diffuser will be compared with and validated against the data available from [43].

2.3.1 Smooth diffuser

The data available for the smooth diffuser are from the measurements performed in [17], and are shown in table (2):

X [m]	h [cm]	U_e [m/s^{-1}]	δ [m]	θ [m]	H [-]	G [-]	β [-]	$\frac{dp_e}{dx}$	τ_w [N/m^2]	C_f*10^{-3} [-]	Re_θ [-]
3.0	48.4	22.35	0.1091	0.0176	1.793	20.8	12.2	107	0.2754	0.900	25400
3.2	51.3	21.92	0.1257	0.0201	1.840	22.9	14.0	89	0.2343	0.797	28420
3.4	54.1	21.21	0.1394	0.0226	1.901	24.8	15.7	74	0.2011	0.730	30910
3.6	56.7	20.53	0.1538	0.0248	1.936	26.4	16.9	61	0.1753	0.672	33020
3.8	59.1	20.10	0.1672	0.0270	1.957	27.0	17.3	53	0.1618	0.654	34570
4	61.0	19.91	0.1856	0.0301	2.006	29.2	19.9	47	0.1418	0.590	39120
4.2	63.0	19.42	0.1997	0.0325	1.999	29.3	20.0	41	0.1344	0.582	41580
4.4	64.7	19.38	0.2153	0.0348	1.989	29.1	19.6	38	0.1346	0.585	44420
4.6	66.2	18.84	0.2353	0.0374	1.998	29.6	20.1	33	0.1241	0.571	46250
4.8	67.6	18.67	0.2474	0.0400	1.994	29.6	20.2	31	0.1211	0.567	49180
5	68.7	18.30	0.2637	0.0430	1.998	30.2	21.2	28	0.1120	0.546	50980
5.2	70.0	18.04	0.2829	0.0458	1.986	30.2	21.4	25	0.1078	0.541	53970

Table 2: Measured characteristic boundary layer parameters for the smooth diffuser

In addition measured values for the pressure coefficient (C_p) and the corresponding pressure coefficient gradient $\left(\frac{dC_p}{dx}\right)$ through the smooth diffuser are available and will be compared with the simulations for the smooth diffuser.

2.3.2 The rough diffuser

The data available for the rough diffuser are from the measurements performed in [43] and are given in table (3):

X [m]	h [cm]	U_e [m/s^{-1}]	δ [m]	δ^* [m]	θ [m]	H [-]	Re_θ [-]
2.6	42.14	30.3	0.1990	0.0950	0.0280	3.39	58213
3.25	51.70	28.7	0.3485	0.1803	0.0426	4.23	83890
3.6	56.68	27.9	0.3980	0.2138	0.0517	4.14	98973

Table 3: Measured characteristic boundary layer parameters for the rough diffuser

In addition, values for the pressure coefficient (C_p) and the corresponding pressure coefficient gradient $\left(\frac{dC_p}{dx}\right)$ through the rough diffuser are available and will be compared with the simulations for the rough diffuser. Detailed LDA (Laser Doppler anemometer) measurement off the velocity profiles at the respective stations in table (3) are also presented and compared with the simulations.

During simulations the velocity profiles at the different locations in table (2) and (3) have been obtained. From them many of the parameters in the tables have been computed accordingly:

- The free stream velocity U_e was chosen as the highest velocity found on the cross section.
- The boundary layer height δ is computed according to equation (27)
- The displacement thickness δ^* is computed according to equation (28)
- The momentum thickness is computed according to equation (29)
- Clauser shape factor G is computed according to equation (46)
- The non-dimensional pressure gradient β is computed according to equation (44)
- The pressure gradient $\frac{dp_e}{dx}$ is provided by Fluent and is computed by taking the average of the pressure gradient in the free stream cross section. In the simulations, the pressure gradient at the cross sections were seldom constant. Therefore the

values of the pressure gradient in the free stream were averaged to get the most reasonable results.

- The Reynolds number based on momentum thickness is computed according to equation (32)

- The pressure coefficient C_p is computed by equation (49), after the values for the static pressure through the diffuser is given by Fluent. The reference pressure used is the static pressure at the inlet i.e. x=0. The reference dynamic pressure used is according to a free stream velocity of 31 m/s.

- The pressure coefficient gradient $\frac{dC_p}{dx}$ is computed by creating a polynomial function matching the pressure coefficient, and taking the derivative of this function. This process is done using Matlab functions "polyfit()" and "diff()" respectively for creating the polynomial function and for differentiating the function thereafter.

- For the smooth diffuser the wall friction τ_w is provided by Fluent and the friction coefficient is computed by equation (31)

- To obtain the wall friction for the rough diffuser, equation (26), has been applied to the control volume in figure (44), and integrated over one roughness period defined by the red line.

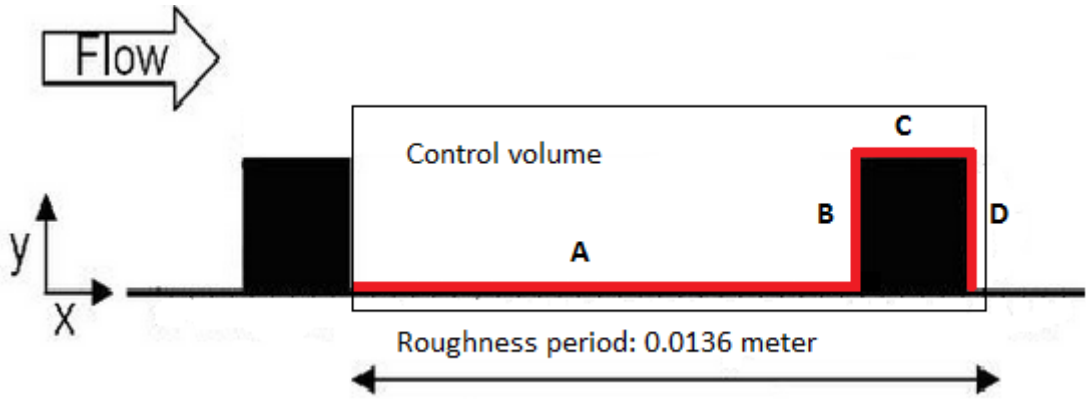

Figure 44: Control volume surrounding roughness period

The viscous drag contribution follows from the horizontal (x direction) red lines, and the contribution from the pressure drag follows from the vertical (y direction) red lines. The length of the roughness period is defined as total horizontal length of the roughness period.

The surface resistance over one roughness period is then found by dividing equation (26), by the roughness period:

$$\frac{D}{Rp} = \frac{\oiint \overrightarrow{\tau_A} \cdot \hat{e}_\infty dS_A - \oiint p_B \hat{n} \cdot \hat{e}_\infty dS_B + \oiint \overrightarrow{\tau_C} \cdot \hat{e}_\infty dS_C - \oiint p_D \hat{n} \cdot \hat{e}_\infty dS_D}{Rp} \tag{107}$$

Friction coefficients for the viscous drag and the pressure drag can be obtained by adding their respective contributions and dividing by the free stream dynamic pressure at the specific cross section. The effective friction coefficient is the sum of the two above.

$$C_{f\_effective} = C_{f\_skin} + C_{f\_pressure} = \frac{D/R_p}{0.5\rho U_e^2} \tag{108}$$

Chapter 3 - Results

3.1 Results from simulations on smooth diffuser

In this chapter the results of the simulation done on the smooth diffuser are presented. As stated in section 2.2.1 only the results from the meshes with the best replication of the physical measurements are presented. First the results from each turbulence model will be given in a table identical to table (2), next follows plots showing the development of some of the most important flow parameters together with their physical measurements. Thereafter will figures displaying the pressure coefficient and the pressure coefficient gradient be presented. Finally, there is a section where some of the flow parameters from the different turbulence models are plotted together for comparison.

As can be seen in appendix (F), the meshes used for the smooth diffuser simulations show very little deviation from each other. Since both of these meshes are relatively light in terms of computational effort, all the results presented in the section are from mesh 1.2.

3.1.1 k-ω SST

In this section the results from the simulations where the turbulence model k-ω SST have been utilized are presented.

In table (4), characteristic boundary layer parameter for the region $3 \leq x \leq 5.2$ meter are presented.

X [m]	h [cm]	U_e [m/s^{-1}]	δ [m]	θ [m]	H [-]	G [-]	β [-]	$\frac{dp_e}{dx}$	τ_w [N/m^2]	C_f*10^3 [-]	Re_θ [-]
3.0	48.4	21.91	0.1104	0.0176	2.1222	29.1	19.3	101	0.1947	0.6621	26406
3.2	51.3	21.23	0.1279	0.021	2.1890	30.6	20.9	82	0.1719	0.6226	29234
3.4	54.1	20.61	0.1413	0.0226	2.2267	31.4	21.5	68	0.1593	0.6122	31990
3.6	56.7	20.10	0.1502	0.0251	2.2489	31,7	21.5	58	0.1521	0.6146	34719
3.8	59.1	19.65	0.1656	0.0277	2.2541	31.6	21.4	50	0.1464	0.6190	37408
4	61.0	19.25	0.1860	0.0303	2.2498	31.3	20.4	43	0.1432	0.6309	40002
4.2	63.0	18.90	0.1932	0.0328	2.2360	30.7	19.7	38	0.1416	0.6471	42504
4.4	64.7	18.58	0.2064	0.0352	2.2158	30.0	18.2	33	0.1414	0.6729	44972
4.6	66.2	18.30	0.2185	0.0376	2.1898	29.2	16.7	29	0.1423	0.6937	47197
4.8	67.6	18.05	0.2300	0.0400	2.1582	28.3	15.6	26	0.1439	0.7211	49504
5	68.7	17.83	0.2416	0.0422	2.1276	27.4	14.2	23	0.1462	0.7508	51588
5.2	70.0	17.62	0.2618	0.0423	2.0930	26.4	12.4	20	0.1492	0.7846	53469

Table 4: Characteristic boundary layer parameters from simulation with k-ω SST turbulence model

In figure (45), the development of the displacement thickness δ^*, momentum thickness θ and boundary layer thickness δ are presented for the region $3 \leq x \leq 5.2$. The measured values of the same parameters are also displayed.

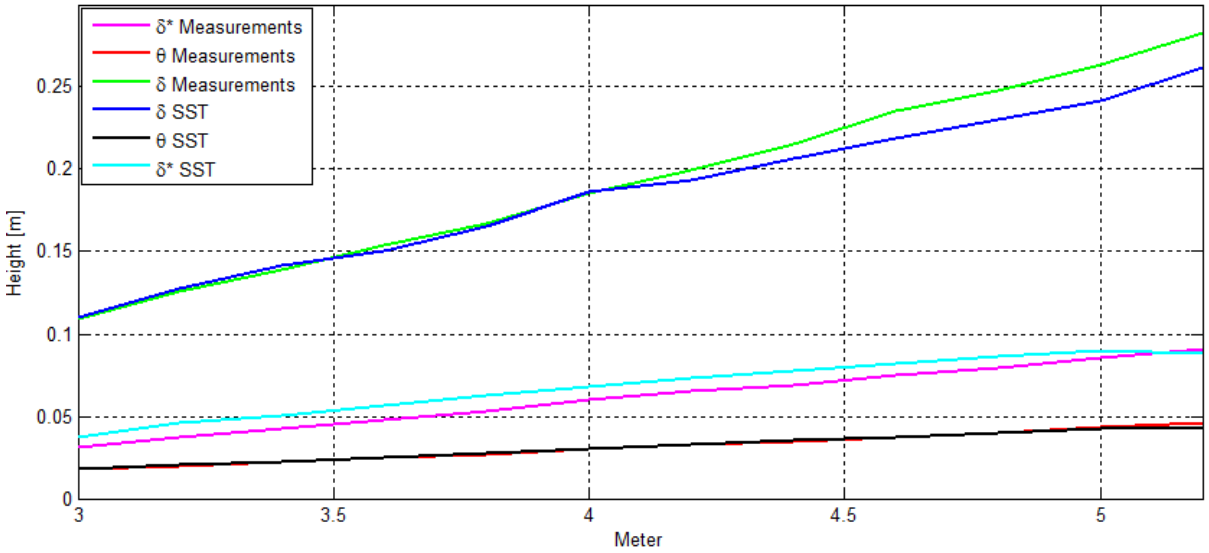

Figure 45: Development of boundary layer parameters for the simulation with k-ω SST mode versus measurements.

In figure (46) the pressure coefficient and the derivative of the pressure coefficient in the streamwise direction are presented together with the measured values of the same parameters. The plots starts from the diffuser inlet and ends at the diffuser outlet.

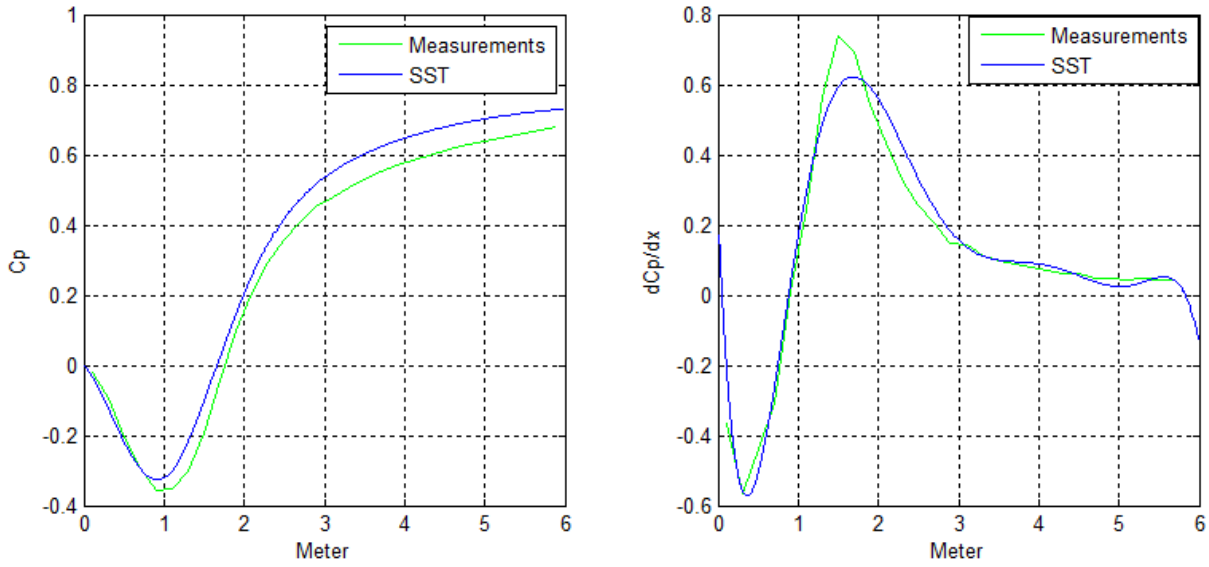

Figure 46: Plots showing pressure coefficient distribution left figure and the derivative of the pressure coefficient in the streamwise direction right figure for the k-ω SST model versus measurements

3.1.2 k-ε RNG

In this section the results from the simulations where the turbulence model k-ε RNG have been utilized are presented.

In table (5), characteristic boundary layer parameter for the region $3 \leq x \leq 5.2$ meter are presented.

X [m]	h [cm]	U_e [m/s^{-1}]	δ [m]	θ [m]	H [-]	G [-]	β [-]	$\frac{dp_e}{dx}$	τ_w [N/m^2]	C_f*10^3 [-]	Re_θ [-]
3.0	48.4	21.22	0.1207	0.0188	1.76	19.31	13.5	113	0.2761	1.00111	27347
3.2	51.3	20.43	0.1279	0.0217	1.80	20.50	14.5	89	0.2402	0.93879	30457
3.4	54.1	19.76	0.1513	0.0247	1.82	21.05	15.0	73	0.2197	0.91865	33554
3.6	56.7	19.19	0.1601	0.0277	1.83	21.441	14.9	60	0.2040	0.90443	36429
3.8	59.1	18.70	0.1768	0.0305	1.84	21.55	14.6	50	0.1932	0.90202	39184
4	61.0	18.29	0.1962	0.0334	1.84	21.44	13.8	42	0.1864	0.90973	41863
4.2	63.0	17.93	0.2130	0.0360	1.84	21.16	12.7	35	0.1822	0.92530	44330
4.4	64.7	17.63	0.2293	0.0387	1.82	20.76	12.1	31	0.1801	0.94603	46777
4.6	66.2	17.36	0.2369	0.041	1.81	20.3	11.2	27	0.1793	0.97026	48988
4.8	67.6	17.09	0.2414	0.0434	1.79	19.7	10.4	24	0.1796	1.00395	50885
5	68.7	16.91	0.2688	0.0458	1.77	19.2	9.5	21	0.1808	1.00322	53088
5.2	70.0	16.72	0.2954	0.0478	1.75	18.6	8.3	18	0.1829	1.06815	54828

Table 5: Characteristic boundary layer parameters from simulation with k-ε RNG turbulence model

In figure (47), the development of the displacement thickness δ^*, momentum thickness θ and boundary layer thickness δ are presented for the region $3 \leq x \leq 5.2$. The measured values of the same parameters are also displayed.

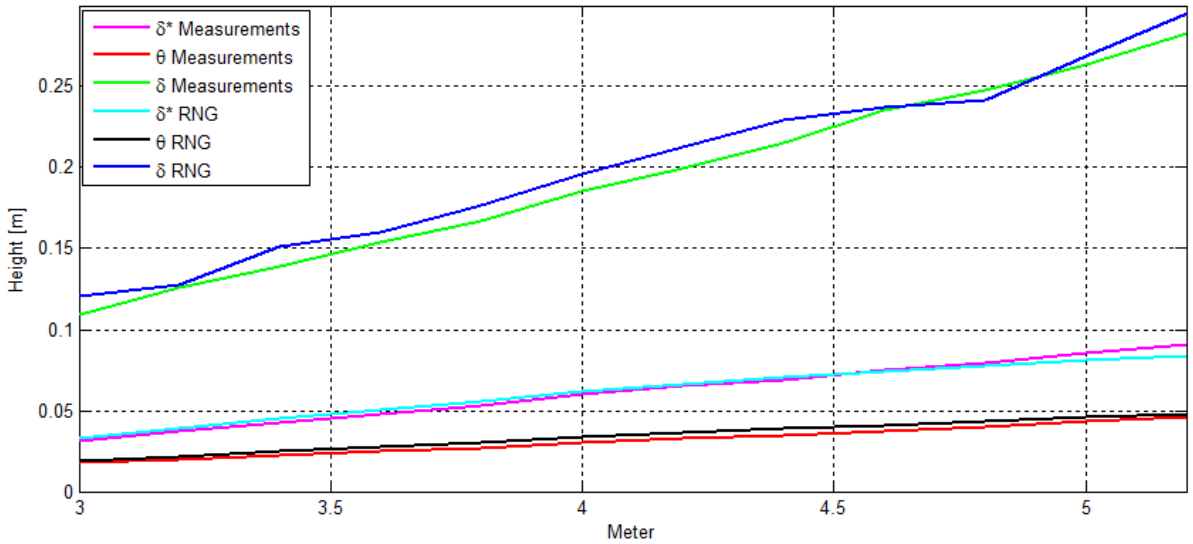

Figure 47 : Development of boundary layer parameters for the simulation with k-ε RNG model versus measurements.

In figure (48), the pressure coefficient and the derivative of the pressure coefficient in the axial direction are presented together with the measured values of the same parameters. The plots starts from the diffuser inlet and ends at the diffuser outlet.

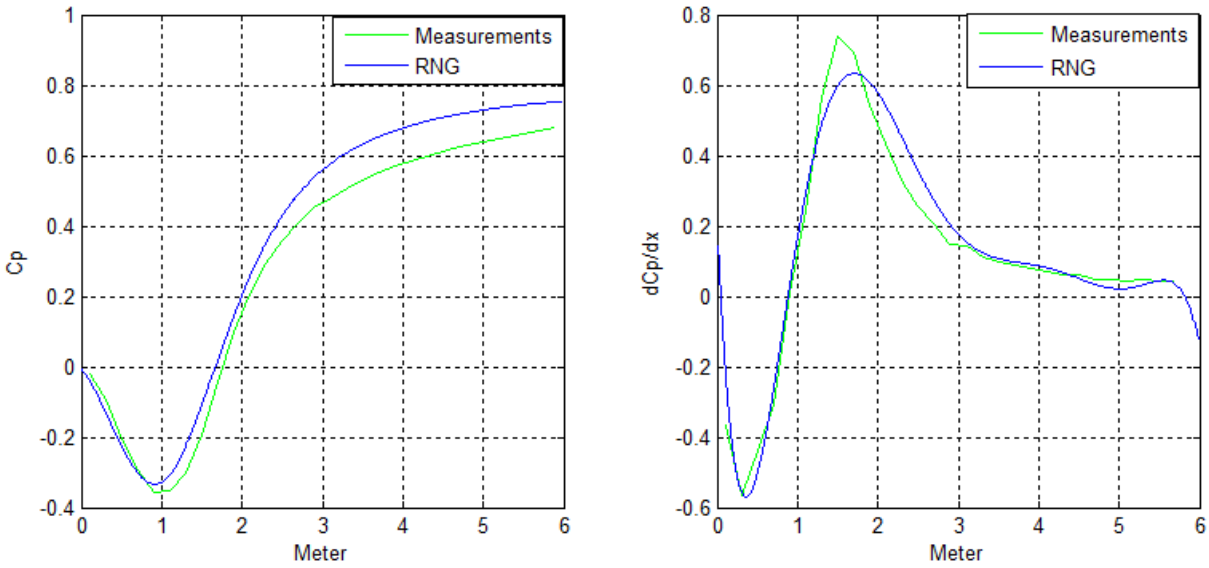

Figure 48: Plots showing pressure coefficient distribution left figure and the derivative of the pressure coefficient in the streamwise direction right figure for the k-ε RNG model versus measurements

3.1.3 Spalart-Allmaras

In this section the results from the simulations where the turbulence model Spalart-Allmaras have been utilized are presented.

In table (6), characteristic boundary layer parameter for the region $3 \leq x \leq 5.2$ meter are presented.

X [m]	h [cm]	U_e [m/s^{-1}]	δ [m]	θ [m]	H [-]	G [-]	β [-]	$\frac{dp_e}{dx}$	τ_w [N/m^2]	C_f*10^3 [-]	Re_θ [-]
3.0	48.4	21.6	0.1283	0.0180	1.89	27.7	21.2	103	0.1646	0.57599	26630
3.2	51.3	20.9	0.1366	0.0205	1.95	31.4	25.1	81	0.1292	0.48291	29390
3.4	54.1	20.3	0.1513	0.0230	2.00	34.7	29.5	67	0.1050	0.41600	32076
3.6	56.7	19.83	0.1701	0.0256	2.04	37.5	32.8	56	0.0892	0.37035	34826
3.8	59.1	19.39	0.1883	0.0281	2.07	39.6	35.5	48	0.0785	0.34089	37320
4	61.0	19.00	0.1962	0.0304	2.09	40.9	36.3	41	0.0718	0.32472	39687
4.2	63.0	18.66	0.2130	0.0328	2.09	41.5	36.5	36	0.0677	0.31744	41974
4.4	64.7	18.36	0.2293	0.0351	2.09	41.4	35.7	32	0.0659	0.31918	44186
4.6	66.2	18.09	0.2370	0.0373	2.09	40.8	34.6	29	0.0653	0.32578	46320
4.8	67.6	17.85	0.2508	0.0396	2.07	39.6	30.8	25	0.0664	0.34024	48441
5	68.7	17.63	0.2598	0.0416	2.05	38.2	28.6	23	0.0687	0.36087	50303
5.2	70.0	17.44	0.2954	0.0436	2.03	36.8	24.9	20	0.0710	0.38112	52137

Table 6: Characteristic boundary layer parameters from simulation with Spalart-Allmaras turbulence model

In figure (49), the development of the displacement thickness δ^*, momentum thickness θ and boundary layer thickness δ are presented for the region $3 \leq x \leq 5.2$ meter. The measured values of the same parameters are also displayed.

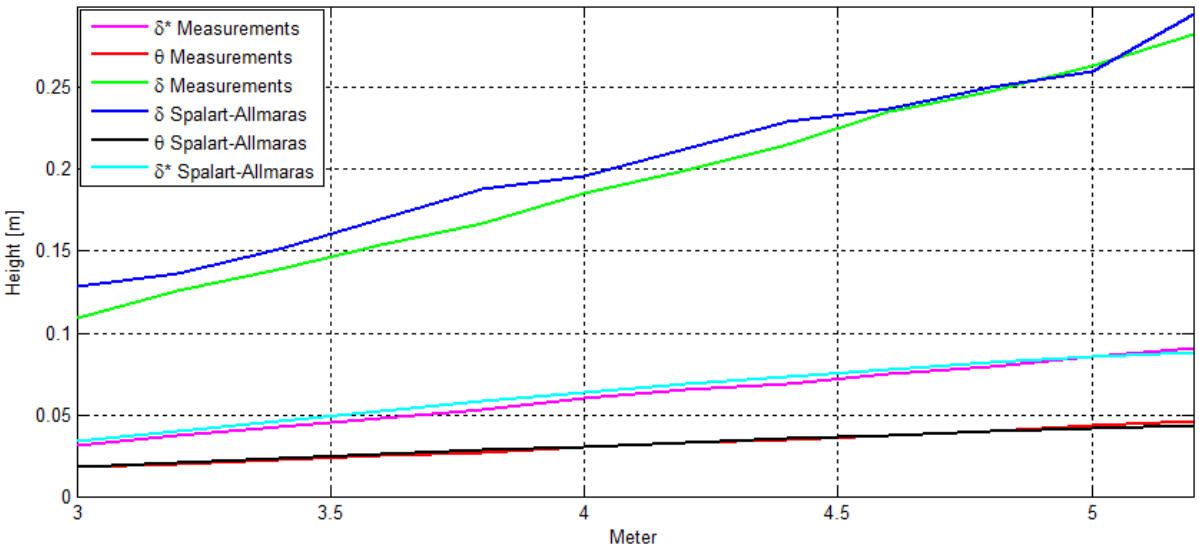

Figure 49: Development of boundary layer parameters for the simulation with Spalart-Allmaras model versus measurements.

In figure (50), the pressure coefficient and the derivative of the pressure coefficient in the axial direction are presented together with the measured values of the same parameters. The plots starts from the diffuser inlet and ends at the diffuser outlet.

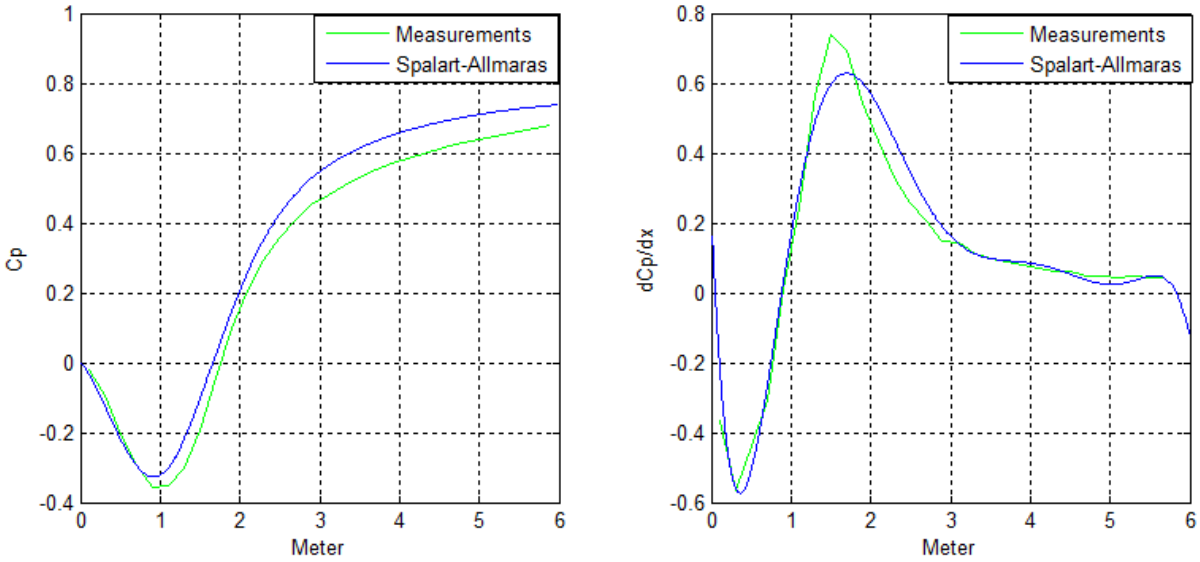

Figure 50: Plots showing pressure coefficient distribution left figure and the derivative of the pressure coefficient in the streamwise direction right figure for the Spalart-Allmaras model versus measurements

3.1.4 Comparing results from smooth diffuser simulations

In this section some of the boundary layer parameters from the different turbulence models are compared with each other and with the physical measurements.

In figure (51), C_p values obtained from the different turbulence models are plotted together with the physical measurements. The plots starts at the diffuser inlet and ends at the diffuser outlet.

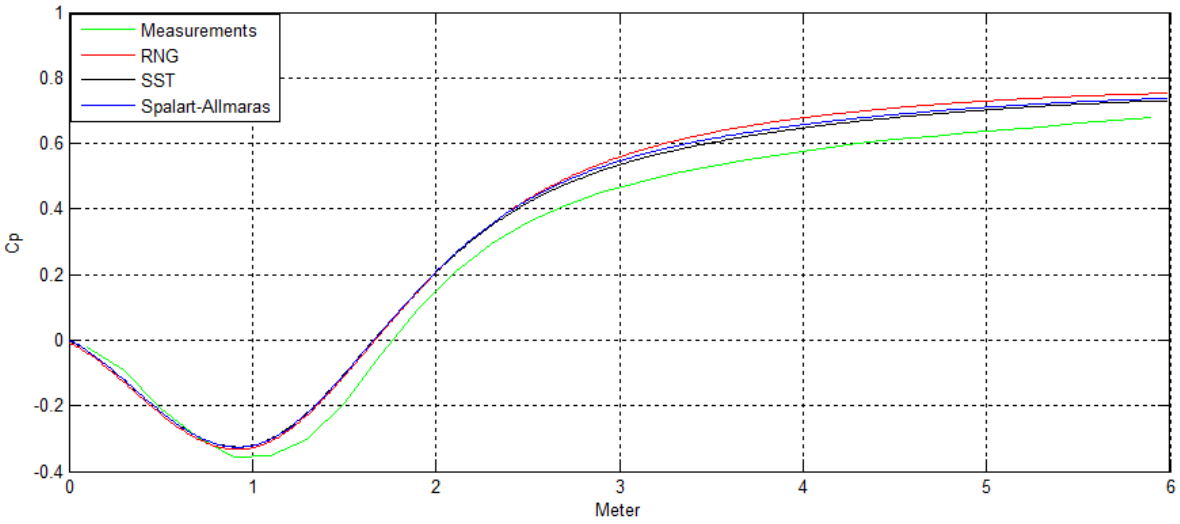

Figure 51: Pressure coefficient distribution with applied turbulence model versus measured distribution

In figure (52), dC_p/dx from the different turbulence models are plotted together with the C_p gradient in the axial direction obtained from the physical measurements.

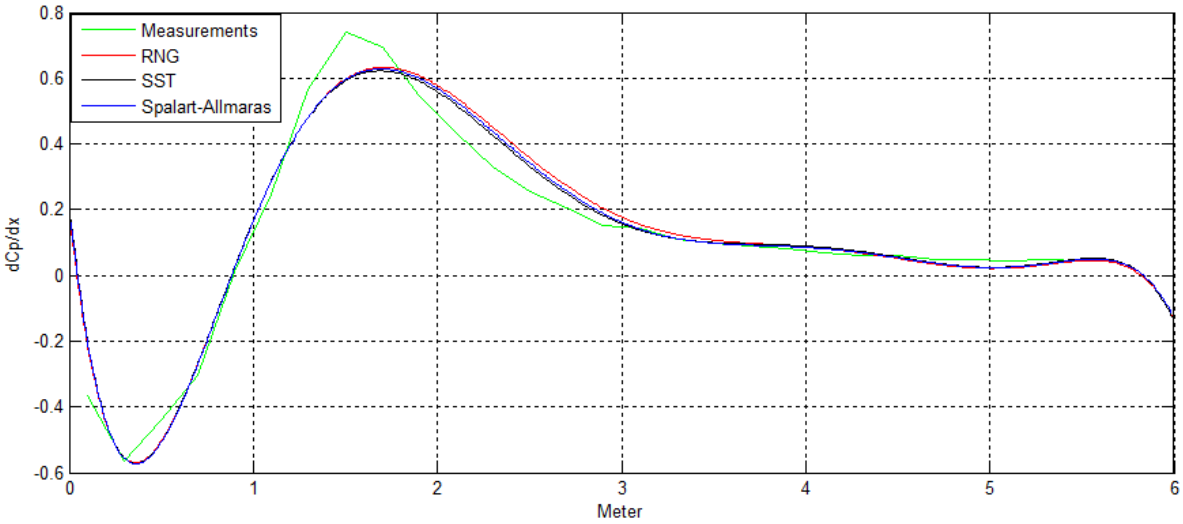

Figure 52: Pressure coefficient gradient for applied turbulence models versus measured distribution

In figure (53), the Clauser pressure parameter (β) is plotted for the different turbulence models, together with the physical measurements in the region $3 \leq x \leq 5.2$ meter.

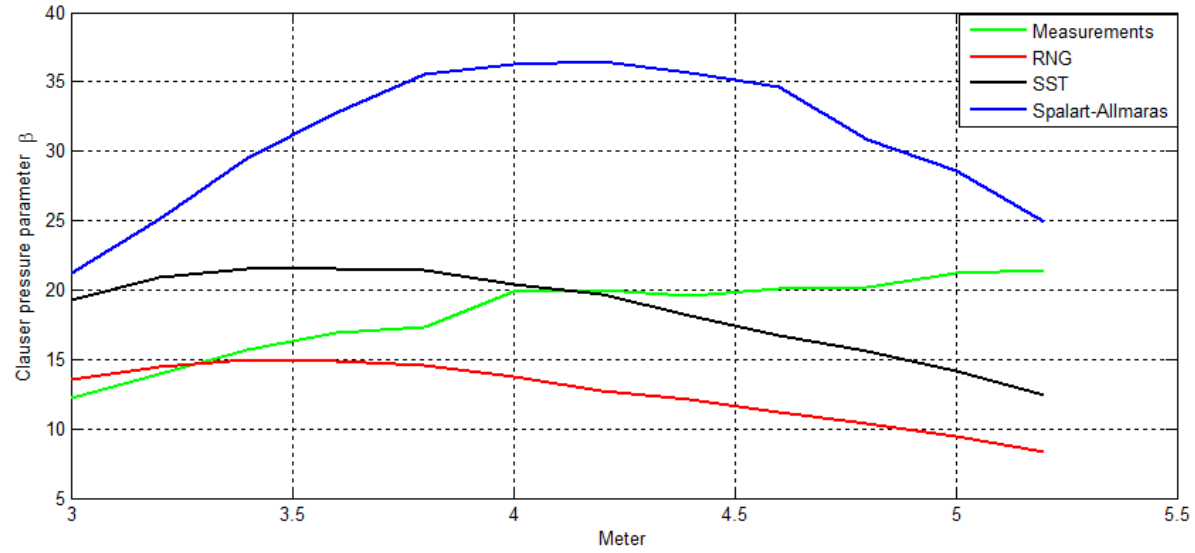

Figure 53: Clauser pressure parameter β for applied turbulence models versus measured values

In figure (54), the shape factor (H) is plotted for the different turbulence models, together with the physical measurements in the region $3 \leq x \leq 5.2$ meter.

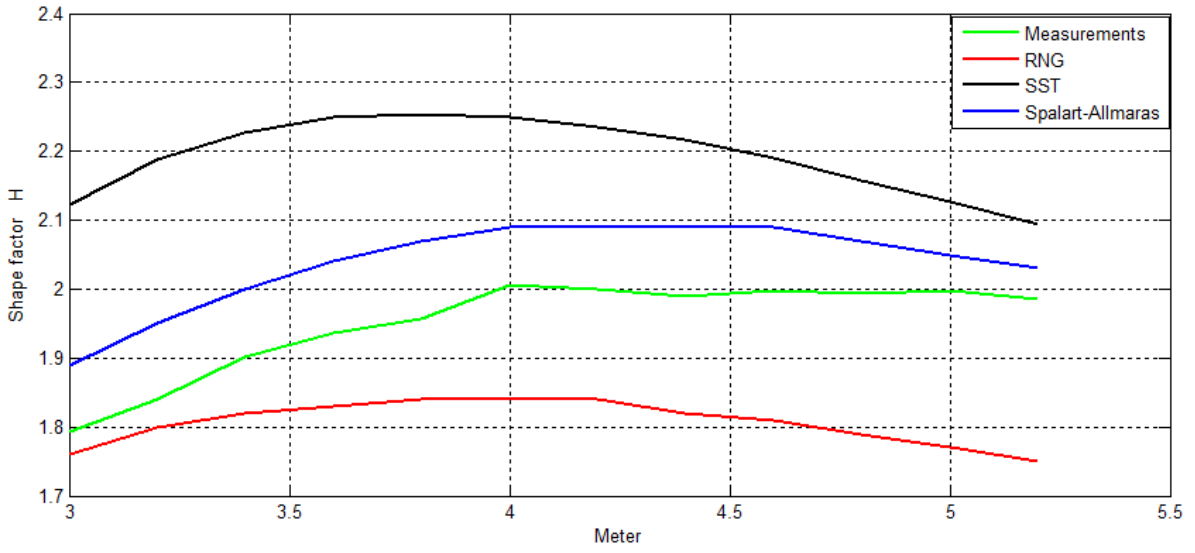

Figure 54: Shape factor H for applied turbulence models versus measured values

In figure (55), the Clauser shape factor (G) is plotted for the different turbulence models, together with the physical measurements in the region $3 \leq x \leq 5.2$ meter.

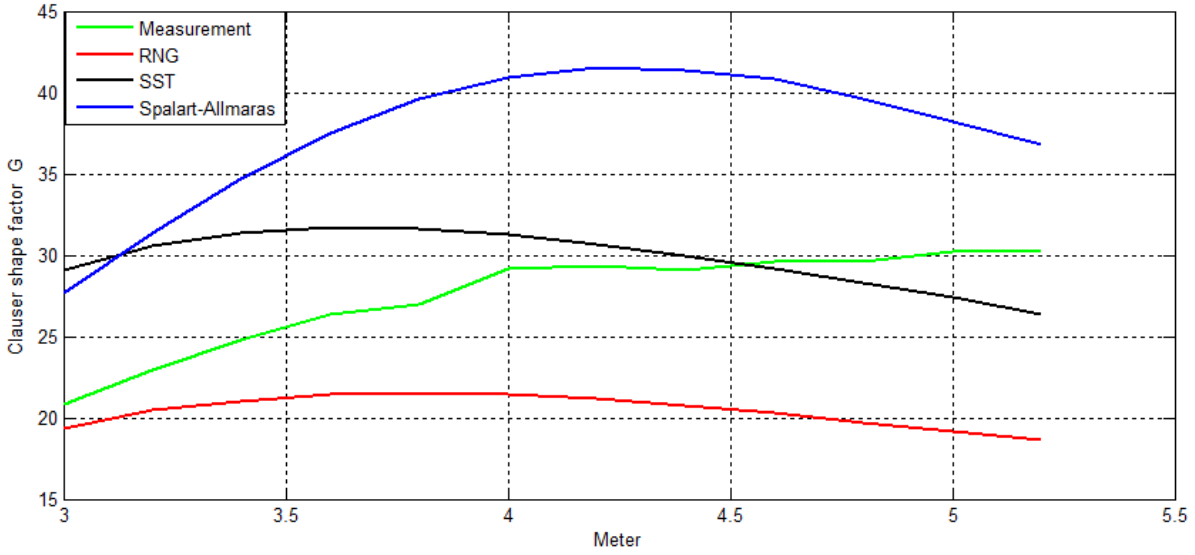

Figure 55: Clauser shape factor G for applied turbulence model versus measured values

In figure (56), the friction coefficient C_f is plotted for the different turbulence models, together with the physical measurements in the region $3 \leq x \leq 5.2$ meter. The C_f values displayed are for $C_f * 10^3$.

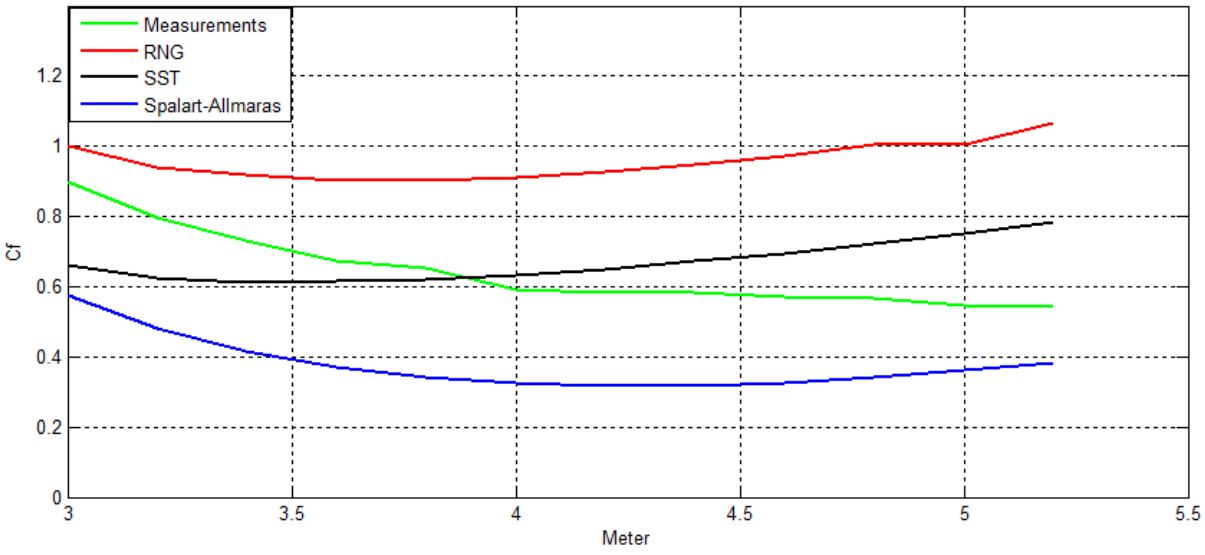

Figure 56: Friction coefficient for applied turbulence models versus measured values

3.2 Results from simulations on rough diffuser

In this chapter the results of the simulation done on the rough diffuser are presented. From appendix (F) it can be seen that there are some mesh dependencies on several of the turbulence models, therefore as stated in section 2.2.1 only the results from the meshes with the best replication of the physical measurements are presented. The results of the simulations will first be given in a table identical to table (3), next follows detailed velocity profiles produced by the different turbulence models at the respective locations where the physical measurements from the LDA is at hand. Thereafter will figures displaying the pressure coefficient and the pressure coefficient gradient be presented. Finally, there is a section where some of the flow parameters from the different turbulence models are plotted together for comparison. Attention has been given to the development of the flow along the floor of the diffuser where the roughness elements are placed. Therefore, the velocity plots which are all presented in [m/s] has only been plotted up until the cross sectional height presented in [m] where the freestream velocity starts.

3.2.1 k-ω SST

In this section the results from the simulations where the turbulence model k-ω SST have been utilized on mesh 2.4 are presented.

In table (7), characteristic boundary layer parameters for the region $2.6 \leq x \leq 3.6$ meter are presented.

X [m]	h [cm]	U_e [m/s^{-1}]	δ [m]	δ^* [m]	θ [m]	H [-]	Re_θ [-]
2.6	42.14	26.8	0.1683	0.0831	0.0207	4.01	38046
3.25	51.70	24.9	0.2641	0.1544	0.0315	4.90	53744
3.6	56.68	24.2	0.3117	0.1879	0.0373	5.03	61963

Table 7: Boundary layer parameters for the k-ω SST turbulence model

In figure (57) the velocity profiles given by the k-ω SST model at 2.6, 3.25 and 3.6 meter are presented together with the physical LDA measurements

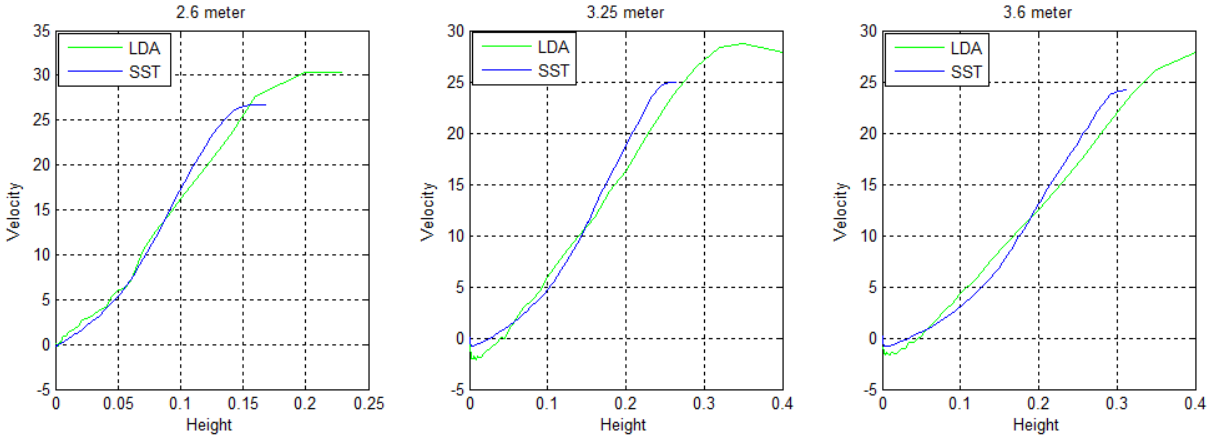

Figure 57: The k-ω SST velocity profiles presented in [m/s] versus the cross sectional height presented in [m], plotted together with the physical measurements at the respective locations.

In figure (58), the pressure coefficient and the derivative of the pressure coefficient in the axial direction are presented together with the measured values of the same parameters. The plots starts from the diffuser inlet and ends at the diffuser outlet.

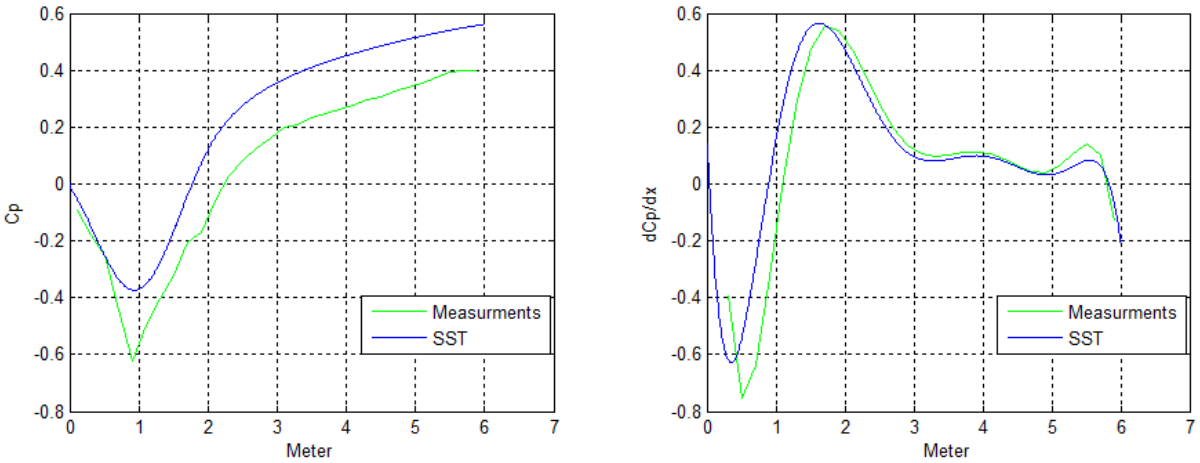

Figure 58: The k-ω SST pressure coefficient distribution to the left and the pressure coefficient gradient to the right versus their physical measurements.

3.2.2 Standard k-ω

In this section the results from the simulations where the standard k-ω turbulence model have been utilized on mesh 2.4 are presented.

In table (8), characteristic boundary layer parameters for the region $2.6 \leq x \leq 3.6$ meter are presented.

X [m]	h [cm]	U_e [m/s^{-1}]	δ [m]	δ^* [m]	θ [m]	H [-]	Re_θ [-]
2.6	42.14	26.4	0.1697	0.0776	0.0232	3.34	42064
3.25	51.70	24.7	0.2564	0.1510	0.0325	4.64	55145
3.6	56.68	24.2	0.3112	0.1867	0.0372	5.01	61827

Table 8: Boundary layer parameters for the standard k-ω turbulence model

In figure (59) the velocity profiles given by the standard k-ω model at 2.6, 3.25 and 3.6 meter are presented together with the physical LDA measurements

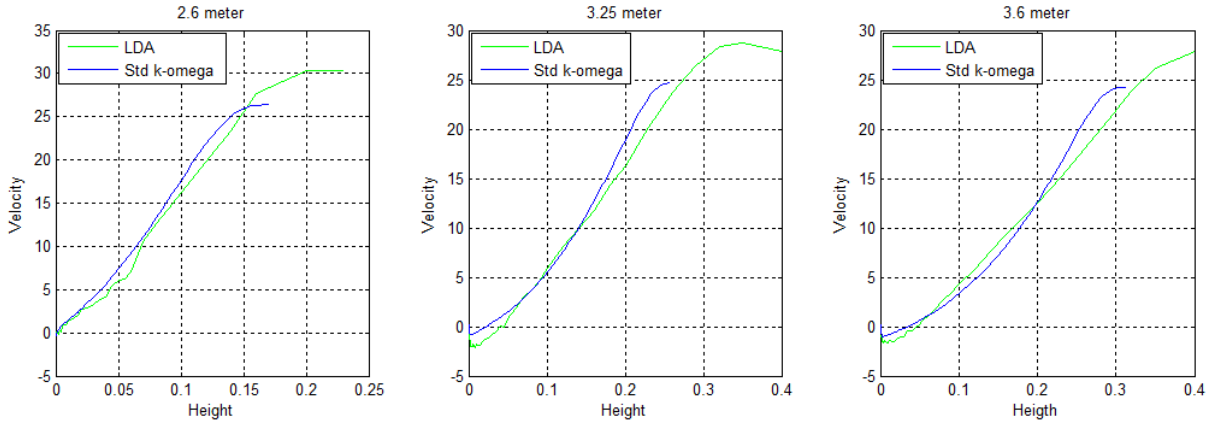

Figure 59: The standard k-ω velocity profiles presented in [m/s] versus the cross sectional height presented in [m], plotted together with the physical measurements at the respective locations.

In figure (60), the pressure coefficient and the derivative of the pressure coefficient in the axial direction are presented together with the measured values of the same parameters. The plots starts from the diffuser inlet and ends at the diffuser outlet.

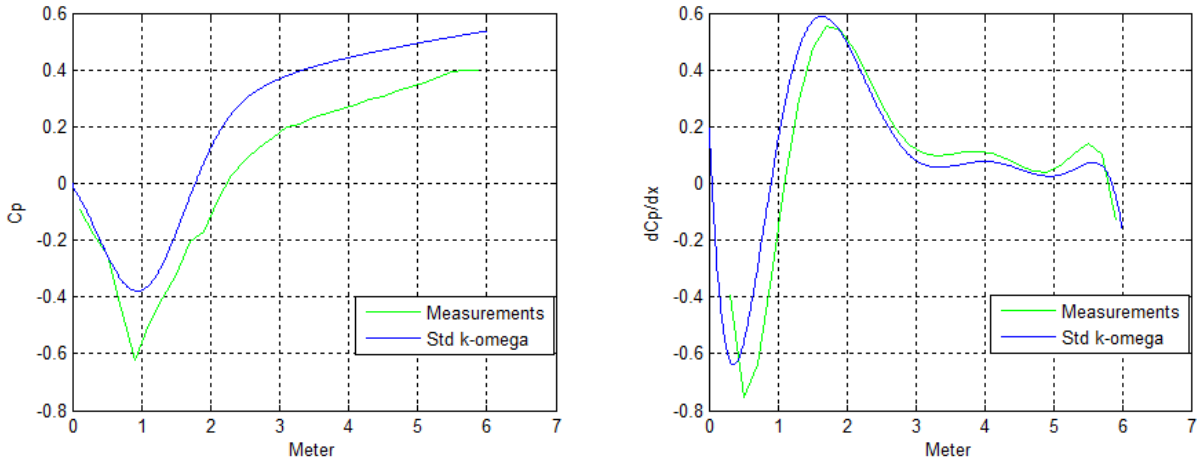

Figure 60: The standard k-ω pressure coefficient distribution to the left and the pressure coefficient gradient to the right versus their physical measurements.

3.2.3 k-ε RNG

In this section the results from the simulations where the turbulence model k-ε RNG have been utilized on mesh 2.3 are presented.

In table (9), characteristic boundary layer parameters for the region $2.6 \leq x \leq 3.6$ meter are presented.

X [m]	h [cm]	U_e [m/s^{-1}]	δ [m]	δ^* [m]	θ [m]	H [-]	Re_θ [-]
2.6	42.14	26.6	0.1698	0.0801	0.0260	3.1	47406
3.25	51.70	24.5	0.2722	0.1464	0.0398	3.7	66973
3.6	56.68	23.7	0.3223	0.1777	0.0469	3.8	76266

Table 9: Boundary layer parameters for the k-ε RNG turbulence model

In figure (61) the velocity profiles given by the k-ε RNG model at 2.6, 3.25 and 3.6 meter are presented together with the physical LDA measurements

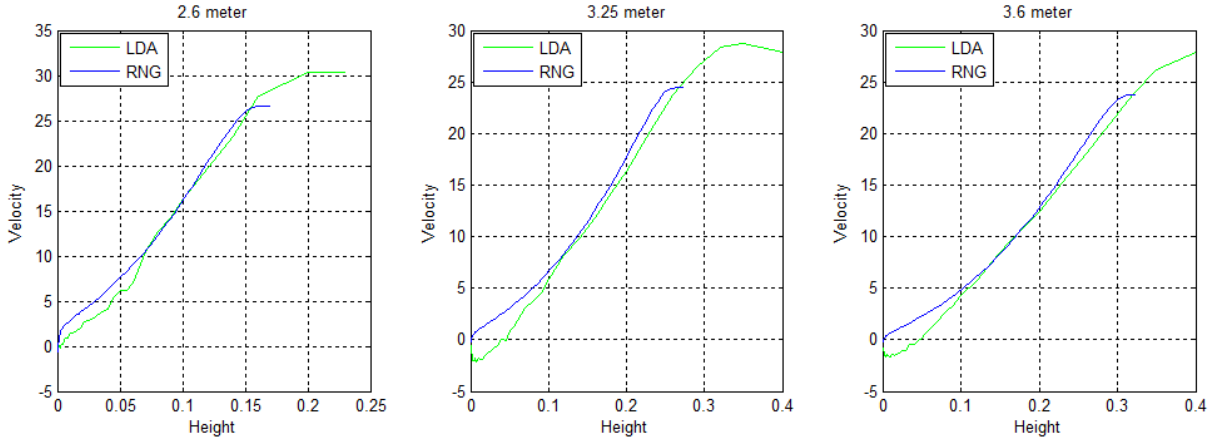

Figure 61: The k-ε RNG velocity profiles presented in [m/s] versus the cross sectional height presented in [m], plotted together with the physical measurements at the respective locations.

In figure (62), the pressure coefficient and the derivative of the pressure coefficient in the axial direction are presented together with the measured values of the same parameters. The plots starts from the diffuser inlet and ends at the diffuser outlet.

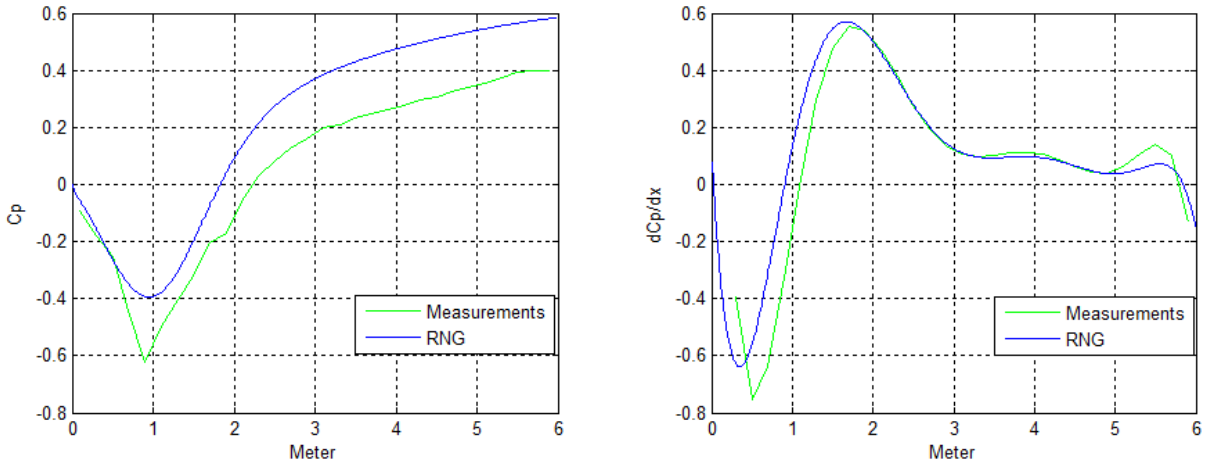

Figure 62: The k-ε RNG pressure coefficient distribution to the left and the pressure coefficient gradient to the right versus their physical measurements.

3.2.4 k-ε Realizable

In this section the results from the simulations where the turbulence model k-ε Realizable have been utilized on mesh 2.3 are presented.

In table (10), characteristic boundary layer parameters for the region $2.6 \leq x \leq 3.6$ meter are presented.

X [m]	h [cm]	U_e [m/s^{-1}]	δ [m]	δ^* [m]	θ [m]	H [-]	Re_θ [-]
2.6	42.14	26.3	0.1698	0.0754	0.0269	2.8	48618
3.25	51.70	24.1	0.2618	0.1407	0.0412	3.4	68713
3.6	56.68	23.4	0.3229	0.1717	0.0478	3.6	76815

Table 10: Boundary layer parameters for the k-ε Realizable turbulence model

In figure (63) the velocity profiles given by the k-ε Realizable model at 2.6, 3.25 and 3.6 meter are presented together with the physical LDA measurements

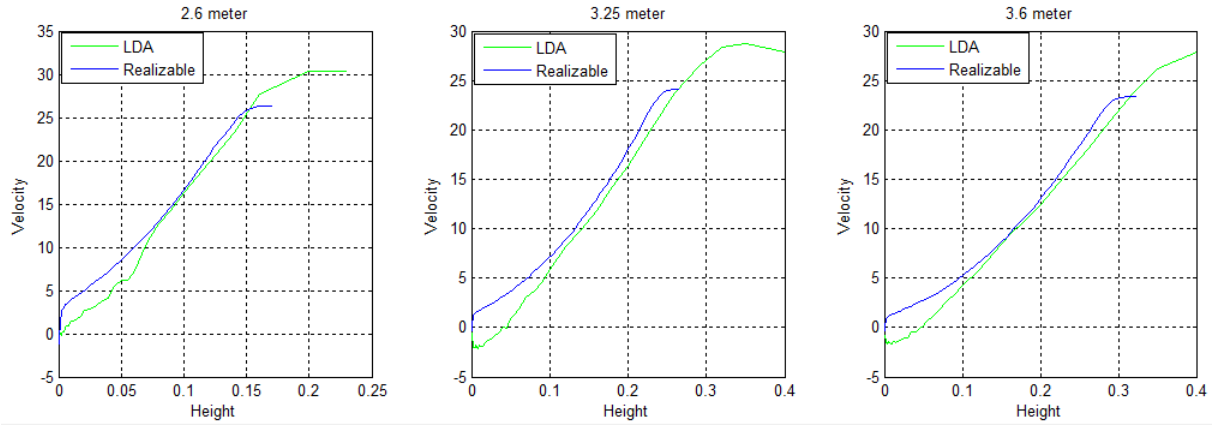

Figure 63: The k-ε Realizable velocity profiles presented in [m/s] versus the cross sectional height presented in [m], plotted together with the physical measurements at the respective locations.

In figure (64), the pressure coefficient and the derivative of the pressure coefficient in the axial direction are presented together with the measured values of the same parameters. The plots starts from the diffuser inlet and ends at the diffuser outlet.

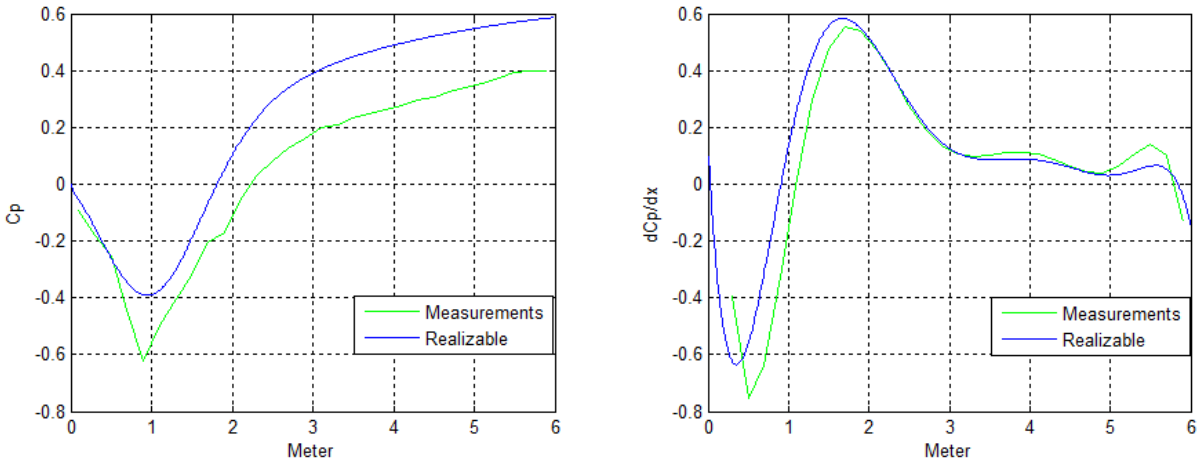

Figure 64: The k-ε Realizable pressure coefficient distribution to the left and the pressure coefficient gradient to the right versus their physical measurements.

3.2.5 RSM

In this section the results from the simulations where the RSM turbulence model have been :

In table (11), characteristic boundary layer parameters for the region $2.6 \leq x \leq 3.6$ meter are presented.

X [m]	h [cm]	U_e [m/s^{-1}]	δ [m]	δ^* [m]	θ [m]	H [-]	Re_θ [-]
2.6	42.14	28.4	0.2235	0.1034	0.0370	2.8	72026
3.25	51.70	26.5	0.3377	0.1773	0.0538	3.3	97838
3.6	56.68	25.9	0.3981	0.2124	0.0623	3.4	110690

Table 11: Boundary layer parameters for the RSM turbulence model

In figure (65) the velocity profiles given by the RSM model at 2.6, 3.25 and 3.6 meter are presented together with the physical LDA measurements

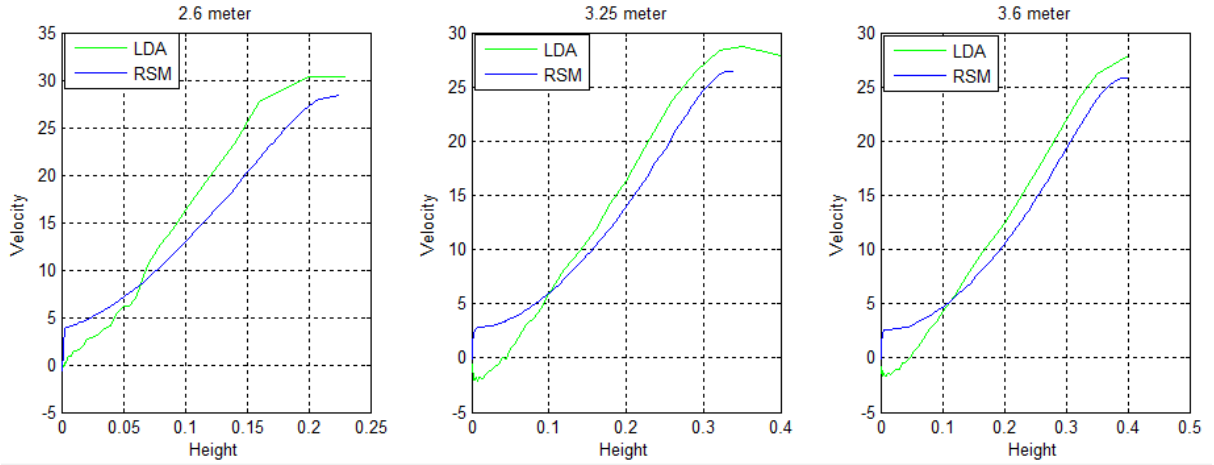

Figure 65: The RSM velocity profiles presented in [m/s] versus the cross sectional height presented in [m], plotted together with the physical measurements at the respective locations.

In figure (66), the pressure coefficient and the derivative of the pressure coefficient in the axial direction are presented together with the measured values of the same parameters. The plots starts from the diffuser inlet and ends at the diffuser outlet.

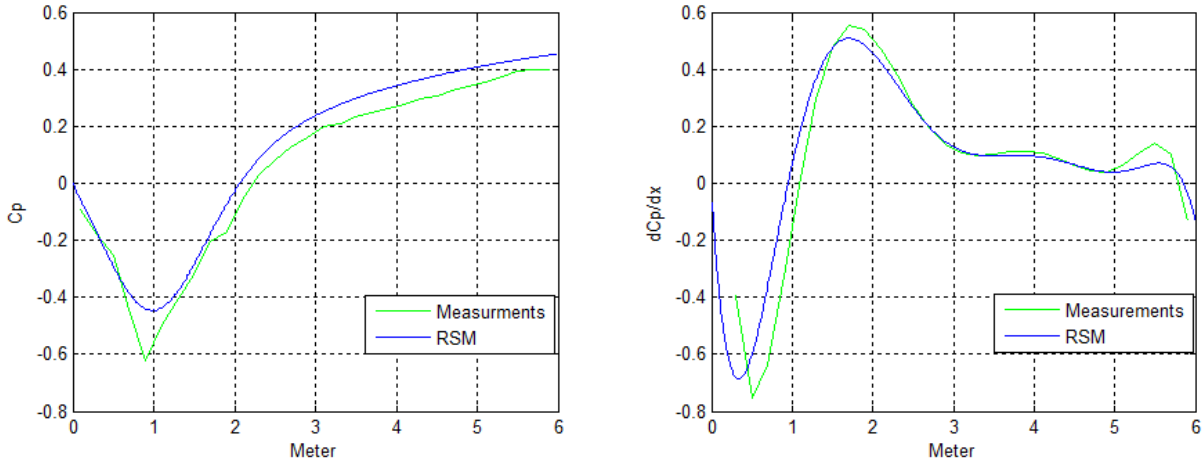

Figure 66: The RSM pressure coefficient distribution to the left and the pressure coefficient gradient to the right versus their physical measurements.

3.2.6 Spalart-Allmaras

In this section the results from the simulations where the Spalart-Allmaras turbulence model have been utilized on mesh 2.3 are presented.

In table (12), characteristic boundary layer parameters for the region $2.6 \leq x \leq 3.6$ meter are presented.

X [m]	h [cm]	U_e [m/s^{-1}]	δ [m]	δ^* [m]	θ [m]	H [-]	Re_θ [-]
2.6	42.14	27.5	0.1815	0.0927	0.0218	4.25	41131
3.25	51.70	26.2	0.2895	0.1738	0.0292	5.96	52338
3.6	56.68	25.8	0.3450	0.2119	0.0332	6.4	58795

Table 12: Boundary layer parameters for the Spalart-Allmaras turbulence model

In figure (67) the velocity profiles given by the Spalart-Allmaras model at 2.6, 3.25 and 3.6 meter are presented together with the physical LDA measurements

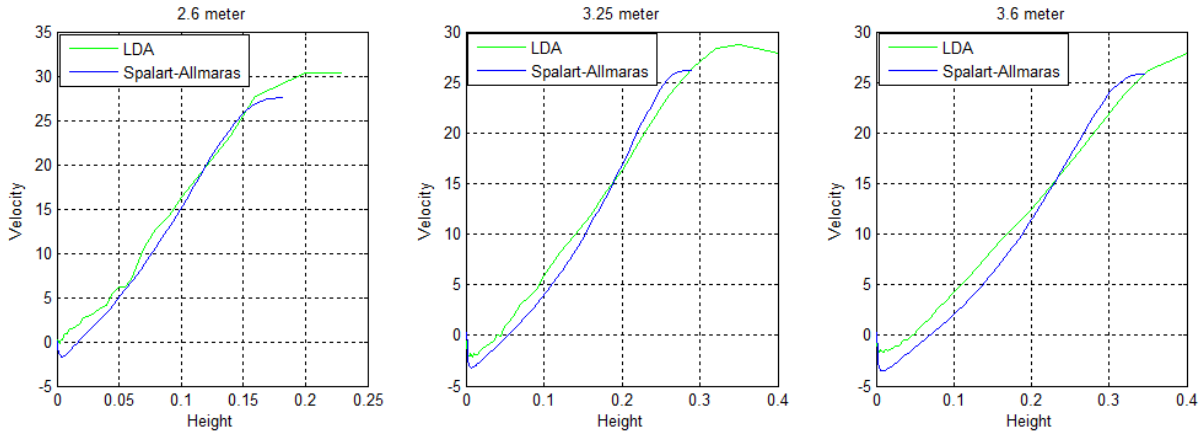

Figure 67: The Spalart-Allmaras velocity profiles presented in [m/s] versus the cross sectional height presented in [m], plotted together with the physical measurements at the respective locations.

In figure (68), the pressure coefficient and the derivative of the pressure coefficient in the axial direction are presented together with the measured values of the same parameters. The plots starts from the diffuser inlet and ends at the diffuser outlet.

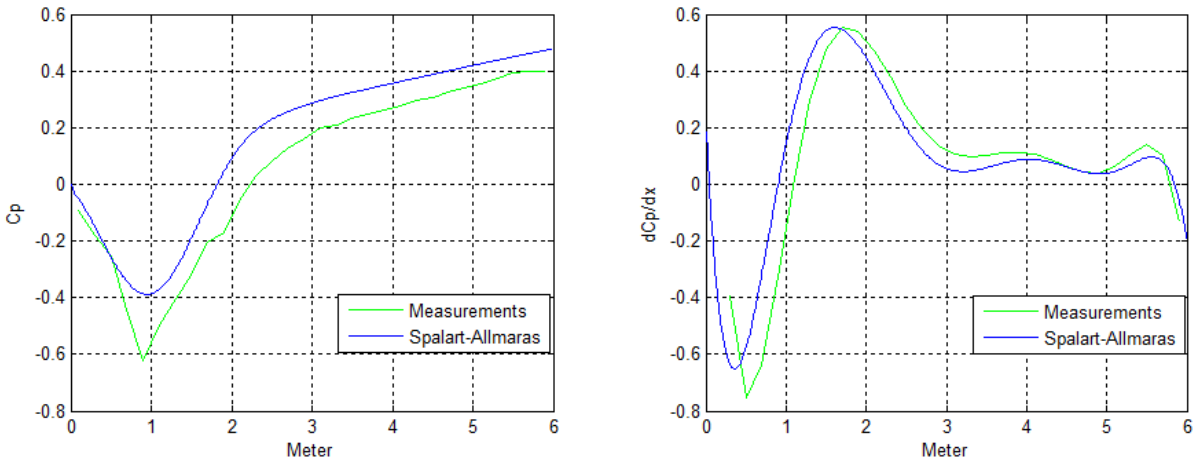

Figure 68: The Spalart-Allmaras pressure coefficient distribution to the left and the pressure coefficient gradient to the right versus their physical measurements.

3.2.7 Comparing results from rough diffuser simulations

In figure (69) the distribution of the pressure coefficient of the respective turbulence models and the physical measurements are presented

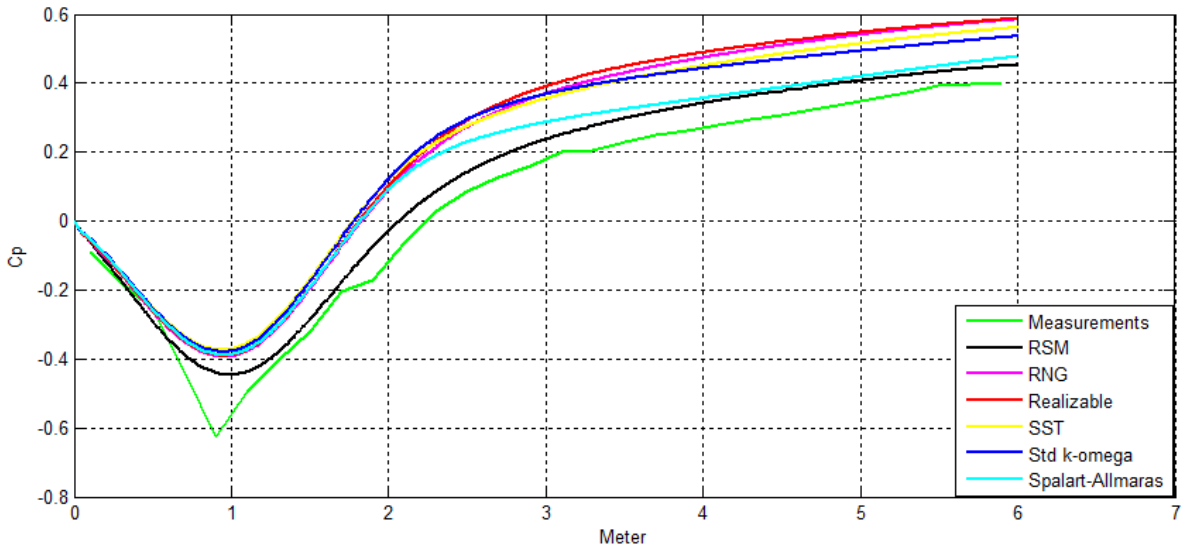

Figure 69: Pressure coefficient distribution for the applied turbulence models versus the physical measurements.

In figure (70) the pressure coefficient gradient for the respective turbulence models are presented together with the physical measurements.

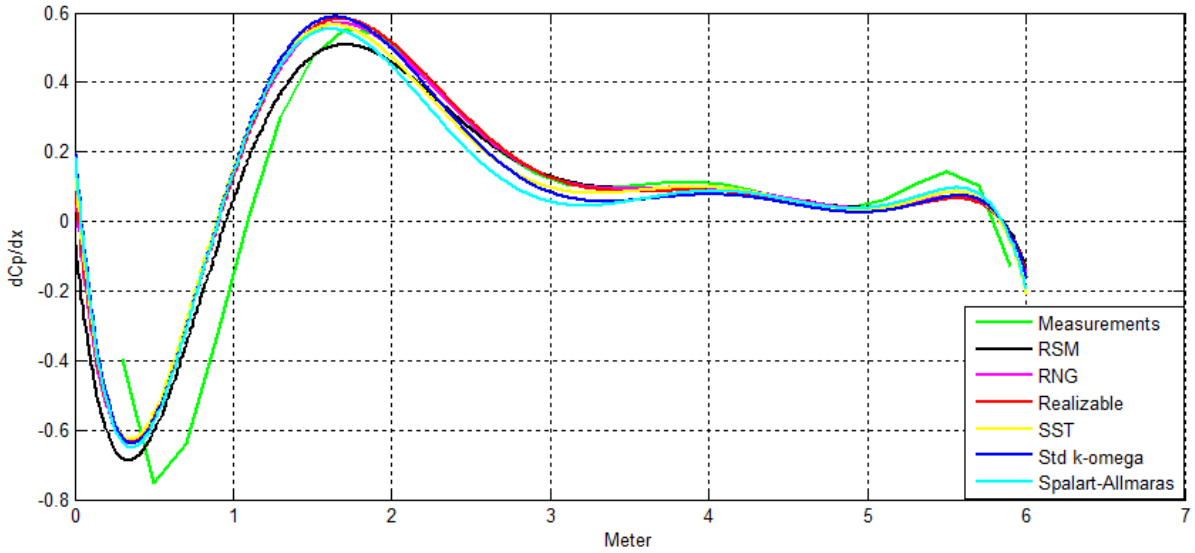

Figure 70: The pressure coefficient gradient for the applied turbulence models versus the physical measurements

In figure (71), the development of the boundary layer thickness δ, is presented for the respective turbulence models and the physical measurements in the region $2.6 \leq x \leq 3.6$ meter.

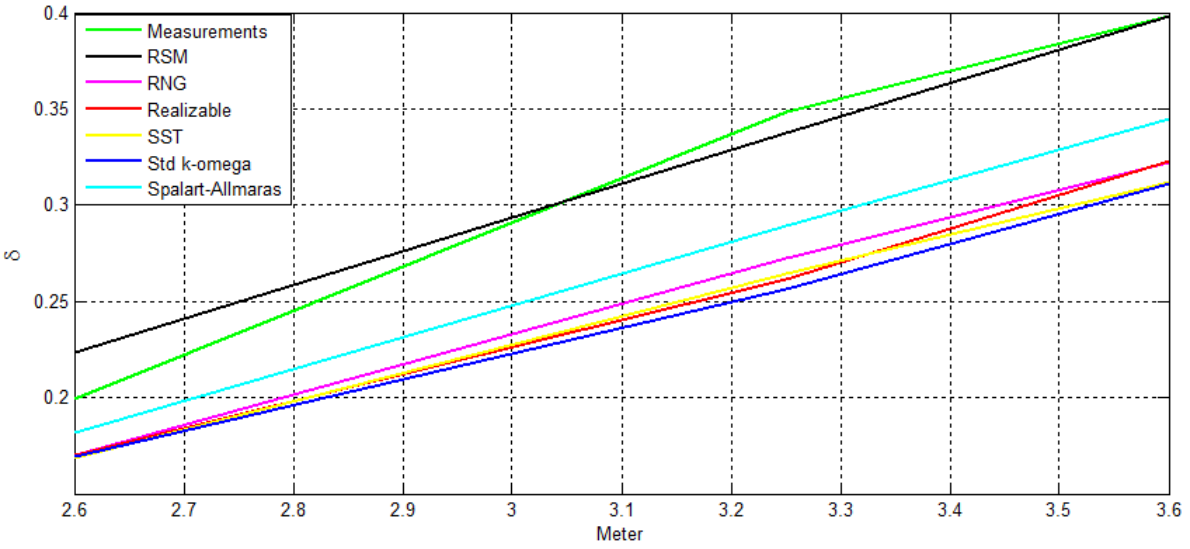

Figure 71: Development of boundary layer thickness [m] for applied turbulence models versus physical measurements

In figure (72), the development of the boundary layer thickness δ^*, is presented for the respective turbulence models and the physical measurements in the region $2.6 \leq x \leq 3.6$ meter.

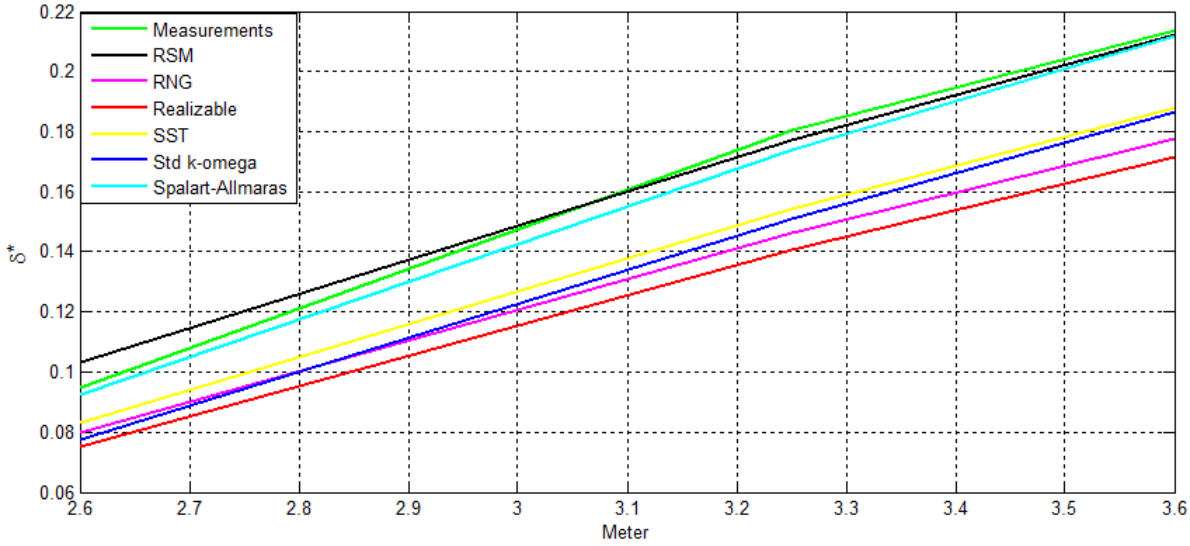

Figure 72: Development of the displacement thickness [m] for the applied turbulence models versus the physical measurements

In figure (73), the development of the Shape factor is presented for the respective turbulence models and the physical measurements in the region $2.6 \leq x \leq 3.6$ meter.

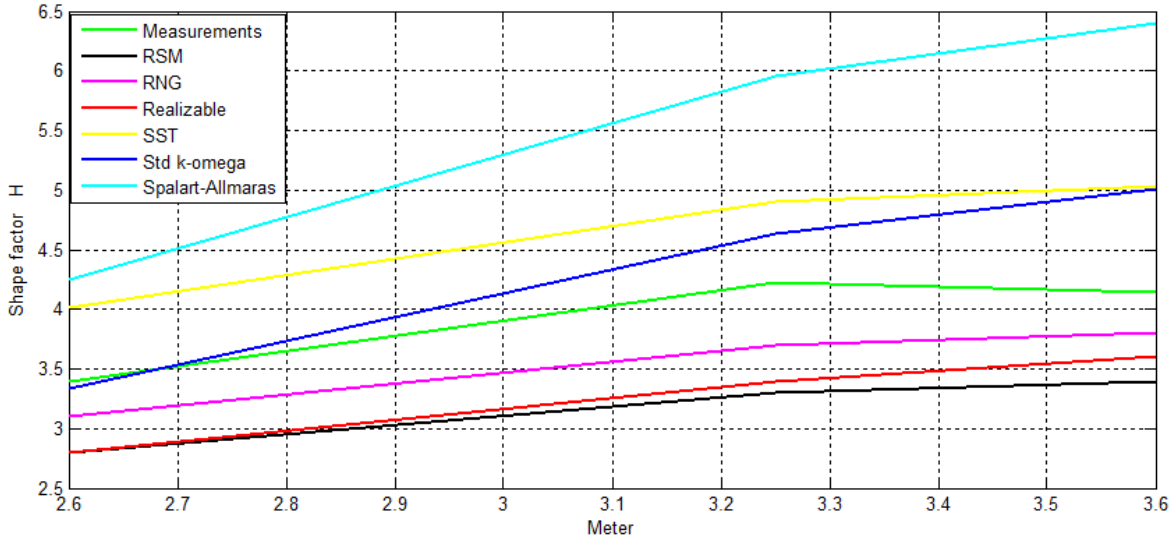

Figure 73: Development of the shape factor H for the applied turbulence models versus the physical measurements

In figure (74), the development of the momentum thickness θ, is presented for the respective turbulence models and the physical measurements in the region $2.6 \leq x \leq 3.6$ meter.

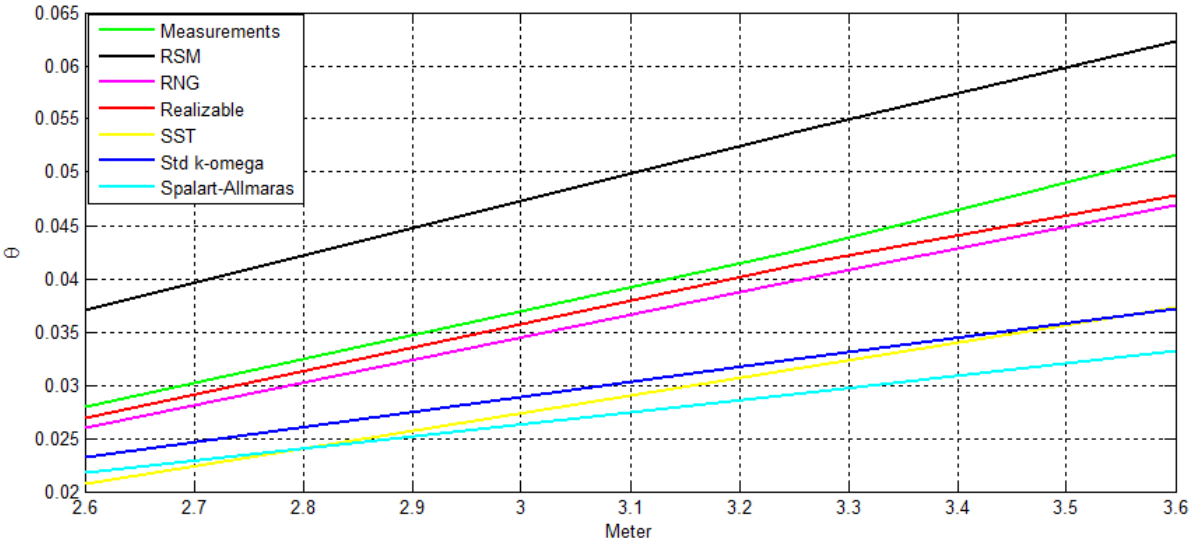

Figure 74: The development of the momentum thickness [m] for the applied turbulence models versus the physical measurements

In figure (75), the velocity profiles produced by the different turbulence models at 2.6 meters are plotted and displayed together with the physical measurements obtained from the LDA.

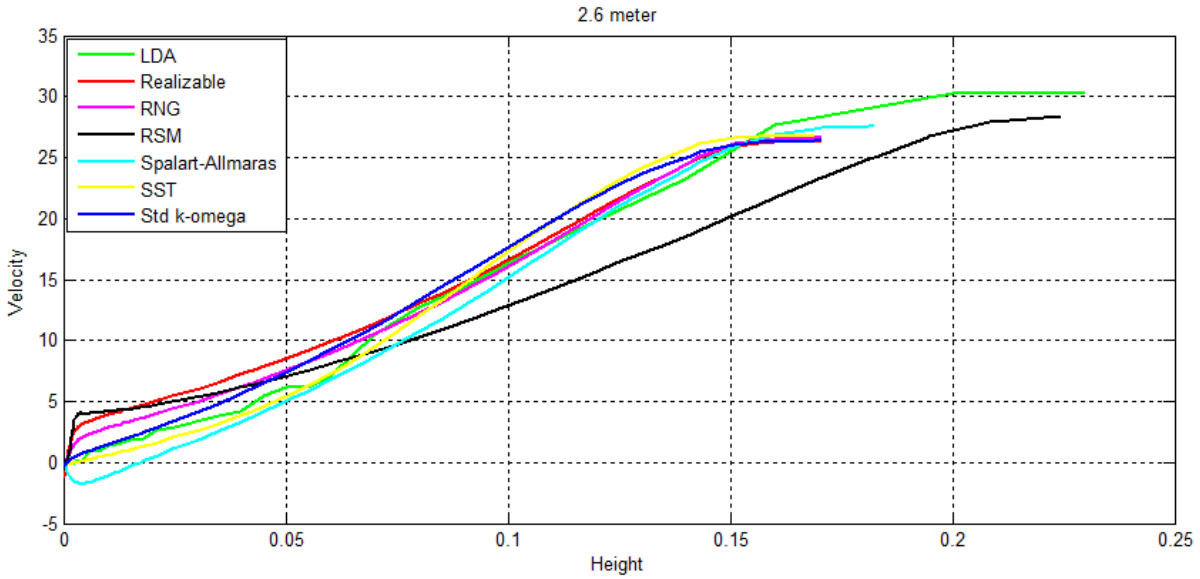

Figure 75: Velocity profiles [m/s] for the applied turbulence models versus the physical measurements plotted at 2.6 meter. Cross sectional height given in [m].

In figure (76), the velocity profiles produced by the different turbulence models at 3.25 meters are plotted and displayed together with the physical measurements obtained from the LDA.

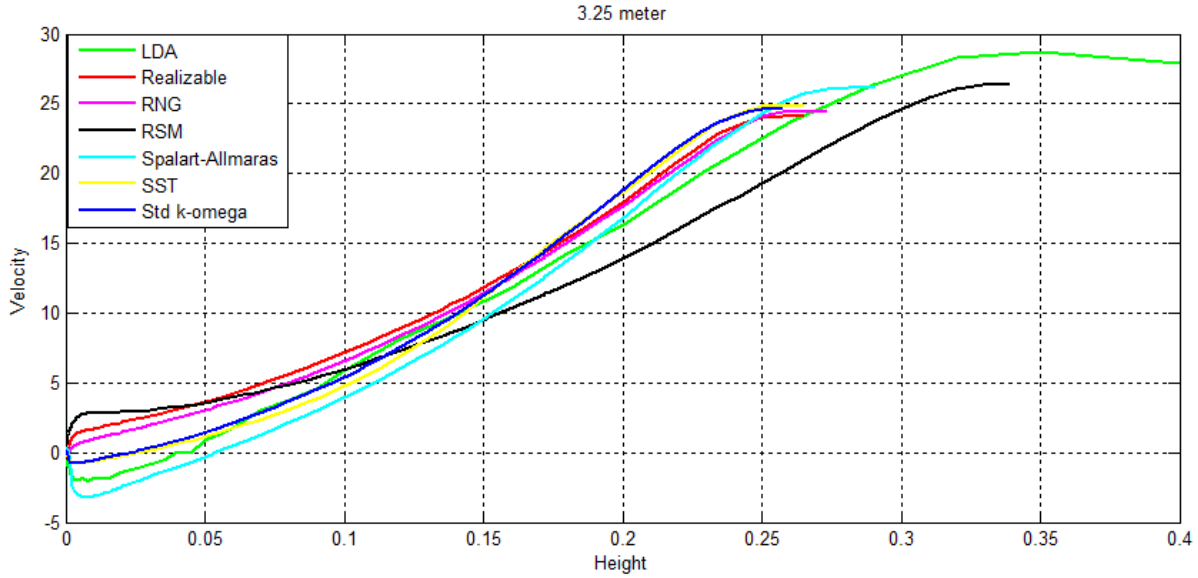

Figure 76: Velocity profiles [m/s] for the applied turbulence models versus the physical measurements plotted at 3.25 meter. Cross sectional height given in [m].

In figure (77), the velocity profiles produced by the different turbulence models at 3.6 meters are plotted and displayed together with the physical measurements obtained from the LDA

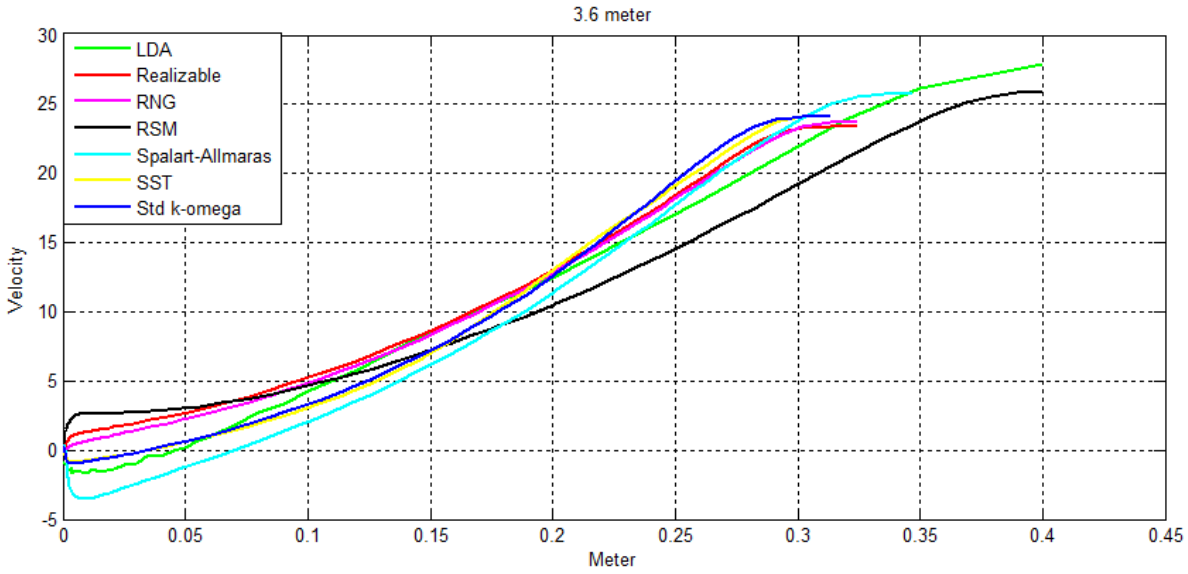

Figure 77: Velocity profiles [m/s] for the applied turbulence models versus the physical measurements plotted at 3.6 meter. Cross sectional height given in [m].

Chapter 4 - Discussion of CFD results

In this chapter the results from the simulations are discussed. First the simulations performed on the smooth diffuser are discussed, secondly follows the discussion of the results from the rough diffuser.

4.1 Smooth diffuser

In this section the results from the smooth diffuser simulations are discussed. First the two equation models will be discussed in the same section. Thereafter follows a discussion of the results from the Spalart-Allmaras one equation model. In the article [17] equilibrium boundary layer flow was obtained in the region $4 \leq x \leq 5$ meter, therefore most of the data will be for the region $3 \leq x \leq 5.2$ meter, from now on denoted "measurement area". As can be seen from appendix (F), the smooth diffuser simulations shows little mesh dependencies between the applied meshes. Nevertheless, there might be that a certain threshold value in relation to the number of cells in the geometry have not been met. It is therefore possible that the simulations will continue to show similar results until the mesh refinement reaches this threshold value. It is however assumed that the refinement made to the mesh was adequately to discovery any mesh dependencies.

4.1.1 Two equation models

In this section the results from the two equation turbulence models k-ω SST and k-ε RNG are discussed. They are discussed together because the results from the simulations utilizing the k-ω SST and k-ε RNG models where quite similar.

As can be seen from the figures (45) and (47) the development of the boundary layer, displacement and momentum thickness shows strong resemblance with the physical measurements for both models. However, in the region $4 \leq x \leq 5.2$ both models have a period where the boundary layer curve flattens. This happens for the k-ω SST model at 4 meter and for the k-ε RNG model at 4.4 meter. The same occurrence takes place for the displacement and momentum thicknesses but not before 4.8 meters and at slower pace. Consequently the two equation models does not show a linear growth rate of the boundary layer thickness in the region where equilibrium flow where obtained in [17, p.323].

From the C_p values in the figures (46) and (48) one can see that the k-ω SST and k-ε RNG models does not replicate the high velocities found in the throat of the diffuser, this is because the boundary layer at the throat has not developed as much as for the physical measurements, and thereby the two equation models produces lower free stream velocities. Accordingly the two equation models shows better pressure recovery than what is physically measured.

- For the Clauser pressure parameter β, one can see in figure (53) that the two equation models follows similar trends. Both start off with an increasing development lasting from 3 meter until 3.4 meter. Then follows reasonable constant β values for a short period stretching from $3.4 \leq x \leq 3.6$ meter for which the k-ω SST model has a β value of 21.5, and the k-ε RNG model has a β value of 15. Thereafter decreases the slope of the simulated β values until the end of the measurement area. The measured β values in [17] does also have a positive development in the start but rises faster and reaches a constant β value of 20 in the region $4 \leq x \leq 4.8$ meter, from where it grows a small positive slope and end off at a β of around 21. The reason behind the decreasing slope for the β values of the two equation models is that the simulated wall friction drops quite fast in the beginning of the measurement area and starts to level out at 3.6 meter and even increases towards the end of the measurement area, whilst the wall friction obtained in [17] decreases more or less all the way. The two equation models does therefore clearly not give a constant β value at the equilibrium region in [17].

- The friction coefficient obtained from the k-ω SST and k-ε RNG models displayed in figure (56), shows both clear deviation from the values obtained in [17]. As mentioned above the wall friction in the two equation models are increasing towards the end of the measurement area and therefore also gives increasing C_f values. The C_f obtained in [17] showed virtually constant values of in the region $4 \leq x \leq 5$ meter, this is evidently not the case for the two equation models. They do however create some regions of approximately constant C_f which for the k-ε RNG model is found between $3.5 \leq x \leq 4$ meter with a $C_f \approx 0.0009$ and then again at $4.8 \leq x \leq 5.2$ with a $C_f \approx 0.0001$. For the k-ω SST model a region of nearly constant C_f is found $3.5 \leq x \leq 3.8$ with a $C_f \approx 0.00061$.

- The shape factor H obtained from [17] shows an increasing slope from the start of the measurement area until it flattens out and remains constant from 4 meters. Both the two equation models follows the same trend in the beginning of the measurement area but starts to flatten out at around 3.5 meter. The k-ω SST model shows a small region of constant shape factor of 2.25 at the section $3.6 \leq x \leq 3.8$ meter, from where after it has a decreasing slope until the end of the measurement area. The k-ε RNG model also has a section of constant shape factor with a value of 1.84 but this region has shifted location to $3.8 \leq x \leq 4.4$ meter from where it too has a decreasing slope. The decreasing slope of the two equation models is however

not substantial, and small changes in displacement or momentum thickness causes deviations from the measured values. For the two equation models the displacement thickness flattens out a bit before the momentum thickness and thereby causes the small decreasing slope of the shape factor.

- For the Clauser shape factor G, both the k-ω SST and the k-ε RNG models show similar trends, but as the C_f and the shape factor H is not constant in the measurement area for neither of them, nor will the Clauser shape factor be either.

4.1.2 Spalart Allmaras

In this section the results from the one equation Spalart-Allmaras turbulence model is discussed.

One can see from figure (49) that the development of the displacement and momentum thickness follows the measured values in [17] closely. The boundary layer thickness is a bit larger for the Spalart-Allmaras model in the region $3 \leq x \leq 4.5$ meter before it collapses smoothly at 4.6, 4.8 and 5 meter with the measured values in [17]. Even though the simulated boundary layer produced by the Spalart-Allmaras model follows the same trend as the measured values in [17], it is apparent that the boundary layer does not have a linear growth rate in the region $4 \leq x \leq 5$ meters and hence the displacement, momentum and boundary layer will not share a common virtual origin based on their values in the region $4 \leq x \leq 5$ meter where equilibrium flow where obtained in [17].

In figure (50), one can see as for the two equation models that also the Spalart-Allmaras model produces lower free stream velocities at the throat of the diffuser, and thereby obtains a better pressure recovery than the actual measured values in [17]. This is because the boundary layer in the throat of the diffuser in the Spalart-Allmaras model has not developed as much as the one measured in [17]. However, the Spalart-Allmaras model together with the k-ω SST model has the closest match to the measured C_p curve. Due to the higher throat velocities in the physical measurements, there will naturally also be a stronger adverse pressure gradient in the physical diffuser then in the simulated diffuser, this can be seen in figure (51).

- The Clauser pressure gradient β produced by the Spalart-Allmaras simulations shows somewhat higher β values compare with the two equation models and the measured values in [17]. The pressure gradients for the two equation models, Spalart-Allmaras model and the physical measurements are not particularly different, but the wall friction is much lower in the Spalart-Allmaras model then in its comparisons. As a consequence, the Spalart-Allmaras model produces higher β values then what is physically measured. The β values in the Spalart-Allmaras model are a bit high, but shows a period of more or less constant values in the region $3.8 \leq x \leq$4.6 meter which is close to the equilibrium region obtained in [17].

- In figure (56) one can see that the C_f values produced by the Spalart-Allmaras model is the lowest by its comparisons. The low C_f is an effect of the low wall friction made by the model. Nevertheless these values are the closest to have a constant curve in the equilibrium region $4 \leq x \leq 5$ meter as obtained in [17].

- The shape factor obtained in [17] had a rising slope from the start of the measurement area until it developed a constant value of approximately 2 in the equilibrium region $4 \leq x \leq 5$ meter. The shape factor produced by the Spalart-Allmaras model shows in figure (54) very good resemblance with the measured value, and develops a constant shape factor curve of 2.1 in the region $4 \leq x \leq 4.6$ meters. From there the slope decreases slightly until the end of the measurement area.

- The Clauser shape factor G produced by the Spalart-Allmaras model shows similar trends as the two equation models but the G curve for the Spalart-Allmaras model has shifted to the right and peaks at about 4.25 meters, whilst the k-ω SST and the k-ε RNG peaked both at around 3.6 meter. The Spalart-Allmaras G curve also consists of higher values, which are a reflection of the low C_f made by the Spalart-Allmaras model.

4.2 Rough Diffuser

In this section the results from the rough diffuser simulations are discussed. First, the two equation models K-ω and K-ε are discussed, where after a discussion of the RSM model follows. Finally the one equation Spalart-Allmaras model is discussed. Detailed LDA measurements of the velocity profiles at 2.6, 3.25 and 3.6 meter have been carried out in[43], therefore most of the discussion of the rough diffuser simulations will be about this region.

4.2.1 K-ω models

In this section the results from the k-ω models are discussed.

The k-ω SST model was the first turbulence model that were tested in this thesis. Simulations with this model were first conducted utilizing the second order upwind scheme described in section (1.7.1). However, it was discovered as can be seen in appendix (H), that the QUICK scheme gave better results, producing higher free stream velocities and more separation. Therefore it was decided to switch to QUICK scheme for all later simulations

By investigating the respective velocity profiles produced by the k-ω models at 2.6, 3.25 and 3.6 meter in figure (57) and (59), it is evident that both k-ω models predicts separating boundary layers. It is also visible that the k-ω models have not separated at 2.6 meter which was also the case for the LDA measurements, thereby the models correctly predicts the onset of separation. The magnitude of separation that the k-ω models displays are however not as large as the physical LDA measurements revealed. Consequently, the k-ω models also under predicts the boundary layer thickness recognized in figure (71). The effective flow area will therefore be larger with the k-ω models then in the physical rough diffuser. Therefore the k-ω models fail to replicate the correct magnitude of the free stream velocities which can be seen from figures (57) and (59) are substantially lower than the LDA measurements. The velocity deviation observed in the k-ω models are also due to considerably lower velocities in the throat of the diffuser, caused by a less developed boundary layer for the k-ω models then what was the case for the real diffuser flow. The result is that the k-ω model displays a higher pressure recovery at the exit of the diffuser then the physical measurements, and thereby over predicts the diffuser performance.

The slope for the development of the boundary layer thickness produced by the k-ω models as can be seen in figure (71), grows a bit slower than the physical measurements, this occurs until 3.25 meter where the growth rate of the physical measured boundary layer slows down. The same event is viewable in figure (72) for the displacement thickness but to a lesser extent. The magnitude of the boundary layer is also less then what is physically measured, because of what is already discussed above.

In figure (73), one can see that the k-ω SST model displays the same profile as the curve of the measured shape factor, although with a bit higher values. The shape factor curve of the

standard k-ω model grows faster and don't have the same flattening at 3.25 meter as the k-ω SST model and the physical measurements.

The development of the momentum thickness is quite similar for both k-ω models, and follows a curve with a lesser gradient than the curve of the measurements, as can be seen in figure (74). The lower momentum thickness values are because of the thinner boundary layer produced by the k-ω models.

4.2.2 K-ε models

In this section the results from the k-ε models are discussed.

By inspecting figure (61) and (63) it is evident that neither of the k-ε models applied, manage to predict the boundary layer separation occurrence of physical rough diffuser. The free stream velocities in the throat also suffers from lack of boundary layer development compared with the measured values, and consequently the C_p values in the throat is higher than the measurement. The result is an over prediction of the pressure recovery of the diffuser. Interestingly the shape factors of the k-ε models are quite high, yielding 3.8 and 3.6 respectively for the RNG and Realizable models at 3.6 meters. This suggests that the k-ε models are right on the verge of separation.

As stated in section (1.8.4), the k-ε model is developed for high Reynolds number flow, and tends to produce large turbulent length scales in the near wall region, this amplifies the turbulent kinetic energy and thereby suppresses or delays flow separation. The origin of the overproduction of turbulent kinetic energy in the k-ε model is found in the defect layer. Therefore specialized versions of the k-ε model like the RNG and Realizable models, where viscous correction and extra terms for strained flow is included, should not necessarily cure the k-ε models inconsistency in the defect layer. Therefore it is nor surprising that the k-ε models do not display any separating flow, neither at the designated comparison stations, nor throughout the rest of the diffuser.

The k-ε models are therefore not applicable for analyzing the roughness caused boundary layer separation in this thesis.

4.2.3 RSM model

In this section the results from the RSM model is discussed.

The RSM model is the most advanced model utilized in this thesis. As in this case, for two-dimensional simulations the RSM model employs 5 extra partial differential equations to obtain a solution to the flow. The model required the longest simulation time of all the other models in this thesis and was particularly difficult to converge. It was not succeeded to converge the RSM model in steady state mode, and therefore transient simulation had to be employed. Also during transient simulation there were difficulties, to make the model converge, the transient simulation had to start from the converged steady state solution of the k-ω SST model in addition some of the relaxation coefficients had to be adjusted accordingly:

Pressure: 0.3 Momentum: 0.5 Turbulent kinetic energy: 0.6

Reynolds Stresses: 0.4

The rest of the relaxation coefficient where held in their default values. Because of limited computer power available, it was only possible to load mesh (2.3) back into Fluent for relaxation coefficient adjusting. Which was needed when the RSM model diverged. Therefore only results from mesh (2.3) is available for this model.

In figure (65), the velocity profiles produced by the RSM model are plotted together with the physical measurements. Rather surprising, at these locations the RSM simulations show no flow separation, nor at these point or in the rest of the domain, the boundary layer is therefore attached to the wall. From table (11), one can see that even though the boundary layer has not separated, the shape factors at the different locations are quite high. At 3.6 meter the shape factor of the RSM model is 3.4, which is below the measured value but still fairly high. Relatively to the other models, one can see from figure (73) that the RSM model is however the model with the least signs of flow separation.

As for the other turbulence models discussed so far, the RSM model also does not produce the high velocities in the throat of the diffuser as the measured values, this is because the boundary layer has not developed as much as the for the flow in the physical diffuser. Nevertheless the RSM model gives the most authentic C_p distribution of all the turbulence models applied in this thesis. Meaning that the free stream velocities produced by the RSM model are in a reasonable agreement with the free stream velocities in the physical diffuser, recognized in figure (75), (76) and (77). This can also be seen from figure (71), where the boundary layer development of the RSM model and of the physical diffuser has the best fit of all the turbulence models.

The RSM model produces the most authentic replication of the pressure recovery measured in the physical diffuser. Thereby, even though it does not show separation, it indicates that the roughness severely effects the performance of the diffuser. The reason why the RSM model does not produce flow separation might be:

- Turbulence is a 3-dimensional problem, and by making the flow, 2-dimensional the RSM model might not work as effectively as intended because it loses some of the information that is carried sideways by the Reynolds stresses. The loss of this information can affect the ability of the RSM model to reproduce real physical flows, which of course are 3-dimensional.

- In a 3-dimesnional flow, there will also be boundary layers developing along not only the roof and floor of the diffuser, but also at the side walls. The boundary layer at the side walls can alter the boundary layer developing at the floor and roof of the diffuser. By running a 2-dimensional simulation theses effects will not be reflected into the solution of the flow.

- Secondary flows occurs in rectangular ducts, and can play an important role in the boundary layer characteristics, these effects are not captured in a two-dimensional simulation

- The mesh resolution can also be to coarse in the near wall region for the RSM model to effectively handle the presence of a wall.

4.2.4 Spalart-Allmaras

In this section the results from the Spalart-Allmaras models is discussed.

The one equation model Spalart-Allmaras is the least computational expensive and easiest model to converge of all the models utilized in this thesis. From figure (68) one can see that the model does not show the same velocity magnitudes at the throat of the diffuser as the physical measurements, because of a lack in the boundary layer development up to this point. By investigating figure (67) one can see that the model predicts the largest amount of flow separation of all the other turbulence model, also when compared with the actual measured values at the designated locations. Because of the models successfulness in predicting the massively flow separation that occurred in the physical rough diffuser, the boundary layer produced by the Spalart-Allmaras model is also thicker than the boundary layer predicted by the two-equation models as seen in figure (71).

Following the development of the displacement thickness in figure (72) it is clear that the Spalart-Allmaras model produces quite accurate mass deficit values which by continuity also

produces a thicker boundary layer. Consequently, the effective flow area of the diffuser goes down which as displayed in figure (75), (76) and (77) generates higher freestream velocities.

The freestream velocities predicted by the Spalart-Allmaras model are all within 10 percent of the physical measured values at the designated locations in table (3), this is unfortunately not the case for the two equation models. The higher free stream velocities hinders the static pressure from rising as much as the geometry would indicate. Therefore one can identify from figure (69), that the Spalart-Allmaras model predicts one of the best replications of the physical rough diffusers pressure recovery among the models applied in this thesis. The RSM model showed slightly better pressure recovery at the outlet of the diffuser, but as mentioned did not separate. As seen in figure (73) the shape factor of the Spalart-Allmaras model is considerable higher then what is physically measured which is consistent with the larger magnitude of separating flow seen in figure (67). The slope of the shape factor is also somewhat steeper than the measured shape factor, and at 3.25 meter the slop of the shape factor produced by the Spalart-Allmaras model continues to grow whilst the physically measured values is slightly decreasing. This indicates a shorter separation zone in the physical rough diffuser than what is predicted by the Spalart-Allmaras model.

The good results produced by the Spalart-Allmaras model is somewhat striking, since according to [33, p.32] the model is weak for strongly separated flow. However the model is especially developed for turbo machinery and aerodynamic applications which includes boundary layers under both adverse and favorable pressure gradients. Also the model is designed to handle mildly separating boundary layers and recirculating flow [44, p.20] What is meant by mildly separating flow is not clear from [44, p.20], but in the author's opinion comparing the separation occurring in the diffuser with a mildly separating airplane wing, then the separation in the rough diffuser might be called mild after all.

Chapter 5 - Smooth versus rough diffuser flow

In this chapter the simulated flow through the smooth and rough diffuser will be compared. This is done by selecting the most physical correct simulation from the smooth diffuser and comparing it with the most physical correct simulation from the rough diffuser. For the smooth diffuser, based on the discussion in chapter (4), the turbulence model that accomplished to replicate the real physical flows in the most accurate way, were the Spalart-Allmaras model. This is because of the following:

- Together with the k-ω SST model the Spalart-Allmaras model produces the best C_p distributions of the models applied. Figure (51)
- The Clauser pressure parameter are for all the models not very accurate, but the Spalart-Allmaras models β values are the ones that are closest to constant in the equilibrium region in [17]. Figure (53)
- The shape factor of the Spalart-Allmaras model has the best fit of all the applied models and are also nearly constant in the equilibrium region in [17]. Figure (54)
- The C_f values of the Spalart-Allmaras model although a bit low, have the most constant curve of all the applied model in the equilibrium region in [17]. Figure (56).

For the rough diffuser, based on the discussion in chapter (4), the turbulence model that accomplished to replicate the real physical flows in the most accurate way, were also the Spalart-Allmaras model. This is because of the following:

- Together with the RSM (which did not show separation) model the Spalart-Allmaras model produces the best C_p distributions of the models applied. Figure (69)
- The boundary layer and displacement thicknesses produced by the Spalart-Allmaras model have the closest match to the measured values in [43], compared with the models that did show separation. Figure (71) and (72).
- The velocity profiles of the Spalart-Allmaras model shows the best alikeness with the values in [43], compared with the models that did show separation. Figures (75), (76) and (77)

Therefore for both the smooth and rough diffuser, extended tables of flow parameters have been generated based on the results from the Spalart-Allmaras model. The extended tables are used to describe the mechanism that caused the boundary layer to separate in the rough diffuser. First the results of the generated extended tables of flow parameters will be presented, followed by figures where specially selected flow parameters are displayed and compared. Secondly, there will be a section where the results from the comparison of the two simulations are discussed.

5.1 Smooth and rough diffuser comparison

In this section the flow through the smooth and rough diffuser will be compared in figures and contour plots.

In table (13), characteristic boundary layer parameter for the smooth diffuser in the region $0.4 \leq x \leq 5.6$ meter are presented, this region is from now on called the examined area. As seen from table (13), flow parameters are calculated for every 0.4 meters, except for the region $1.8 \leq x \leq 2.4$, where boundary layer separation were observed in the rough diffuser, and hence this region is studied more closely.

Smooth diffuser

X [m]	h [cm]	U_e [m/s]	δ [m]	θ [m]	H [-]	G [-]	β [-]	$\frac{dp_e}{dx}$	C_f 10^3	Re_θ [-]
0.4	25.7	34.1	0.0158	0.0012	1.34	5.96	-0.18	-306	3.64034	2709
0.8	24.4	36.1	0.0264	0.0016	1.31	5.84	-0.08	-97	3.34176	4112
1.2	25.1	35.4	0.0372	0.0025	1.33	6.42	0.35	247	2.92526	5988
1.6	28.1	32.2	0.0459	0.0040	1.39	8.20	1.50	395	2.31277	8912
1.8	30.4	30.2	0.0556	0.0052	1.44	9.65	2.54	376	1.97778	10808
2	33.0	28.2	0.0656	0.0067	1.49	11.5	3.13	333	1.65339	12924
2.2	35.9	26.4	0.0773	0.0085	1.57	13.9	6.32	274	1.35309	15404
2.4	39.0	24.9	0.0873	0.0108	1.64	16.8	9.32	218	1.08889	18384
2.8	45.3	22.5	0.1144	0.0155	1.81	23.9	16.7	130	0.70405	23947
3.2	51.3	20.9	0.1366	0.0205	1.95	31.4	25.1	81	0.48291	29390
3.6	56.7	19.83	0.1701	0.0256	2.04	37.5	32.8	56	0.37035	34826
4	61.1	19.00	0.1962	0.0304	2.09	40.9	36.3	41	0.32472	39687
4.4	64.7	18.36	0.2293	0.0351	2.09	41.4	35.7	32	0.31918	44186
4.8	67.6	17.85	0.2508	0.0396	2.07	39.6	30.8	25	0.34024	48441
5.2	70.0	17.44	0.2954	0.0436	2.03	36.8	24.9	20	0.38112	52137
5.6	71.7	17.11	0.3001	0.0471	1.98	33.1	16.3	14	0.44541	55251

Table 13: Extended table of characteristic boundary layer parameters for the smooth diffuser with the Spalart-Allmaras turbulence model

In table (14), characteristic boundary layer parameter for the rough diffuser in the region 0.4 $\leq x \leq 5.6$ meter are presented. The Clauser shape factor G, is not defined for the region after 2 meter. This is because of negative C_f values, and by equation (46) the Clauser shape factor becomes complex. Flow separation was found to occur at about 2.1 meter. Therefore, more calculations have been carried out in this region to obtain more information from the location where the boundary layer separated.

Rough diffuser

X [m]	h [cm]	U_e [m/s]	δ [m]	θ [m]	H [-]	G [-]	β [-]	$\frac{dp_e}{dx}$	$C_{f\_effective}$ *10^3	Re_θ [-]
0.4	25.7	34.7	0.0301	0.0025	2.33	8.2	-0.27	-341	9.7933	5980
0.8	24.4	36.9	0.0454	0.0037	2.12	8.3	-0.15	-129	8.7199	9269
1.2	25.1	36.5	0.0552	0.0054	2.06	9.9	0.54	218	5.4340	13470
1.6	28.1	33.6	0.0788	0.0087	2.13	15.5	4.09	360	2.6392	20000
1.8	30.4	31.9	0.0915	0.0112	2.27	24.2	12.8	333	1.0728	24711
2	33.0	30.3	0.1169	0.0141	2.56	113	296	268	0.0580	29278
2.2	35.9	29.1	0.1288	0.0169	3.01	-	-50	194	-0.3812	33786
2.4	39.0	28.2	0.1567	0.0195	3.61	-	-37.9	141	-0.5378	37720
2.8	45.3	27.0	0.2122	0.0241	4.88	-	-29.5	77.3	-0.6935	44708
3.2	51.3	26.3	0.2817	0.0286	5.83	-	-23.7	47.2	-0.7835	51618
3.6	56.7	25.8	0.3449	0.0322	6.38	-	-22.6	35.4	-0.8125	58795
4	61.1	25.3	0.3992	0.0382	6.51	-	-23.7	29.6	-0.7922	66364
4.4	64.7	24.9	0.4554	0.0444	6.25	-	-23.2	29.1	-0.9188	75943
4.8	67.6	24.5	0.4962	0.0519	5.77	-	-36.3	31.9	-0.7170	87371
5.2	70.0	24.0	0.5346	0.0598	5.25	-	-47.7	38.4	-0.5948	98449
5.6	71.7	23.4	0.5488	0.0679	4.72	-	-56.9	37.8	-0.6759	109059

Table 14: Extended table of characteristic boundary layer parameters for the Rough diffuser with the Spalart-Allmaras turbulence model

In figure (78), the friction coefficients for the smooth and rough diffuser are plotted for the region $0.4 \leq x \leq 5.6$ meter. Notice the dominating pressure form drag.

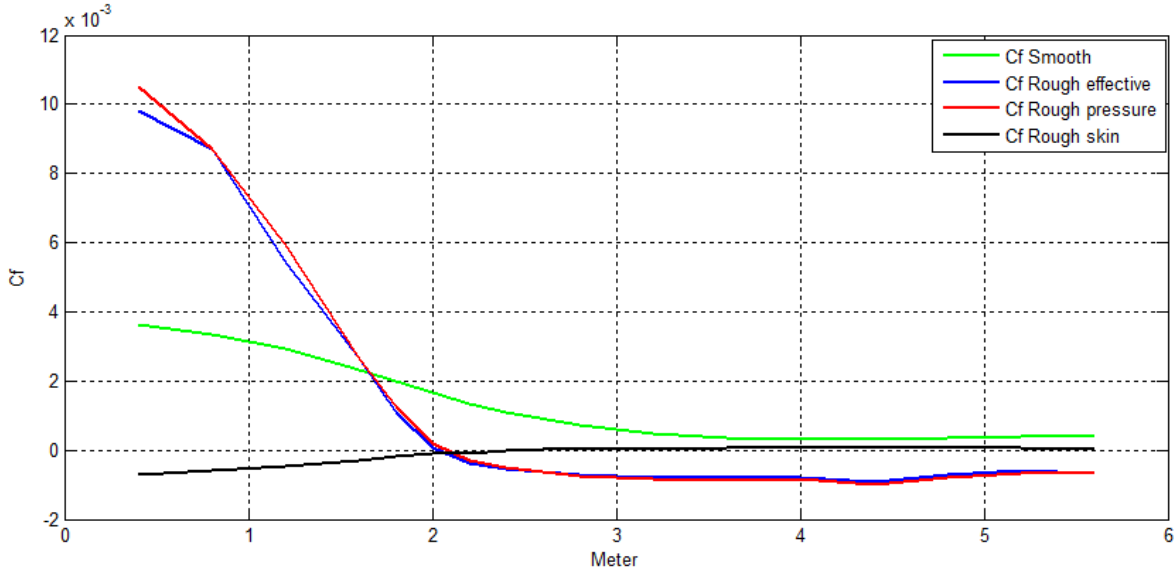

Figure 78: Friction coefficients for the smooth and rough diffuser.

In figure (79), the development of the displacement thickness and momentum thickness are plotted for the smooth and rough diffuser in the region $0.4 \leq x \leq 5.6$ meter.

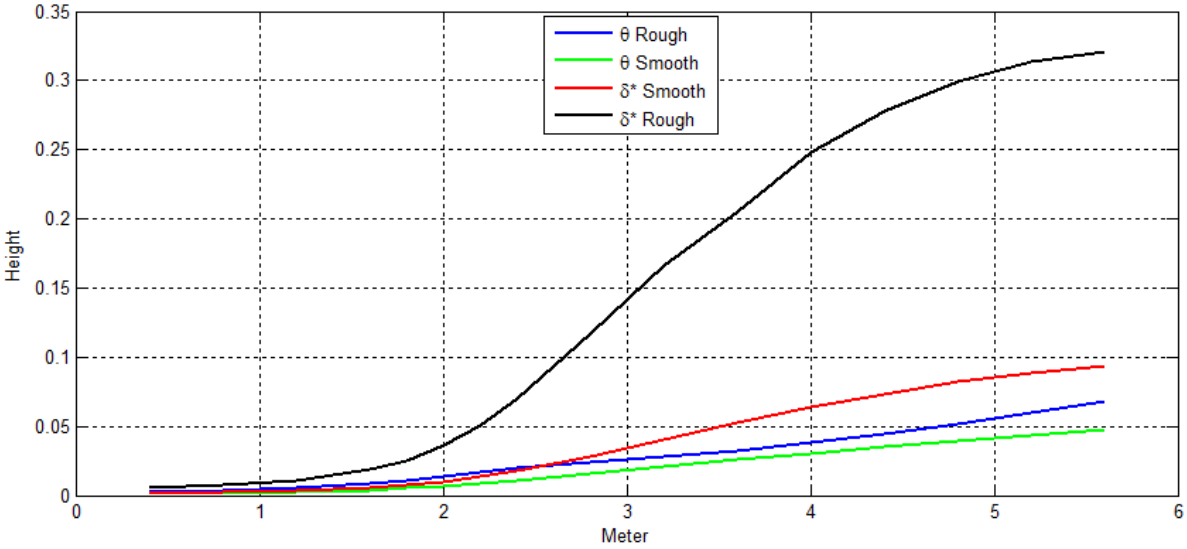

Figure 79: Displacement and momentum thickness for smooth and rough diffuser height in [m]

In figure (80), the development of the boundary layer for the smooth and rough diffuser are plotted in the region $0.4 \leq x \leq 5.6$ meter.

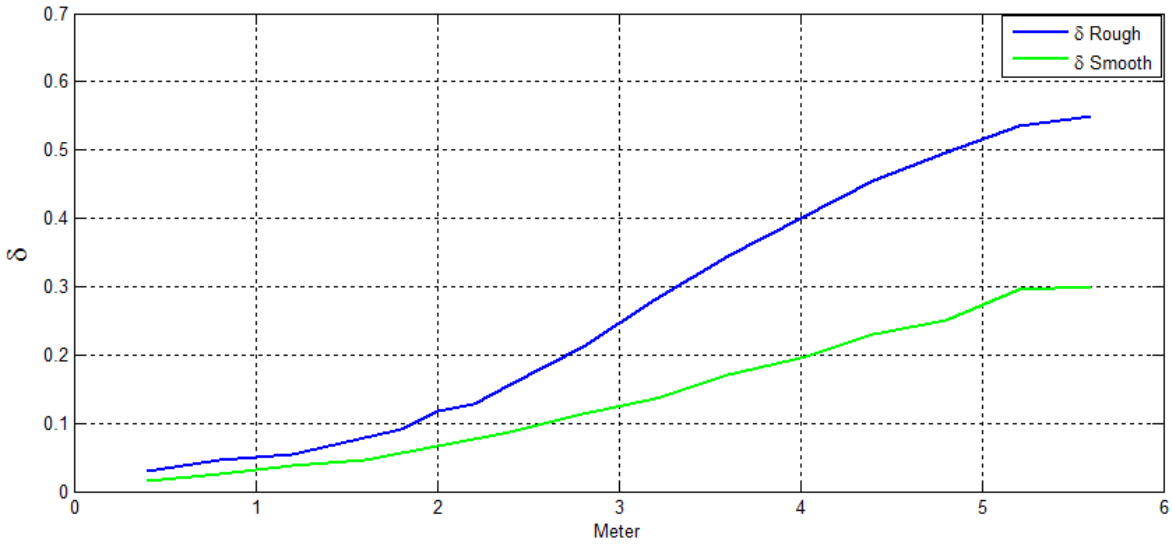

Figure 80: Boundary layer profiles for smooth and rough diffuser displayed in [m]

In figure (81), the ratio of the displacement thickness in the rough and smooth diffuser are plotted together with the ratio of the momentum thickness of the rough and smooth diffuser for the region $0.4 \leq x \leq 5.6$ meter.

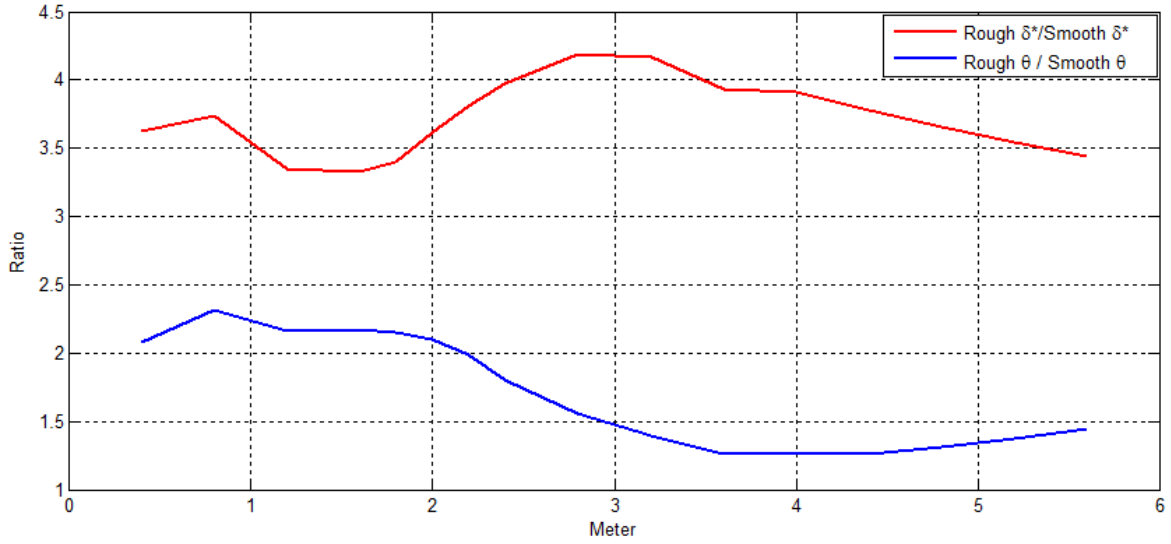

Figure 81: Ratio of displacement and momentum thickness for the rough diffuser to the smooth diffuser.

In figure (82), the stream wise pressure gradients of the smooth and rough diffuser are plotted in the region $0.4 \leq x \leq 5.6$ meter.

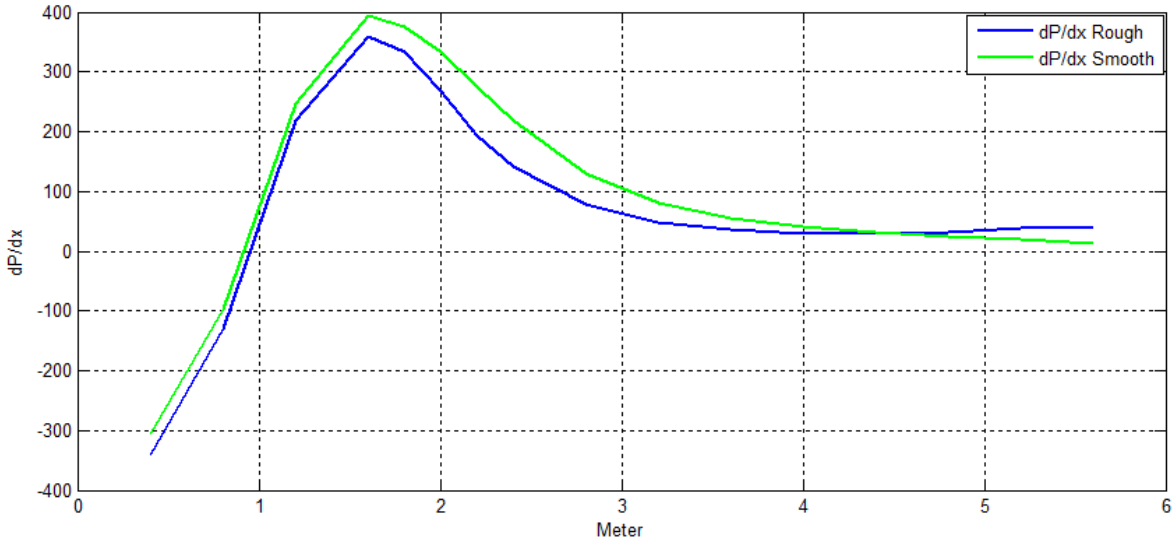

Figure 82: Free stream Pressure gradient in the stream wise direction for smooth and rough diffuser

In figure (83), the freestream velocities of the rough and smooth diffuser are plotted for the region $0.4 \leq x \leq 5.6$ meter.

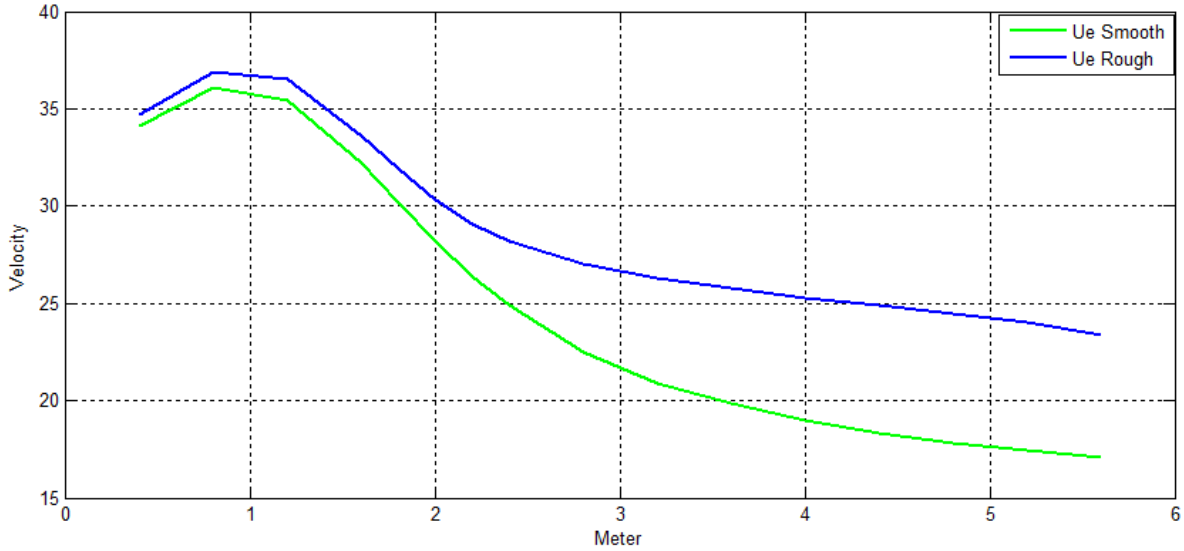

Figure 83: Freestream velocities [m/s] for smooth and rough diffuser

In figure (84), the development of the shape factor for the smooth and rough diffuser are plotted in the region $0.4 \leq x \leq 5.6$ meter.

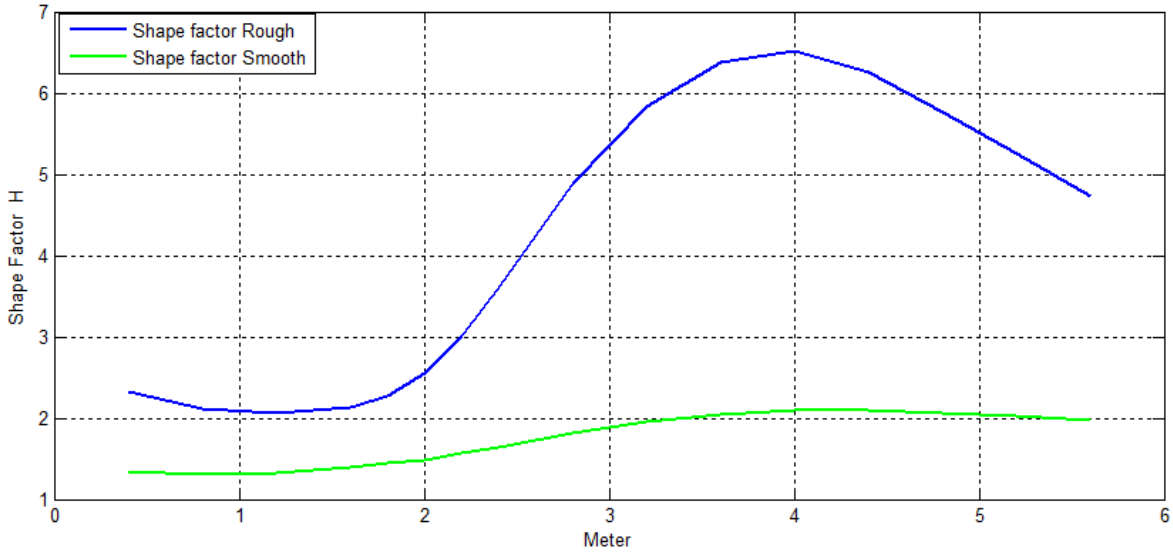

Figure 84: Shape factor development for smooth and rough diffuser

In figure (85) velocity and eddy viscosity contours for the smooth diffuser are presented. In addition detailed profiles for the velocity and eddy viscosity distribution at different cross sections are available from appendix (B) and (C). In appendix (A) an in depth view of the flow in the immediate vicinity of the wall for the smooth and rough diffuser are presented in the form of vector and streamline plots.

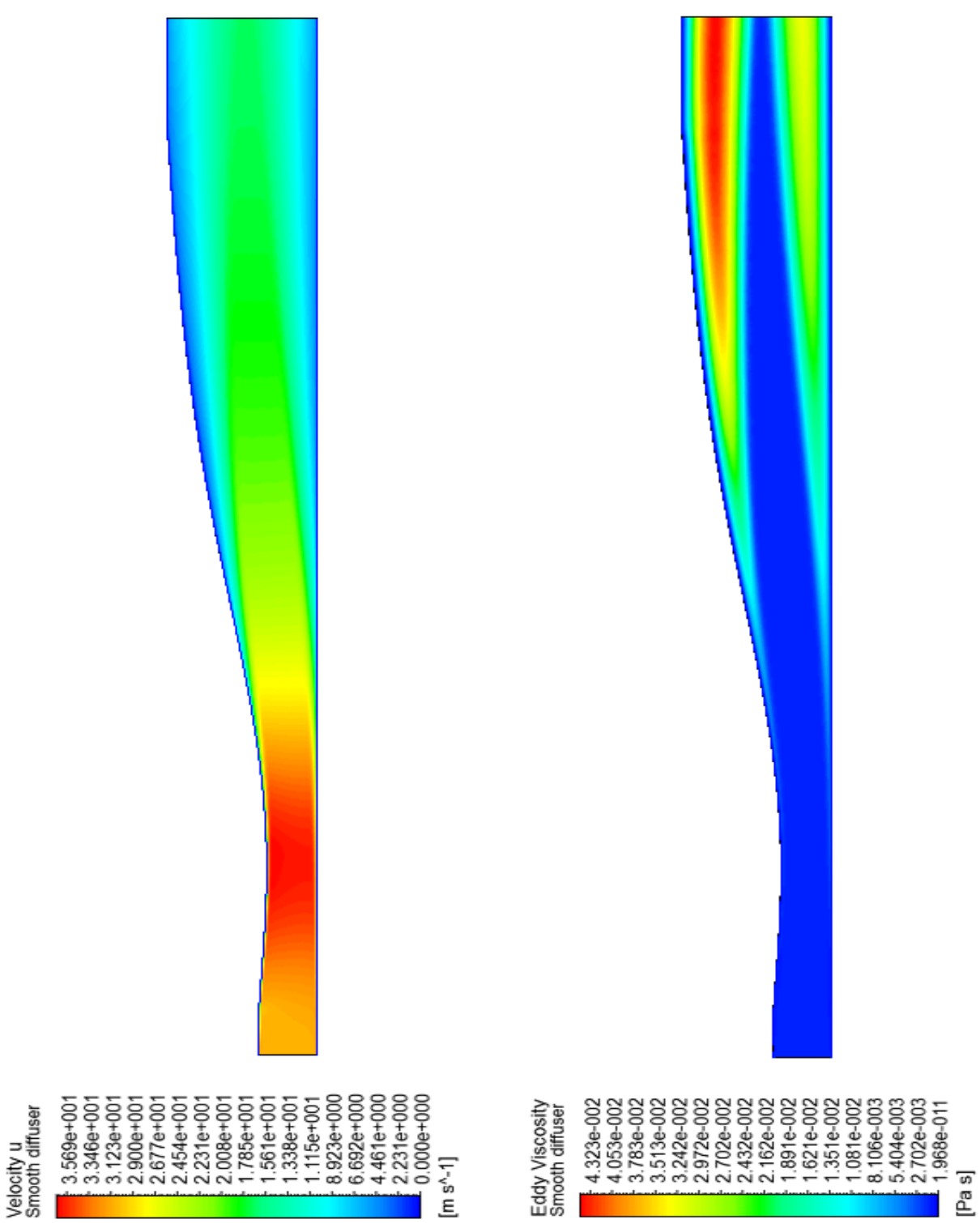

Figure 85: Velocity contour left and eddy viscosity contour right of the smooth diffuser

In figure (86) velocity and eddy viscosity contours for the smooth diffuser are presented. In addition detailed profiles for the velocity and eddy viscosity distribution at different cross sections are available from appendix (B) and (C). In appendix (A) an in depth view of the flow in the immediate vicinity of the wall for the smooth and rough diffuser are presented in the form of vector and streamline plots.

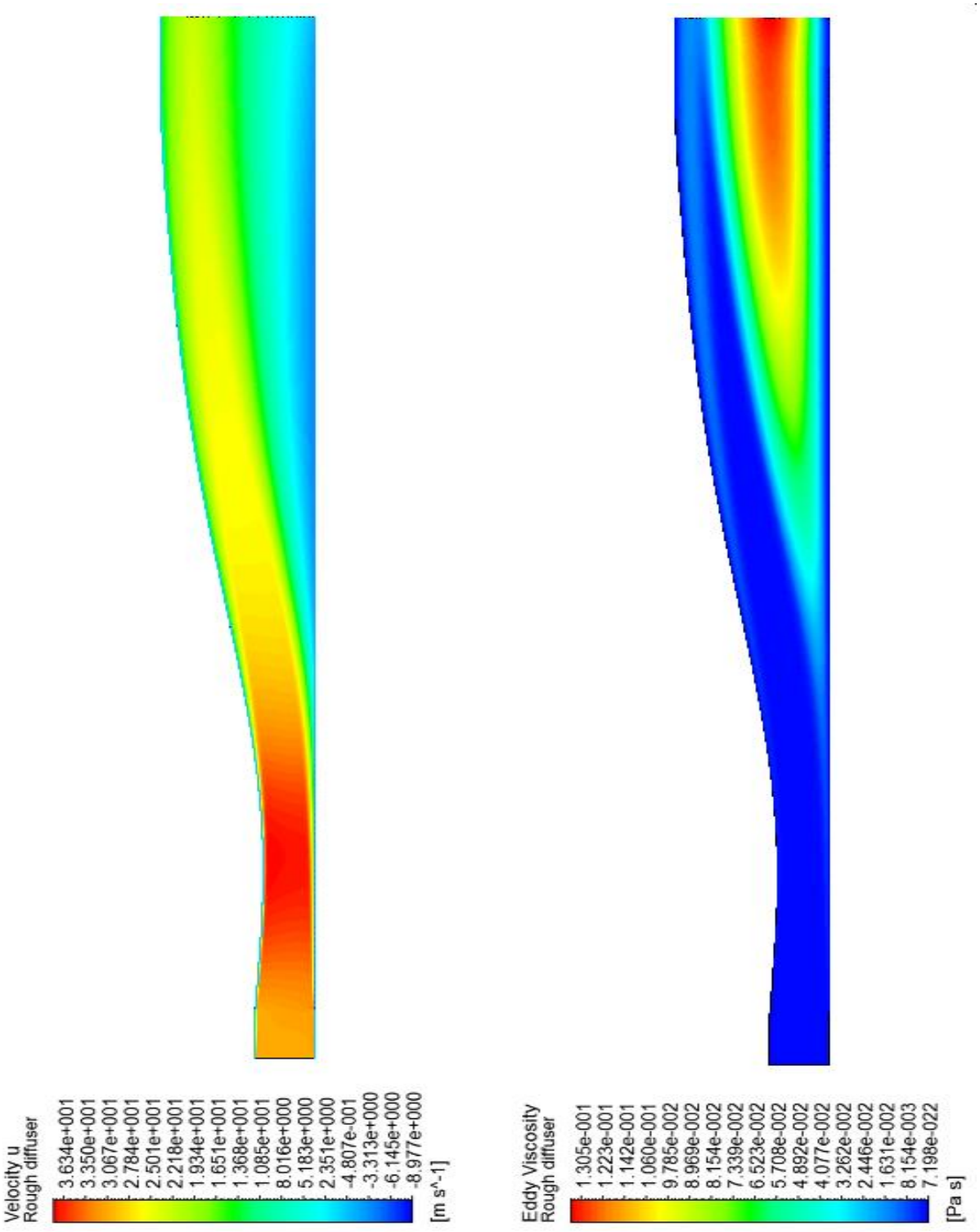

Figure 86: Velocity contour left and eddy viscosity contour right of the rough diffuser

In figure (87) the wall shear stress produced by the smooth and rough diffusers along the top or roof of the diffuser are displayed and compared

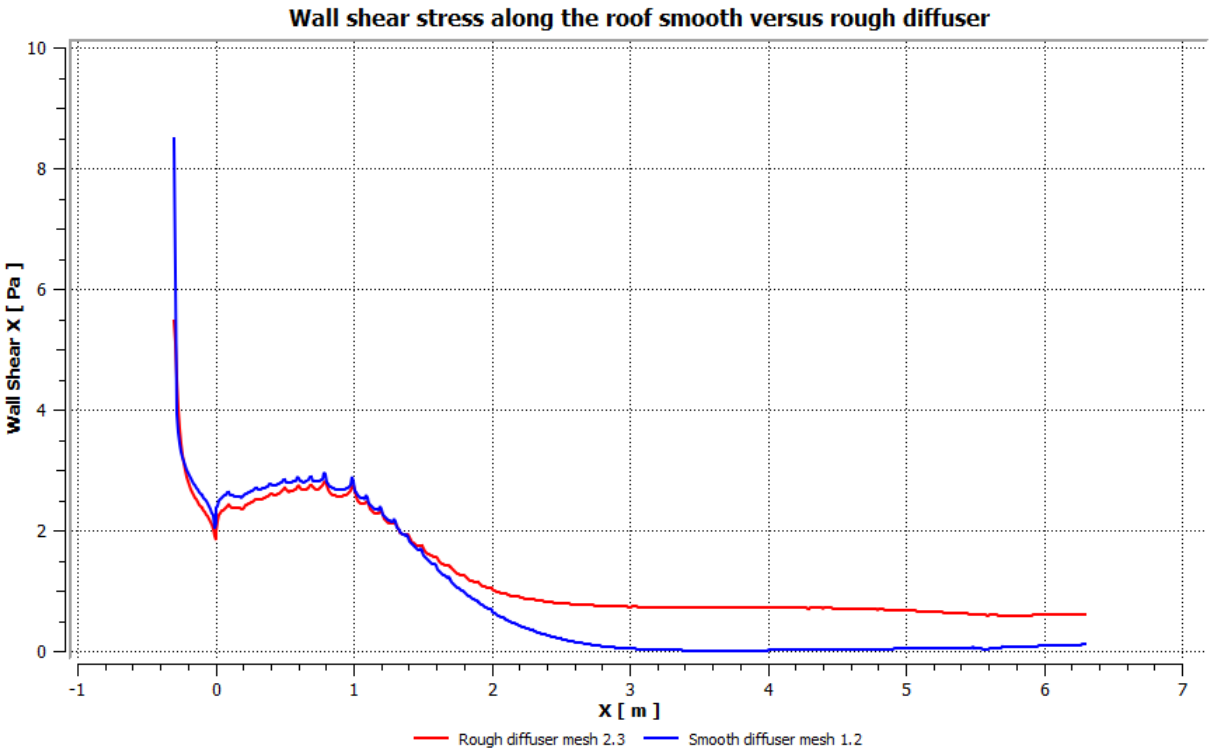

Figure 87: Wall shear stress along the roof

5.2 Discussion of smooth versus rough diffuser flow

In this section the figures and plots presented in section (5.1) are discussed.

When investigating figure (78) it is clear that the roughness elements causes an increase in the friction coefficient and thereby contributes to higher drag characteristics in the rough diffuser. The higher drag in the rough diffuser is evidently explained by the form drag produced by the roughness elements, which is by far the dominant source of drag in figure (78). The influence of the skin friction to the effective friction coefficient in the rough diffuser is almost negligible except at the beginning of the examined area. Noticeably, the effective friction coefficient in the rough diffuser becomes negative at 2 meters, meaning that the boundary layer has separated and is flowing in the opposite direction of the mean free stream. The Clauser shape factor G, is from equation (46) therefore not defined for the region after 2 meters because of negative C_f values.

In figure (79), the displacement and momentum thicknesses for the rough and smooth diffuser are plotted. As seen in figure (79), the displacement and momentum thicknesses are substantially higher in the rough diffuser. The higher mass and momentum deficit in the rough diffuser are consistent with the increased form drag caused by the roughness elements, meaning that the fluid particles hitting the roughness elements imparts more of their momentum to the wall as compared to the corresponding smooth wall.

The higher mass and momentum deficits caused by the roughness elements will by the continuity equation, lead to a larger boundary layer in the rough diffuser as observed in figure (80). Consequently, the increased boundary layer decreases the available effective flow area, thereby generates stronger favorable pressure gradients, but unfortunately also less powerful adverse pressure gradients, as recognized in figure (82). Therefore higher free stream velocities are observed from figure (83) in the rough diffuser.

In figure (84), the shape factors for the rough and smooth diffuser are plotted. As seen from figure (84), already at the start of the examined area the shape factor of the rough diffuser is about twice as high as its comparison. From there the slope of the rough shape factor decreases some towards the throat of the diffuser, whilst the shape factor of the smooth diffuser is rather unchanged in the same area. Meaning that the converging channel has more influence on the velocity profile of the rough diffuser by making the velocity profile relatively fuller. From about 2 meter, the shape factor of the rough diffuser increases substantially, which implicates that the relative motion between fluid layers near the wall is reduced and the wall shear stress becomes close to zero, this is recognized and consistent with table (78). Further down the diffuser the rough shape factor continues to grow, peaking at 4 meter with a shape factor of 6.51 which is very high and is an almost certain indication of flow separation, which also is demonstrated in table (78), where negative C_f values are

identified. The higher shape factor values in the rough diffuser also shows that the roughness is more efficient in producing mass deficits than momentum deficits. Noticeably in figure (84), the shape factor of the smooth diffuser is also quite high, peaking at 4 meter with a value of 2.09, meaning that the boundary layer is close to separation, this is verified by the low friction coefficient displayed figure (78).

In figure (85) and (86) the velocity and eddy viscosity contours of the smooth and rough diffuser are displayed. From these plots it is clearly shown that the roughness generates a substantially thicker boundary layer, decreasing the effective flow area and thereby produces significantly higher freestream velocities. The increased boundary layer produced by the roughness elements pushes the free stream upwards towards the roof of the diffuser and thereby increases the velocity gradients at the upper wall, meaning that the wall shear stress in this location intensifies, which is demonstrated in figure (87).

By examining the eddy viscosity in the contour plots in figure (85) and (86) it is apparent that the roughness elements has significantly increased the turbulence levels in the rough diffuser compared with the smooth diffuser. In the immediate vicinity of the wall the velocity gradients are much larger than the turbulent fluctuations for both diffuser. However from appendix (C) one can see that the roughness elements amplifies the magnitude of the turbulent fluctuations close to the wall even long before the boundary layer separate at about 2.1 meter from figure (78). When comparing the eddy viscosity in the free stream of the rough and smooth diffuser, one can see that they are both very small, which is consistent with the nearly uniform free stream velocities observed in both diffusers in appendix (B). The boundary layer separation at about 2.1 meter in the rough diffuser causes an increases in the turbulent fluctuations as from figure (14) and section (1.5.2), this is recognized in figure (86).

In total the roughness has increased the turbulent mixing and thereby enhanced the boundary layers resistance to separation. Contrary it has also amplified the drag characteristics of the diffuser and consequently, produced a thicker boundary layer and heavier mass and momentum deficits. These deficits far overwhelms the increased turbulent mixing and causes the boundary layer to separate.

From Appendix (A), it is evident that the roughness elements significantly alters the flow in the immediate vicinity of the wall. At the throat of the diffuser (0.9 meter) there exist two recirculation zones in between the roughness elements and local separation is also evident at the top of the roughness element. The streamlines curve inward, causing significant interactions with the flow above the crest and the roughness elements. This is consistent with the theory in section (1.4.2). The flow in the immediate vicinity of the wall in the smooth diffuser at 0.9 meter reveals strong velocity gradients consistent with a turbulent

boundary layer as described in section (1.3.1). At the separation point of the rough diffuser (2.1 meter) the flow between the roughness elements has a tendency to build one large recirculation zone, meaning that the interaction with the overlaying flow and thereby the wall shear stress is less than before, which is consistent with a the theory of section (1.5.1). Following the flow further down the rough diffuser, one can identify at 4 meter, where there is heavy boundary layer separation apparent from figure (84), that two recirculation zones has again developed between the roughness elements. No local separation is however captured by the model at 4 meters.

For the smooth diffuser, one can recognize the decay of the velocity gradients near the wall as the geometry of the diffuser is expanding, which is consistent with the theory from section (1.5) and figure (78). In total the figures in appendix (A) suggest that the roughness elements generates significant amounts of vorticity in the near wall region, compared with the smooth diffuser.

As seen in from figure (81) the roughness generates higher mass and momentum deficits, indicating by continuity that the free stream velocities must increase in the rough diffuser. The higher free stream velocities and increased displacement and momentum thicknesses eventually leads to boundary layer separation in the rough diffuser. In order to investigate if equilibrium flow is also attainable in the rough diffuser, the geometry needs to be changed. From figure (84) one can see that the converging section of the diffuser has to some extent greater impact on the shape factor of the rough diffuser then its comparison the smooth diffuser. Therefore the shape factor of the rough diffuser can be reduced by decreasing the size of the throat of the diffuser, bringing more momentum to the boundary layer. In the converging section the roof of the diffuser then has to be lowered considerably, and also significantly lengthened in the streamwise direction in order to facilitate the correct pressure recovery. This process will however increase the friction in the diffuser by equation (24), which again will affect the boundary layer development and pressure gradients to the extent that if equilibrium flow is possible when the diffuser is covered with roughness elements, the diffuser might be unmanageable for industrial use.

By placing more roughness elements of the same shape along the floor of the diffuser, one will generate d-type roughness and in this way decrease the surface roughness effects on the flow as discussed in section (1.3). For industrial use this procedure might not be feasible since decreasing the surface roughness will often substantially increase the manufacturing cost.

Chapter 6 - Conclusion

In this thesis the flow through the special equilibrium diffuser developed by the department of Energy and Process Engineering at the Norwegian University of Science and Technology has been simulated, both when the walls were smooth and when the floor of the diffuser were covered with k-type roughness elements. The simulations have been accomplished utilizing different turbulence models, where after the results of the simulations have been validated against the physical measurements performed in [17] for the smooth diffuser, and in [43] for the rough diffuser. Finally the results of the simulations on the smooth and rough diffuser have been compared.

The Spalart-Allmaras turbulence model has proven to predict the best results both for the equilibrium flow in the smooth diffuser, and for the massively separated flow over the k-type roughness in the rough diffuser. The meshes utilizing inflation produced the best results for the rough diffuser. For the smooth diffuser the mesh dependencies were negligible. The QUICK scheme was found to predict the most accurate results towards flow separation.

From the results of the simulations on the smooth and rough diffuser it is evident that the surface roughness has severely altered the flow. Close to the wall at the scale of the roughness elements, in contrary to the smooth diffuser, there exist local separation and recirculation zones generating vorticity and increases turbulence. The form drag attributed the roughness elements has amplified the drag characteristics of the rough diffuser and thereby introduced much higher mass and momentum deficits in the flow compared to the smooth diffuser. The associated thicker boundary layer is more prone to separation. In the case of the simulated flow through the rough diffuser, the enlarged displacement and momentum thicknesses far overwhelms the increased turbulent mixing also produced by the roughness elements. The result is that the boundary layer separates.

The effects of the adverse pressure gradient and k-type roughness under the settings in this thesis is therefore to augment each other to the level where the boundary layer separates.

This is because the boundary layer in the smooth diffuser is already on the verge of separation, meaning that the inflection point is just at the point away from the wall where it can sustain enough momentum to the near wall flow to stop it from separating. For the rough diffuser, the k-type roughness elements will have a stronger retarding effect on the near wall flow and thereby intensify the vortex generation. When the flow is from left to right these near wall vortices must be in the clockwise direction. Accordingly the vortex generation produced by the k-type roughness elements have a greater magnitude than the supply rate of counter-clockwise vortices produced close to the inflection point, hence the near wall flow turns away from the wall and the boundary layer separates.

7 - Further work

Surface roughness plays an important role in flow engineering, where phenomenon's such as drag, heat transfer, flow separation and many more are highly connected to the surface texture. It is therefore important to continue to gain insight into the effects emanating from surface roughness.

Due to limited computer resources it was not possible to build a 3-dimensional replication of the diffuser in this thesis. Nevertheless both the physical LDA measurements and several turbulence models shows that the rough diffuser severely separates, and thereby is far from being in equilibrium. A very interesting study would therefore be to build a 3 dimensional replication of the diffuser and apply different turbulence models to see which model that matches the measurements in the most correct way. Thereafter one could adjust the geometry of the diffuser in order to investigate if some of the turbulence models predicts equilibrium flow also with the roughness elements.

By adjusting the spacing between the roughness elements one can generate d-type roughness, as described in section (1.4.2) this will reduce the drag compared to k-type roughness. This can easily be incorporated in the existing model and thereby the effects d-type roughness has one the diffuser can be evaluated and compared with the effects of the k-type roughness.

It would also be very interesting to apply Large Eddy Simulation (LES) or Direct Numerical simulation (DNS) to the diffuser in order to obtain detailed information of the eddies produced by the roughness elements and also acquire a comprehensive picture of the flow scenario in the rough diffuser.

8 - References

[1] Tennekes and Lumley. A First Course in Turbulence, 1973

[2] Web-page from Massachusetts Institute of Technology (MIT). Available from

http://www.mit.edu/course/1/1.061/OldFiles/www/dream/SEVEN/SEVENTHEORY.PDF,

Downloaded 03.02.2014

[3] Frank M. White. Fluid Mechanics, Sixth Edition. McGRAW – HILL International edition

[4] Web-page from Comsol multiphysics. Available from

http://www.comsol.com/blogs/which-turbulence-model-should-choose-cfd-application/

Downloaded 20.02.2014

[5] Jean Mathieu & Julian Scott. An introduction to Turbulent Flow, Cambridge University Press.

[6] Web-page. Available from

http://naimhossain.blogspot.no/2012/08/turbulence-modeling.html

Downloaded 20.04.2014

[7] Web-page from Freestudy.co.uk Free Tutorials on Engineering and Science. Available from

http://freestudy.co.uk/fluid%20mechanics/t1203.pdf

Downloaded 04.02.2014

[8] Web-page from David Apsley: Lecturer in School of Mechanical, Aerospace and Civil Engineering University of Manchetser. Available from

http://personalpages.manchester.ac.uk/staff/david.d.apsley/lectures/turbbl/history.pdf

Downloaded 18.03.2014

[9] Frank M.White. Viscous fluid flow. Third edition. McGRAW – HILL International edition

[10] John J. Bertin & Russel M. Cummings- Aerodynamics for Engineers, fifth edition. Perarson International Edition.

[11] Web-page from David Apsley: Lecturer in School of Mechanical, Aerospace and Civil Engineering University of Manchetser

http://personalpages.manchester.ac.uk/staff/david.d.apsley/lectures/turbbl/integral.pdf

Downloaded 22.02.2014

[12] Ludwig Prandtl, German professor of aerodynamics.

[13] Experiments on Turbulent Flow Separation. Master thesis Jonas Gustavsson. Royal Institute of Technology Department of Mechanics.

[14] Clayton T. Crows, Donald F. Elger, Barbra C. Williams, Johan A. Roberson. Engineering Fluid Mechanics. SI version 9th edition.

[15] Web-page:

http://adri1b.free.fr/moi/rapports/rapport2A.htm

Downloaded 028.01.2014

[16] Ivar S. Ertesvåg. Turbulent Strøyming og Forbrenning. Frå turbulensteori til ingeniørverktøy.

[17] Per-Egil Skåre & Per-Åge Krogstad. A turbulent equilibrium boundary layer near separation. J.Fluid Mech. (1994) vol 272. Cambridge University Press.

[18] Javier Jimenez. Turbulent Flows over Rough Walls. Annu Rev Fluid Mech Center for Turbulence Research Stanford University California.

[19] Moody, Lewis Ferry. American professor of hydraulics in the school of engineering at Princeton

[20] Web-page:

http://www.coolit.co.za/moody/

Downloaded 03.04.2014

[21] Donald J. Bergstrom, Nathan A. Kotey, Mark F. Tachie. The effects off surface roughness on the mean velocity profile in a turbulent boundary layer.

Link:

http://fluidsengineering.asmedigitalcollection.asme.org/

[22] Per-Åge Korgstad & R.A Antonia. Comparison between rough and smooth wall turbulent boundary layers. Cambridge University Press. J.Fluid Mech.

[23] S. Leonardi, P. Orlandi & R.A Antonia. Properties of d- and k-type rougness in turbulent channel flow. AIP Physics of Fluids.

[24] Web-page:

http://cfd.mace.manchester.ac.uk/twiki/bin/view/CfdTm/TestCase021

Downloaded 05.02.2014

[25] Web-page from University of Leeds, Available from

http://www.efm.leeds.ac.uk/CIVE/FluidsLevel1/Unit04/T2.html

Downloaded 09.03.2014

[26] Web-page from Gerald recktenwald Associate Professor and Chair Mechanical and Material Engineering Department Portland State University. Available from

http://web.cecs.pdx.edu/~gerry/class/ME448/notes/pdf/convectionUpwind.pdf

Downloaded 15.02.2014

[27] Web-page from Andre Bakker, director, Fluids Business Unit ANSYS, INC. Lecturer at School of Engineering at Dartmouth College. Available from:

http://www.bakker.org/dartmouth06/engs150/05-solv.pdf

Downloaded 26.02.2014

[28] Web-page from Wikipedia. Available from

http://en.wikipedia.org/wiki/Types_of_mesh

Downloaded 07.04.2014

[29] Web-page from Wikipedia. Available from

http://en.wikipedia.org/wiki/Types_of_mesh

Downloaded 07.04.2014

[30] Web-page from SKODA Research-Fluid department, PLZEN. Available from

http://adri1b.free.fr/moi/rapports/rapport2A.htm

Downloaded 03.17.2014

[31] E–book available from

http://bookboon.com/en/mechanics-ebooks

Title: Computational Fluid Dynamics

Author: Sayma, Abdulnaser

Downloaded: 14.01.2014

[32] Web-page from Wikipedia. Available from

http://en.wikibooks.org/wiki/Parallel_Spectral_Numerical_Methods/Timestepping

Downloaded 02.10.2014

[33] Web-page from ANSYS. Fluent lecture 6, Turbulence modeling. Costumer Training Material. Available from

http://imechanica.org/files/fluent_13.0_lecture06-turbulence.pdf

Downloaded 06.02.2014

[34] H.K Versteeg & W. Malalasekera. An introduction to Computational Fluid Dynamics. The Finite Volume Method, second edition. Pearson Prentice Hall.

[35] Fluent 6.3 user guide. Chapter 12.4.2. Available from

http://aerojet.engr.ucdavis.edu/fluenthelp/html/ug/node479.htm

Downloaded 12.02.2014

[36] Fluent 6.3 user guide. Chapter 12.4.3. Available from

http://aerojet.engr.ucdavis.edu/fluenthelp/html/ug/node480.htm

Downloaded 10.02.2014

[37] Dr. David C. Wilcox. Turbulence modeling for CFD. DCE Industries, Inc. 1993.

[38] Fluent user guide 14.0. Release November 2011. Available from

http://cdlab2.fluid.tuwien.ac.at/LEHRE/TURB/Fluent.Inc/v140/flu_ug.pdf

Downloaded 04.02.2014.

[39] Kongull, NTNU super computer information available from:

https://www.hpc.ntnu.no/display/hpc/Kongull

Downloaded 28.052014

[40] Love Håkansson: Senior Technical Consultant at EDRMedeso.

[41] Per-Åge Krogstad: Professor at The Norwegian University of Science and Technology, Department of Energy and Process Engineering.

[42] Fluent 6.3 user guide. Chapter 12.3.1. Available from

http://aerojet.engr.ucdavis.edu/fluenthelp/html/ug/node469.htm

Downloaded 10.05.2014

[43] Magnus Nytun. Project thesis: Flow in a rough wall diffuser. Norwegian University of Science and technology,. Department of Energy and Process engineering.

[44] Web-page from Andre Bakker, director, Fluids Business Unit ANSYS, INC. Lecturer at School of Engineering at Dartmouth College. Available from:

http://www.bakker.org/dartmouth06/engs150/10-rans.pdf

Downloaded 05.05.2014

[45] Hideomi Hujita, Hajime Yokosawa & Masafumi Hirota. Secondary Flows of the Second Kind in Rectangular Ducts with One Rough Wall. Nagoya University, Japan.

[46] Dr. Florian Menter. Development Manager, Fluid Business Unit. ANSYS, Inc. Leading CFD researcher.

Appendix

Appendix A - Vector and streamline plots rough diffuser

In this section Spalart-Allmaras produced vector and streamline plots are displayed for the rough and smooth diffuser at respectively the throat of the (0.9 meter), at the separation location (2.1 meter in the rough diffuser) and at heavy separation location at 4 meter(in the rough diffuser). The plots are for the floor (lower wall) of the diffuser and the flow direction is from left to right. The meshes utilized are respectively mesh 2.3 and 1.2 for the rough and smooth diffuser.

Vector and streamline plots throat of rough diffuser 0.9 meter

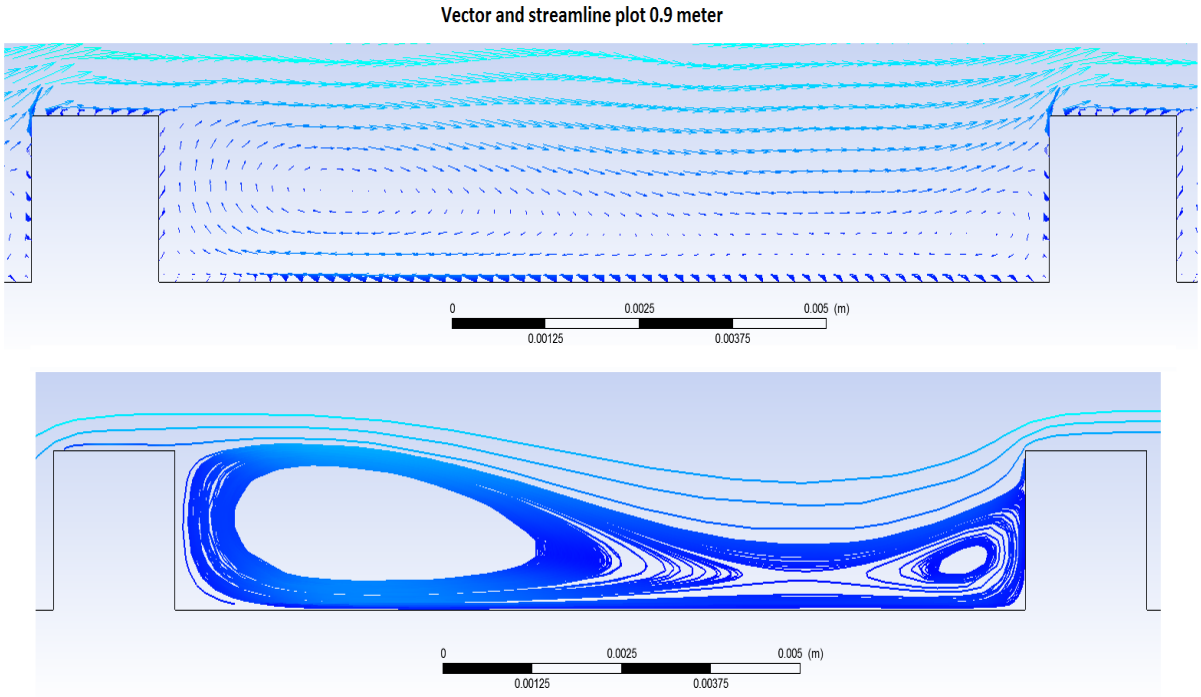

Note, two recirculation zones as of figure (12). At the lower right and left corners there should also have been induced, recirculation zones but these are not captured by the model

Flow at roughness element 0.9 meter

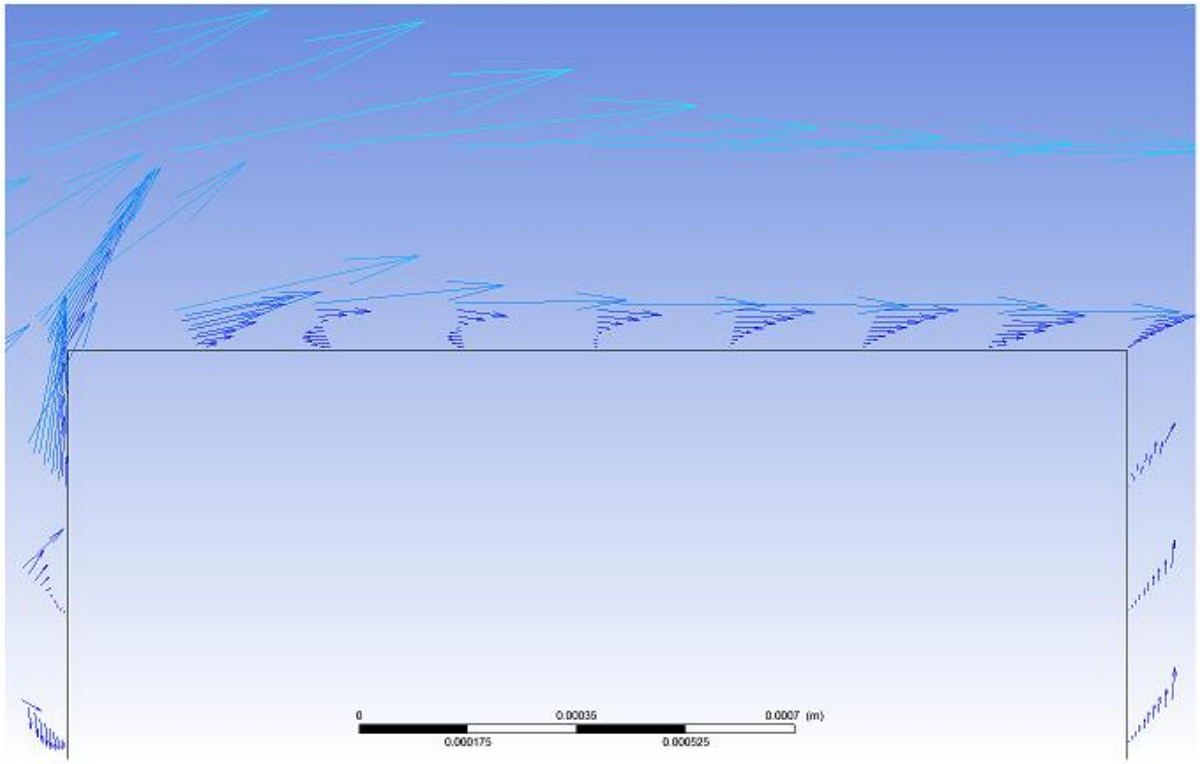

Note, local separation at the roughness element at 0.9 meter.

Vector and streamline plots rough diffuser at separation point 2.1 meter

Vector and streamline plot 2.1 meter

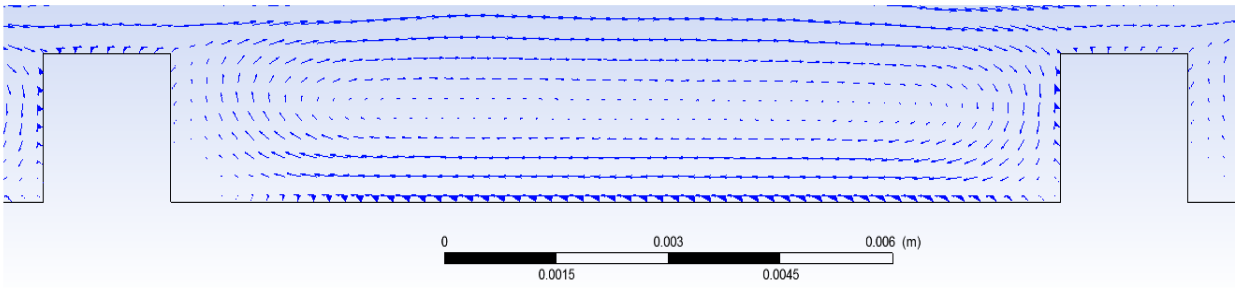

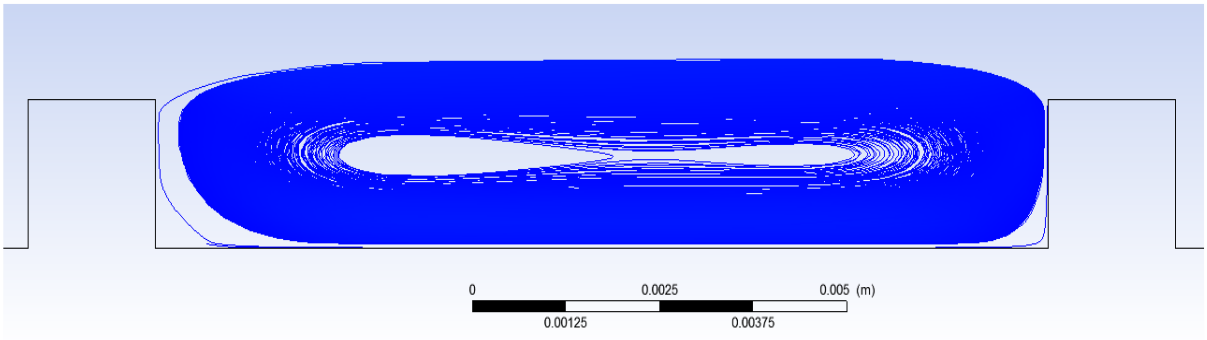

Flow at roughness element 2.1 meter

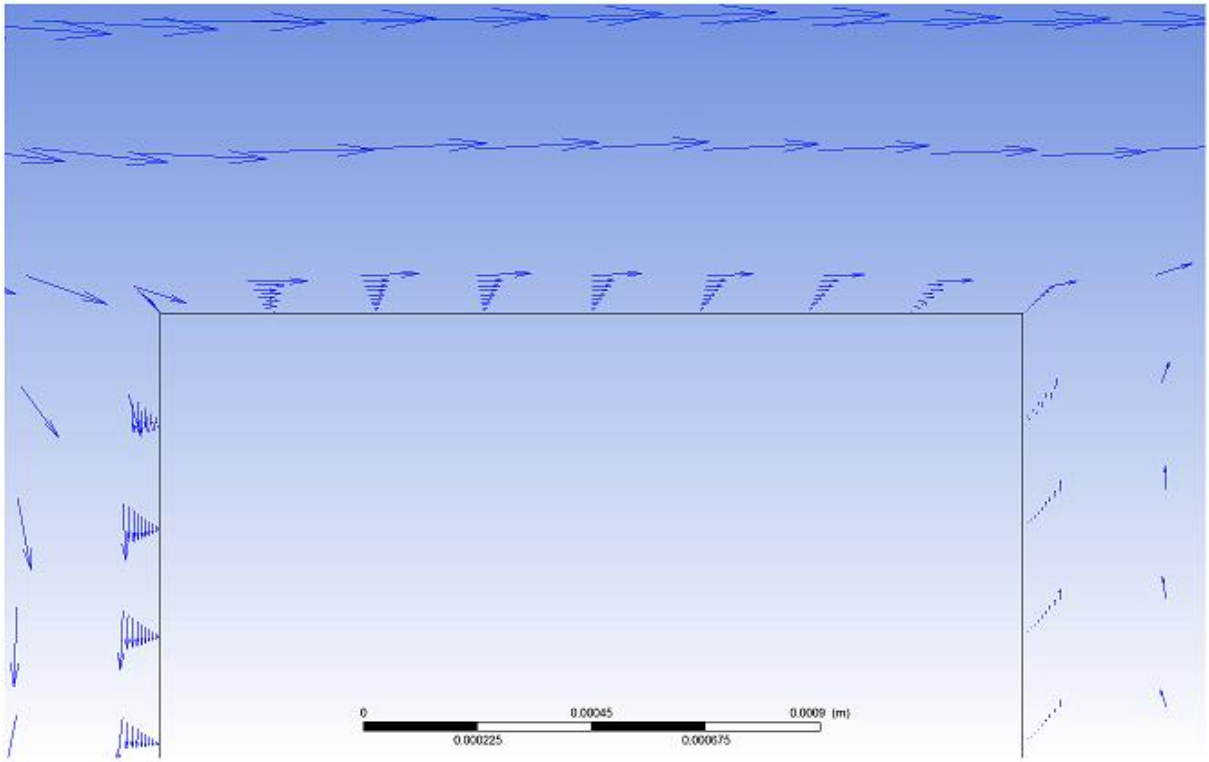

No, local separation visible.

Vector and streamline plots rough diffuser thoroughly separated location 4 meter

Vector and streamline plot 4 meter

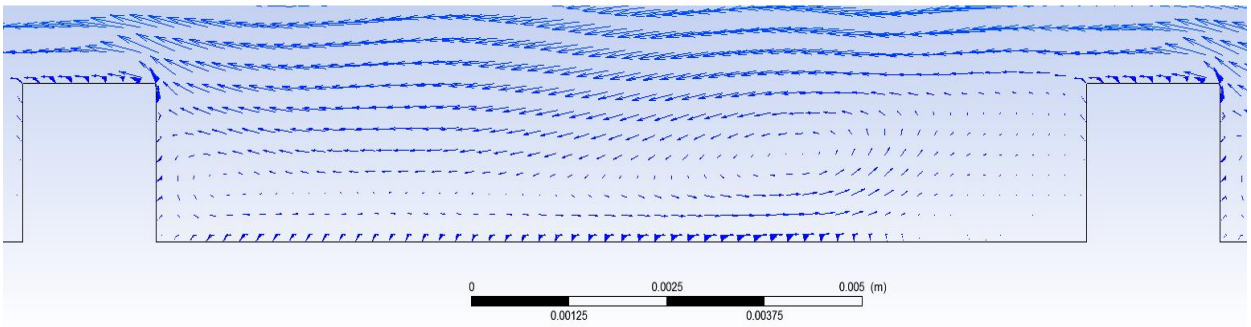

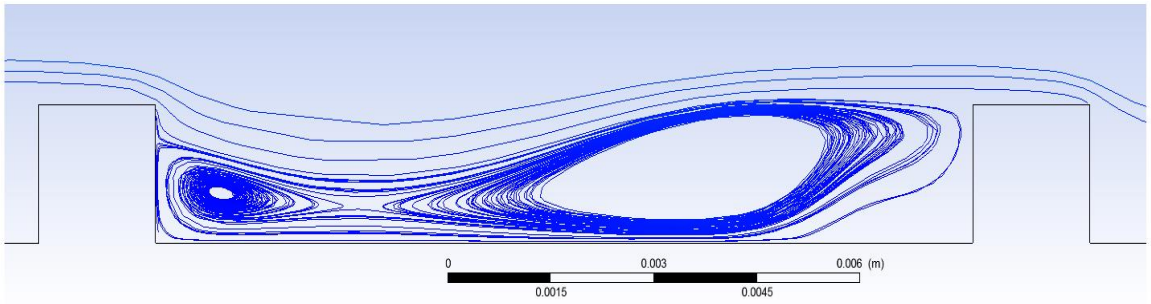

Flow at roughness element 4 meter

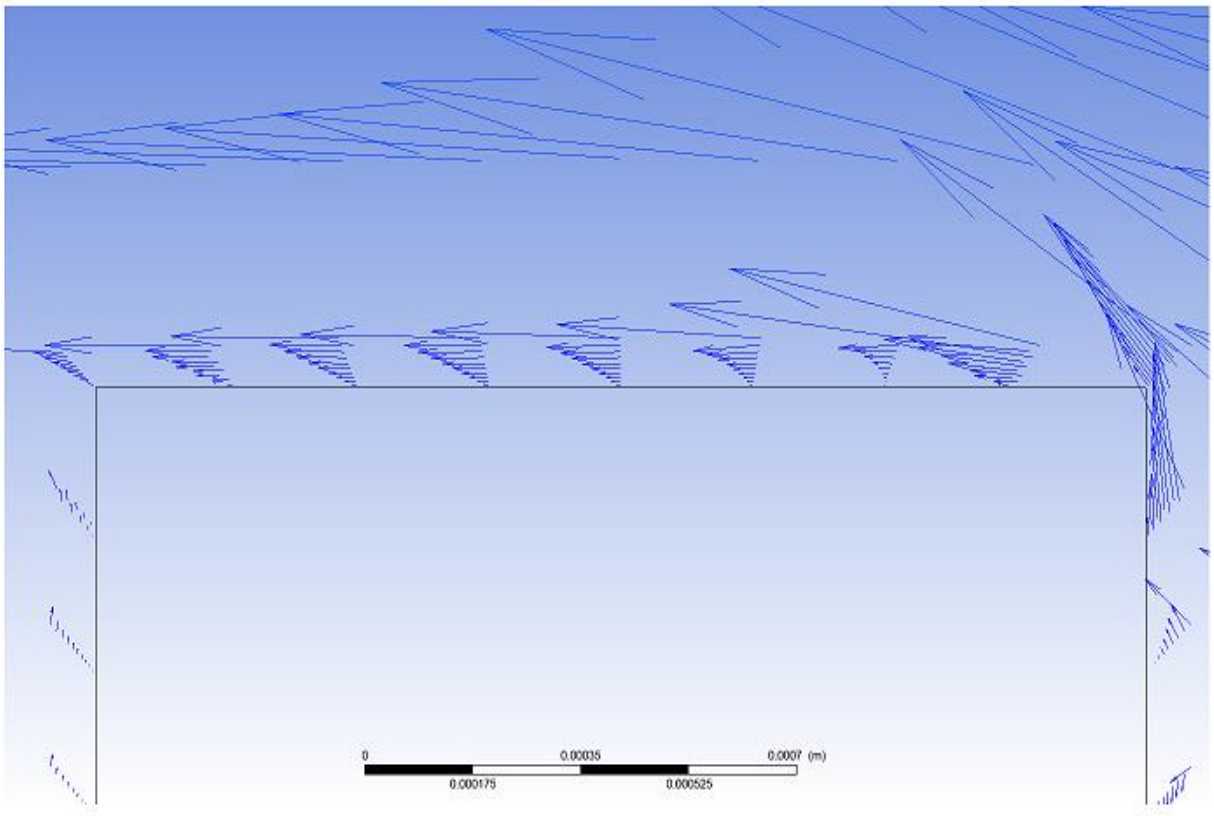

Vector plots smooth diffuser

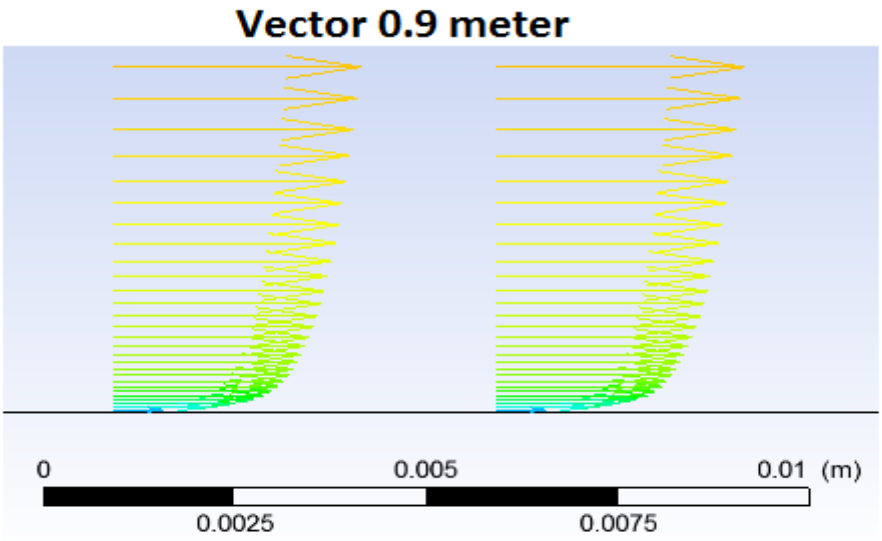

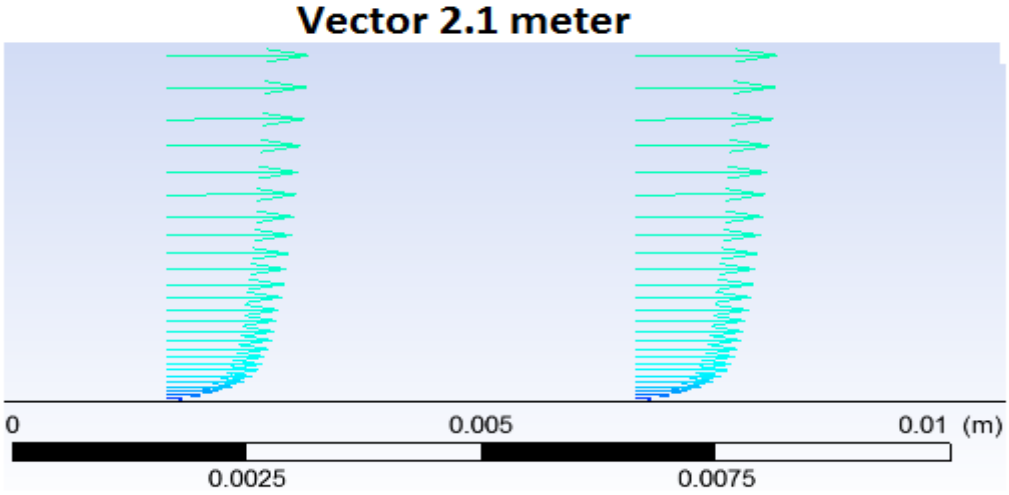

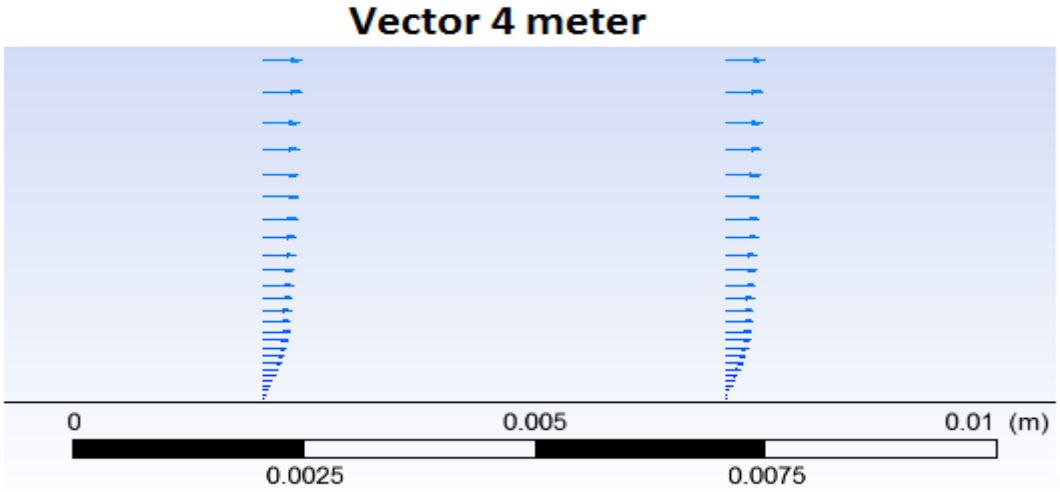

Appendix B - Velocity development smooth versus rough diffuser

The figures in this section presents the development of the velocity profiles for the Spalart-Allmaras simulations thru both the smooth and rough diffuser. For the rough diffuser the velocity profiles from mesh 2.3 are depicted and for the smooth diffuser the velocity profiles for mesh 1.2 are depicted.

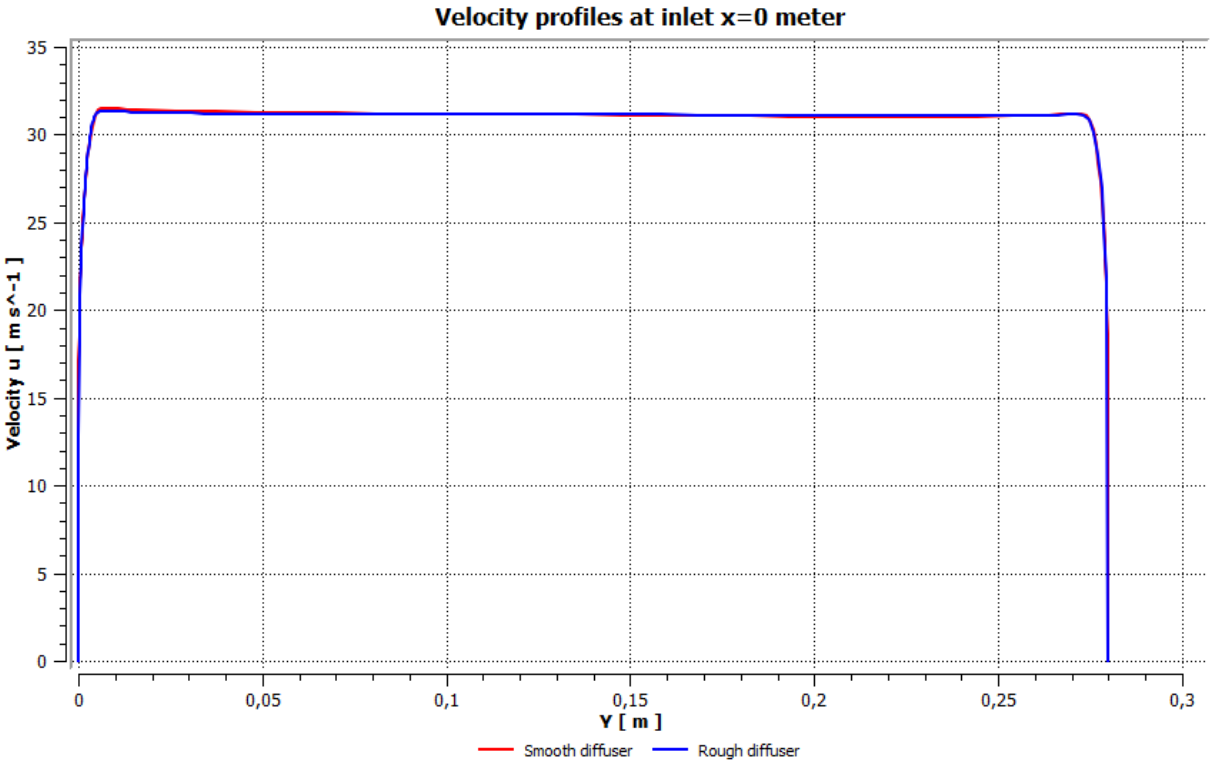

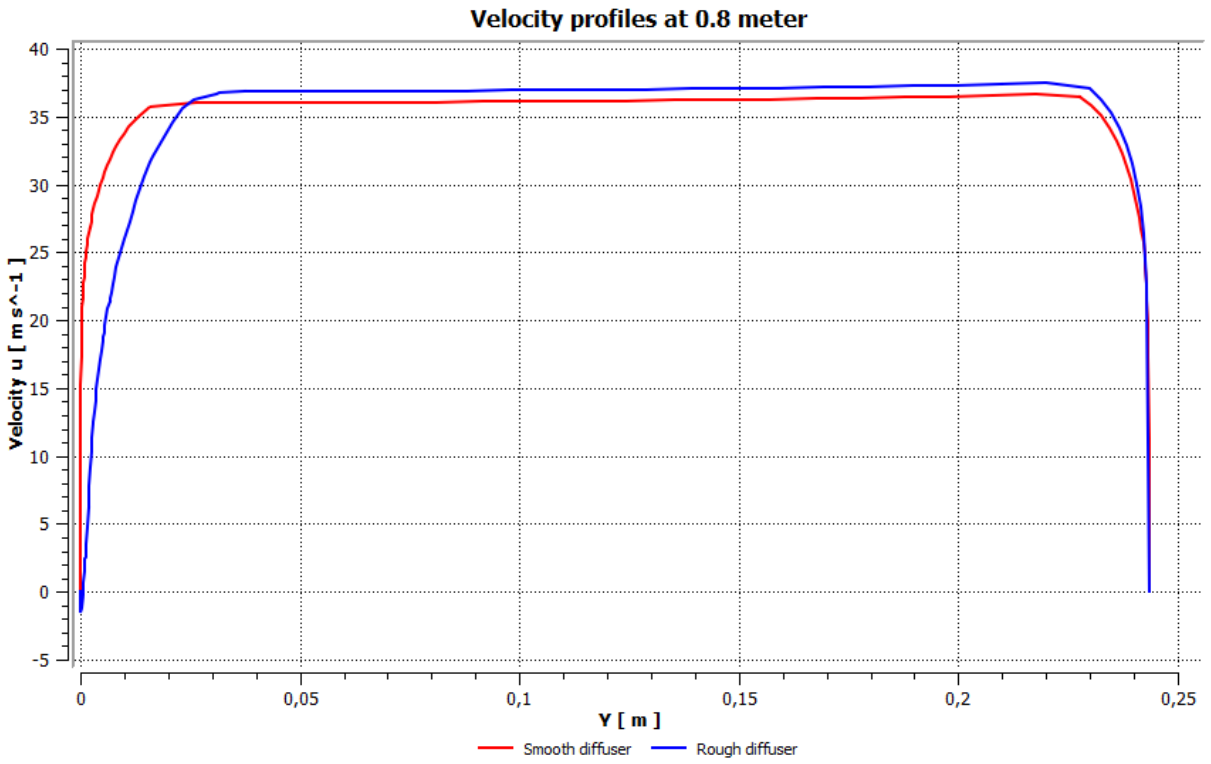
Velocity profiles at 0.8 meter
Velocity u [m s^-1]
40
35
30
25
20
15
10
5
0
-5
0
0,05
0,1
0,15
0,2
0,25
Y [m]
Smooth diffuser
Rough diffuser

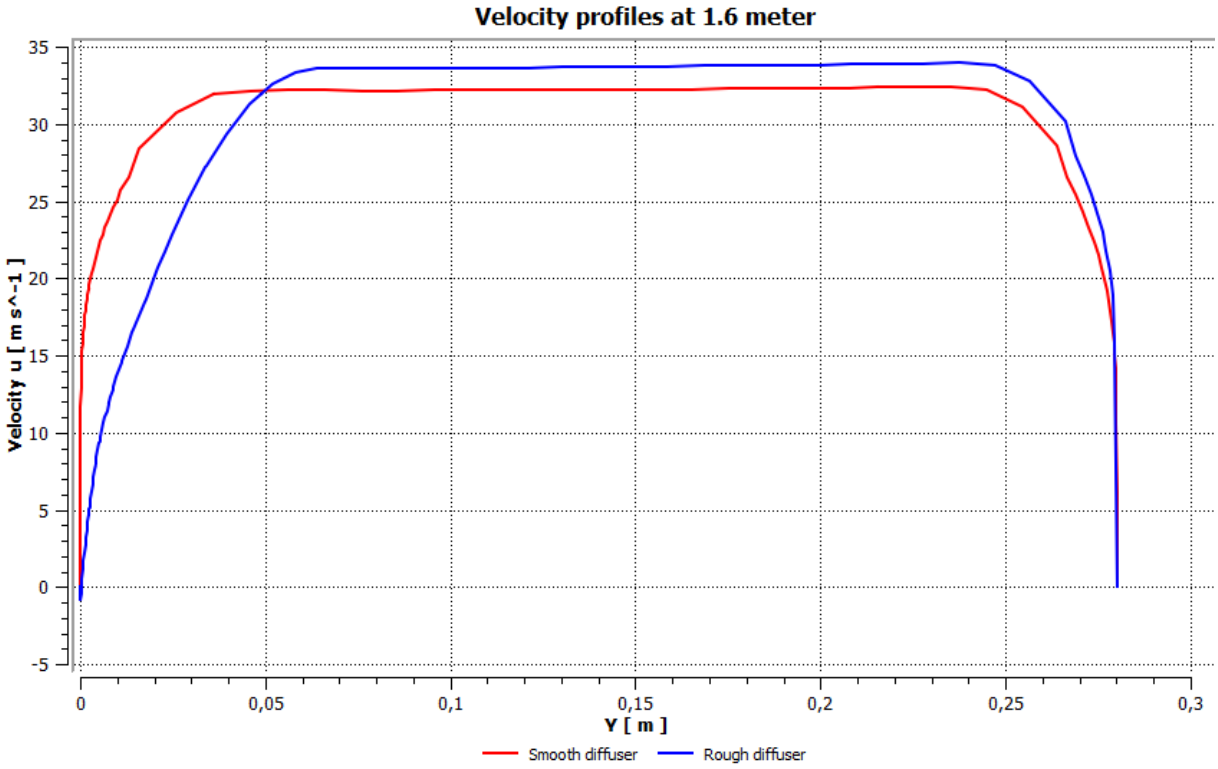
Velocity profiles at 1.6 meter
Velocity u [m s^-1]
35
30
25
20
15
10
5
0
-5
0
0,05
0,1
0,15
0,2
0,25
0,3
Y [m]
Smooth diffuser
Rough diffuser

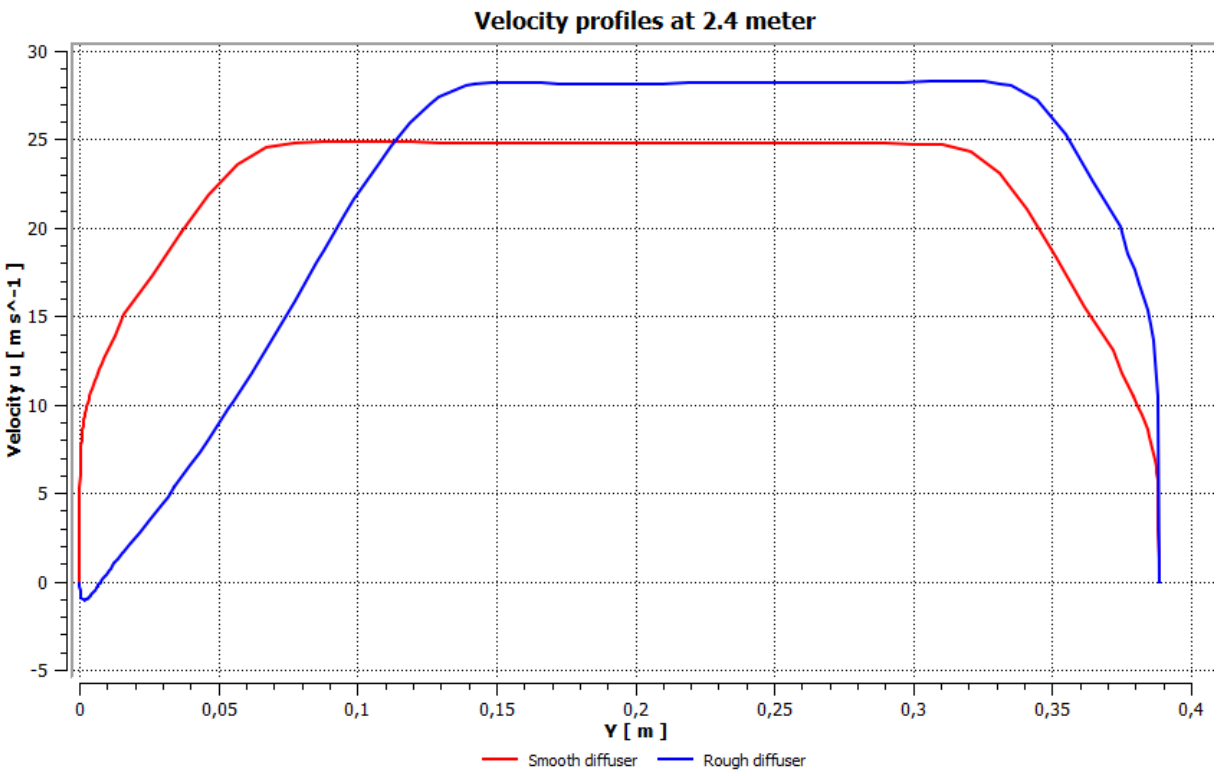
Velocity profiles at 2.4 meter
Velocity u [m s^-1]
30
25
20
15
10
5
0
-5
0
0,05
0,1
0,15
0,2
0,25
0,3
0,35
0,4
Y [m]
Smooth diffuser
Rough diffuser

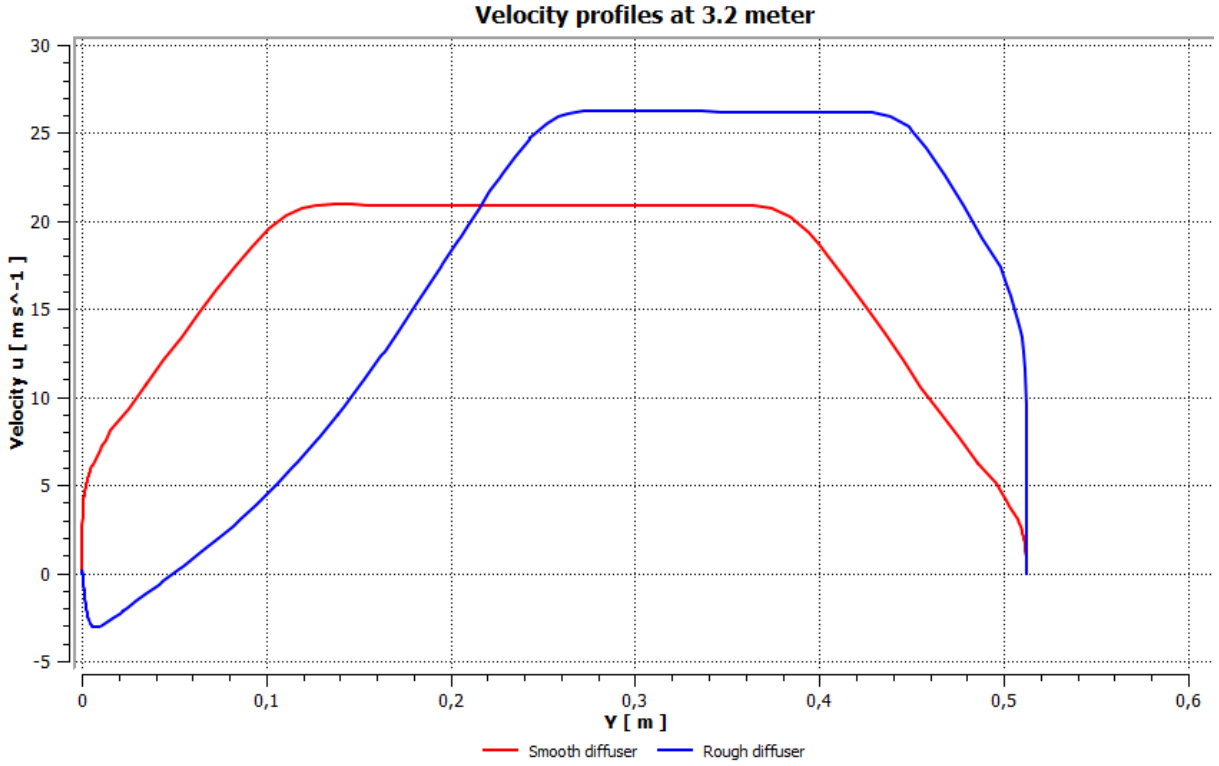
Velocity profiles at 3.2 meter
Velocity u [m s^-1]
30
25
20
15
10
5
0
-5
0
0,1
0,2
0,3
0,4
0,5
0,6
Y [m]
Smooth diffuser
Rough diffuser

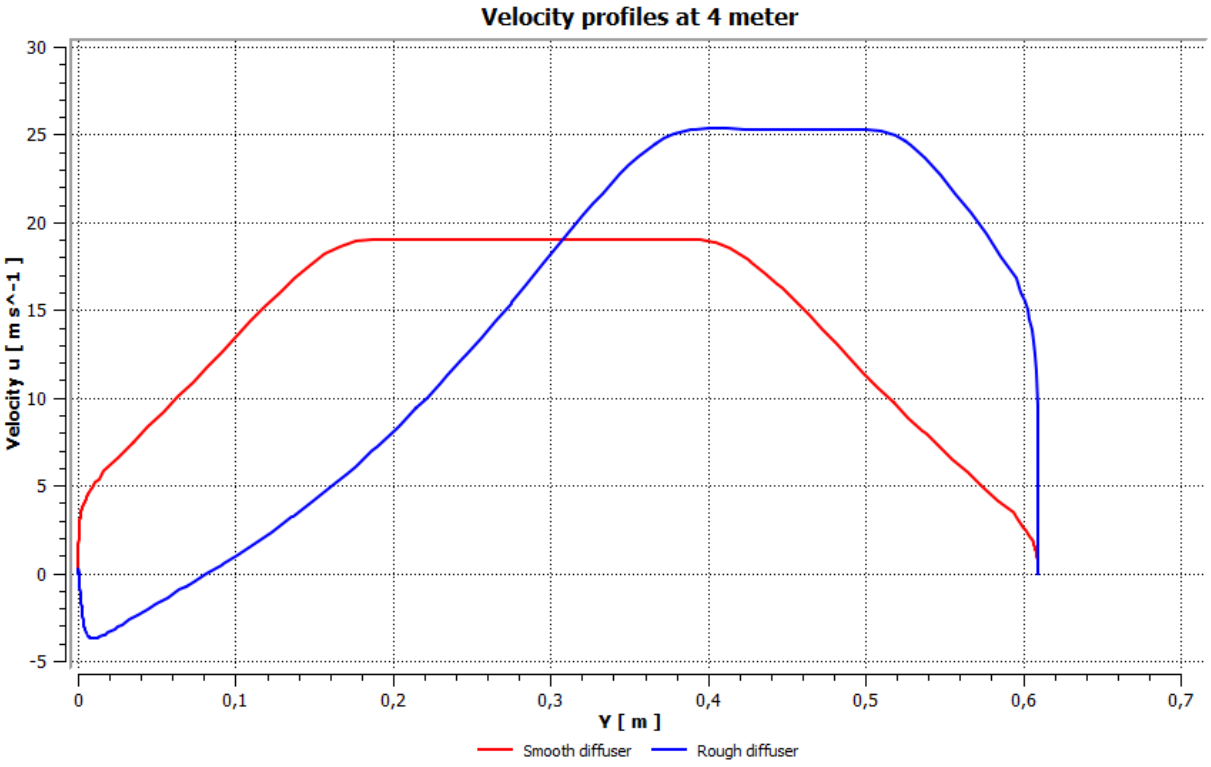
Velocity profiles at 4 meter
Velocity u [m s^-1]
30
25
20
15
10
5
0
-5
0
0,1
0,2
0,3
0,4
0,5
0,6
0,7
Y [m]
Smooth diffuser
Rough diffuser

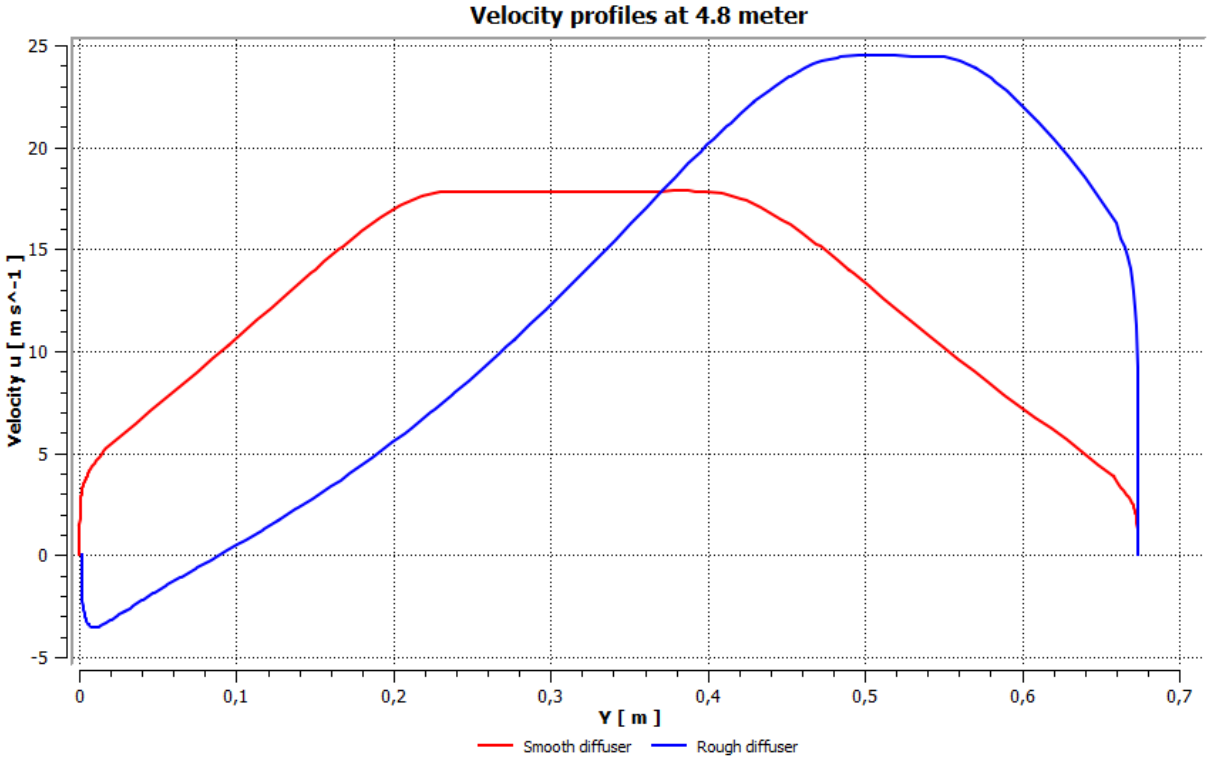
Velocity profiles at 4.8 meter
Velocity u [m s^-1]
25
20
15
10
5
0
-5
0
0,1
0,2
0,3
0,4
0,5
0,6
0,7
Y [m]
Smooth diffuser
Rough diffuser

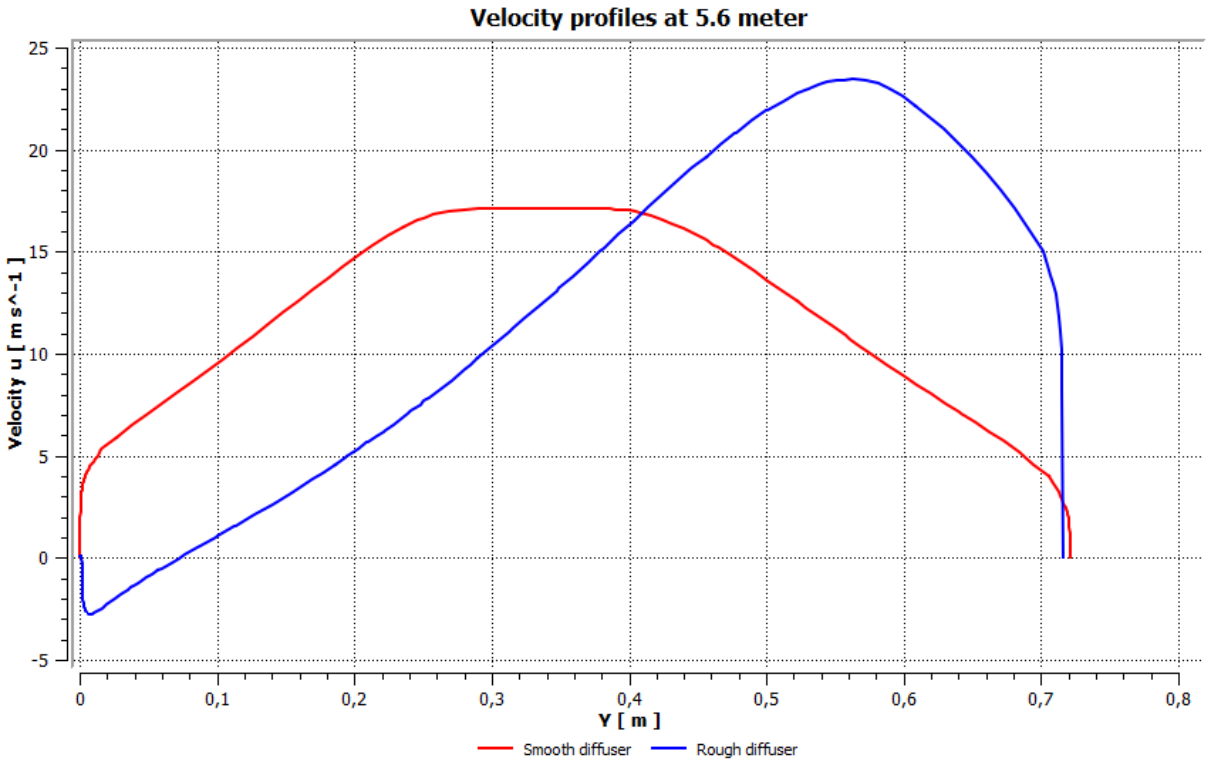
Velocity profiles at 5.6 meter
Velocity u [m s^-1]
25
20
15
10
5
0
-5
0
0,1
0,2
0,3
0,4
0,5
0,6
0,7
0,8
Y [m]
Smooth diffuser
Rough diffuser

Appendix C - Eddy viscosity comparison smooth and rough diffuser

In this section the eddy viscosity for the smooth and rough diffuser are plotted together at different locations throughout the diffuser

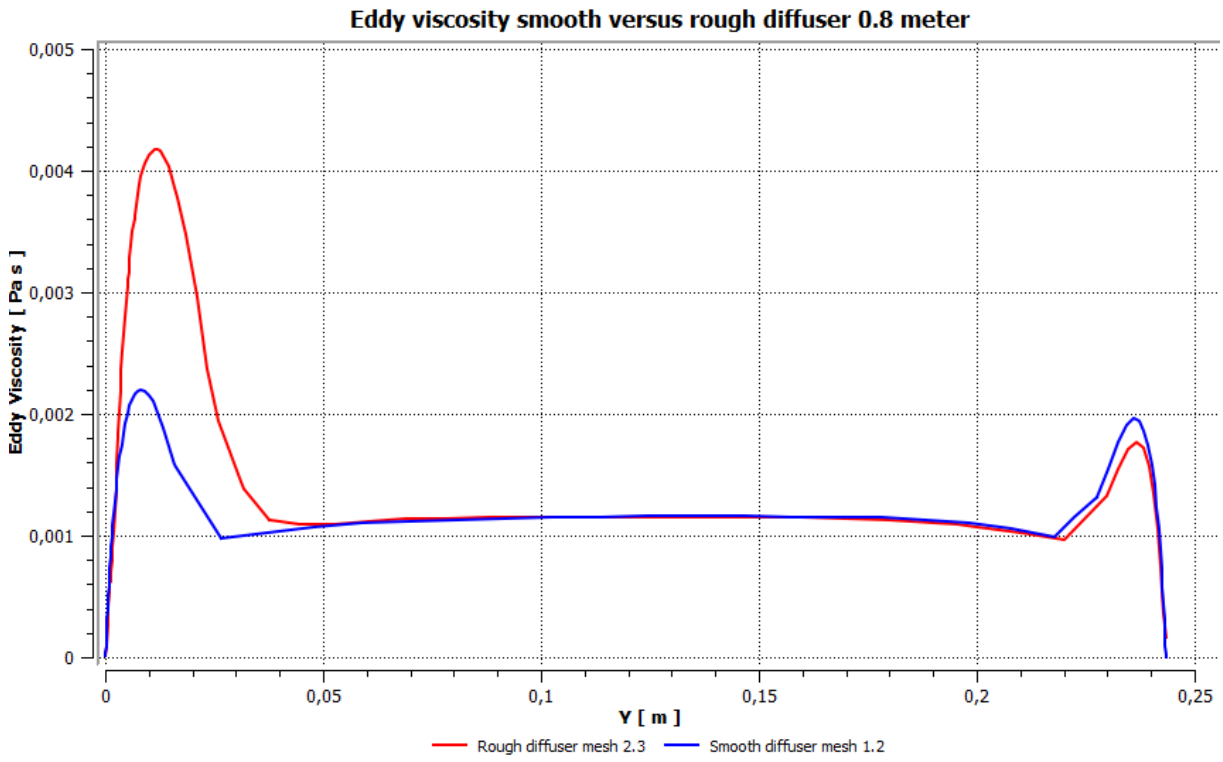

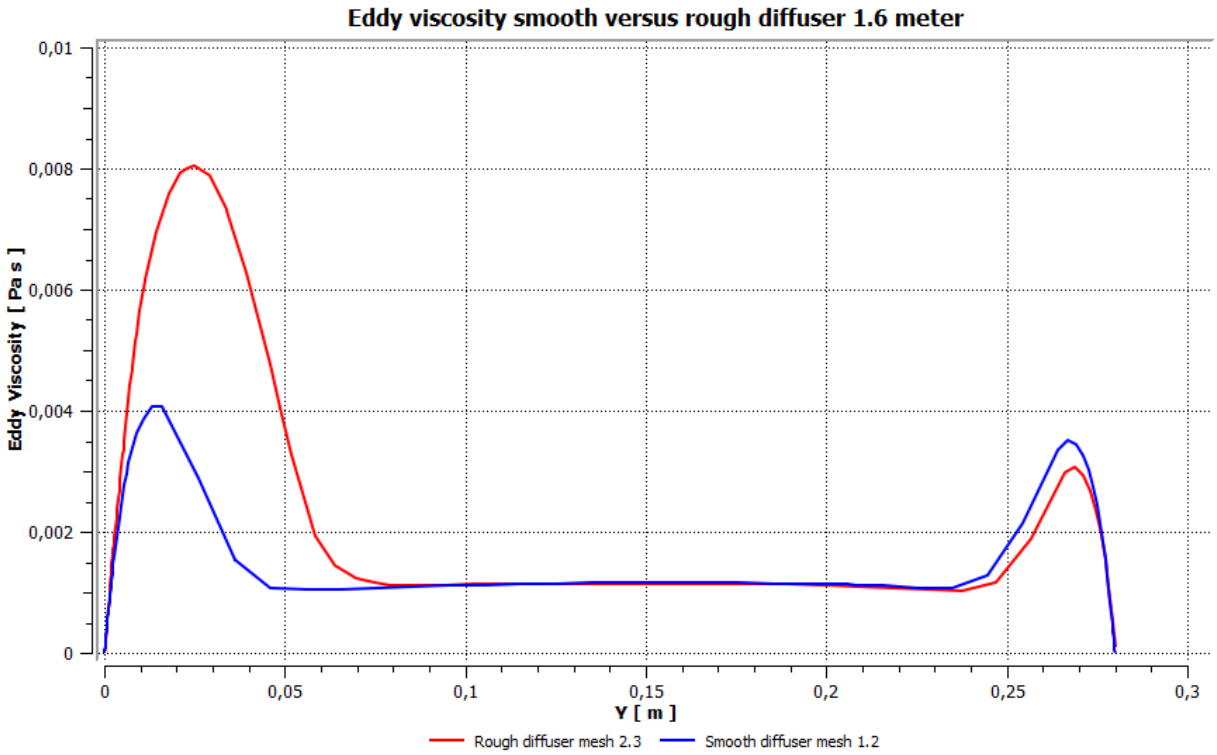
Eddy viscosity smooth versus rough diffuser 1.6 meter
Eddy Viscosity [Pa s]
0,01
0,008
0,006
0,004
0,002
0
0
0,05
0,1
0,15
0,2
0,25
0,3
Y [m]
Rough diffuser mesh 2.3
Smooth diffuser mesh 1.2

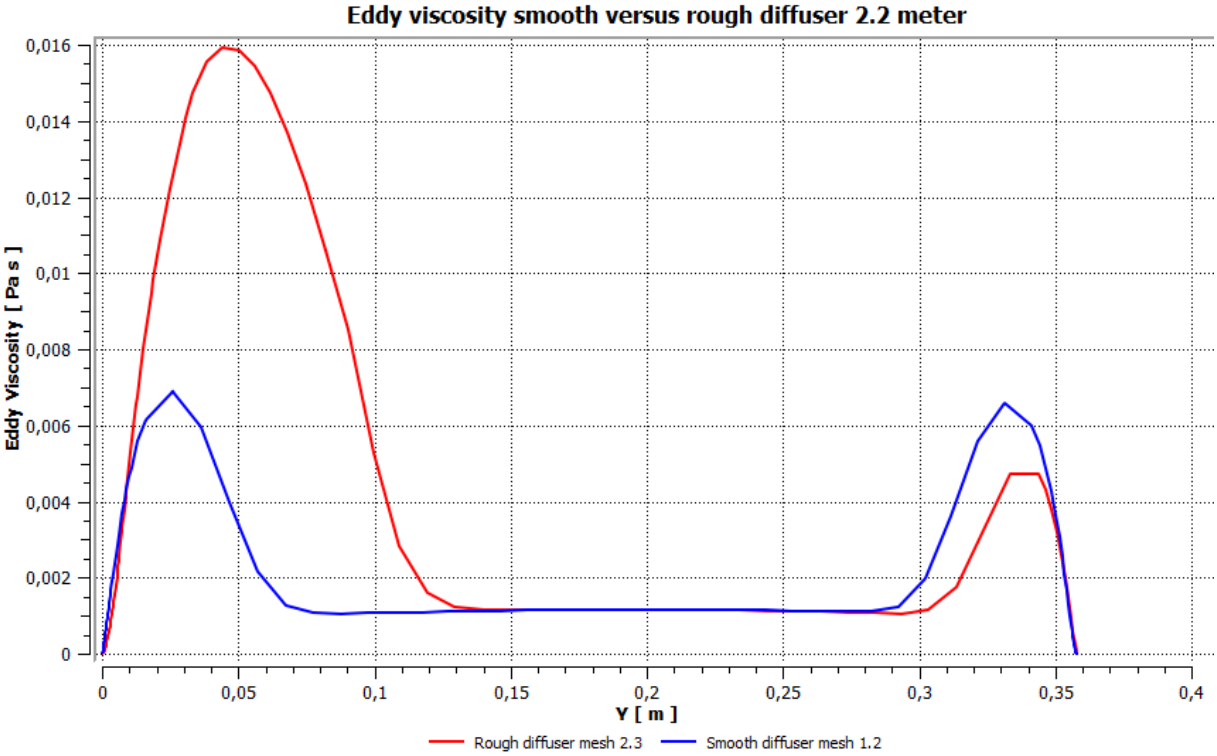
Eddy viscosity smooth versus rough diffuser 2.2 meter
Eddy Viscosity [Pa s]
0,016
0,014
0,012
0,01
0,008
0,006
0,004
0,002
0
0
0,05
0,1
0,15
0,2
0,25
0,3
0,35
0,4
Y [m]
Rough diffuser mesh 2.3
Smooth diffuser mesh 1.2

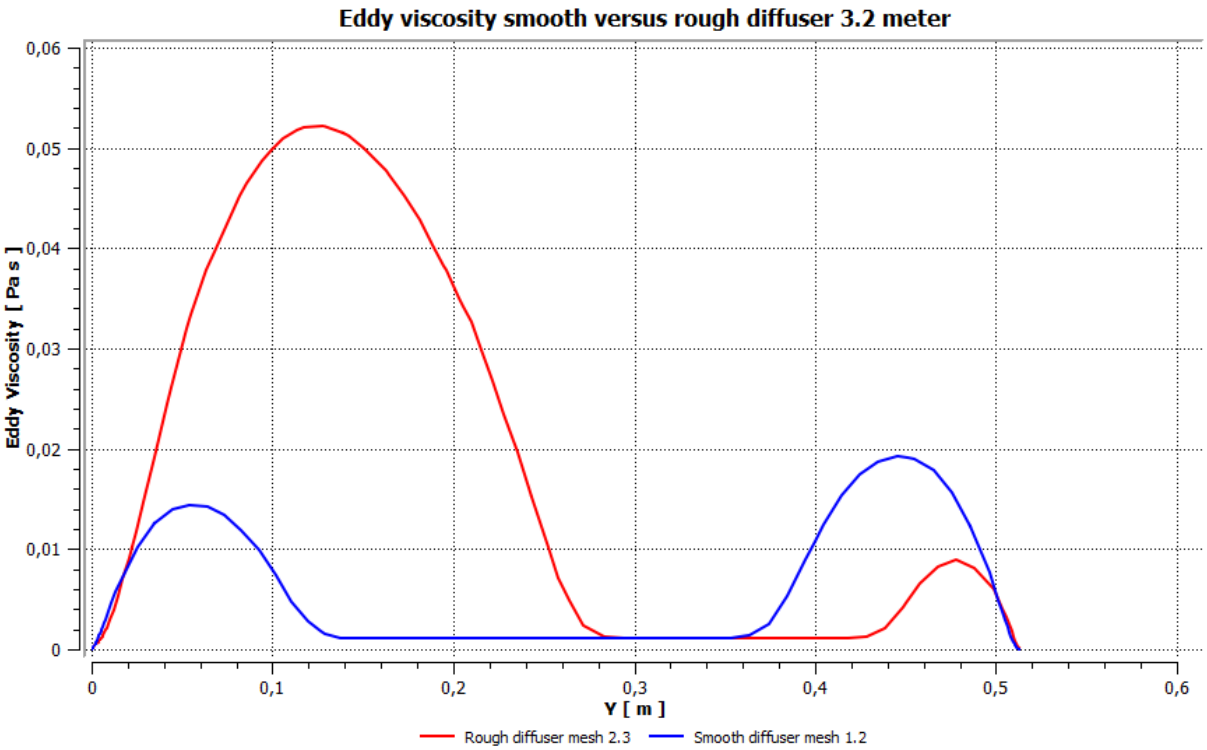
Eddy viscosity smooth versus rough diffuser 3.2 meter
Eddy Viscosity [Pa s]
0,06
0,05
0,04
0,03
0,02
0,01
0
0
0,1
0,2
0,3
0,4
0,5
0,6
Y [m]
Rough diffuser mesh 2.3
Smooth diffuser mesh 1.2

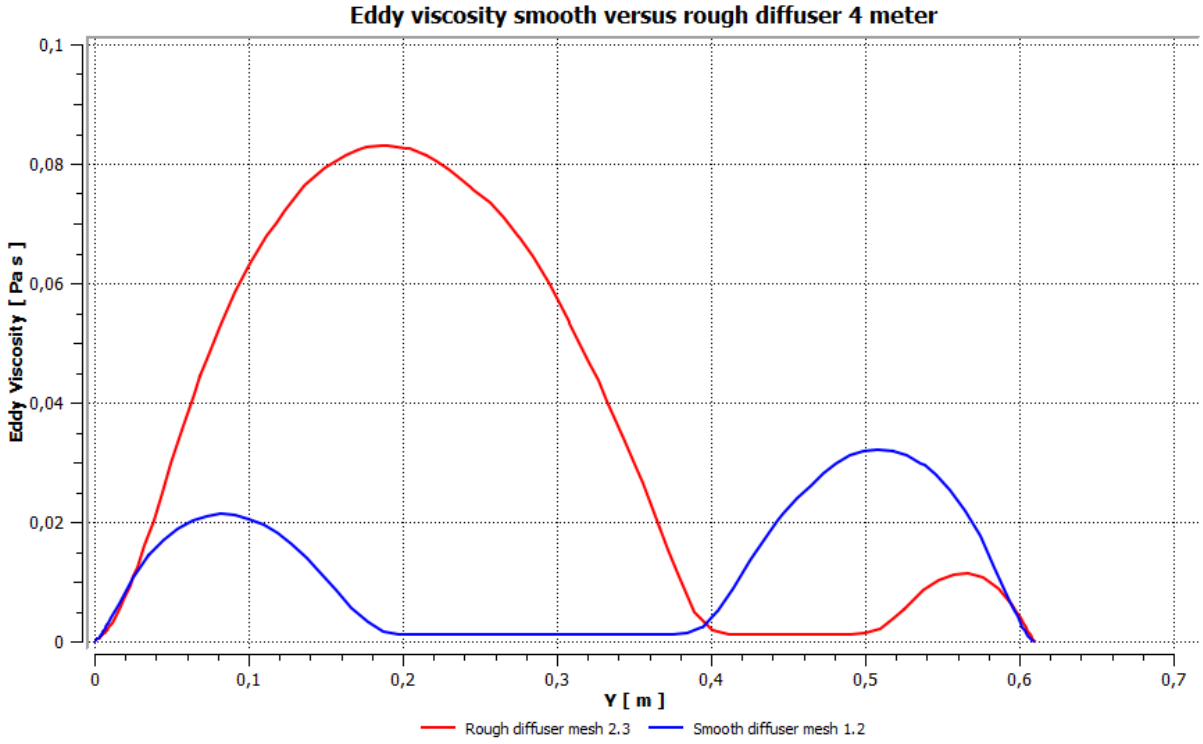
Eddy viscosity smooth versus rough diffuser 4 meter
Eddy Viscosity [Pa s]
0,1
0,08
0,06
0,04
0,02
0
0
0,1
0,2
0,3
0,4
0,5
0,6
0,7
Y [m]
Rough diffuser mesh 2.3
Smooth diffuser mesh 1.2

Appendix D - Contour plots

In this section contour plots for the velocity and eddy viscosity are plotted for some of the turbulence models utilized in this thesis. The plots are all from the meshes which produced the most authentic replication of the physical measurements as given in Chapter 3.

Contour plots smooth diffuser simulations

K-ω SST model

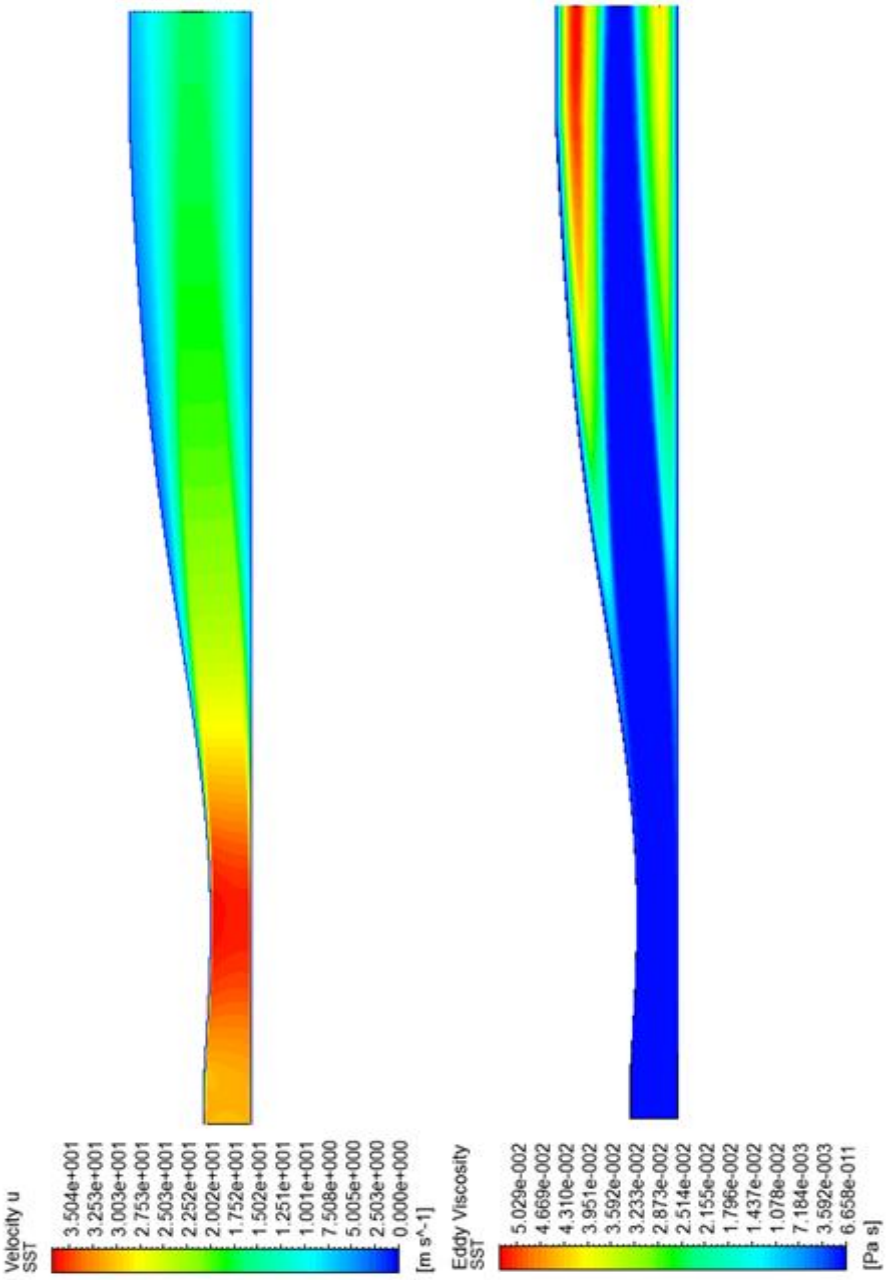

K-ε RNG model

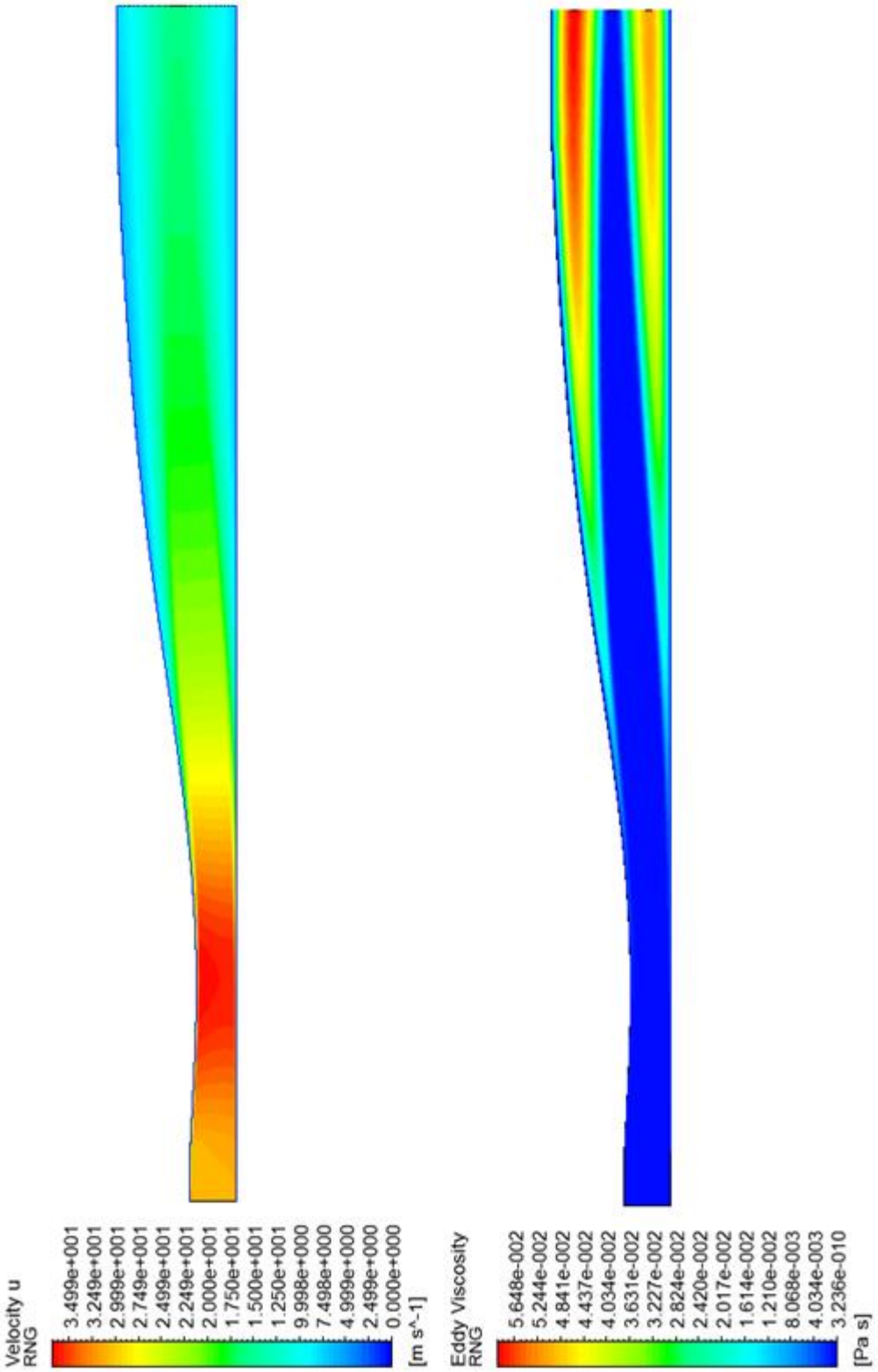
Velocity u
RNG
3.499e+001
3.249e+001
2.999e+001
2.749e+001
2.499e+001
2.249e+001
2.000e+001
1.750e+001
1.500e+001
1.250e+001
9.998e+000
7.498e+000
4.999e+000
2.499e+000
0.000e+000
[m s^-1]
Eddy Viscosity
RNG
5.648e-002
5.244e-002
4.841e-002
4.437e-002
4.034e-002
3.631e-002
3.227e-002
2.824e-002
2.420e-002
2.017e-002
1.614e-002
1.210e-002
8.068e-003
4.034e-003
3.236e-010
[Pa s]

Contour plots rough diffuser simulations

K-ω SST model

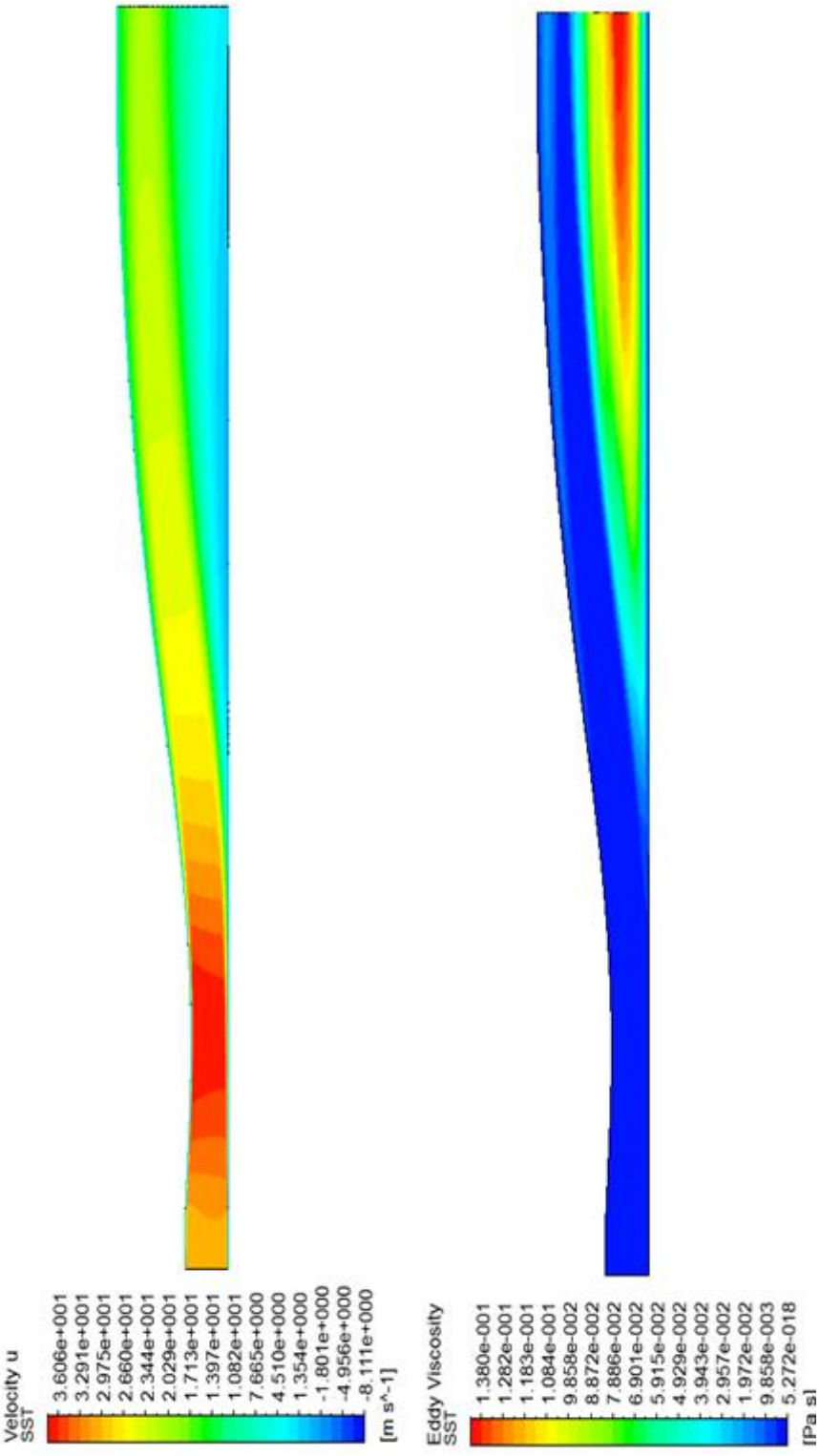

K-ε Realizable

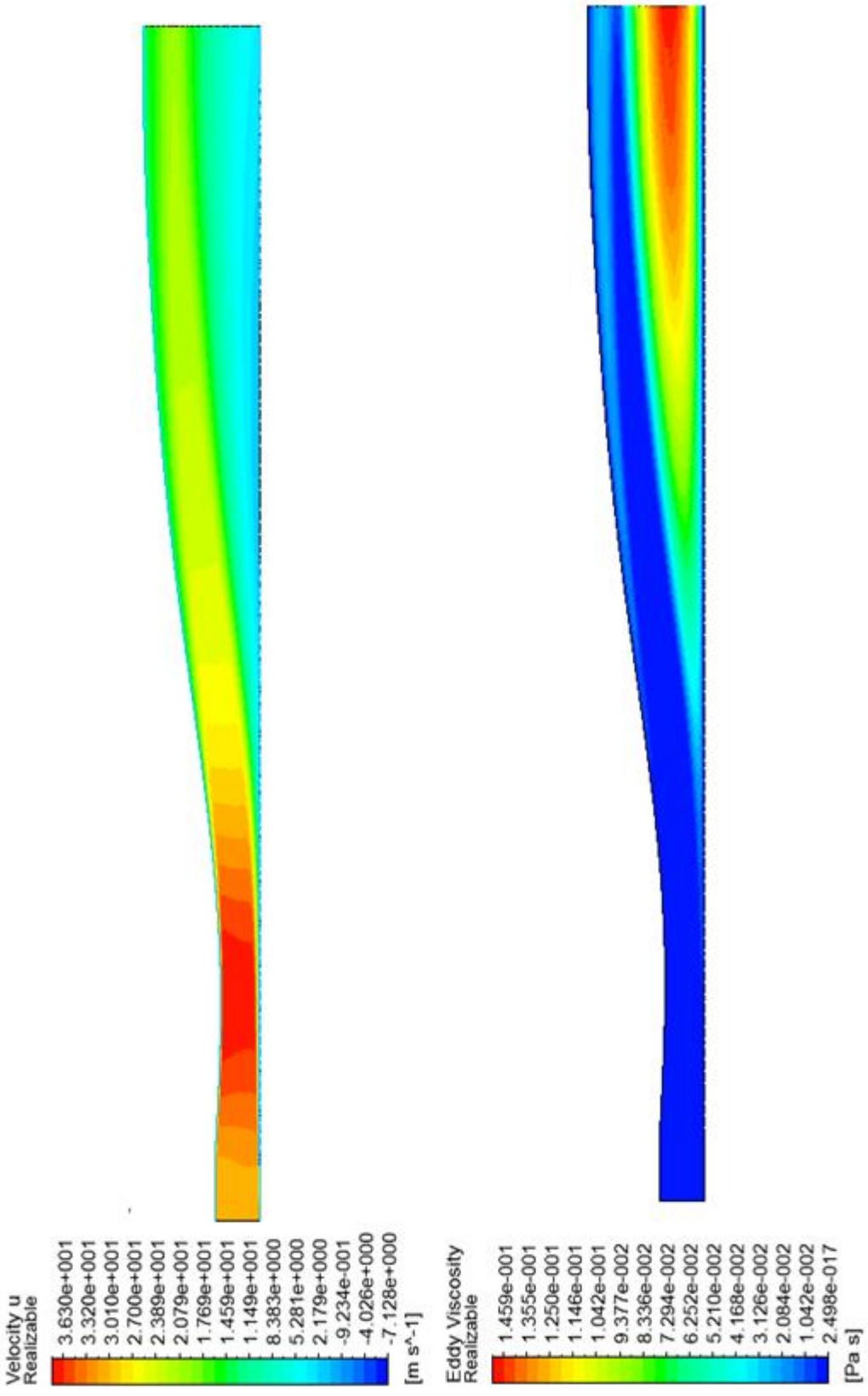

RSM model:

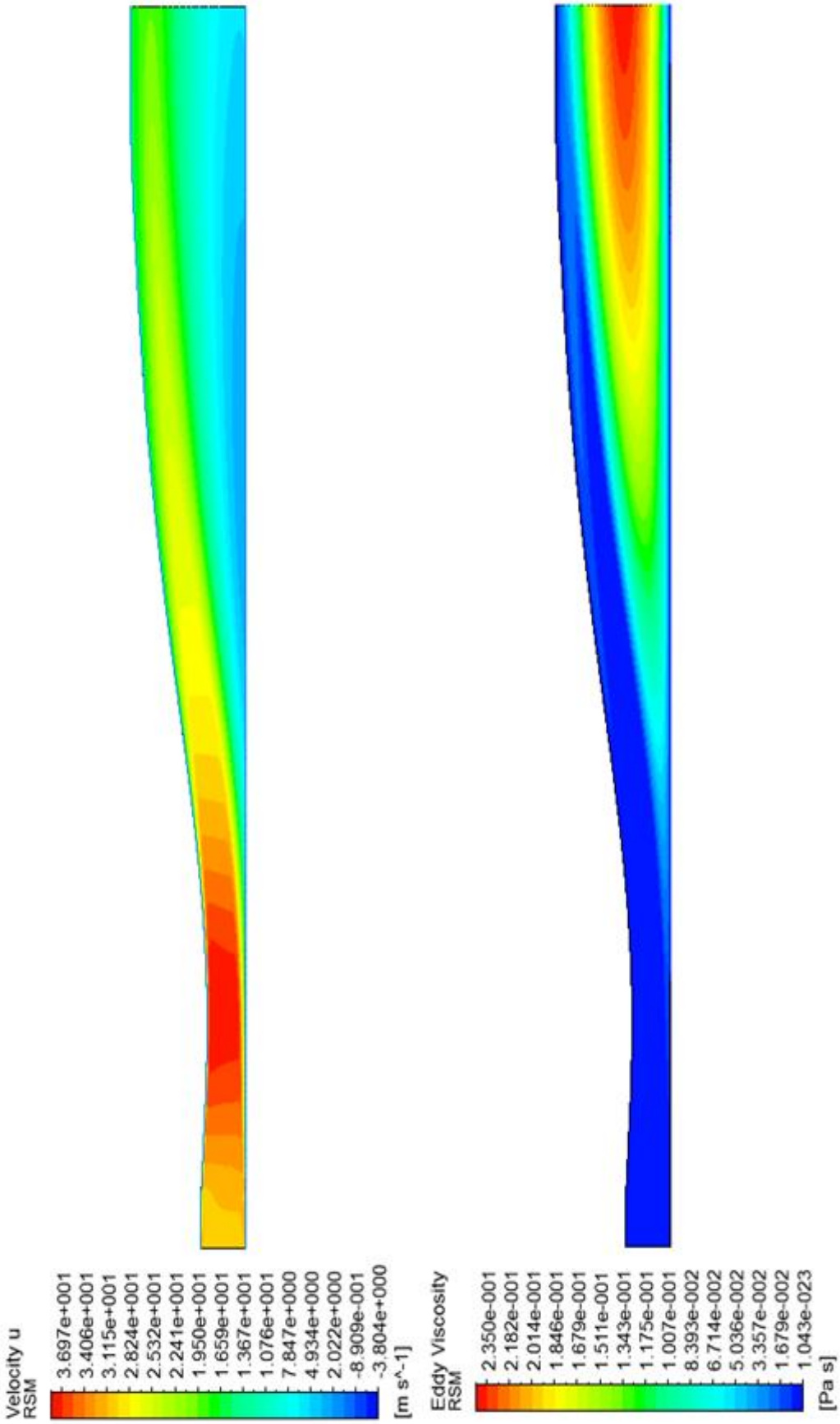
Velocity u
RSM
3.697e+001
3.406e+001
3.115e+001
2.824e+001
2.532e+001
2.241e+001
1.950e+001
1.659e+001
1.367e+001
1.076e+001
7.847e+000
4.934e+000
2.022e+000
-8.909e-001
-3.804e+000
[m s^-1]
Eddy Viscosity
RSM
2.350e-001
2.182e-001
2.014e-001
1.846e-001
1.679e-001
1.511e-001
1.343e-001
1.175e-001
1.007e-001
8.393e-002
6.714e-002
5.036e-002
3.357e-002
1.679e-002
1.043e-023
[Pa s]

Appendix E - Geometry description

In table (A.1) the diffuser geometry is given. In figure (A.1) the geometry of the roughness elements are presented

Length [cm]	Height [cm]
0	28.0
10	27.46
20	26.88
30	26.29
40	25.74
50	25.25
60	24.85
70	24.55
80	24.39
90	24.35
100	24.46
110	24.72
120	25.13
130	25.66
140	26.35
150	27.17
160	28.13
170	29.18
180	30.36
190	31.62
200	32.97

Lenght [cm]	Height [cm]
210	34.40
220	35.88
230	37.4
240	38.96
250	40.55
260	42.14
270	43.73
280	45.31
290	46.87
300	48.41
310	49.91
320	51.13
330	52.27
340	54.13
350	55.43
360	56.68
370	57.87
380	59.0
390	60.07
400	61.08

Length [cm]	Height [cm]
410	62.04
420	62.95
430	63.82
440	64.63
450	65.41
460	66.14
470	66.85
480	67.52
490	68.16
500	68.77
510	69.35
520	69.9
530	70.42
540	70.89
550	71.32
560	71.69
570	71.98
580	72.18
590	72.27
600	72.22

Table A. 1: Diffuser geometry

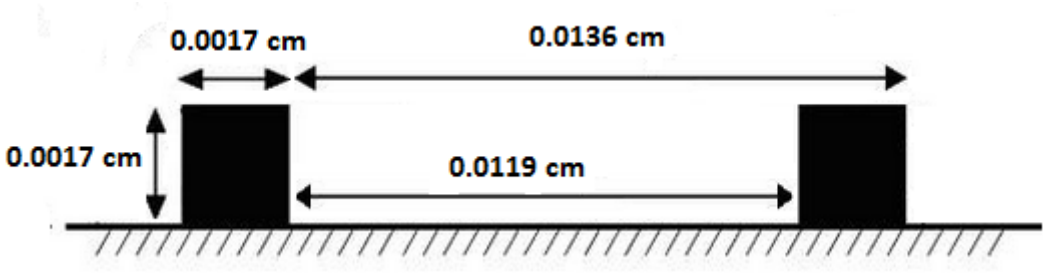

Figure A. 1: Roughness element geometry

Appendix F - Mesh independence analysis

In this section different figures are presented to illustrate the degree of mesh dependency associated with the different simulations and applied meshes. Note that the reference static pressure for the C_p distribution presented in this section is zero gauge, whilst the reference velocity is 31 m/s.

Analysis smooth diffuser meshes:

K-ω SST model

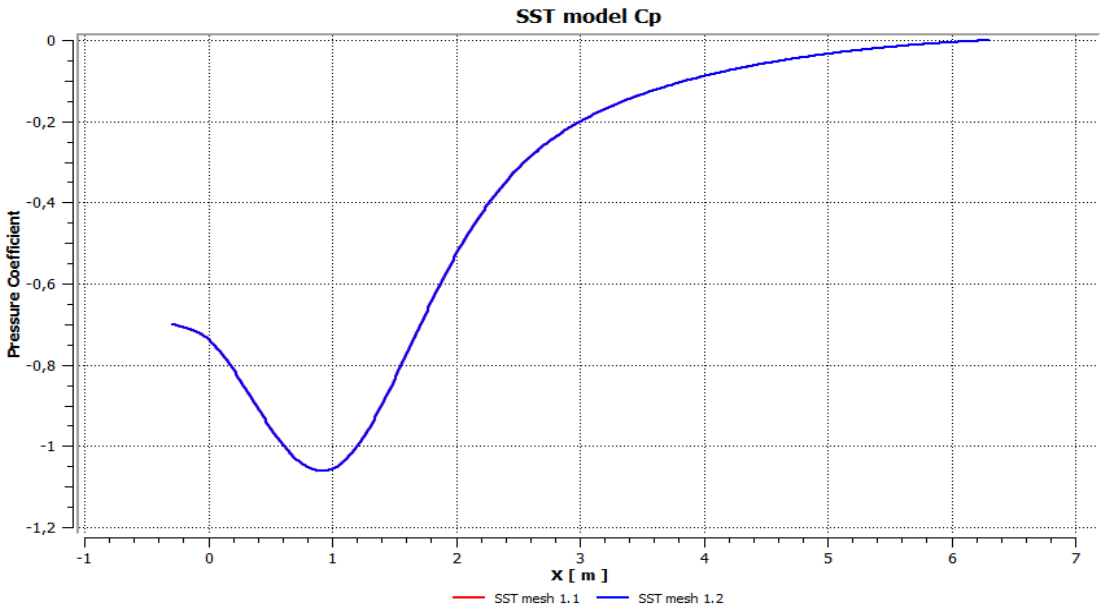

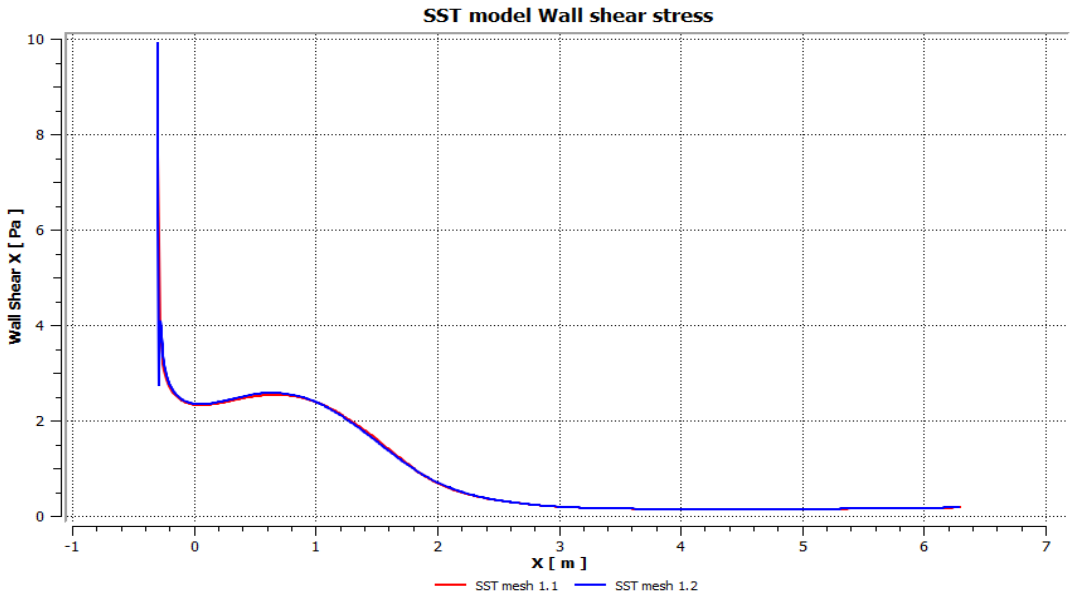

K-ε RNG model

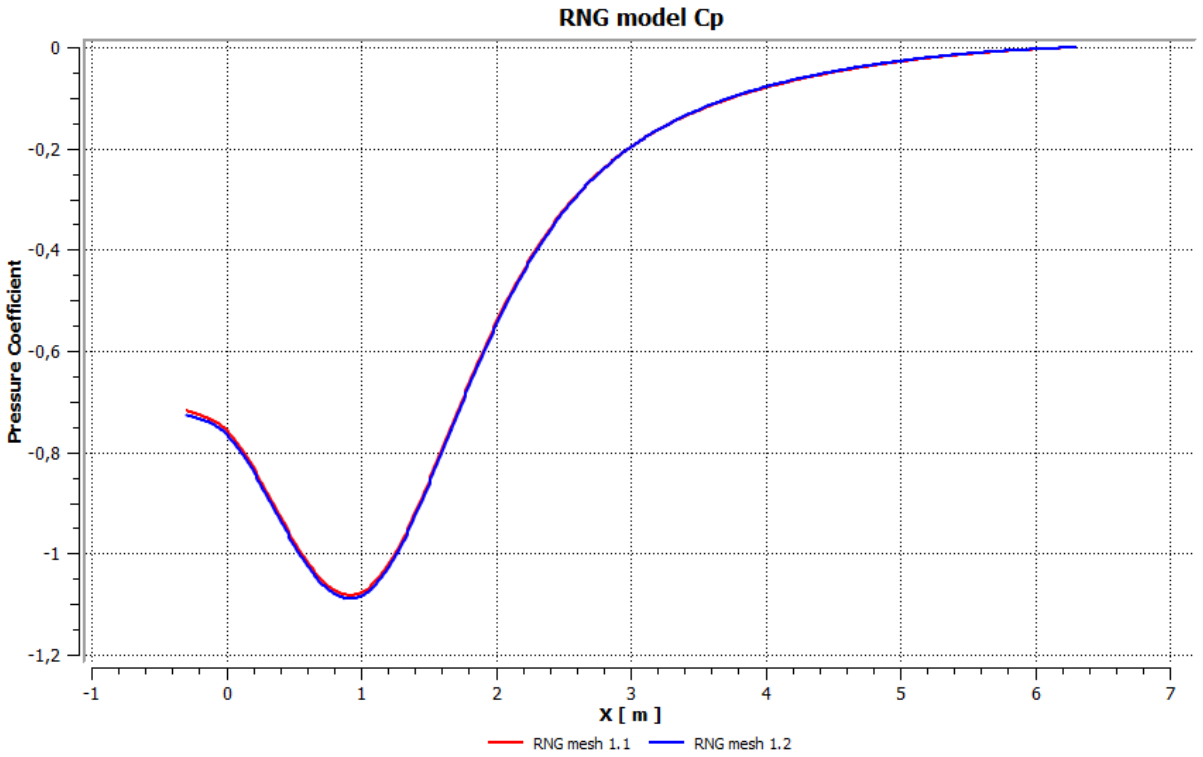
RNG model Cp
Pressure Coefficient
0
-0,2
-0,4
-0,6
-0,8
-1
-1,2
-1
0
1
2
3
4
5
6
7
X [m]
RNG mesh 1.1
RNG mesh 1.2

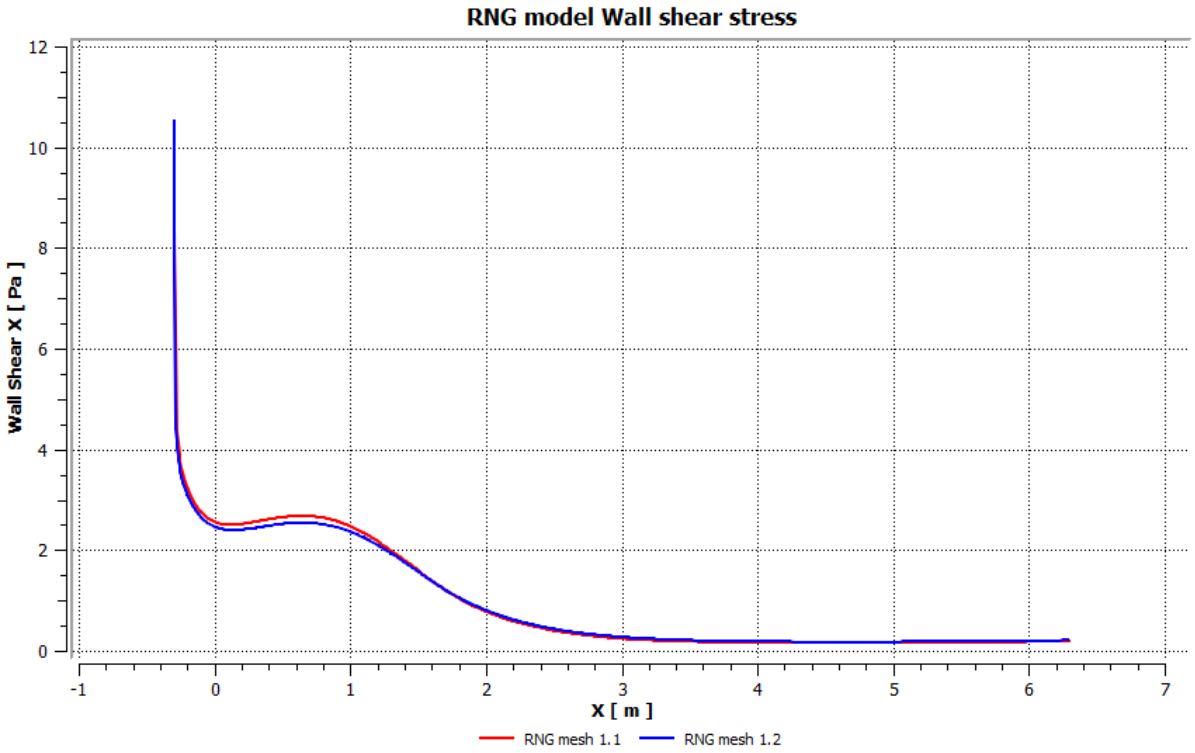
RNG model Wall shear stress
Wall Shear X [Pa]
12
10
8
6
4
2
0
-1
0
1
2
3
4
5
6
7
X [m]
RNG mesh 1.1
RNG mesh 1.2

Spalart-Allmaras model

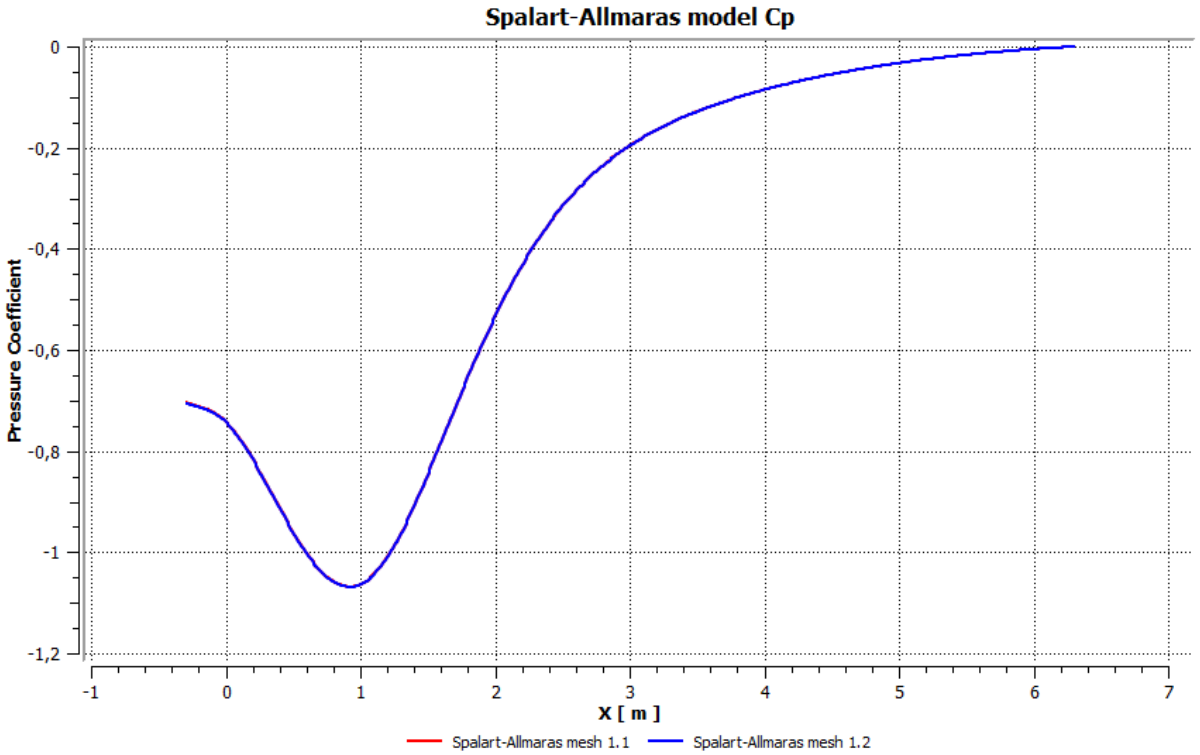

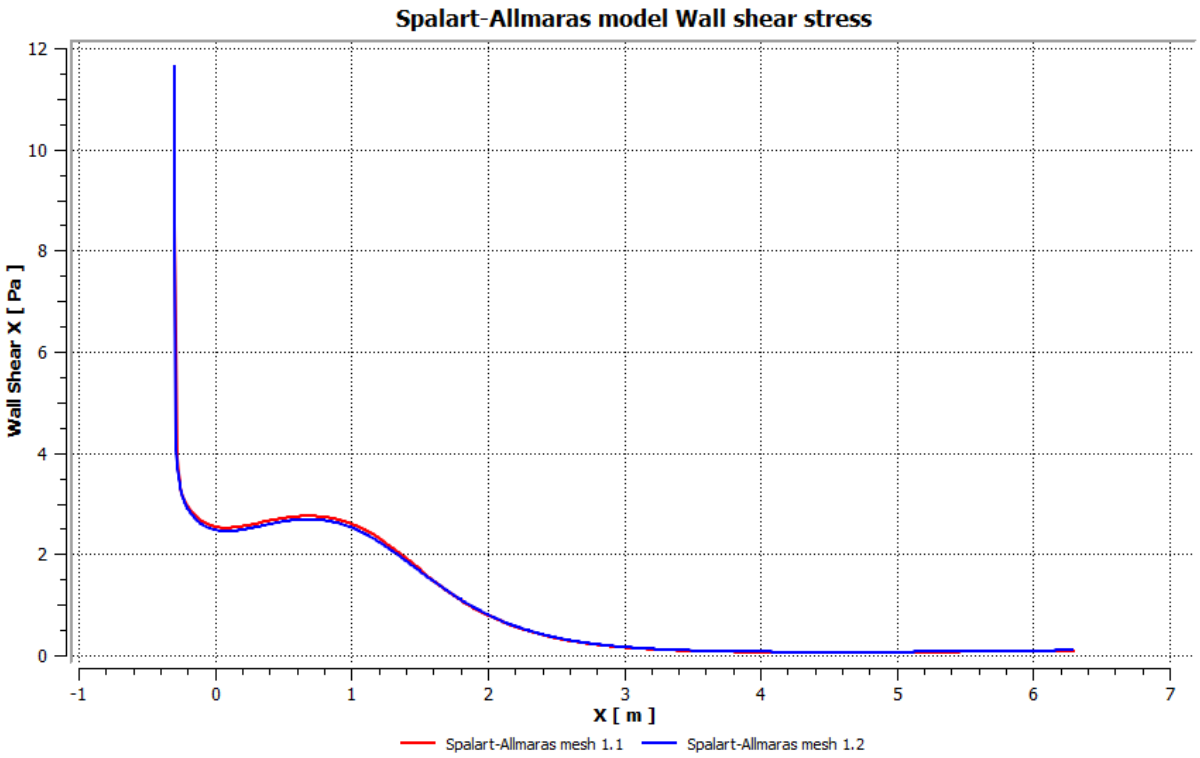

Analysis rough diffuser meshes:

Note that mesh 2.3 and 2.4 had to be plotted separately. This was because the computer resources power available was not sufficient for loading all the solution into the ANSYS post-processor.

K-ω SST model

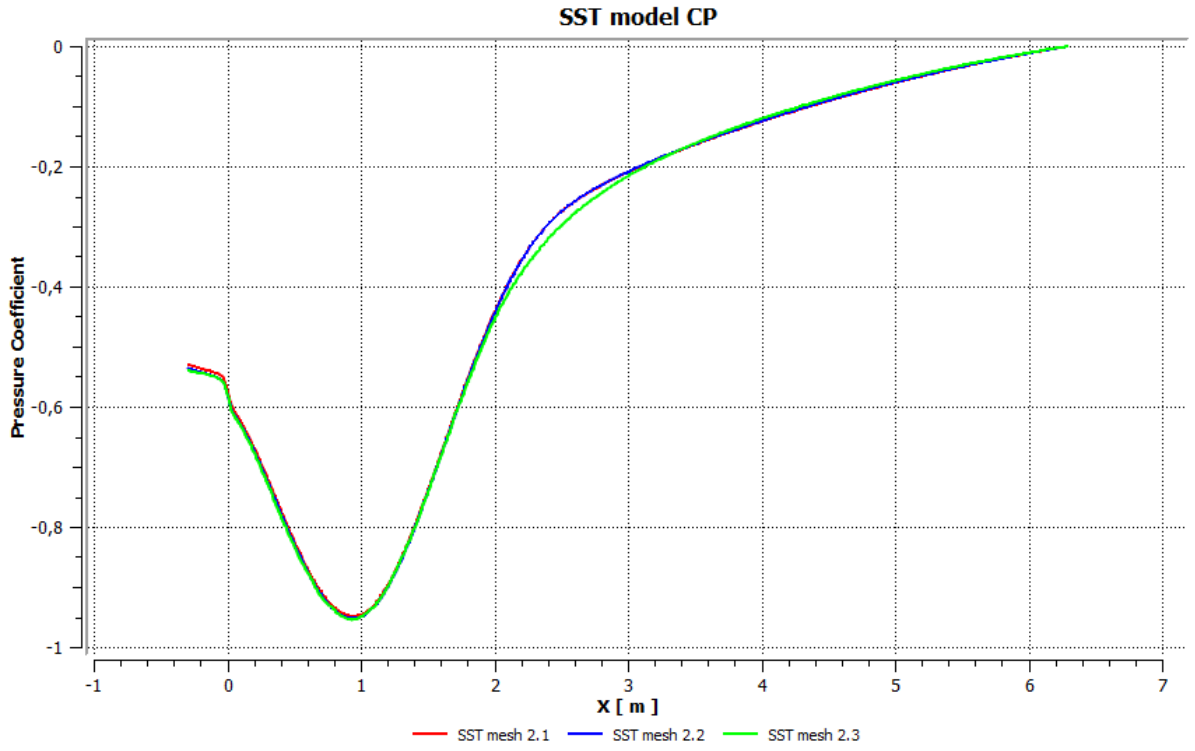

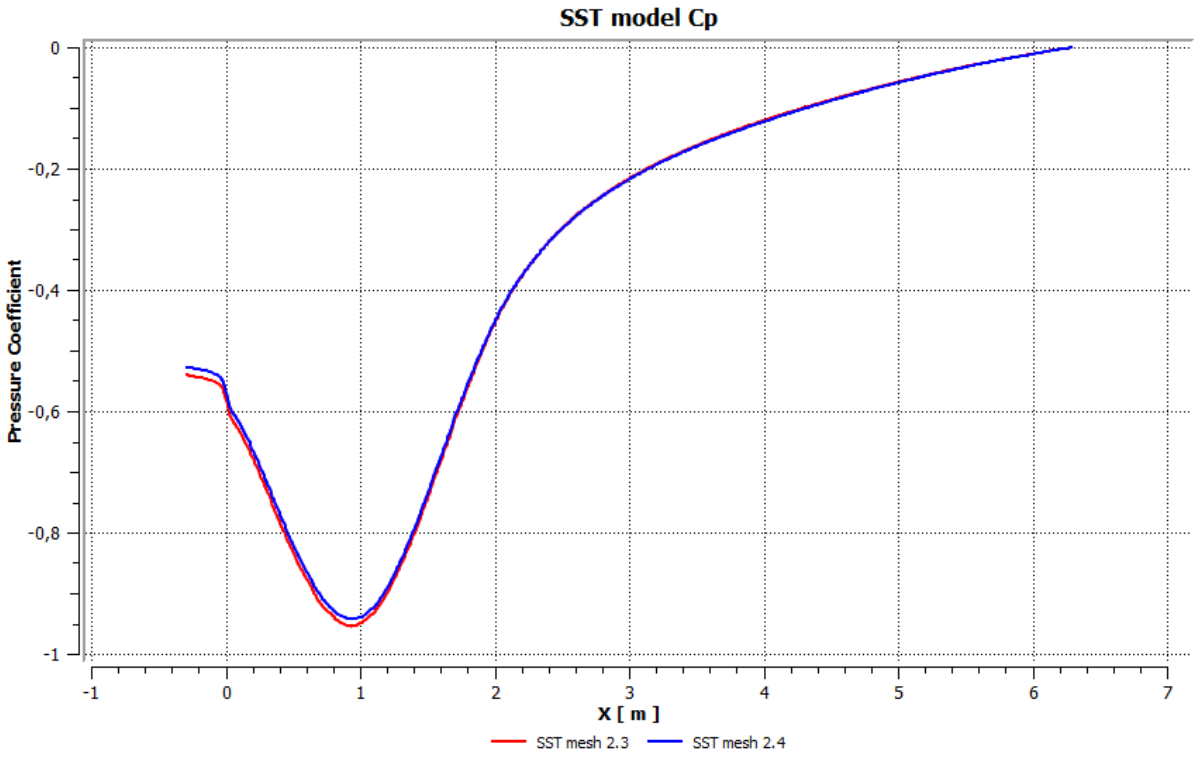
SST model Cp
Pressure Coefficient
0
-0,2
-0,4
-0,6
-0,8
-1
-1
0
1
2
3
4
5
6
7
X [m]
SST mesh 2.3
SST mesh 2.4

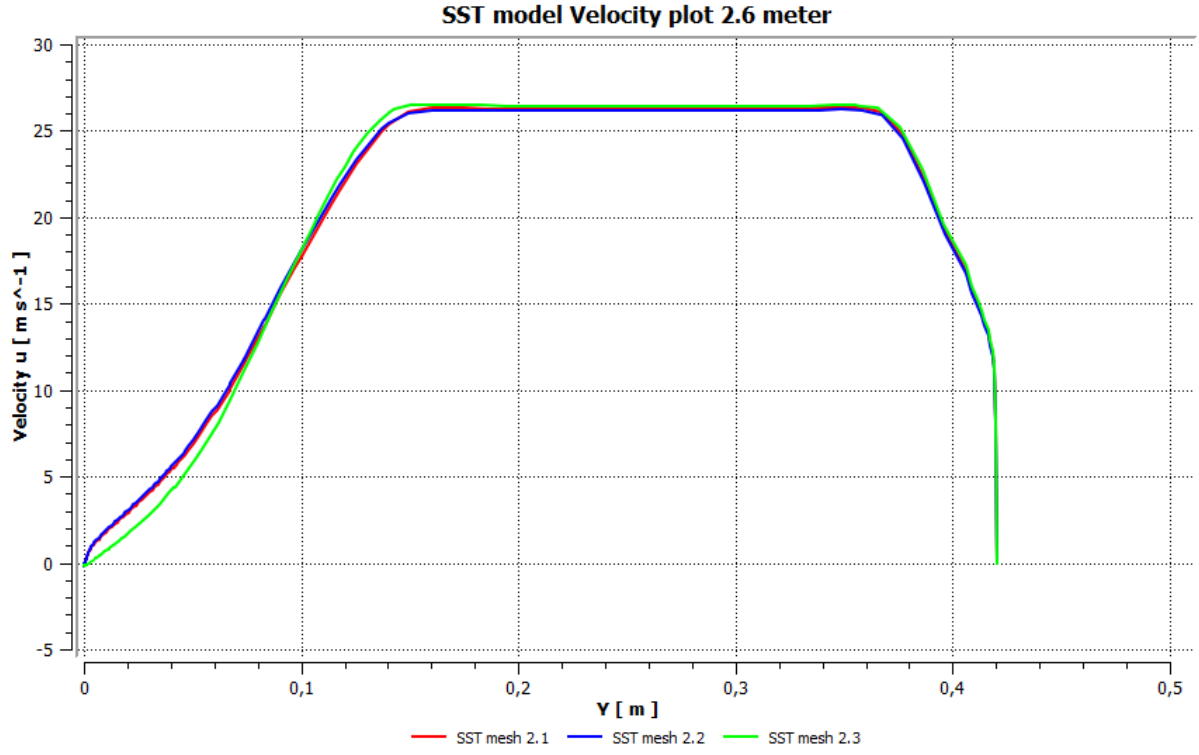
SST model Velocity plot 2.6 meter
Velocity u [m s^-1]
30
25
20
15
10
5
0
-5
0
0,1
0,2
0,3
0,4
0,5
Y [m]
SST mesh 2.1
SST mesh 2.2
SST mesh 2.3

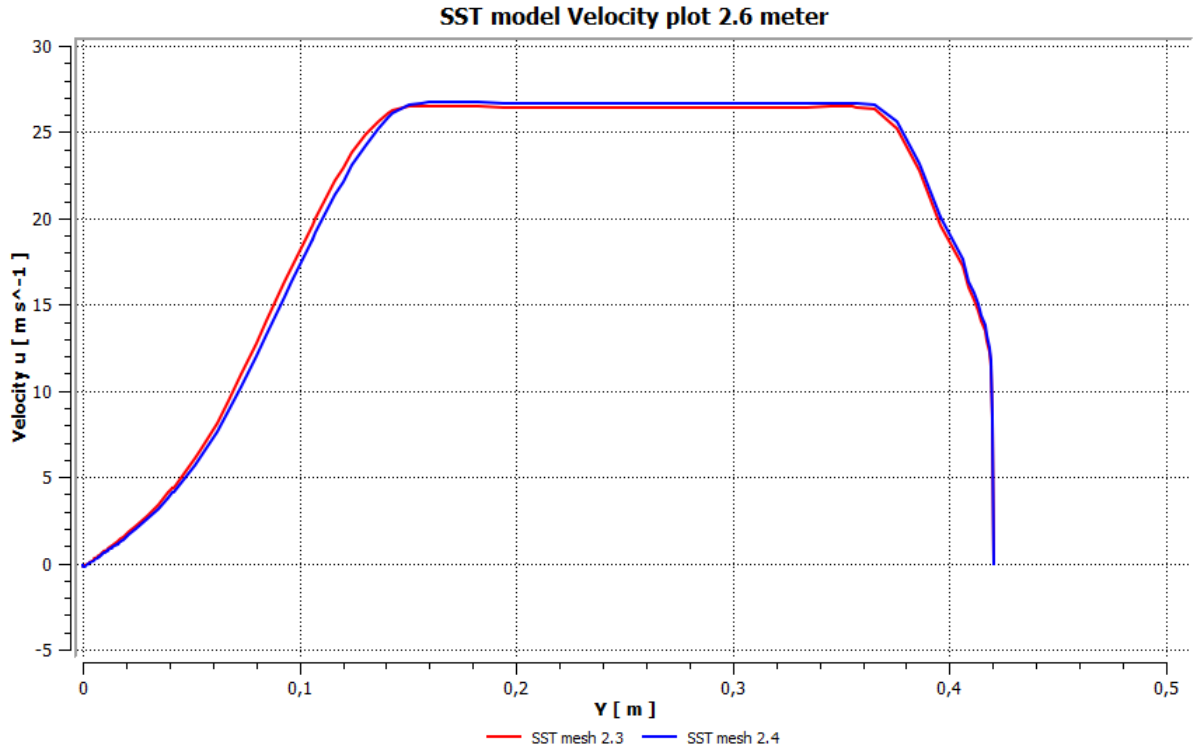
SST model Velocity plot 2.6 meter
Velocity u [m s^-1]
30
25
20
15
10
5
0
-5
0
0,1
0,2
0,3
0,4
0,5
Y [m]
SST mesh 2.3
SST mesh 2.4

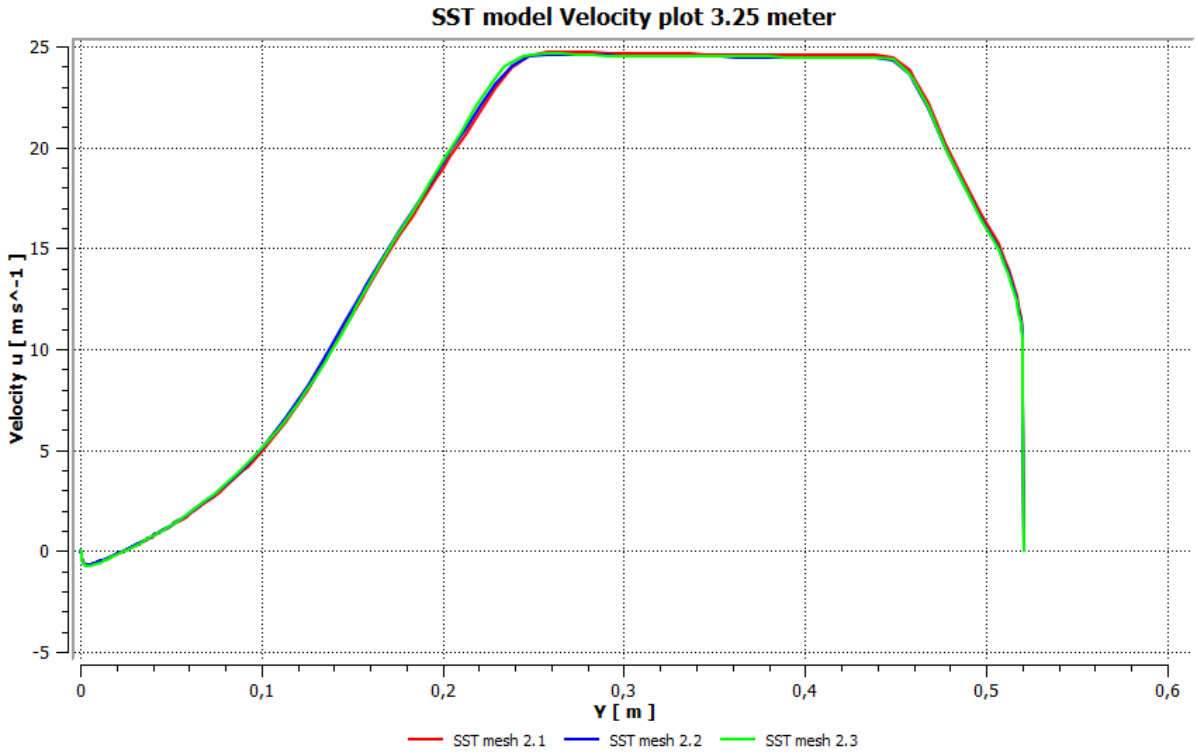
SST model Velocity plot 3.25 meter
Velocity u [m s^-1]
25
20
15
10
5
0
-5
0
0,1
0,2
0,3
0,4
0,5
0,6
Y [m]
SST mesh 2.1
SST mesh 2.2
SST mesh 2.3

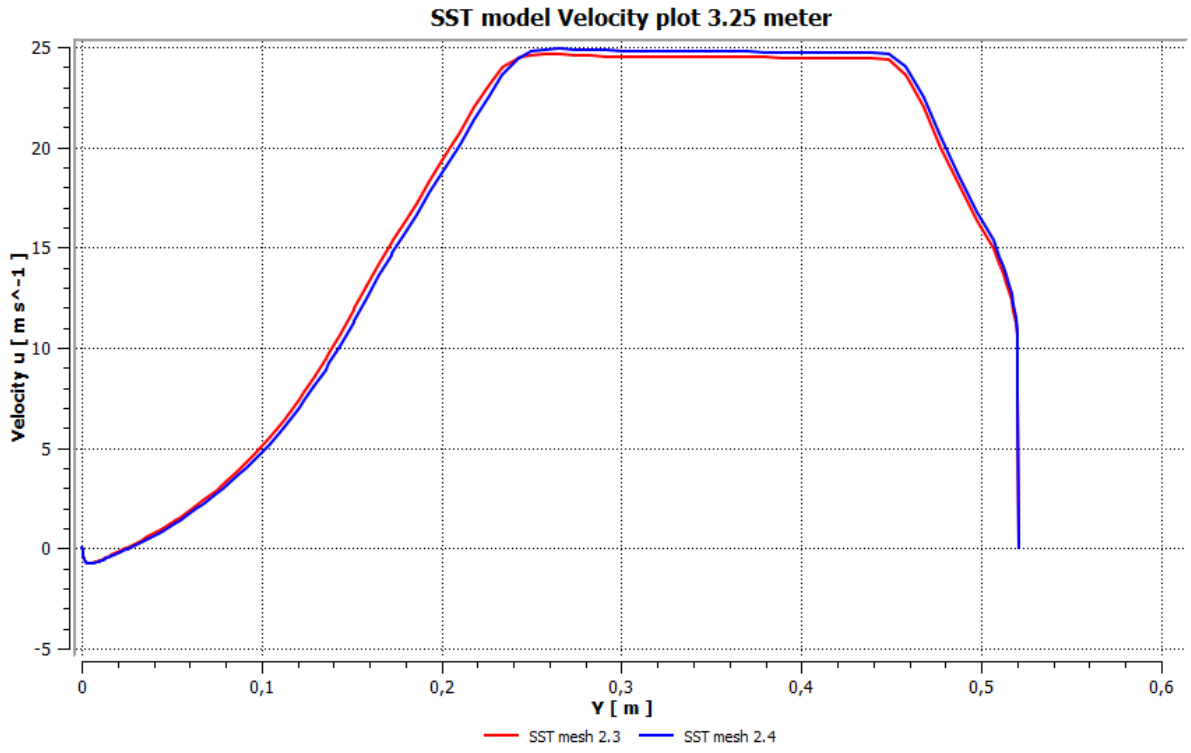
SST model Velocity plot 3.25 meter
Velocity u [m s^-1]
25
20
15
10
5
0
-5
0
0,1
0,2
0,3
0,4
0,5
0,6
Y [m]
SST mesh 2.3
SST mesh 2.4

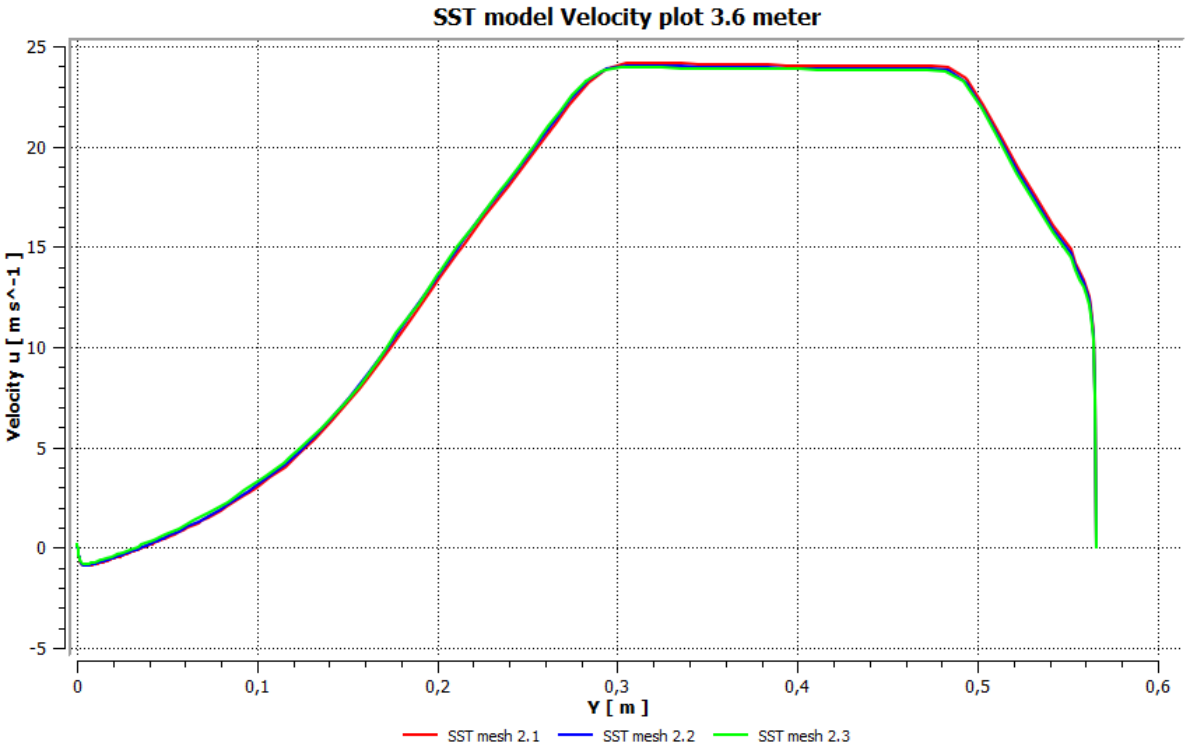
SST model Velocity plot 3.6 meter
Velocity u [m s^-1]
25
20
15
10
5
0
-5
0
0,1
0,2
0,3
0,4
0,5
0,6
Y [m]
SST mesh 2.1
SST mesh 2.2
SST mesh 2.3

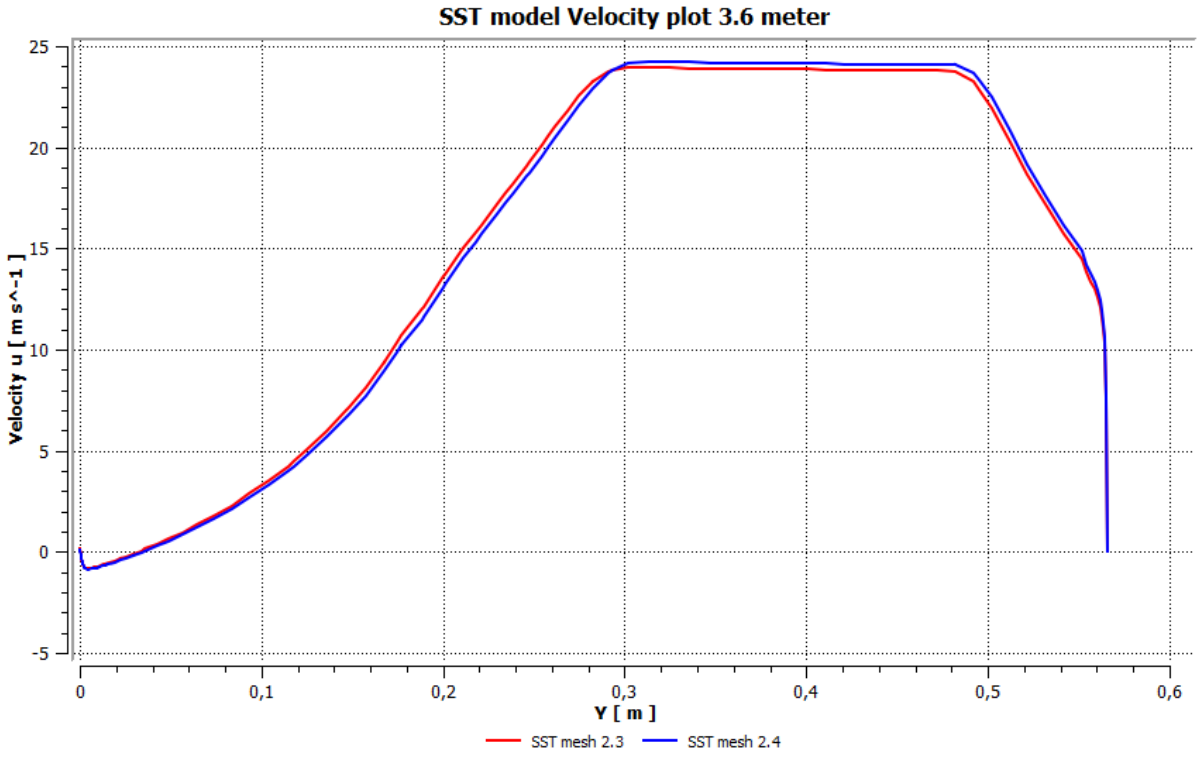

Standard k-ω model

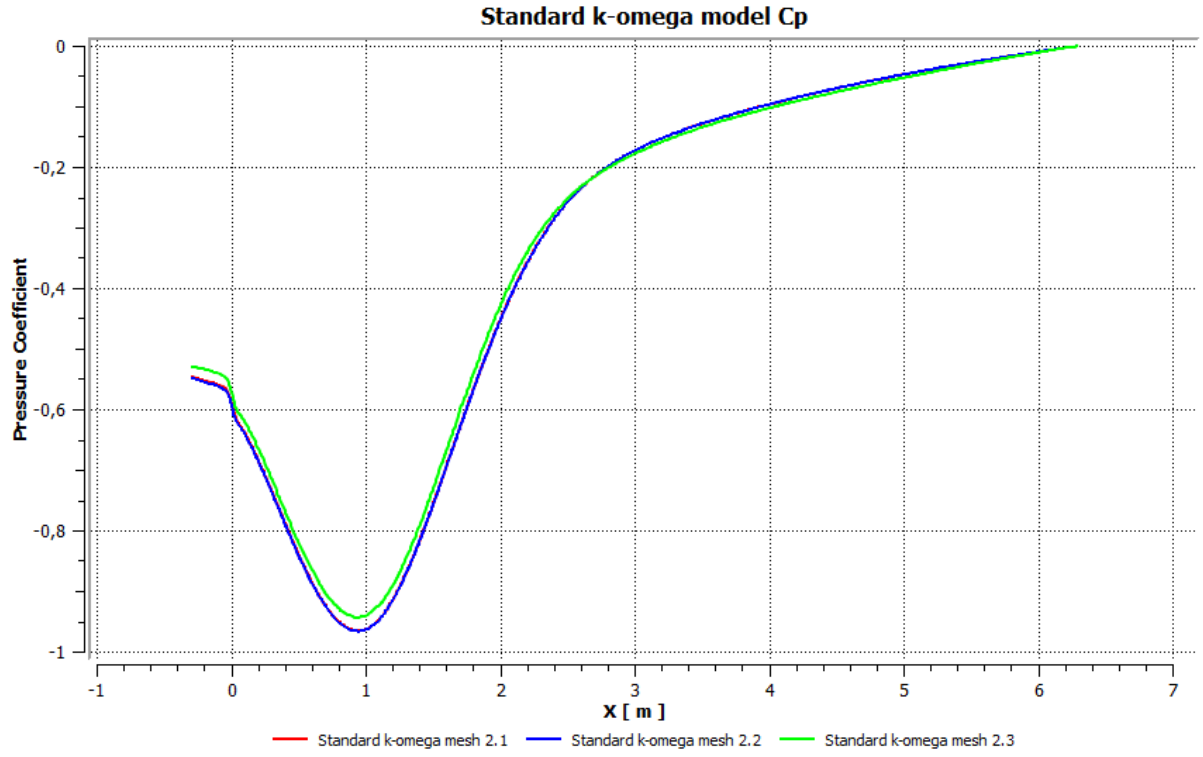

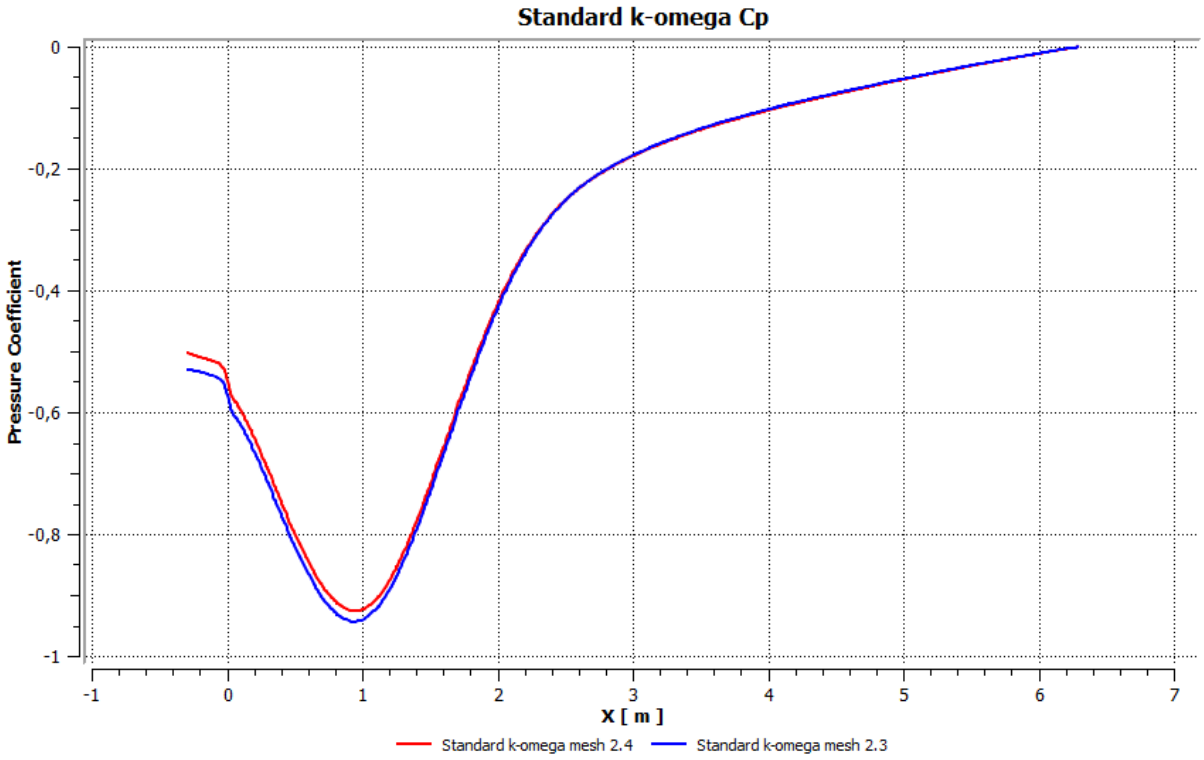
Standard k-omega Cp
Pressure Coefficient
0
-0,2
-0,4
-0,6
-0,8
-1
-1
0
1
2
3
4
5
6
7
X [m]
Standard k-omega mesh 2.4
Standard k-omega mesh 2.3

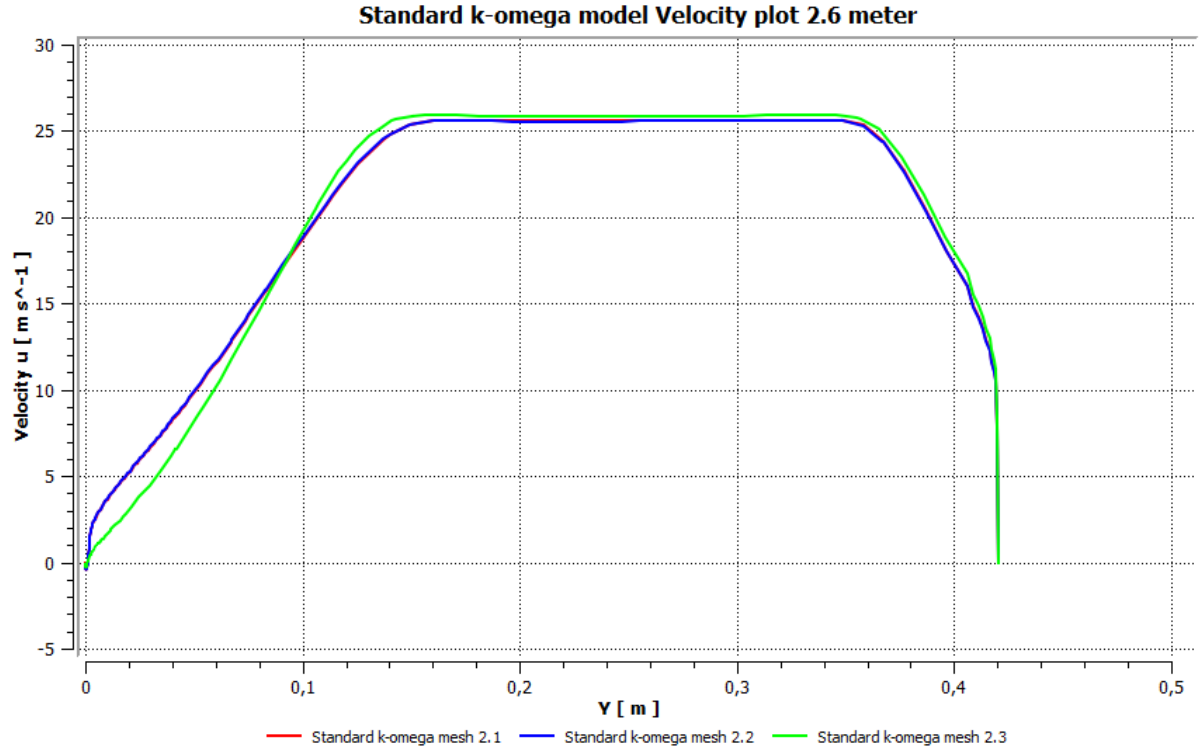
Standard k-omega model Velocity plot 2.6 meter
Velocity u [m s^-1]
30
25
20
15
10
5
0
-5
0
0,1
0,2
0,3
0,4
0,5
Y [m]
Standard k-omega mesh 2.1
Standard k-omega mesh 2.2
Standard k-omega mesh 2.3

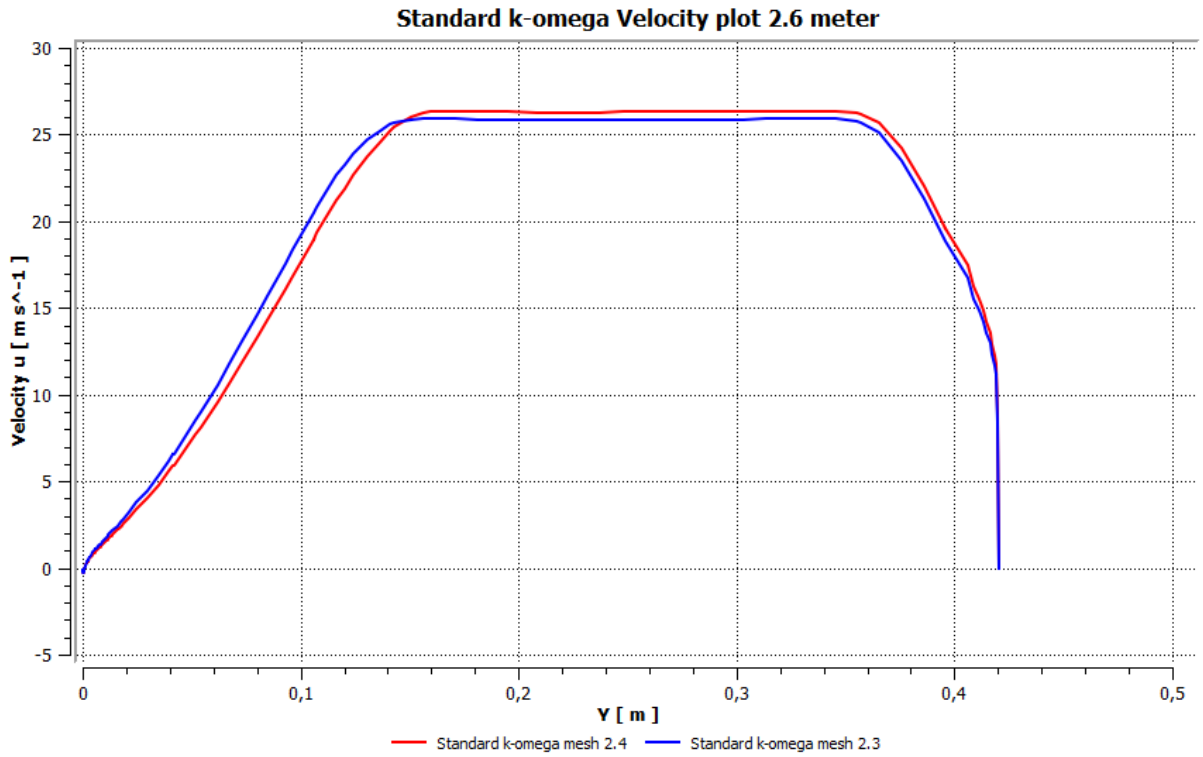
Standard k-omega Velocity plot 2.6 meter
Velocity u [m s^-1]
30
25
20
15
10
5
0
-5
0
0,1
0,2
0,3
0,4
0,5
Y [m]
Standard k-omega mesh 2.4
Standard k-omega mesh 2.3

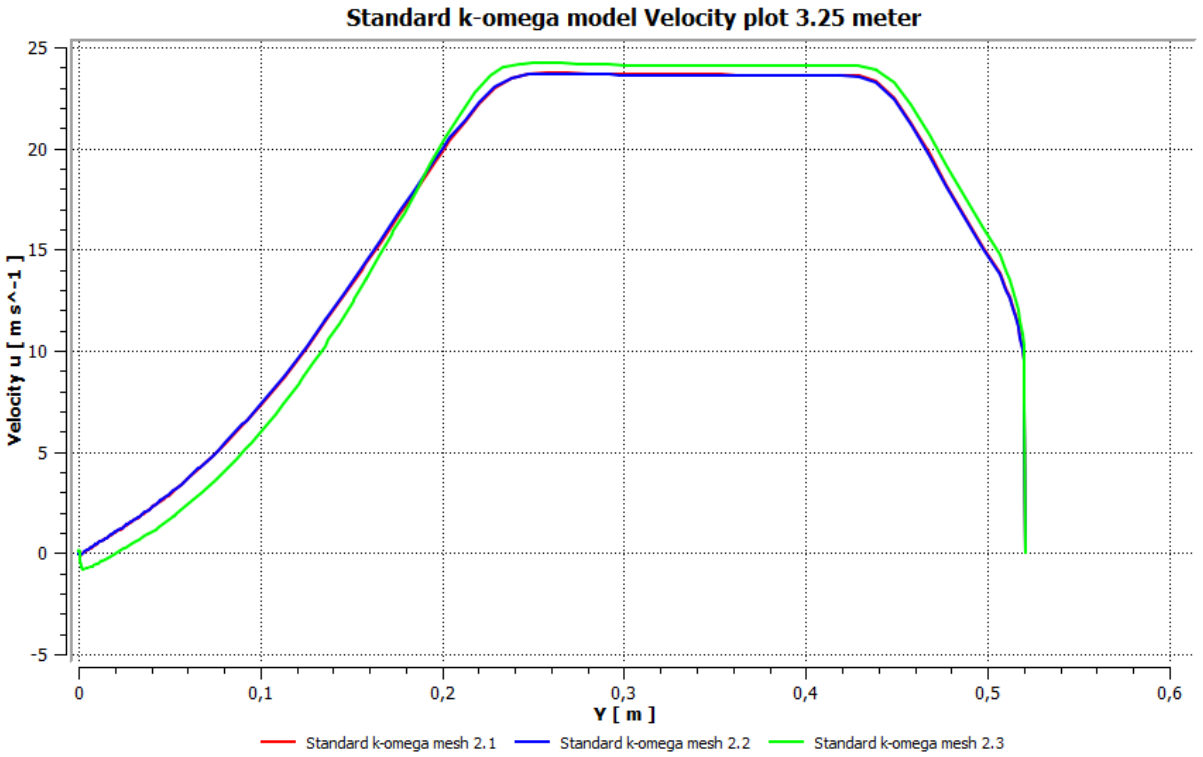
Standard k-omega model Velocity plot 3.25 meter
Velocity u [m s^-1]
25
20
15
10
5
0
-5
0
0,1
0,2
0,3
0,4
0,5
0,6
Y [m]
Standard k-omega mesh 2.1
Standard k-omega mesh 2.2
Standard k-omega mesh 2.3

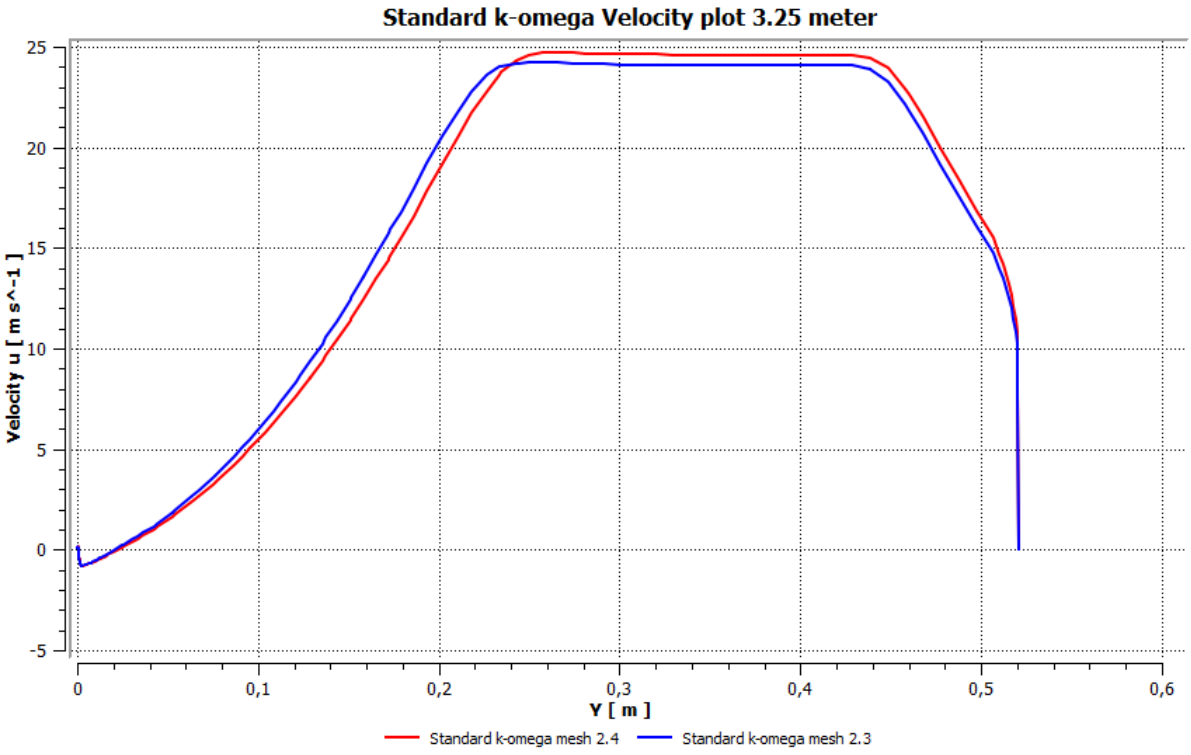
Standard k-omega Velocity plot 3.25 meter
Velocity u [m s^-1]
25
20
15
10
5
0
-5
0
0,1
0,2
0,3
0,4
0,5
0,6
Y [m]
Standard k-omega mesh 2.4
Standard k-omega mesh 2.3

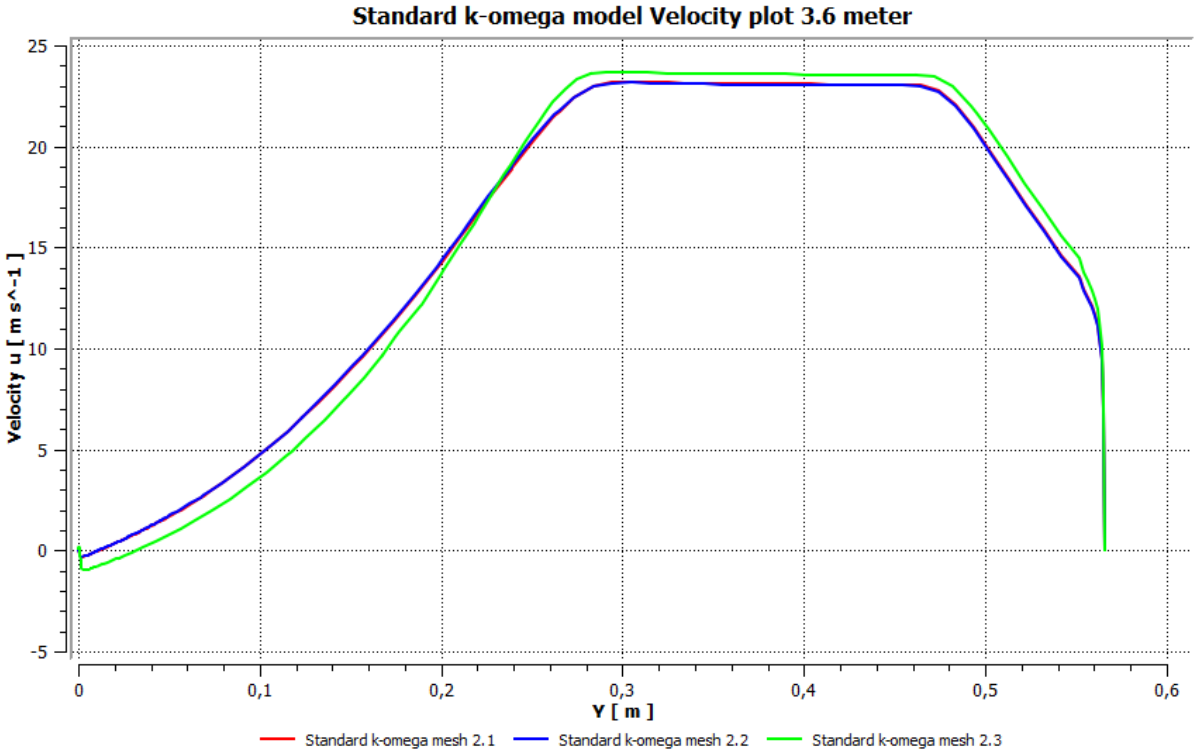
Standard k-omega model Velocity plot 3.6 meter
Velocity u [m s^-1]
25
20
15
10
5
0
-5
0
0,1
0,2
0,3
0,4
0,5
0,6
Y [m]
Standard k-omega mesh 2.1
Standard k-omega mesh 2.2
Standard k-omega mesh 2.3

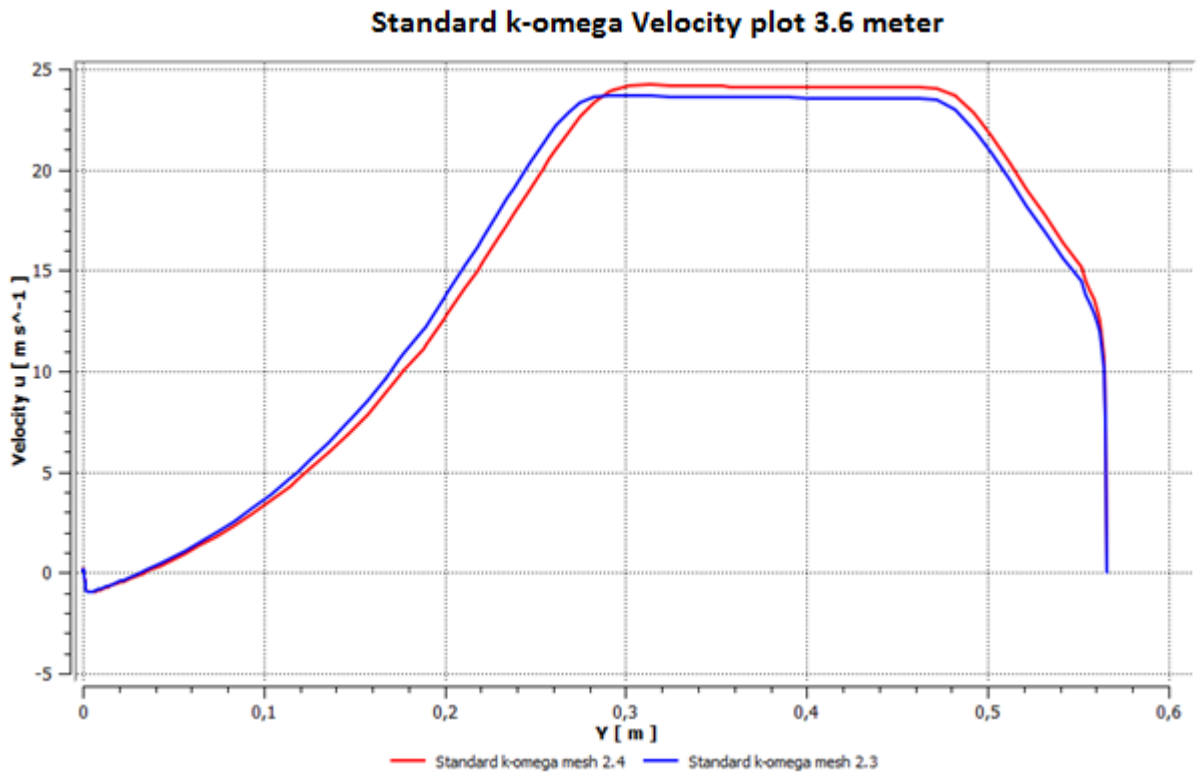
Standard k-omega Velocity plot 3.6 meter
Velocity u [m s^-1]
25
20
15
10
5
0
-5
0
0,1
0,2
0,3
0,4
0,5
0,6
Y [m]
Standard k-omega mesh 2.4
Standard k-omega mesh 2.3

K-ε RNG model

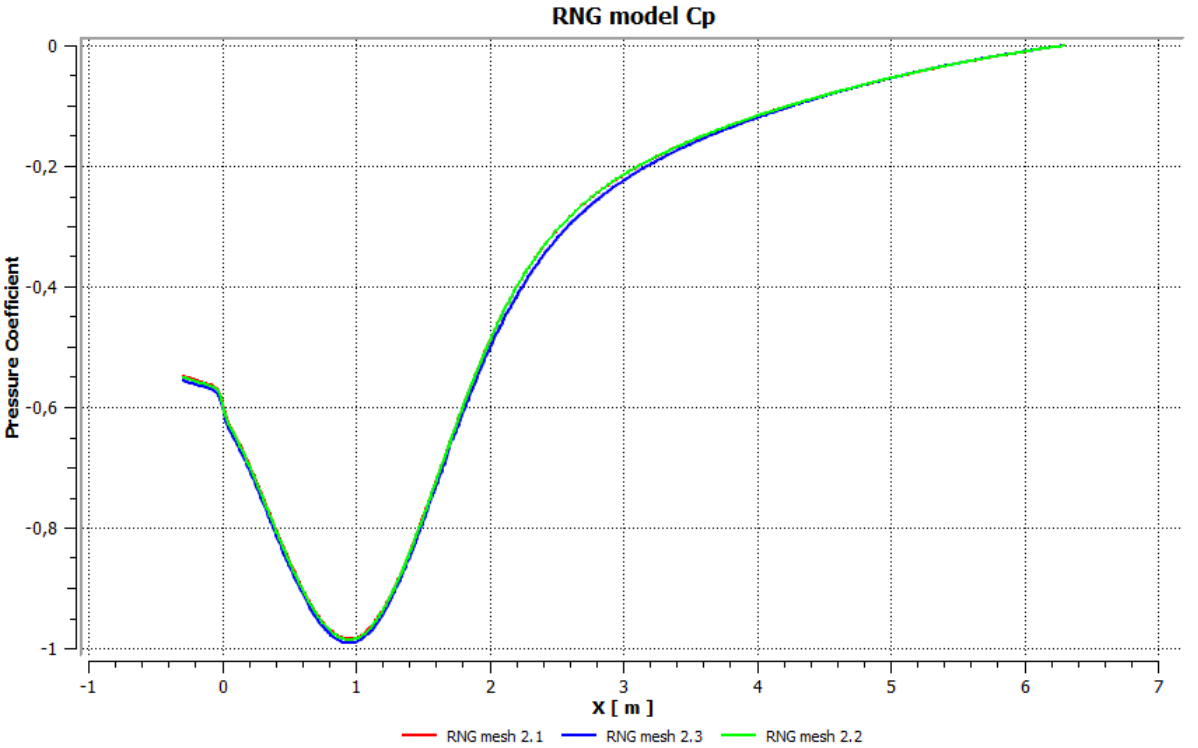
RNG model Cp
Pressure Coefficient
0
-0,2
-0,4
-0,6
-0,8
-1
-1
0
1
2
3
4
5
6
7
X [m]
RNG mesh 2.1
RNG mesh 2.3
RNG mesh 2.2

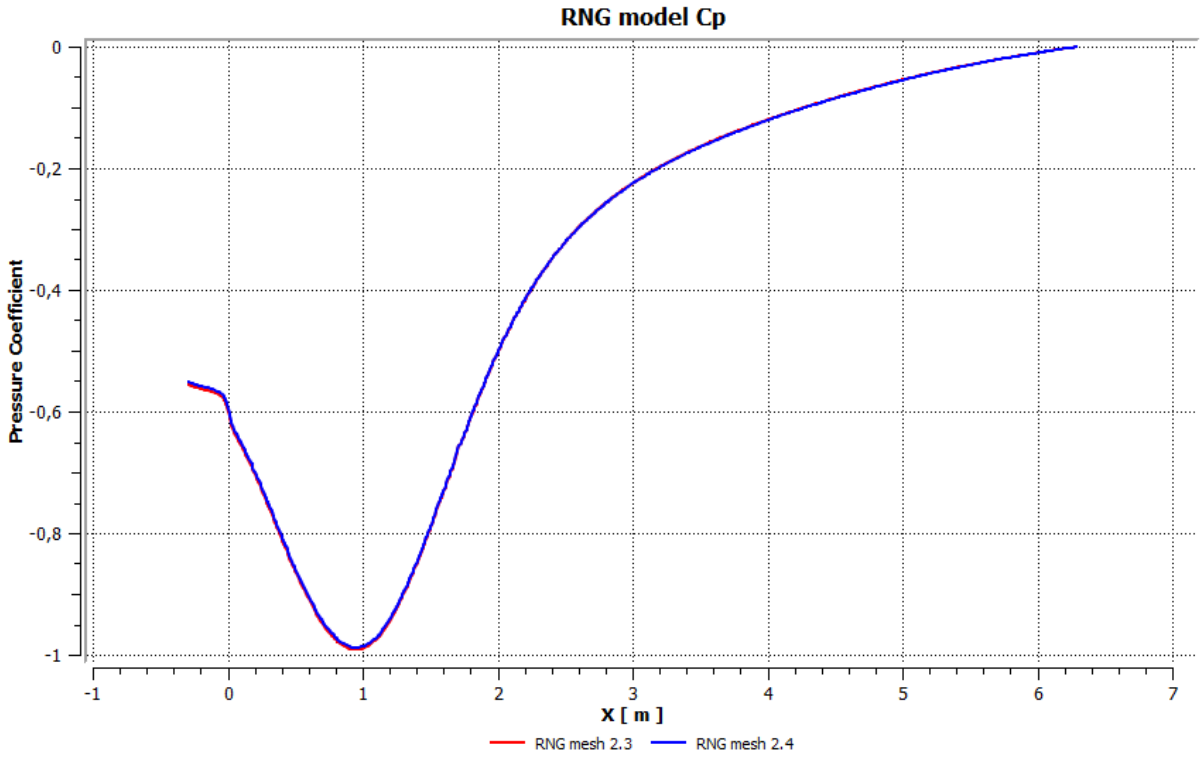
RNG model Cp
Pressure Coefficient
0
-0,2
-0,4
-0,6
-0,8
-1
-1
0
1
2
3
4
5
6
7
X [m]
RNG mesh 2.3
RNG mesh 2.4

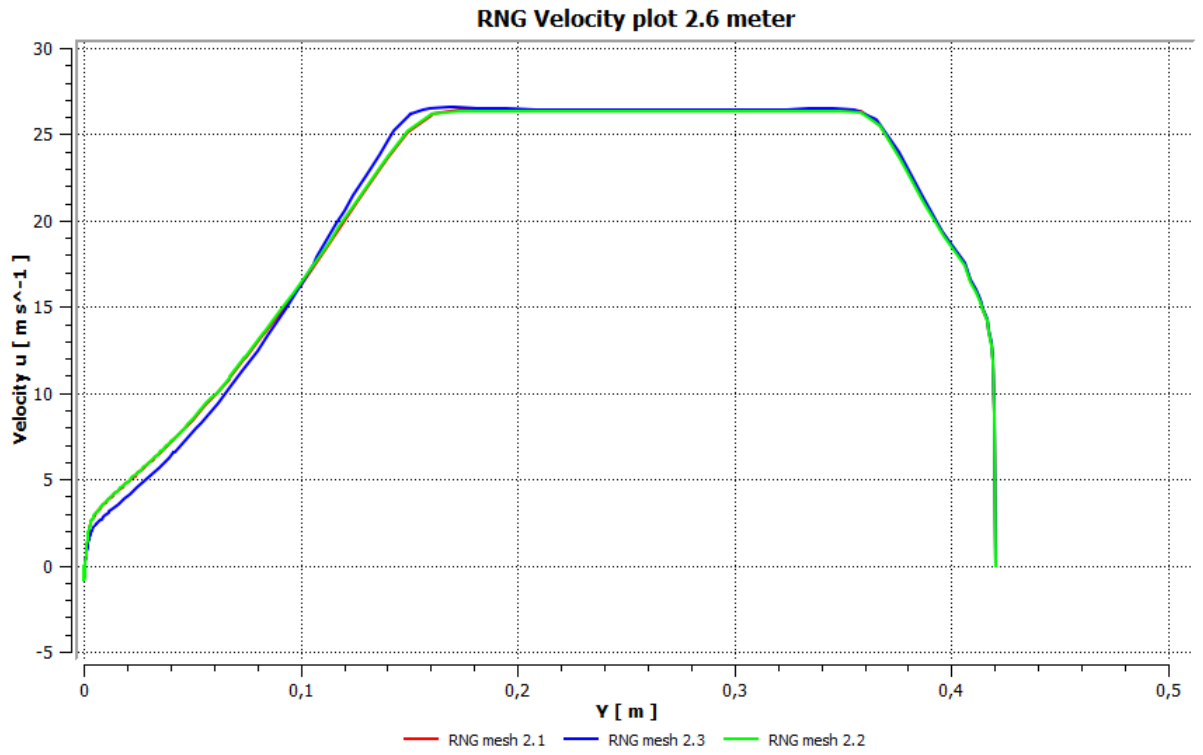
RNG Velocity plot 2.6 meter
Velocity u [m s^-1]
30
25
20
15
10
5
0
-5
0
0,1
0,2
0,3
0,4
0,5
Y [m]
RNG mesh 2.1
RNG mesh 2.3
RNG mesh 2.2

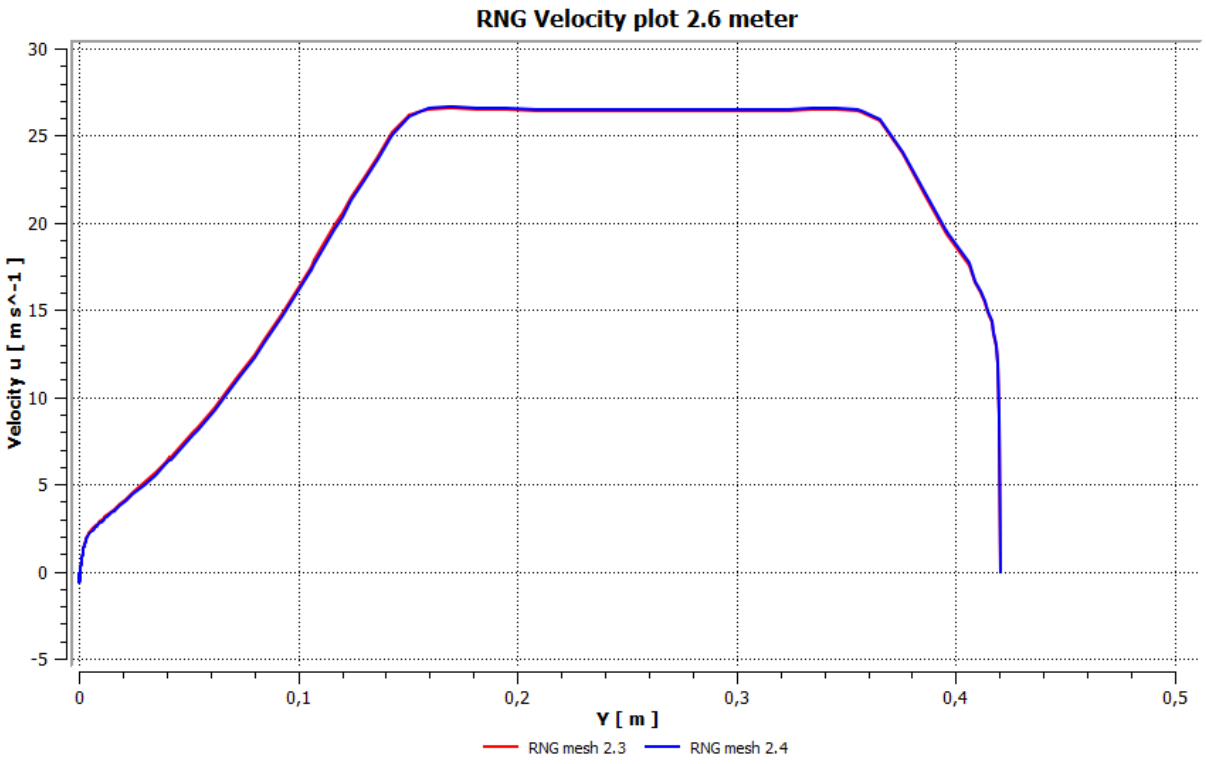
RNG Velocity plot 2.6 meter
Velocity u [m s^-1]
30
25
20
15
10
5
0
-5
0
0,1
0,2
0,3
0,4
0,5
Y [m]
RNG mesh 2.3
RNG mesh 2.4

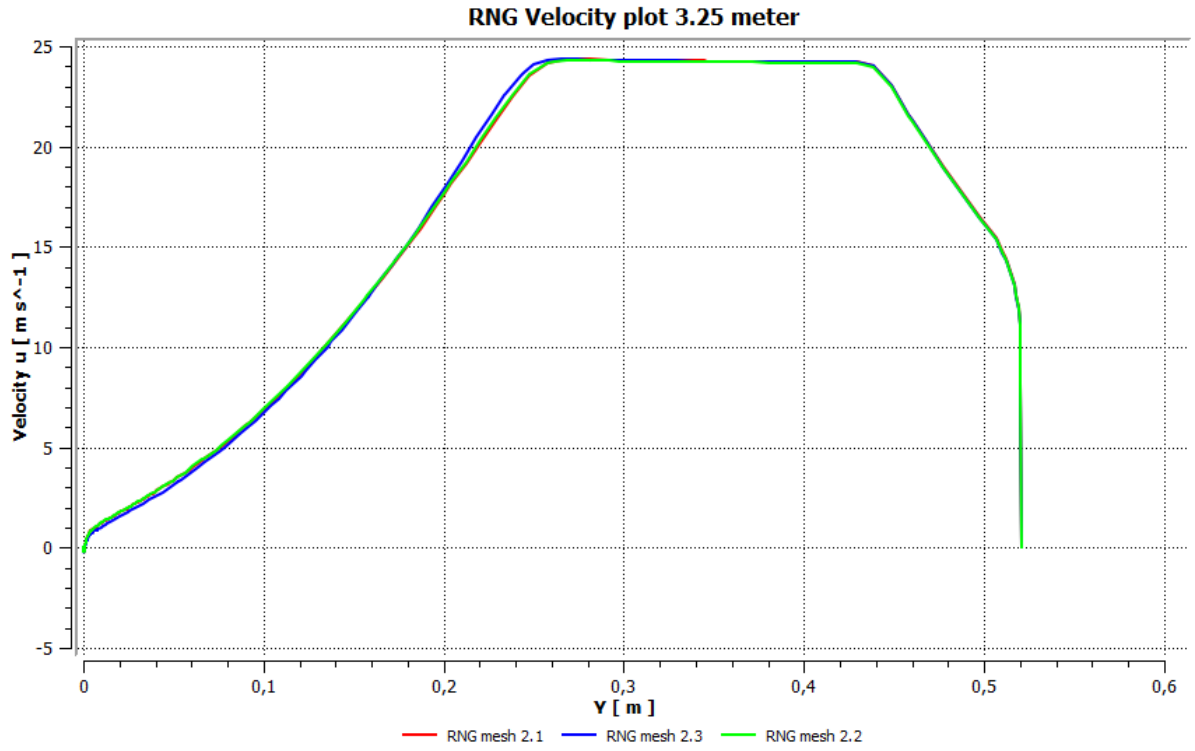
RNG Velocity plot 3.25 meter
Velocity u [m s^-1]
25
20
15
10
5
0
-5
0
0,1
0,2
0,3
0,4
0,5
0,6
Y [m]
RNG mesh 2.1
RNG mesh 2.3
RNG mesh 2.2

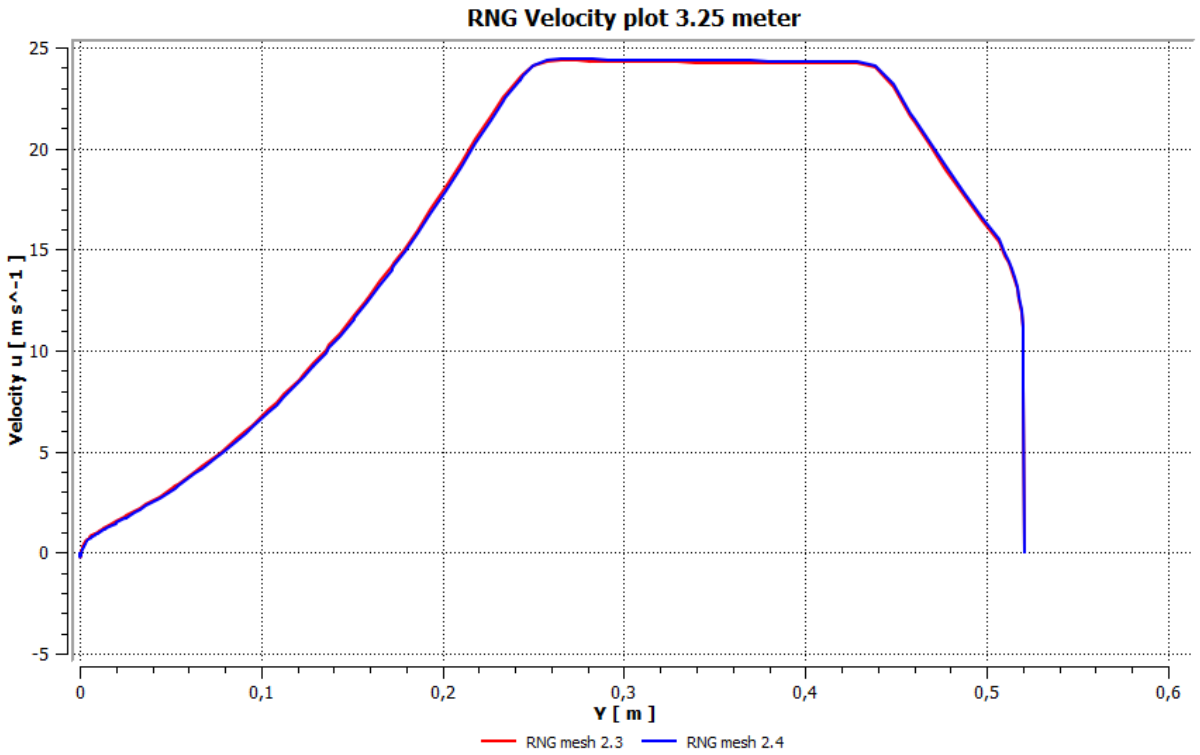
RNG Velocity plot 3.25 meter
Velocity u [m s^-1]
25
20
15
10
5
0
-5
0
0,1
0,2
0,3
0,4
0,5
0,6
Y [m]
RNG mesh 2.3
RNG mesh 2.4

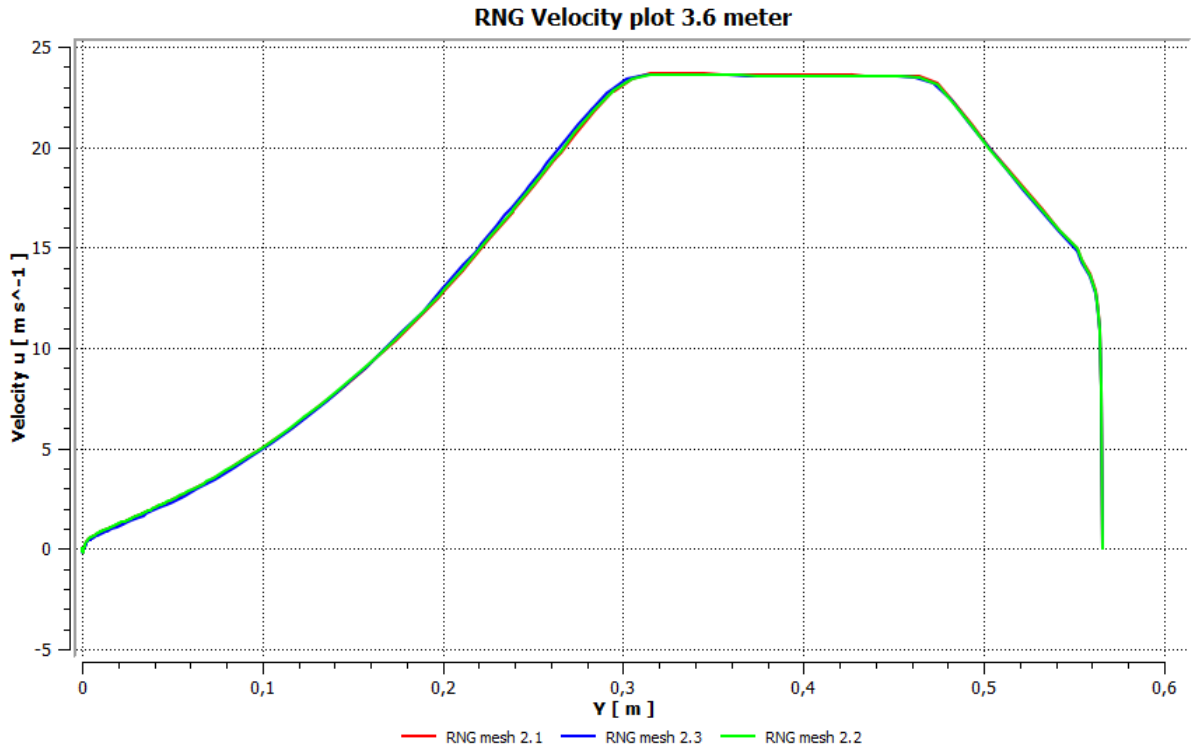
RNG Velocity plot 3.6 meter
Velocity u [m s^-1]
25
20
15
10
5
0
-5
0
0,1
0,2
0,3
0,4
0,5
0,6
Y [m]
RNG mesh 2.1
RNG mesh 2.3
RNG mesh 2.2

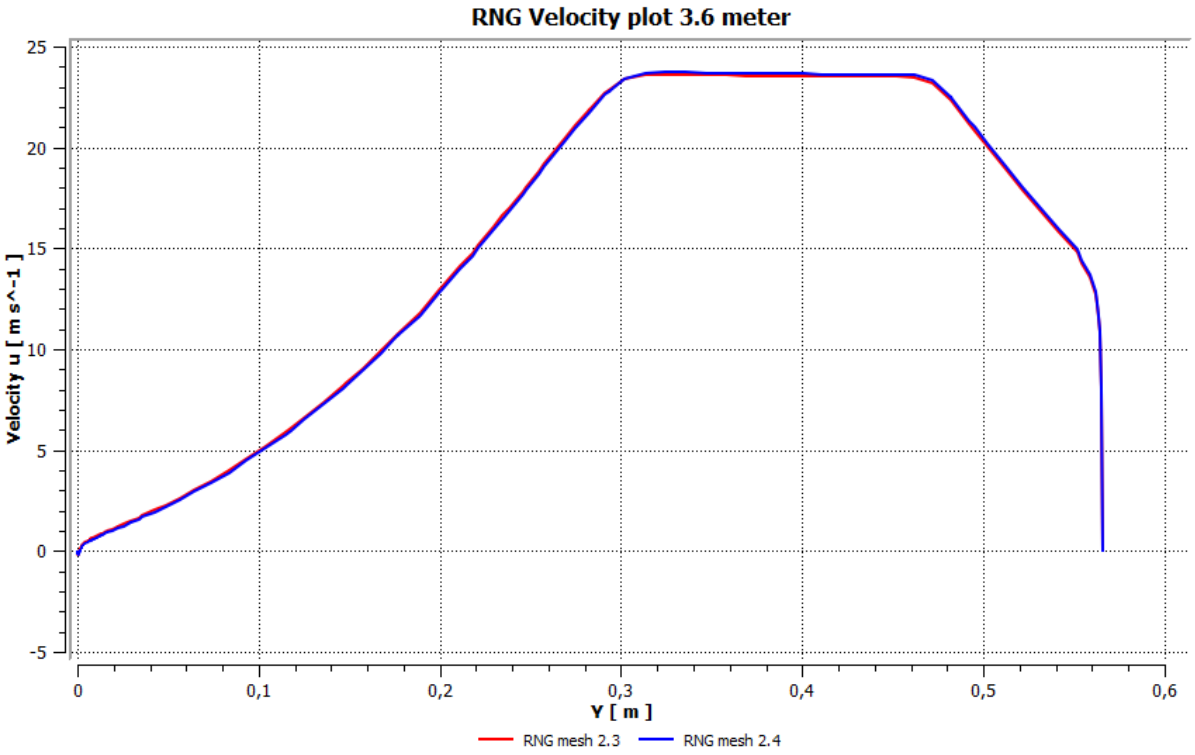

K-ε Realizable model

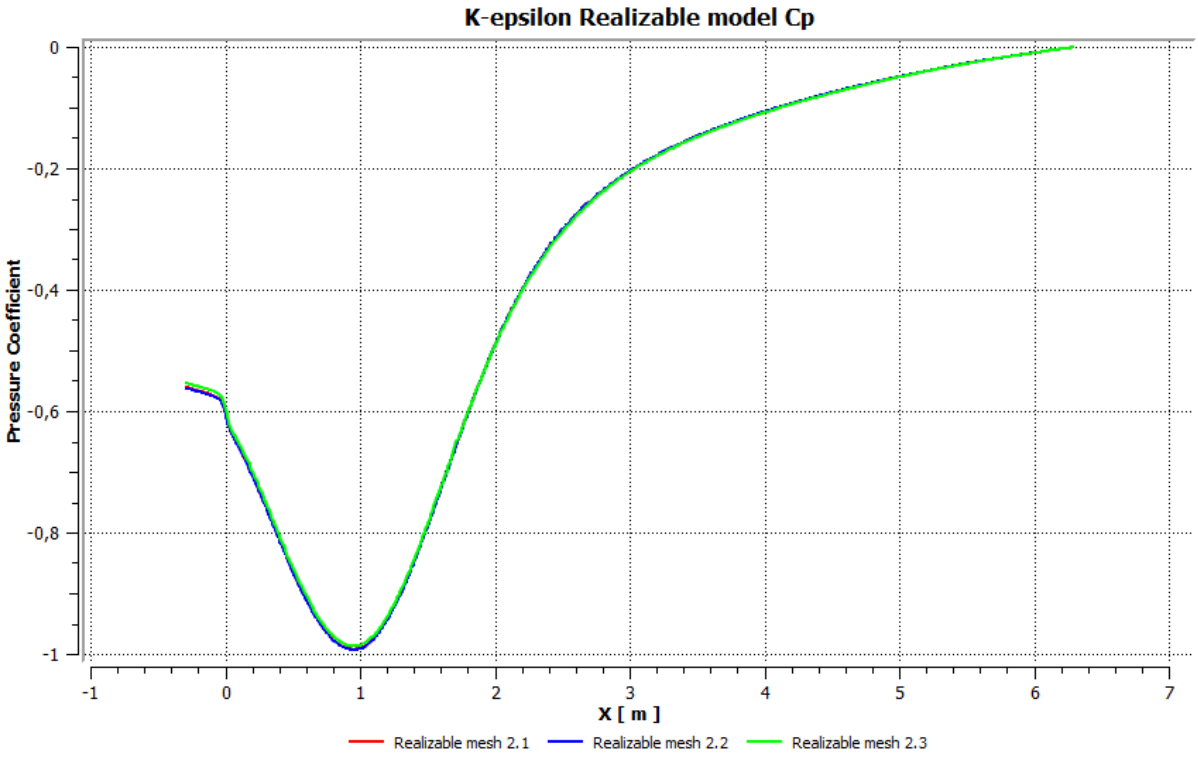

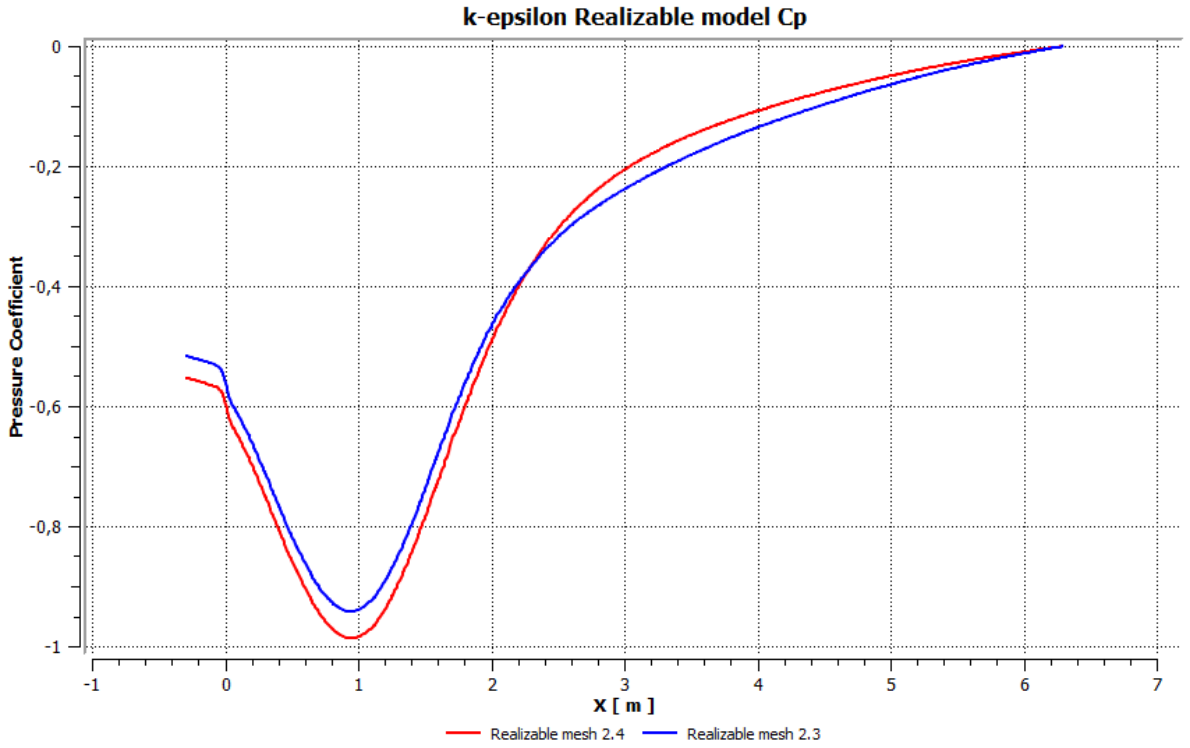
k-epsilon Realizable model Cp
Pressure Coefficient
0
-0,2
-0,4
-0,6
-0,8
-1
-1
0
1
2
3
4
5
6
7
X [m]
Realizable mesh 2.4
Realizable mesh 2.3

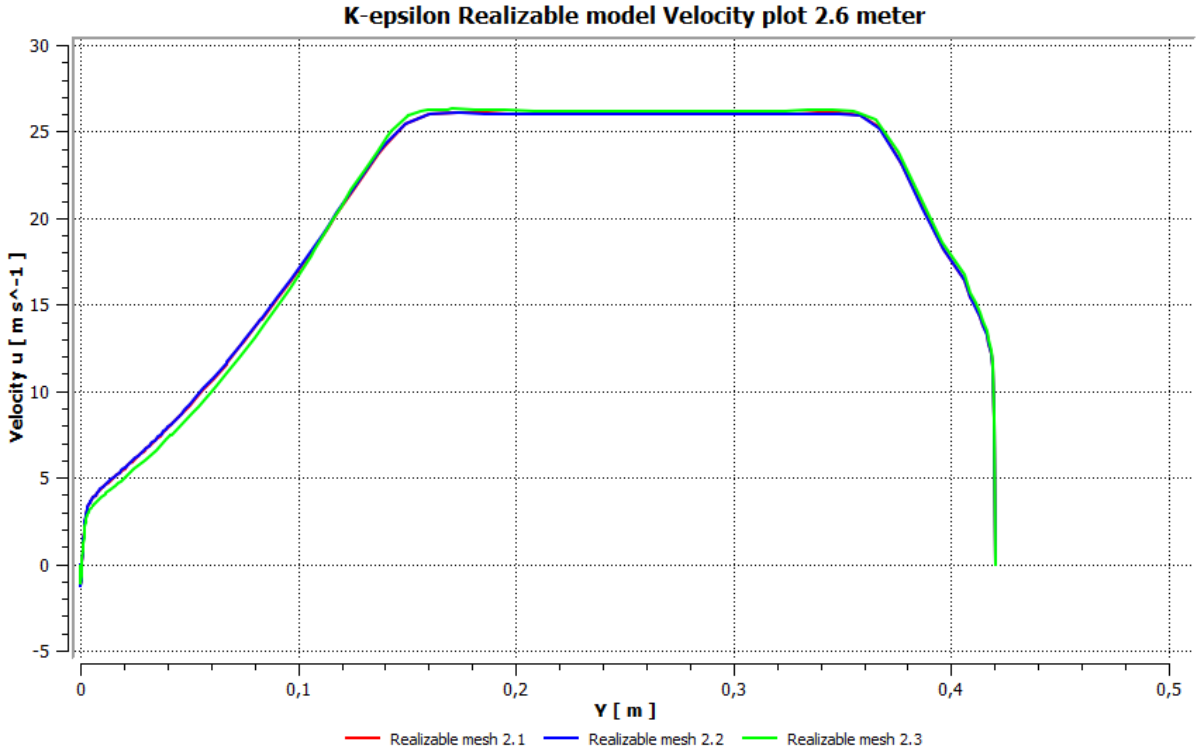
K-epsilon Realizable model Velocity plot 2.6 meter
Velocity u [m s^-1]
30
25
20
15
10
5
0
-5
0
0,1
0,2
0,3
0,4
0,5
Y [m]
Realizable mesh 2.1
Realizable mesh 2.2
Realizable mesh 2.3

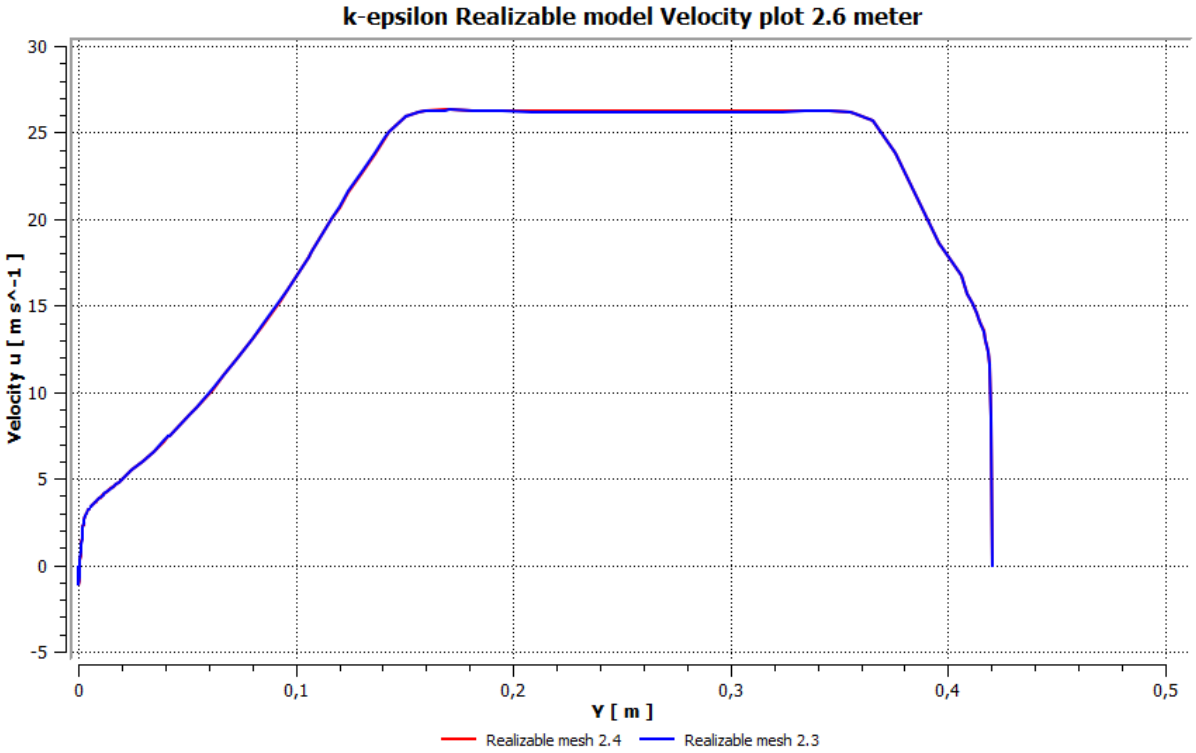
k-epsilon Realizable model Velocity plot 2.6 meter
Velocity u [m s^-1]
30
25
20
15
10
5
0
-5
0
0,1
0,2
0,3
0,4
0,5
Y [m]
Realizable mesh 2.4
Realizable mesh 2.3

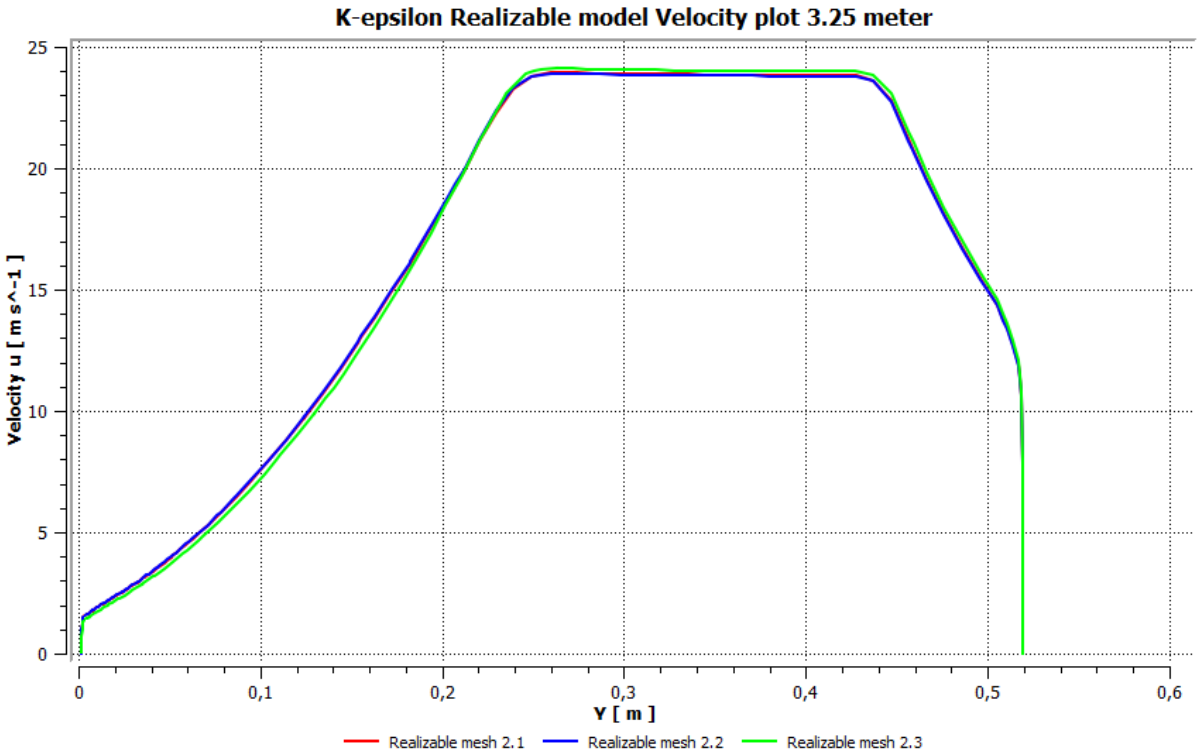
K-epsilon Realizable model Velocity plot 3.25 meter
Velocity u [m s^-1]
25
20
15
10
5
0
0
0,1
0,2
0,3
0,4
0,5
0,6
Y [m]
Realizable mesh 2.1
Realizable mesh 2.2
Realizable mesh 2.3

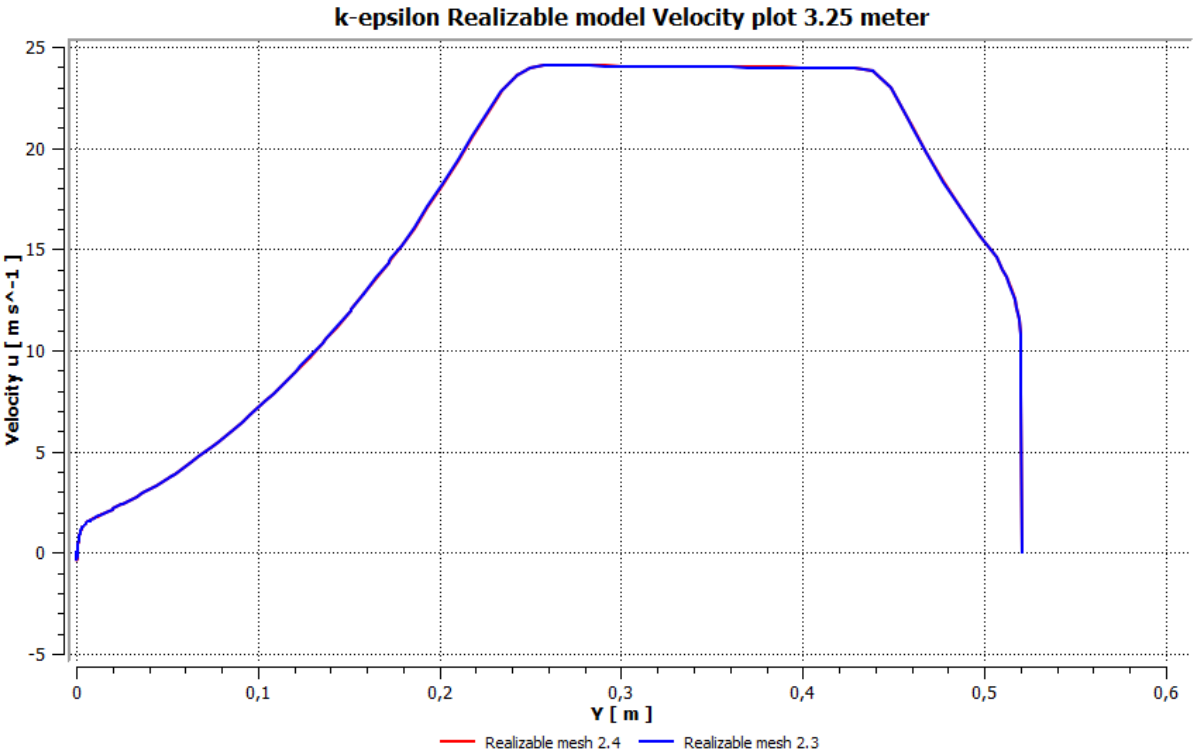
k-epsilon Realizable model Velocity plot 3.25 meter
Velocity u [m s^-1]
25
20
15
10
5
0
-5
0
0,1
0,2
0,3
0,4
0,5
0,6
Y [m]
Realizable mesh 2.4
Realizable mesh 2.3

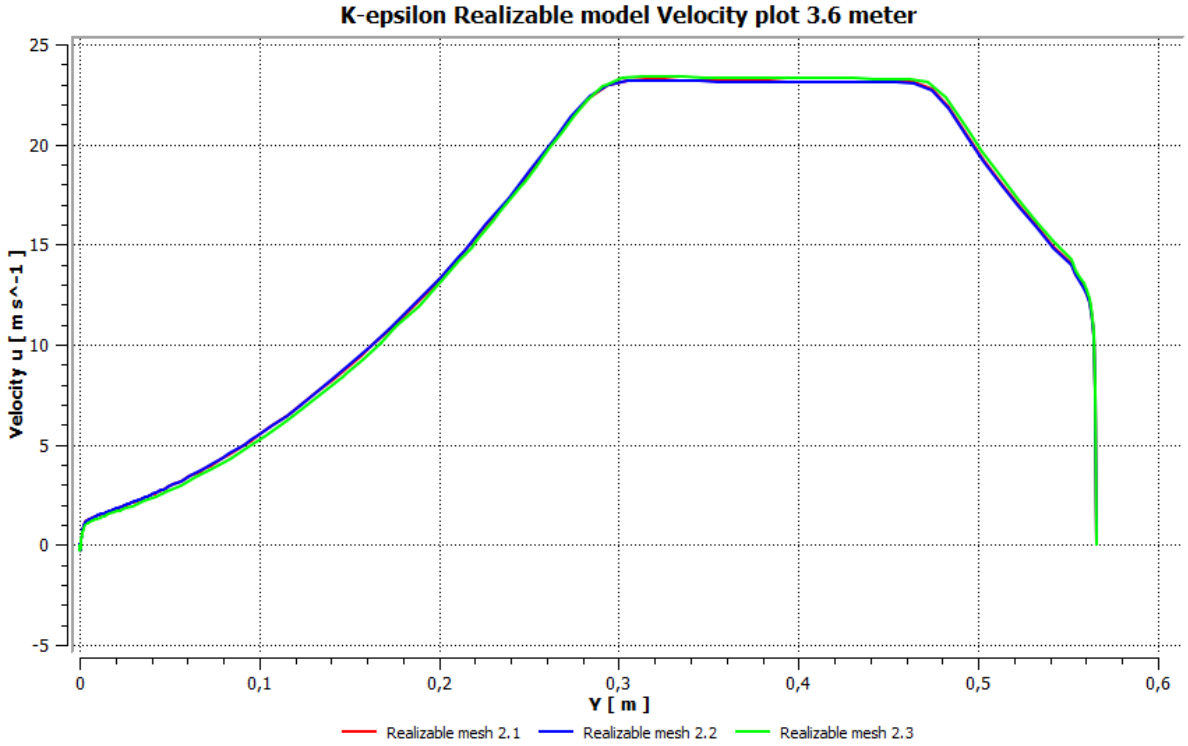
K-epsilon Realizable model Velocity plot 3.6 meter
Velocity u [m s^-1]
25
20
15
10
5
0
-5
0
0,1
0,2
0,3
0,4
0,5
0,6
Y [m]
Realizable mesh 2.1
Realizable mesh 2.2
Realizable mesh 2.3

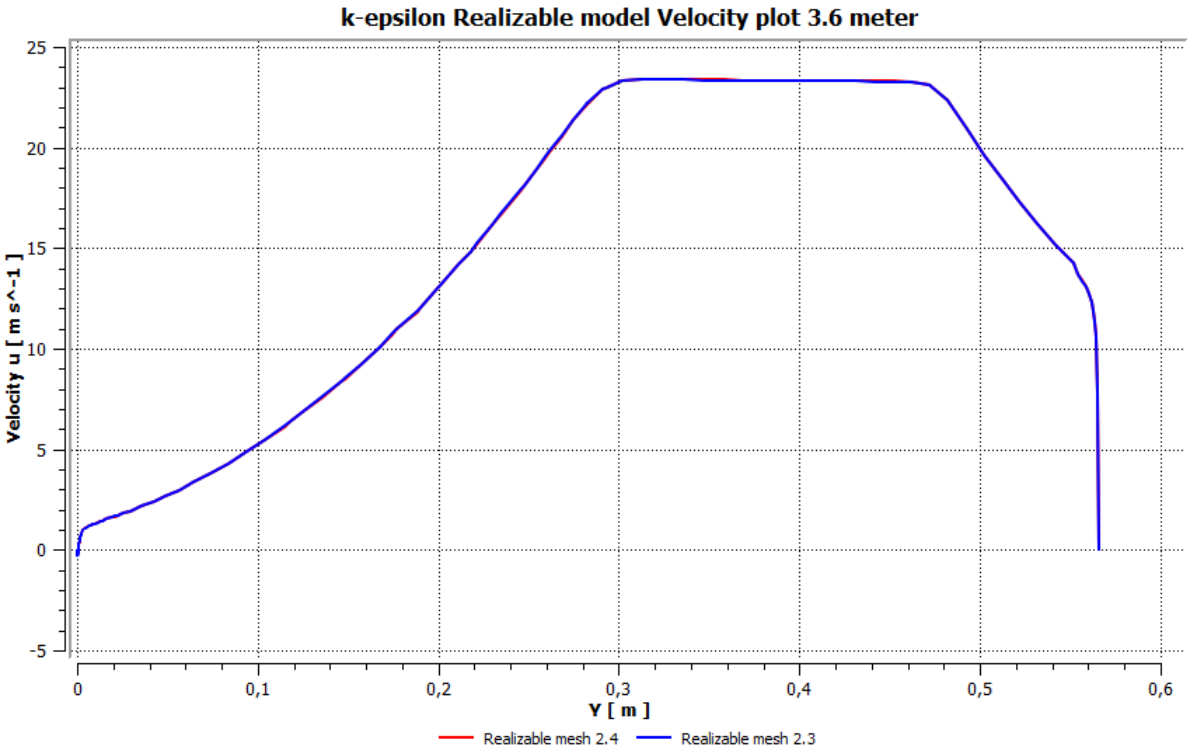
k-epsilon Realizable model Velocity plot 3.6 meter
Velocity u [m s^-1]
25
20
15
10
5
0
-5
0
0,1
0,2
0,3
0,4
0,5
0,6
Y [m]
Realizable mesh 2.4
Realizable mesh 2.3

RSM model

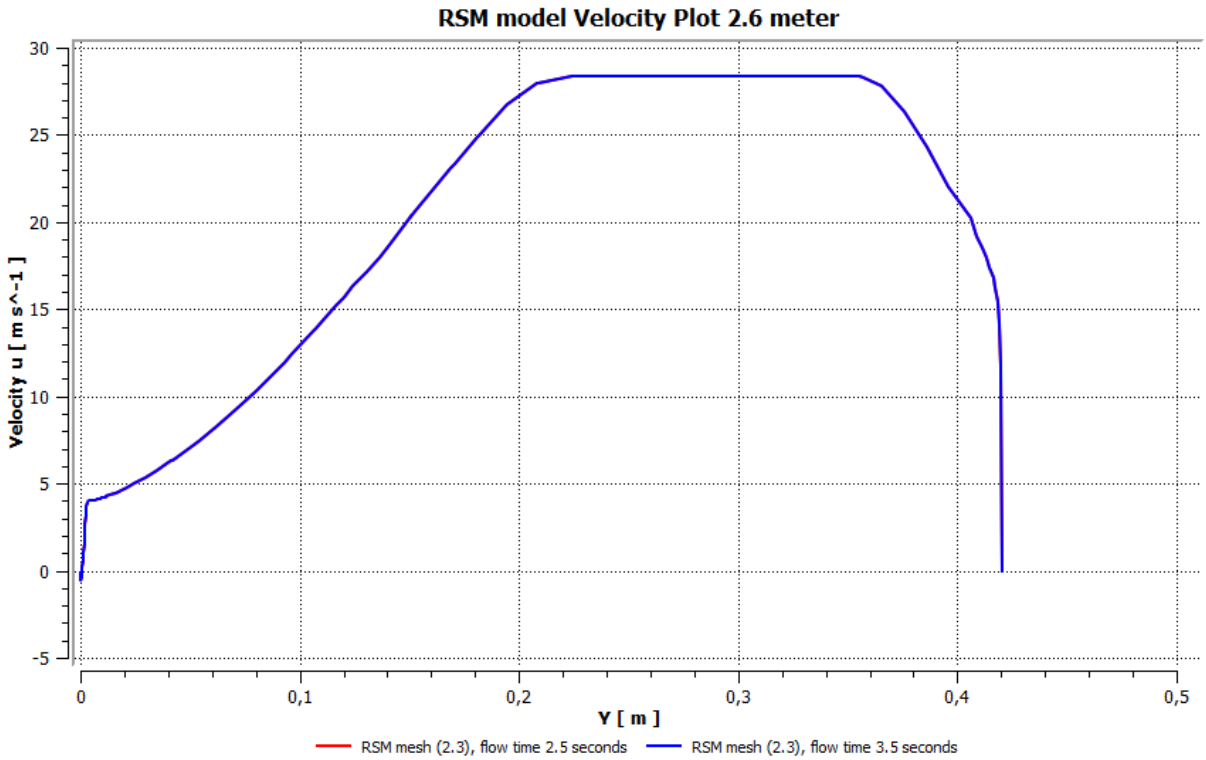
RSM model Velocity Plot 2.6 meter
Velocity u [m s^-1]
30
25
20
15
10
5
0
-5
0
0,1
0,2
0,3
0,4
0,5
Y [m]
RSM mesh (2.3), flow time 2.5 seconds
RSM mesh (2.3), flow time 3.5 seconds

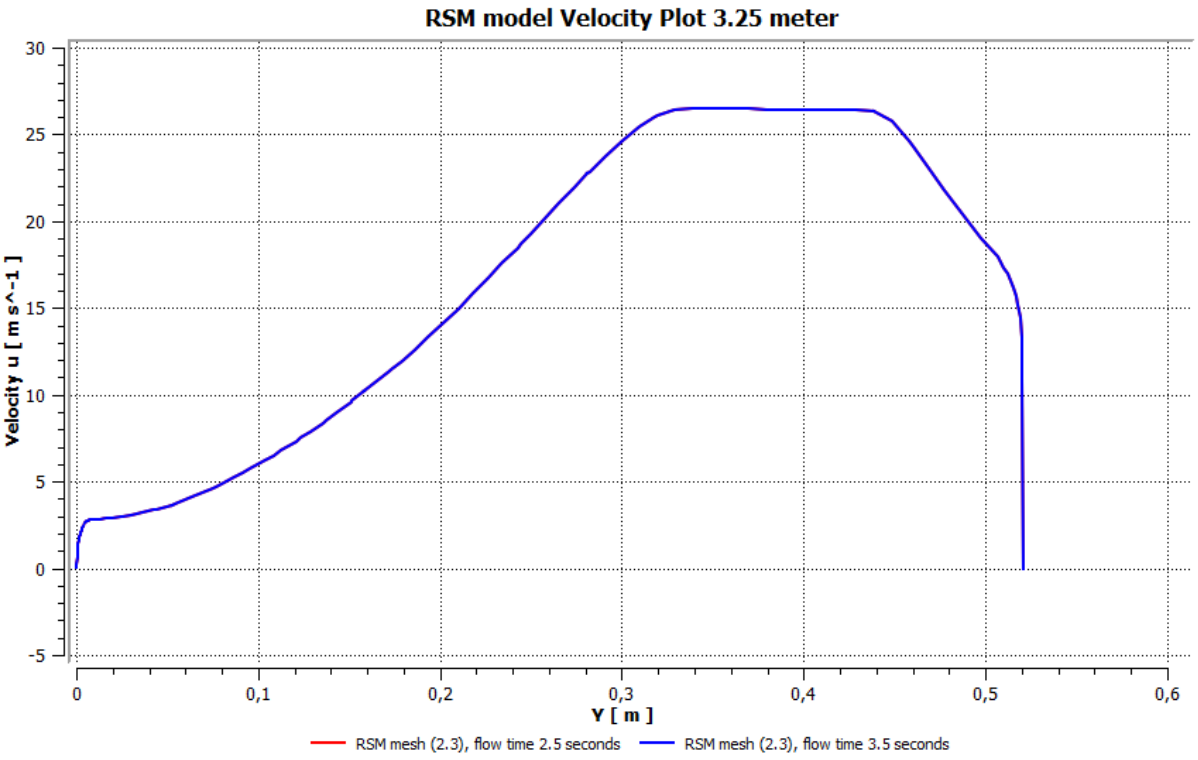
RSM model Velocity Plot 3.25 meter
Velocity u [m s^-1]
30
25
20
15
10
5
0
-5
0
0,1
0,2
0,3
0,4
0,5
0,6
Y [m]
RSM mesh (2.3), flow time 2.5 seconds
RSM mesh (2.3), flow time 3.5 seconds

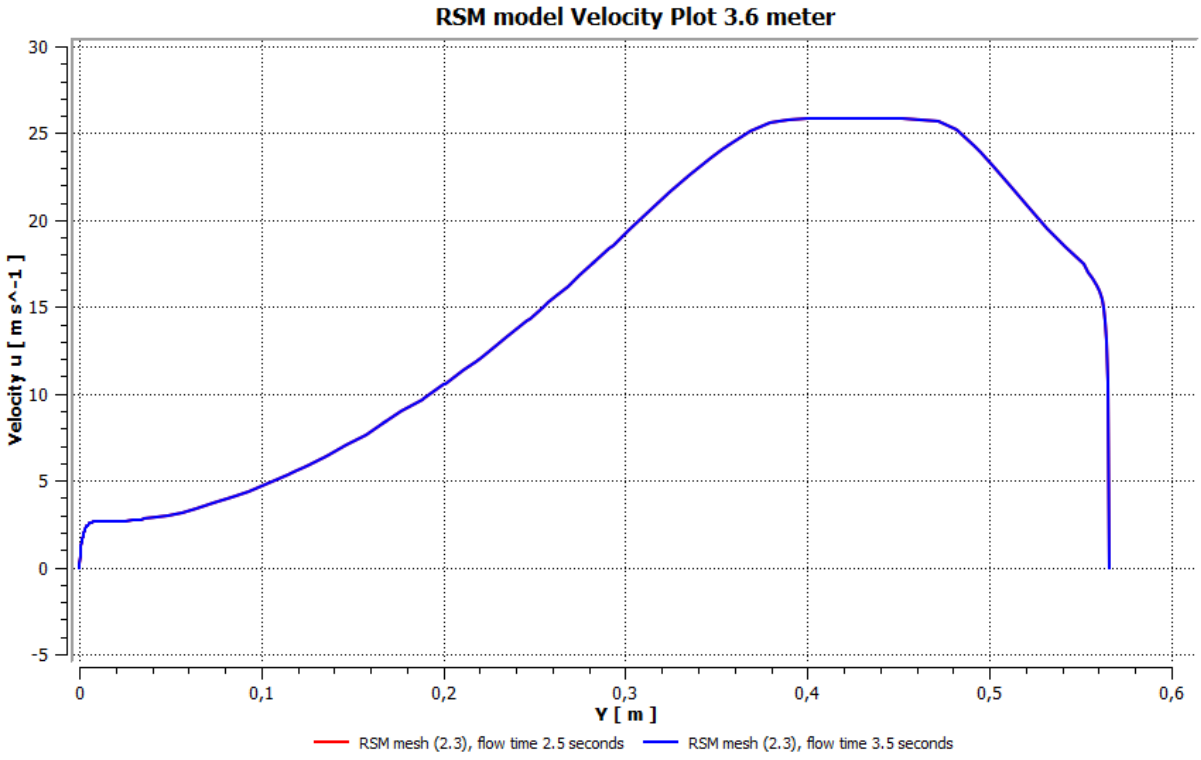
RSM model Velocity Plot 3.6 meter
Velocity u [m s^-1]
30
25
20
15
10
5
0
-5
0
0,1
0,2
0,3
0,4
0,5
0,6
Y [m]
RSM mesh (2.3), flow time 2.5 seconds
RSM mesh (2.3), flow time 3.5 seconds

Spalart –Allmaras model

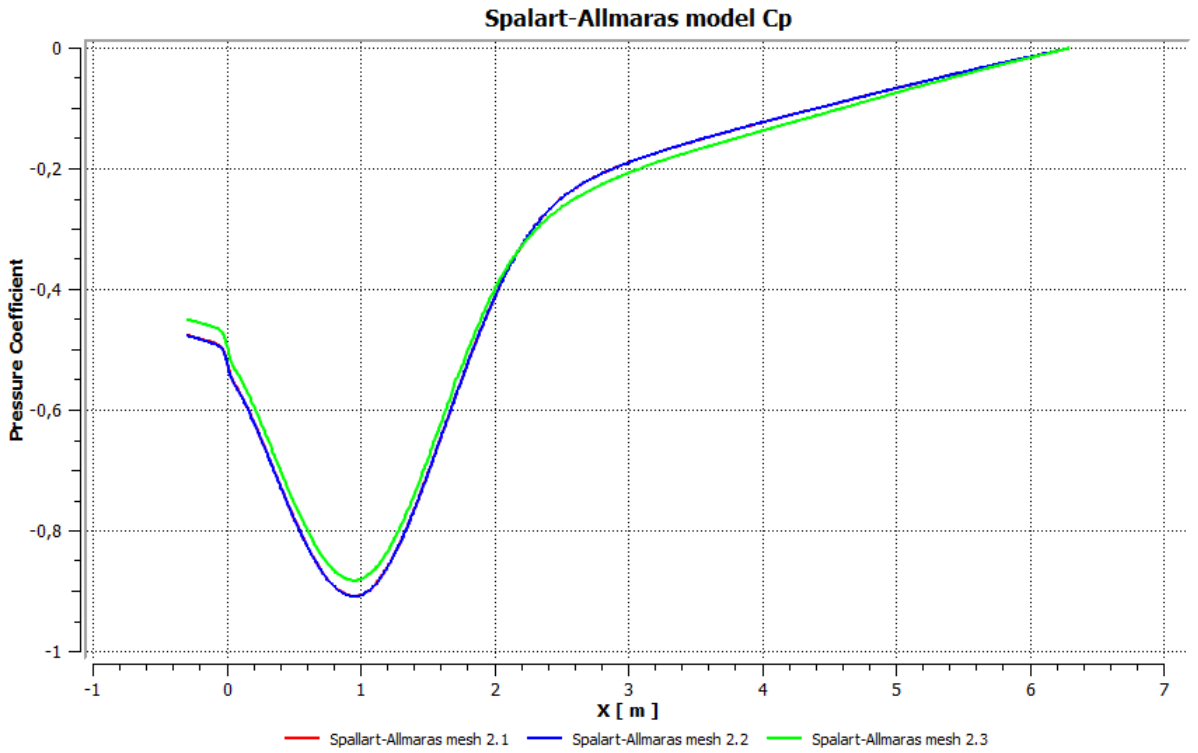

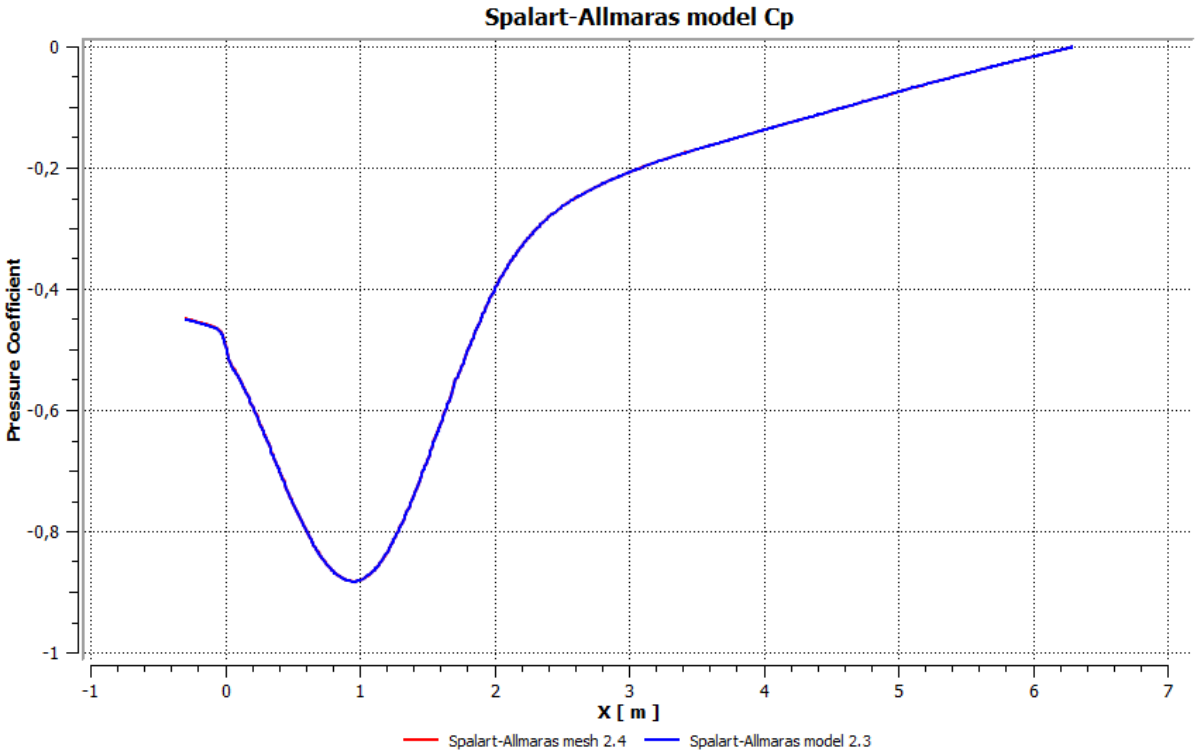

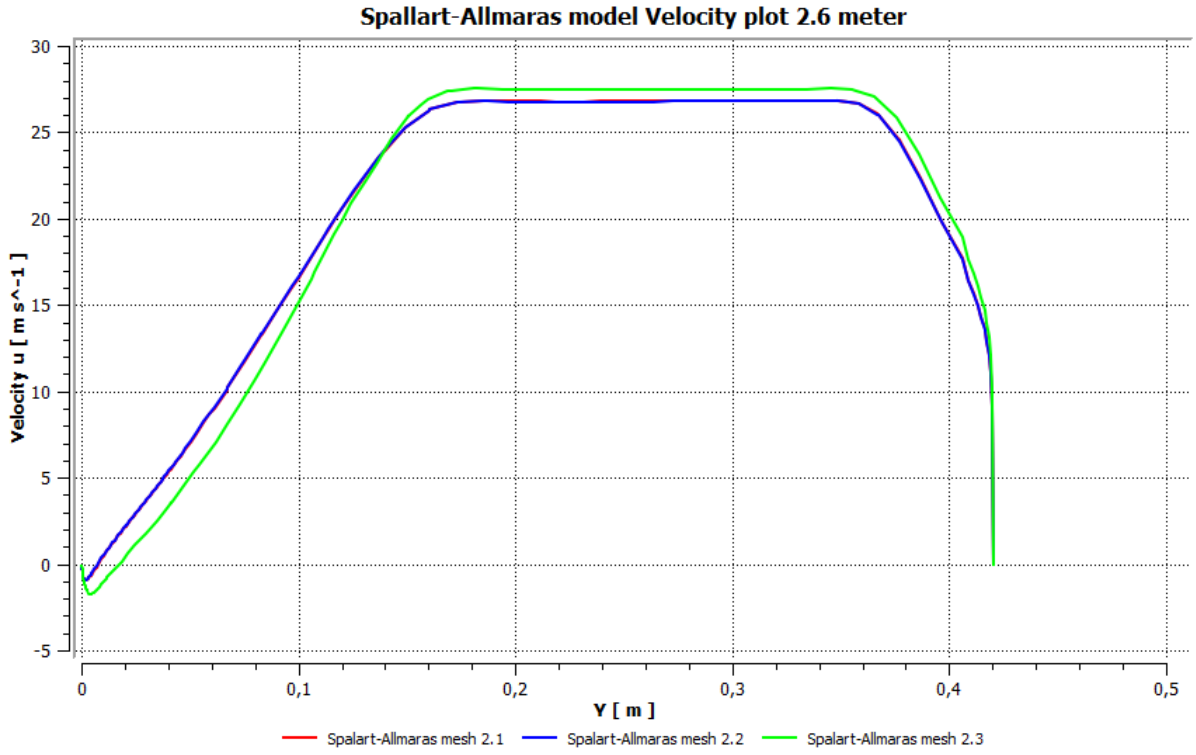
Spallart-Allmaras model Velocity plot 2.6 meter
Velocity u [m s^-1]
30
25
20
15
10
5
0
-5
0
0,1
0,2
0,3
0,4
0,5
Y [m]
Spalart-Allmaras mesh 2.1
Spalart-Allmaras mesh 2.2
Spalart-Allmaras mesh 2.3

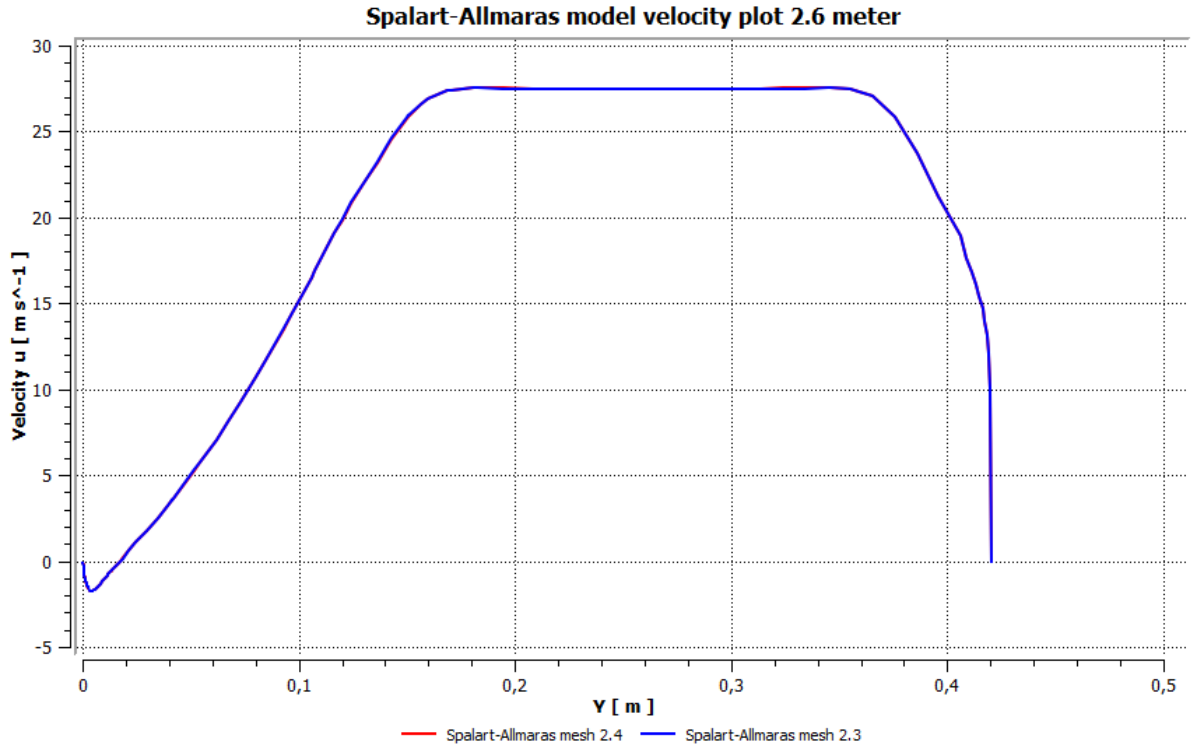
Spalart-Allmaras model velocity plot 2.6 meter
Velocity u [m s^-1]
30
25
20
15
10
5
0
-5
0
0,1
0,2
0,3
0,4
0,5
Y [m]
Spalart-Allmaras mesh 2.4
Spalart-Allmaras mesh 2.3

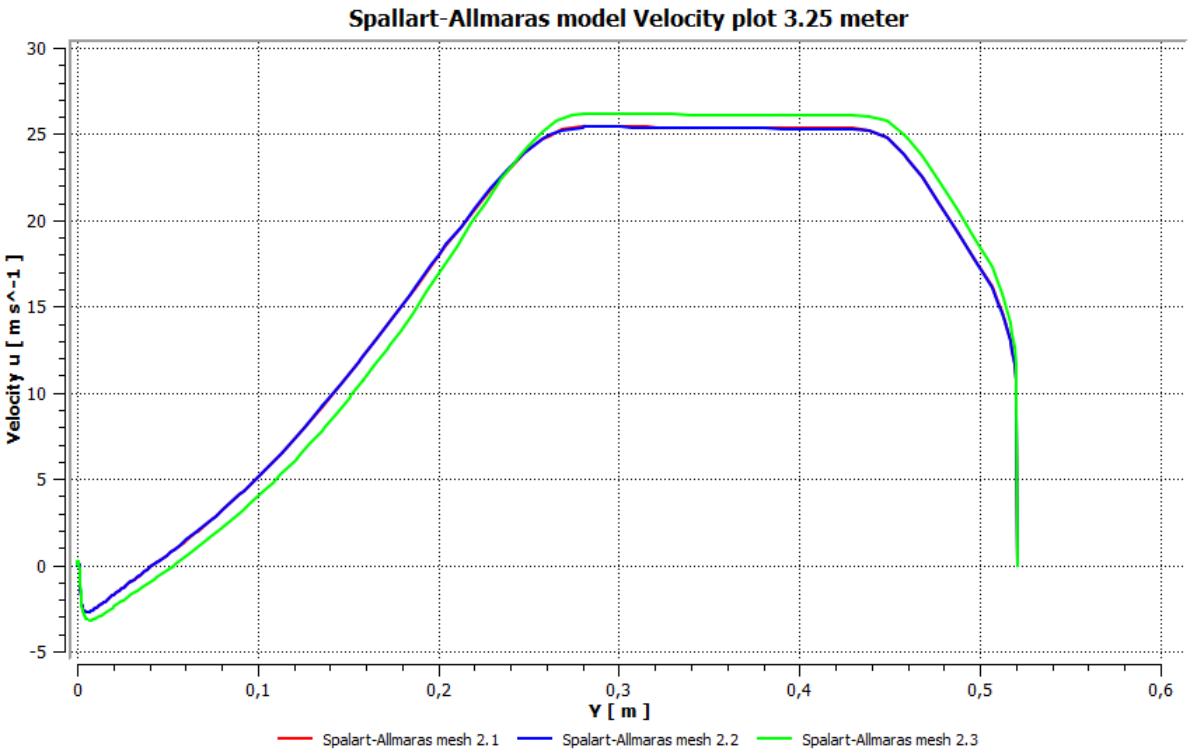
Spallart-Allmaras model Velocity plot 3.25 meter
Velocity u [m s^-1]
30
25
20
15
10
5
0
-5
0
0,1
0,2
0,3
0,4
0,5
0,6
Y [m]
Spalart-Allmaras mesh 2.1
Spalart-Allmaras mesh 2.2
Spalart-Allmaras mesh 2.3

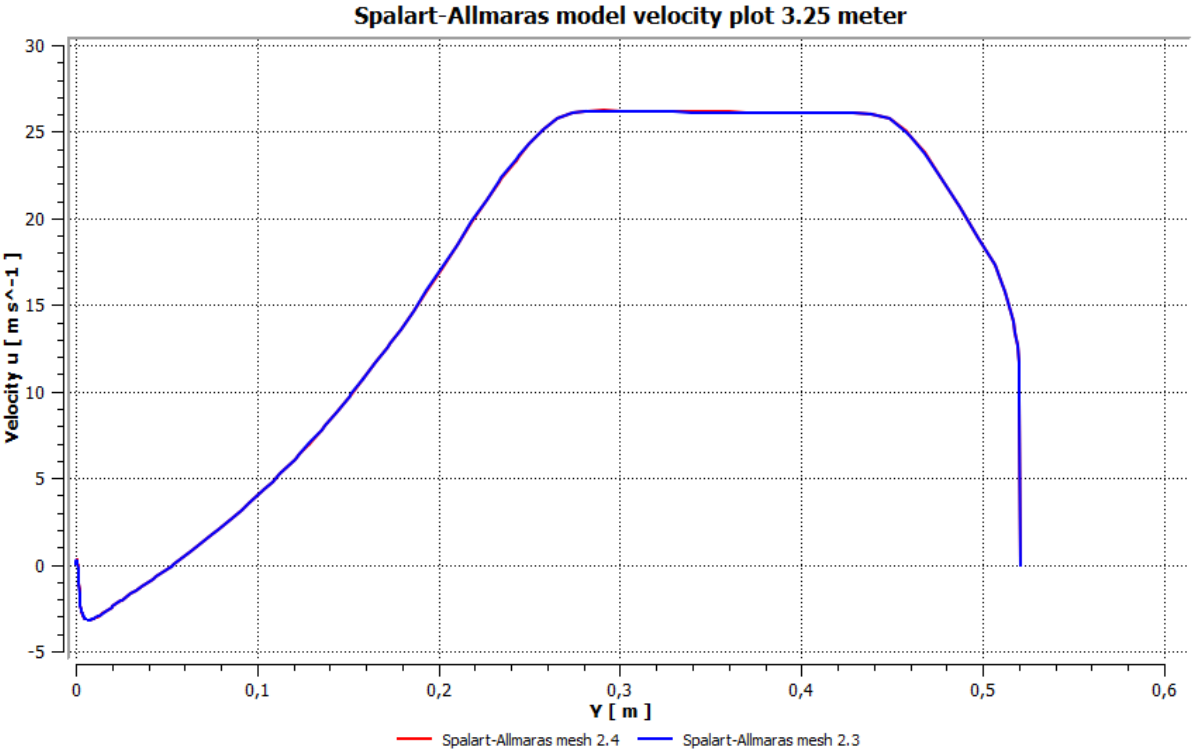
Spalart-Allmaras model velocity plot 3.25 meter
Velocity u [m s^-1]
30
25
20
15
10
5
0
-5
0
0,1
0,2
0,3
0,4
0,5
0,6
Y [m]
Spalart-Allmaras mesh 2.4
Spalart-Allmaras mesh 2.3

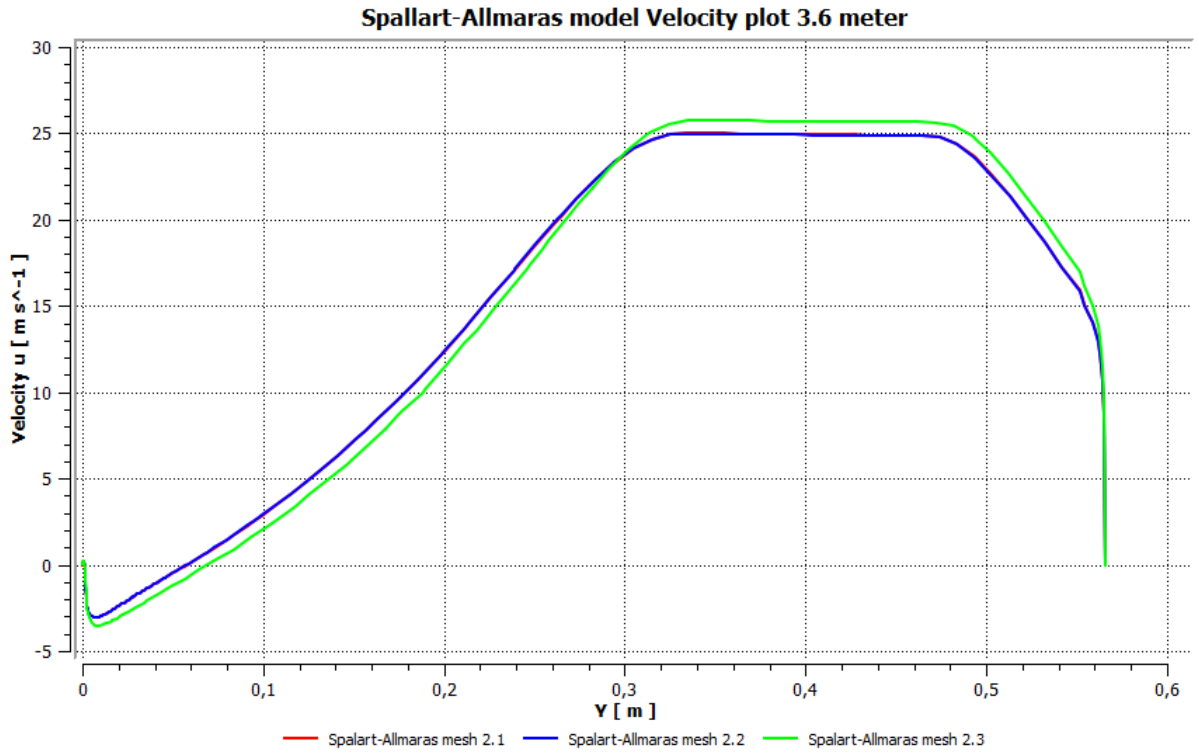
Spallart-Allmaras model Velocity plot 3.6 meter
Velocity u [m s^-1]
30
25
20
15
10
5
0
-5
0
0,1
0,2
0,3
0,4
0,5
0,6
Y [m]
Spalart-Allmaras mesh 2.1
Spalart-Allmaras mesh 2.2
Spalart-Allmaras mesh 2.3

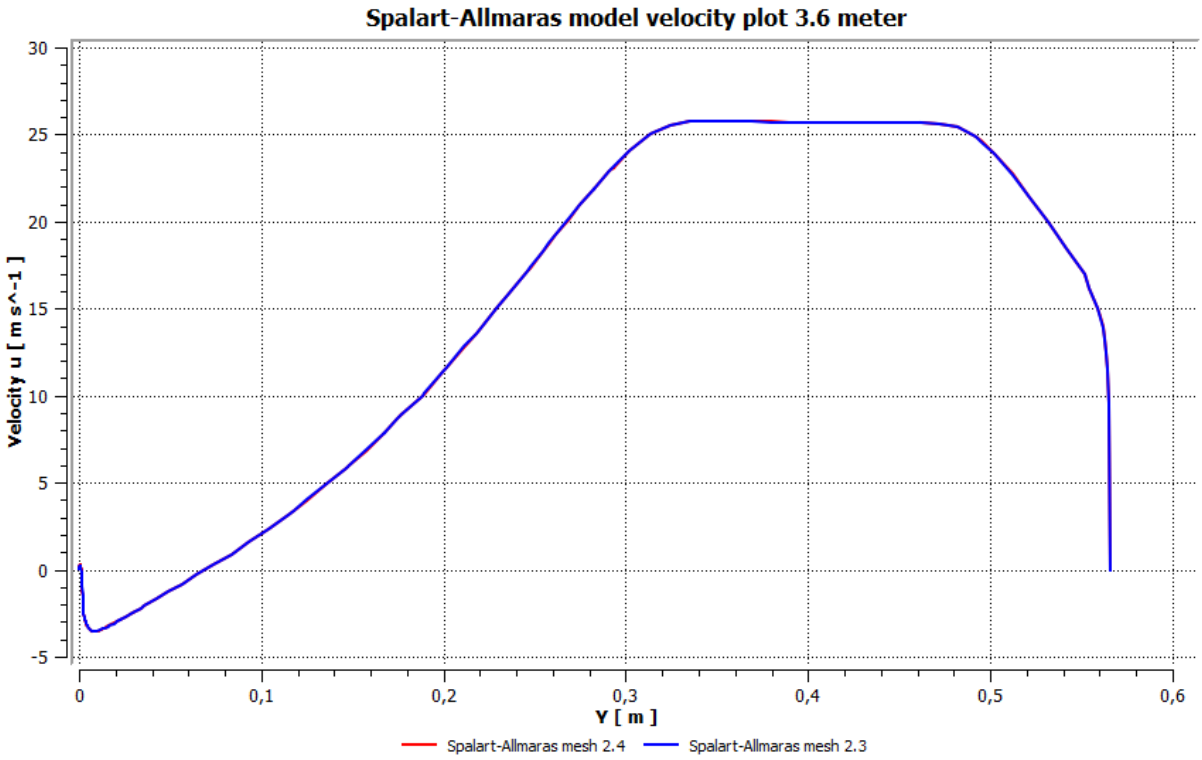
Spalart-Allmaras model velocity plot 3.6 meter
Velocity u [m s^-1]
30
25
20
15
10
5
0
-5
0
0,1
0,2
0,3
0,4
0,5
0,6
Y [m]
Spalart-Allmaras mesh 2.4
Spalart-Allmaras mesh 2.3

Appendix G - Transient dependence

In this section the results from the transient simulations performed on the rough diffuser are presented. As seen from the figures virtually no time dependence is present. All the transient simulations have been performed on mesh 2.3. Time step was set to 0.00001 and number of time step was set to 150000. Effective flow time was therefore 1.5 seconds. For the RSM model, the number of time step was set to 350000, producing an effective flow time of 3.5 seconds. Typical courant number was calculated to 0.02, based on these typical values:

Cell size 1 cm, velocity 20 m/s and time step 0.00001.

Transient k-ω SST simulations:

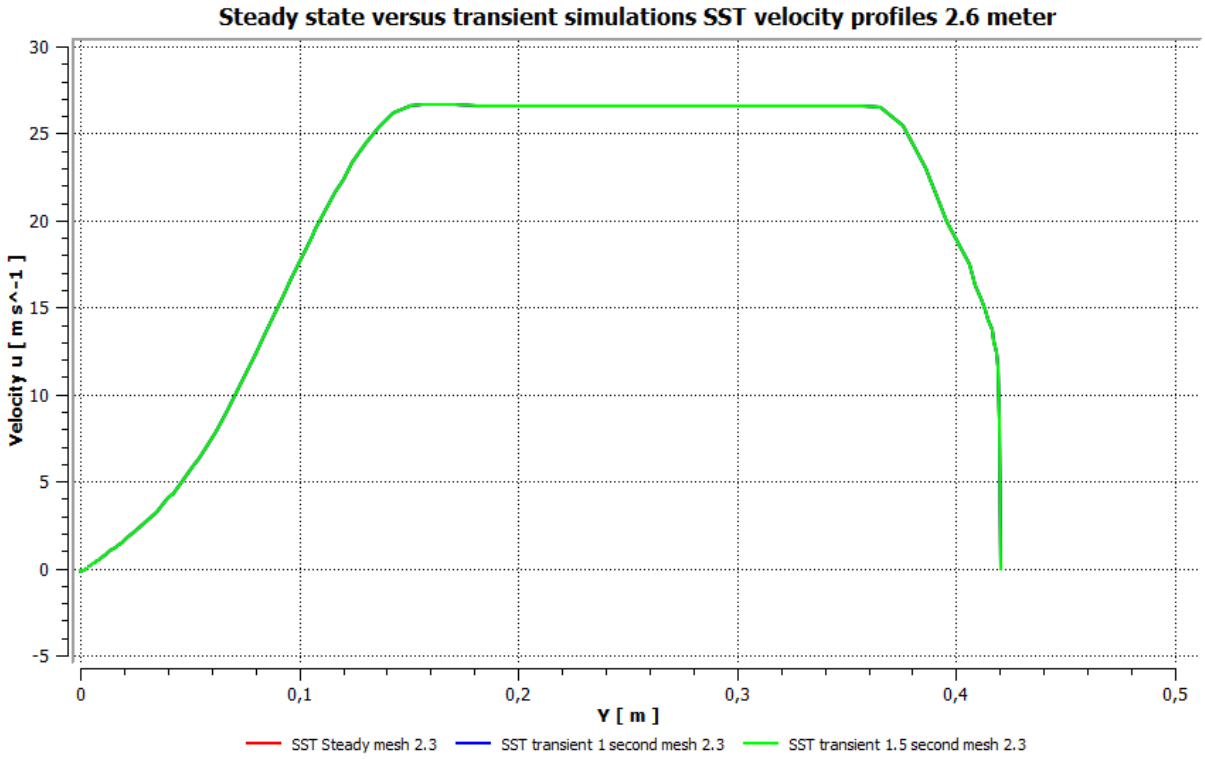

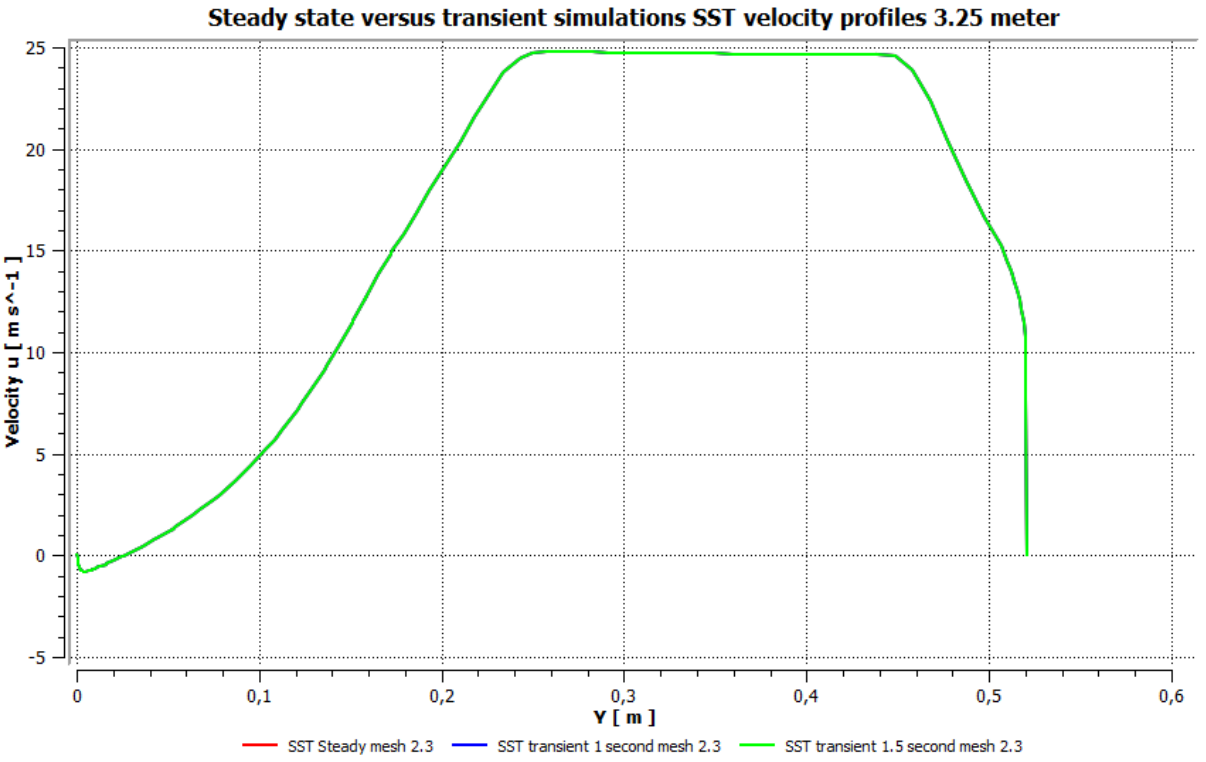
Steady state versus transient simulations SST velocity profiles 3.25 meter
Velocity u [m s^-1]
25
20
15
10
5
0
-5
0
0,1
0,2
0,3
0,4
0,5
0,6
Y [m]
SST Steady mesh 2.3
SST transient 1 second mesh 2.3
SST transient 1.5 second mesh 2.3

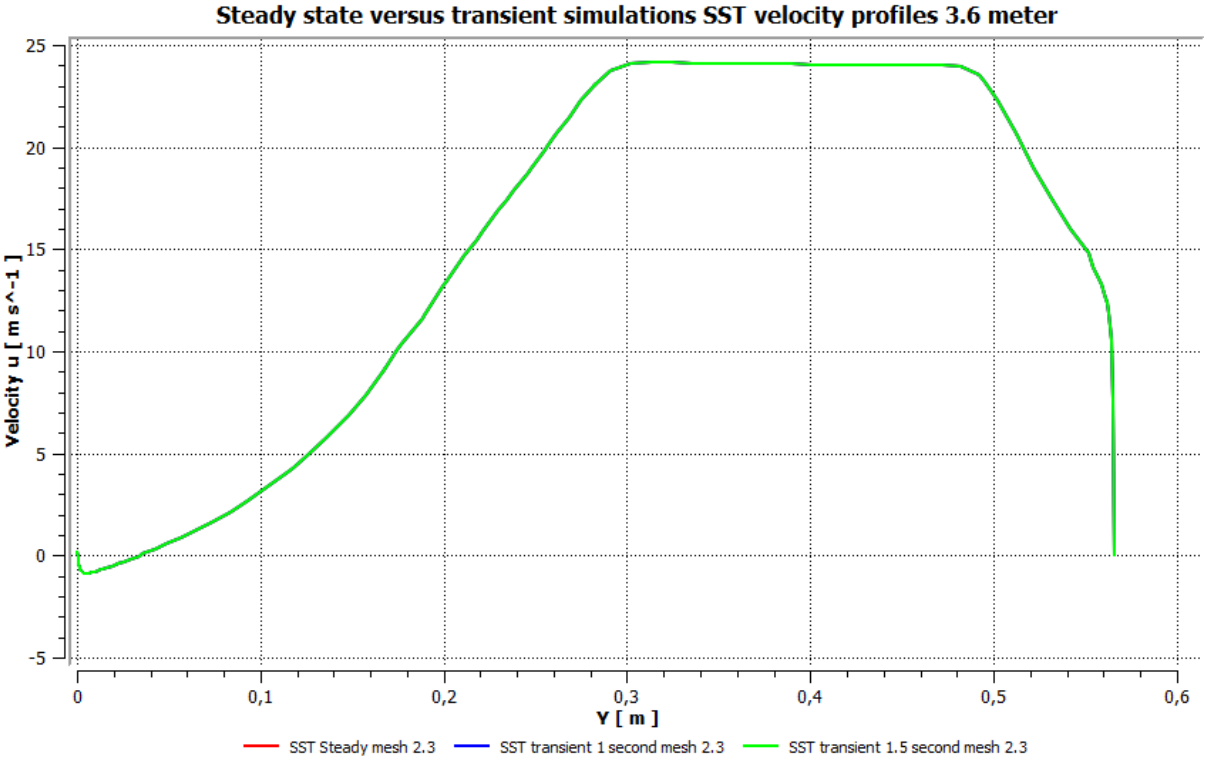
Steady state versus transient simulations SST velocity profiles 3.6 meter
Velocity u [m s^-1]
25
20
15
10
5
0
-5
0
0,1
0,2
0,3
0,4
0,5
0,6
Y [m]
SST Steady mesh 2.3
SST transient 1 second mesh 2.3
SST transient 1.5 second mesh 2.3

Transient k-ε RNG simulations:

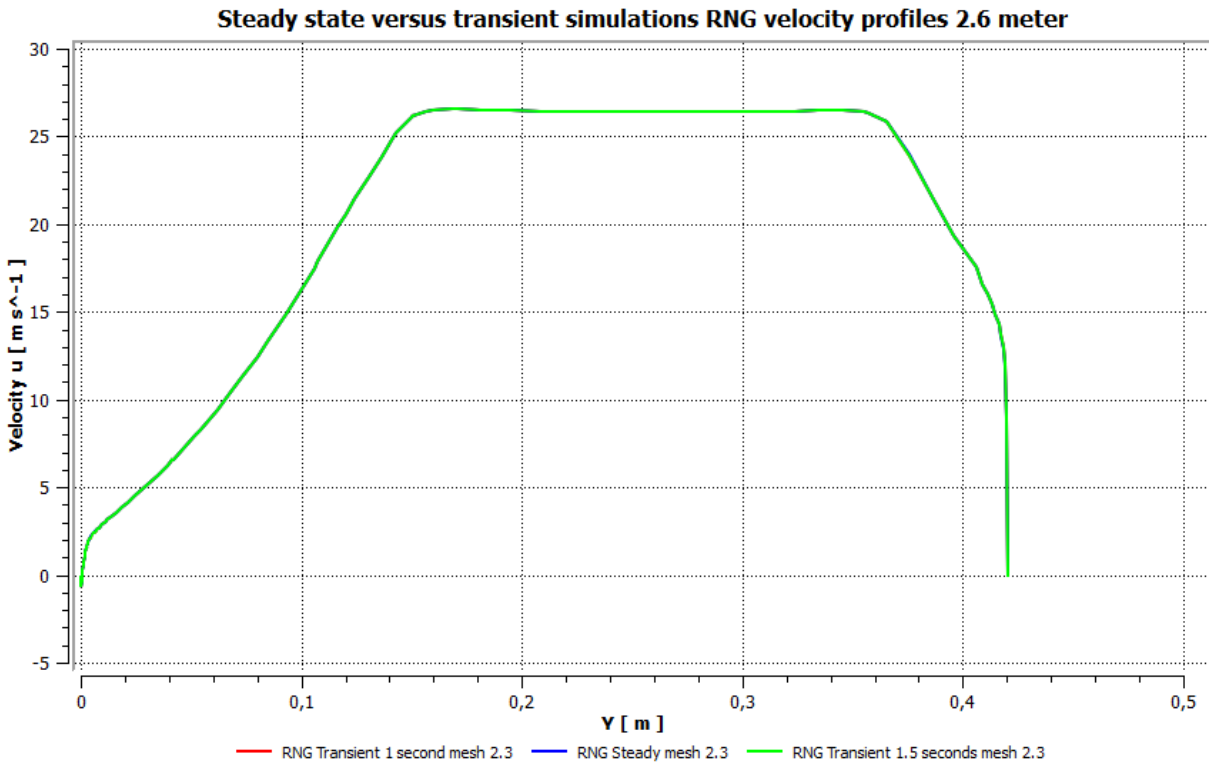

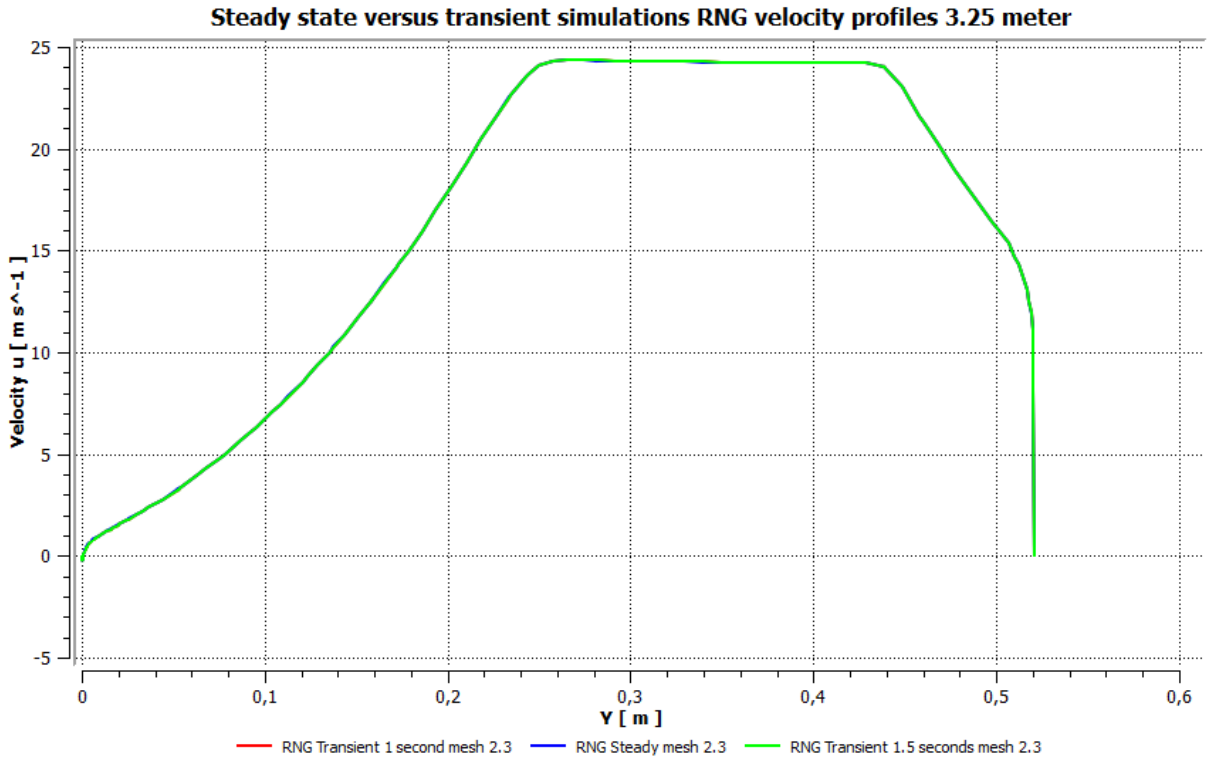

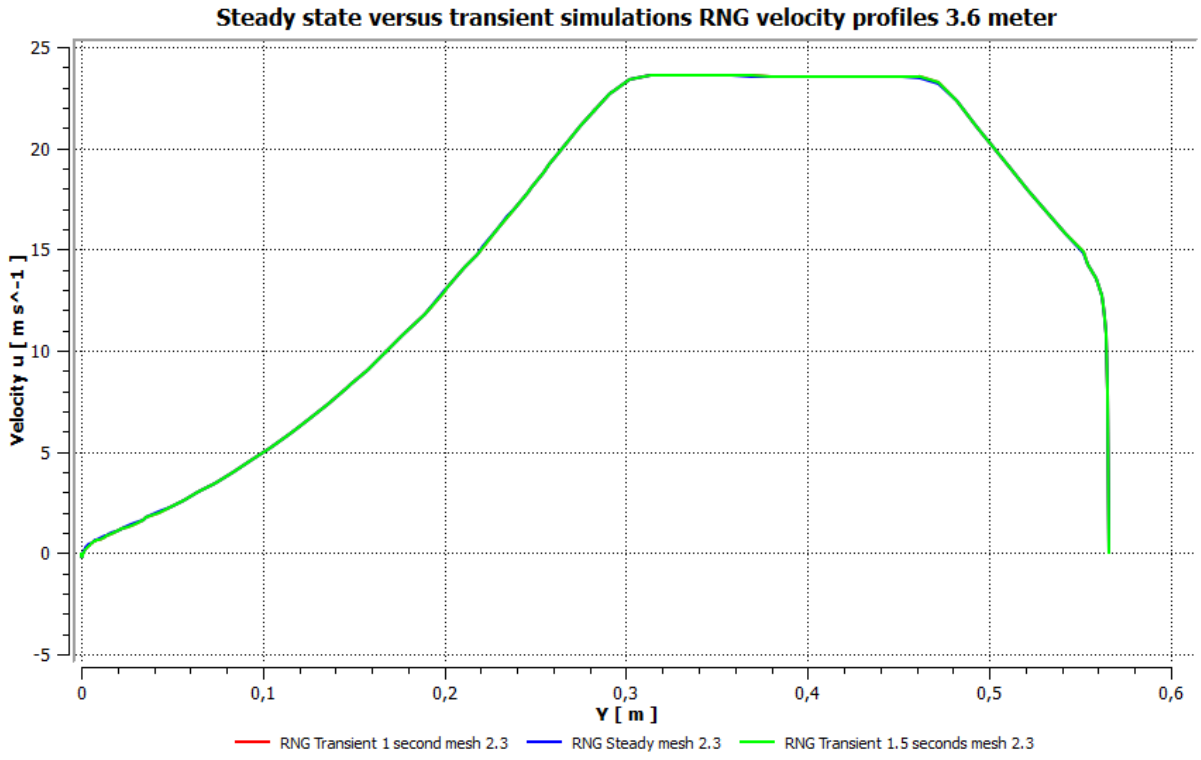

Transient Spalart-Allmaras simulations:

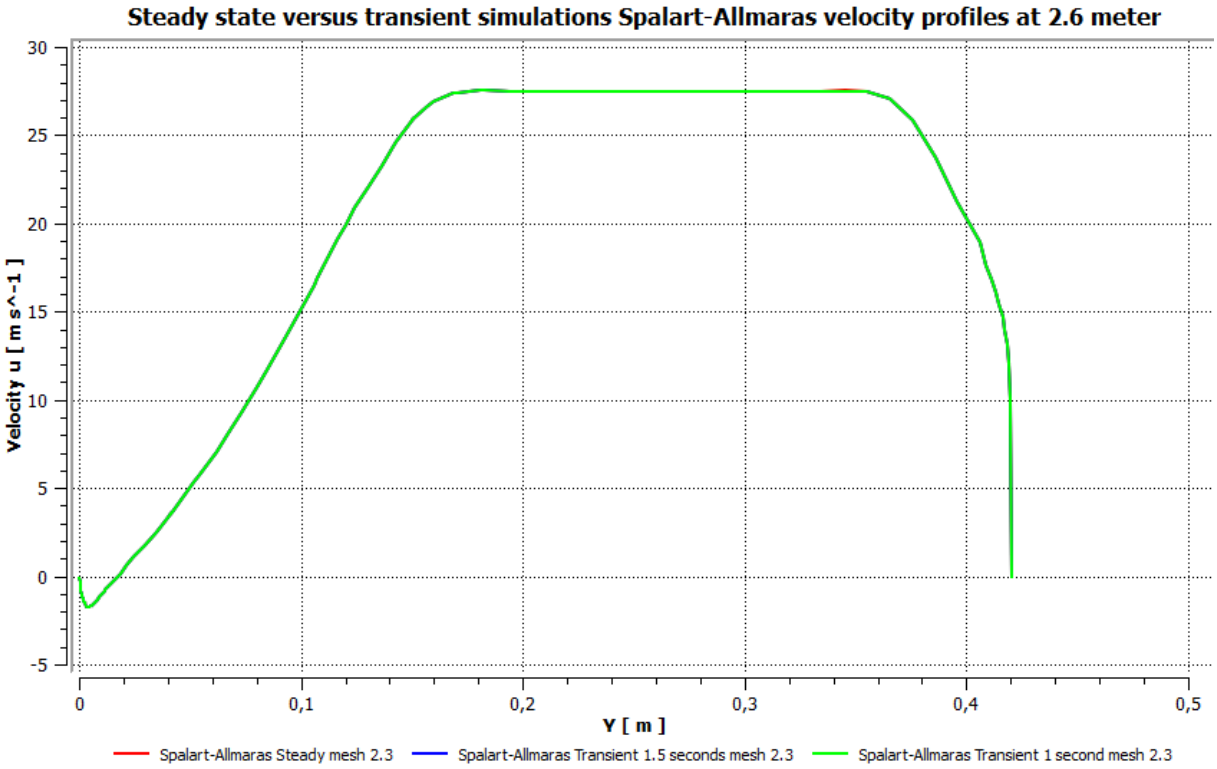

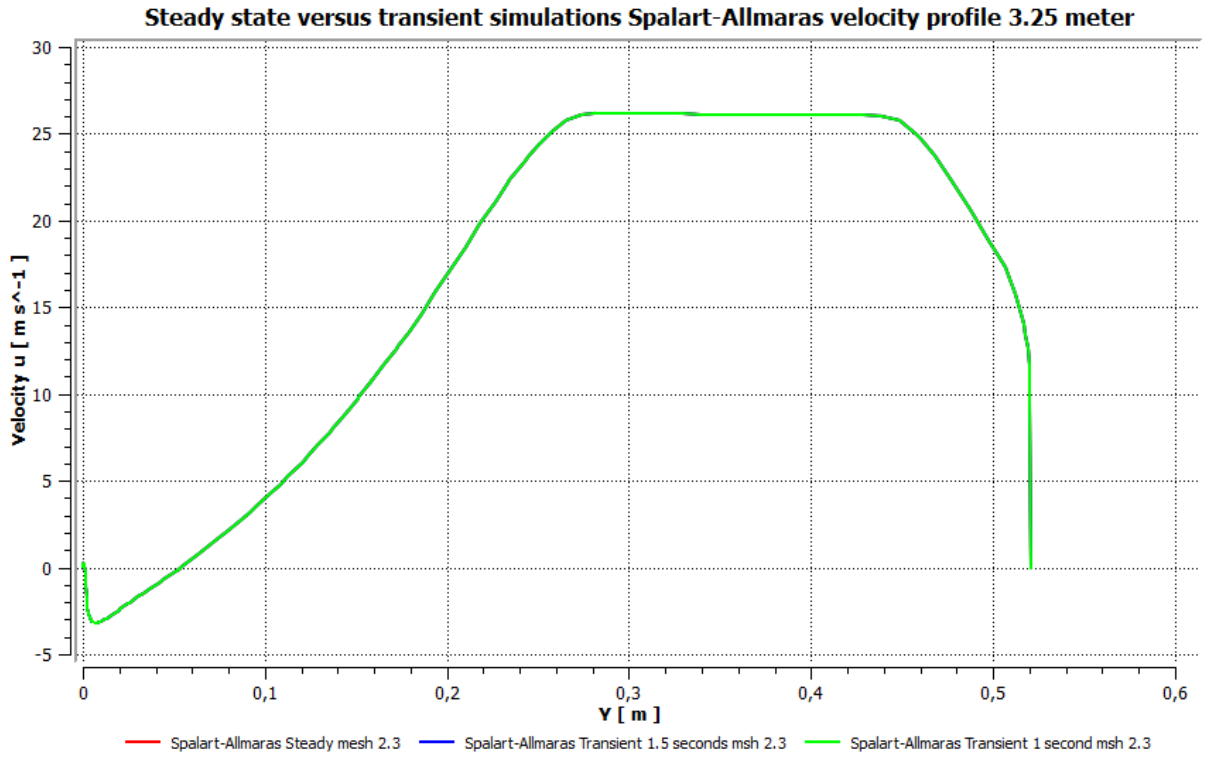
Steady state versus transient simulations Spalart-Allmaras velocity profile 3.25 meter
Velocity u [m s^-1]
30
25
20
15
10
5
0
-5
0
0,1
0,2
0,3
0,4
0,5
0,6
Y [m]
Spalart-Allmaras Steady mesh 2.3
Spalart-Allmaras Transient 1.5 seconds msh 2.3
Spalart-Allmaras Transient 1 second msh 2.3

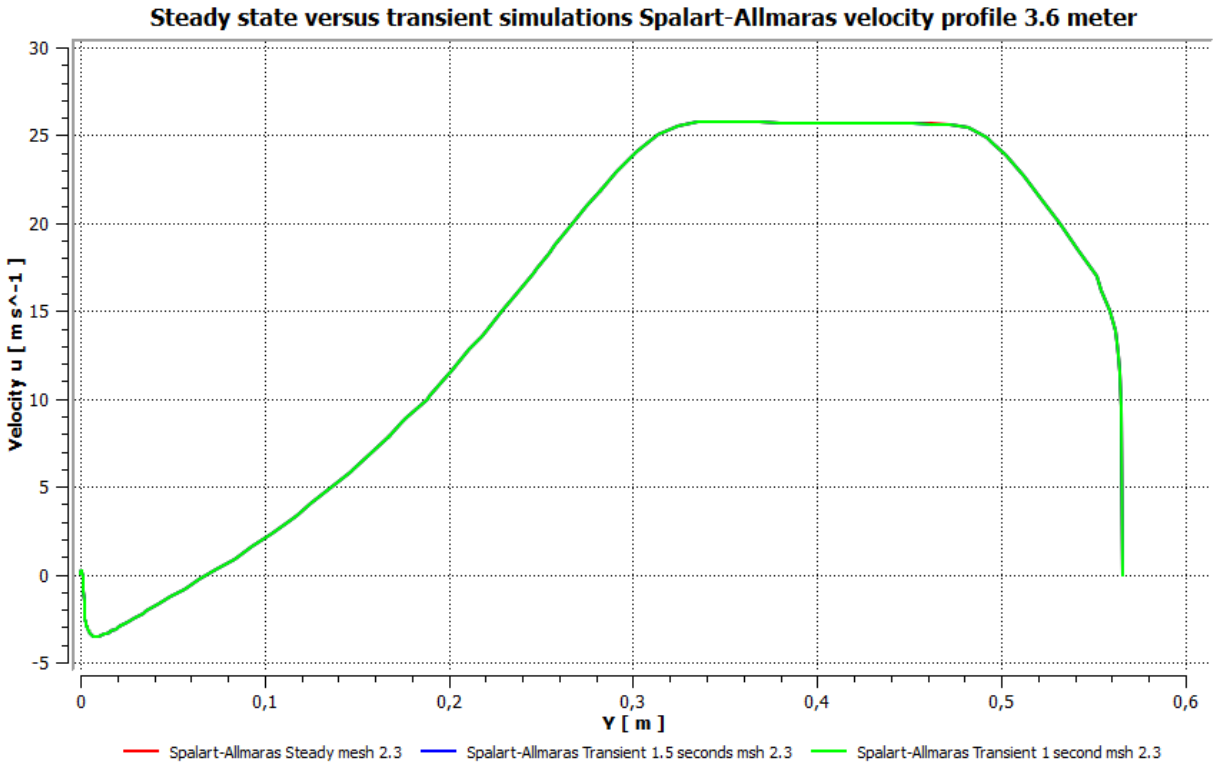
Steady state versus transient simulations Spalart-Allmaras velocity profile 3.6 meter
Velocity u [m s^-1]
30
25
20
15
10
5
0
-5
0
0,1
0,2
0,3
0,4
0,5
0,6
Y [m]
Spalart-Allmaras Steady mesh 2.3
Spalart-Allmaras Transient 1.5 seconds msh 2.3
Spalart-Allmaras Transient 1 second msh 2.3

Transient RSM simulations:

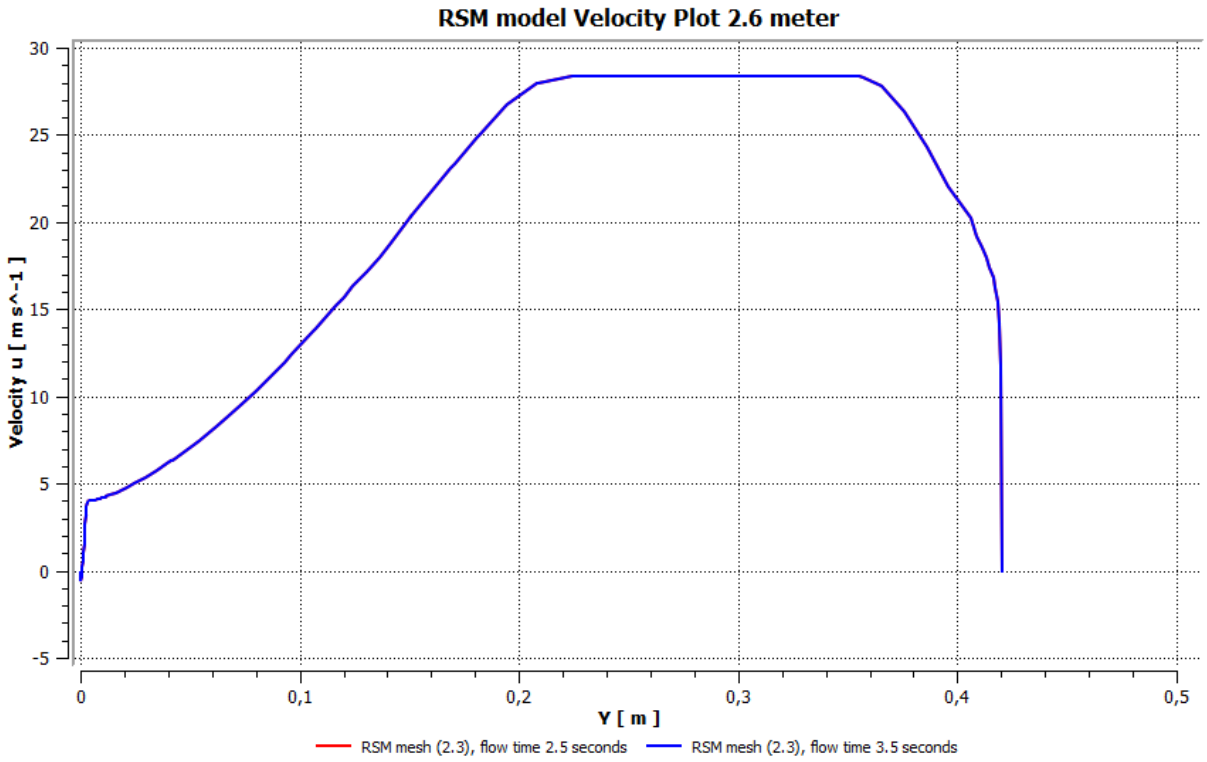

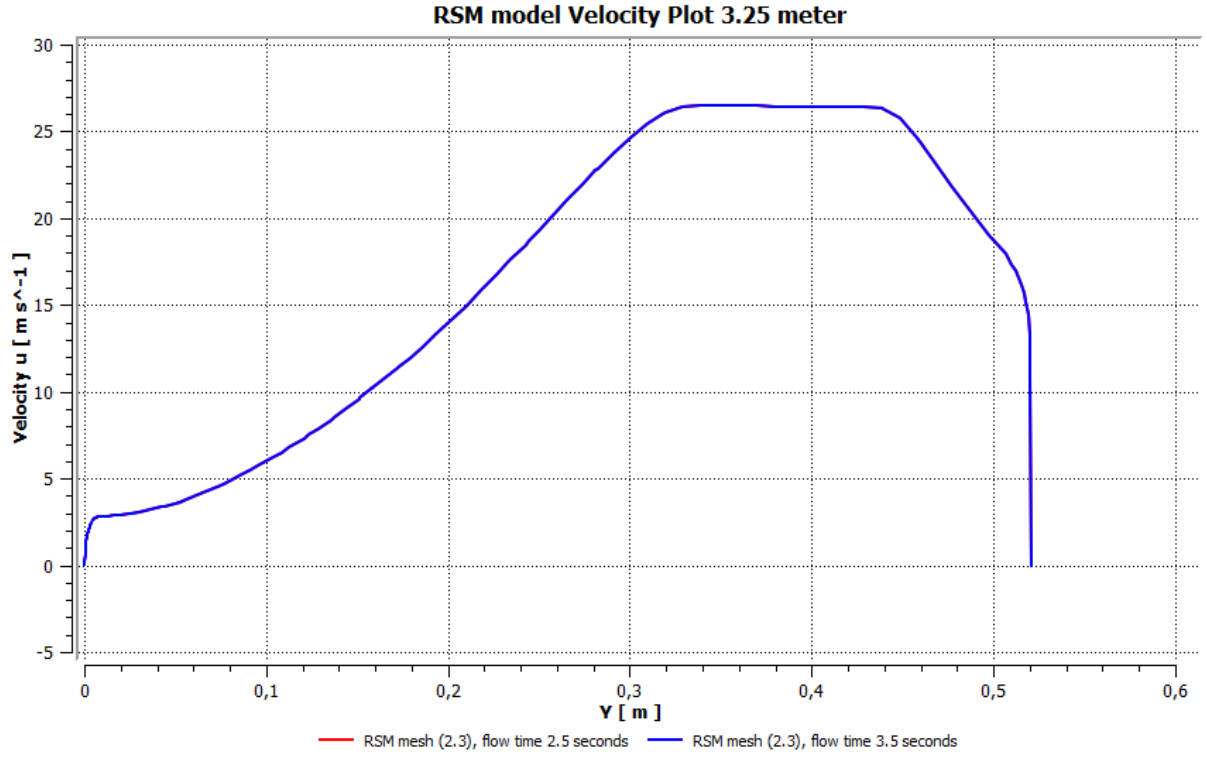

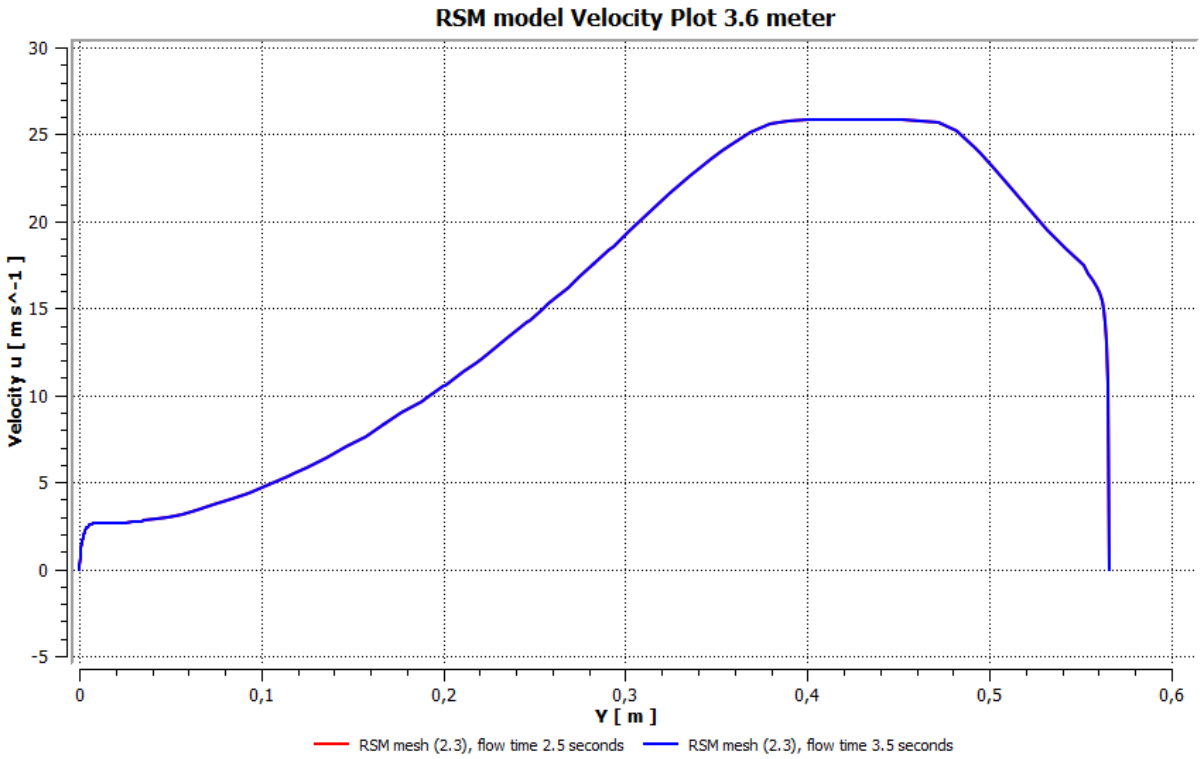
RSM model Velocity Plot 3.6 meter
Velocity u [m s^-1]
30
25
20
15
10
5
0
-5
0
0,1
0,2
0,3
0,4
0,5
0,6
Y [m]
RSM mesh (2.3), flow time 2.5 seconds
RSM mesh (2.3), flow time 3.5 seconds

Appendix H - Second order upwind vs Quick scheme

In this section the improved accuracy of the QUICJK scheme over the second order upwind scheme is visualized. Blue lines represent the velocity profiles of the second order upwind scheme and red lines represent the QUICK scheme

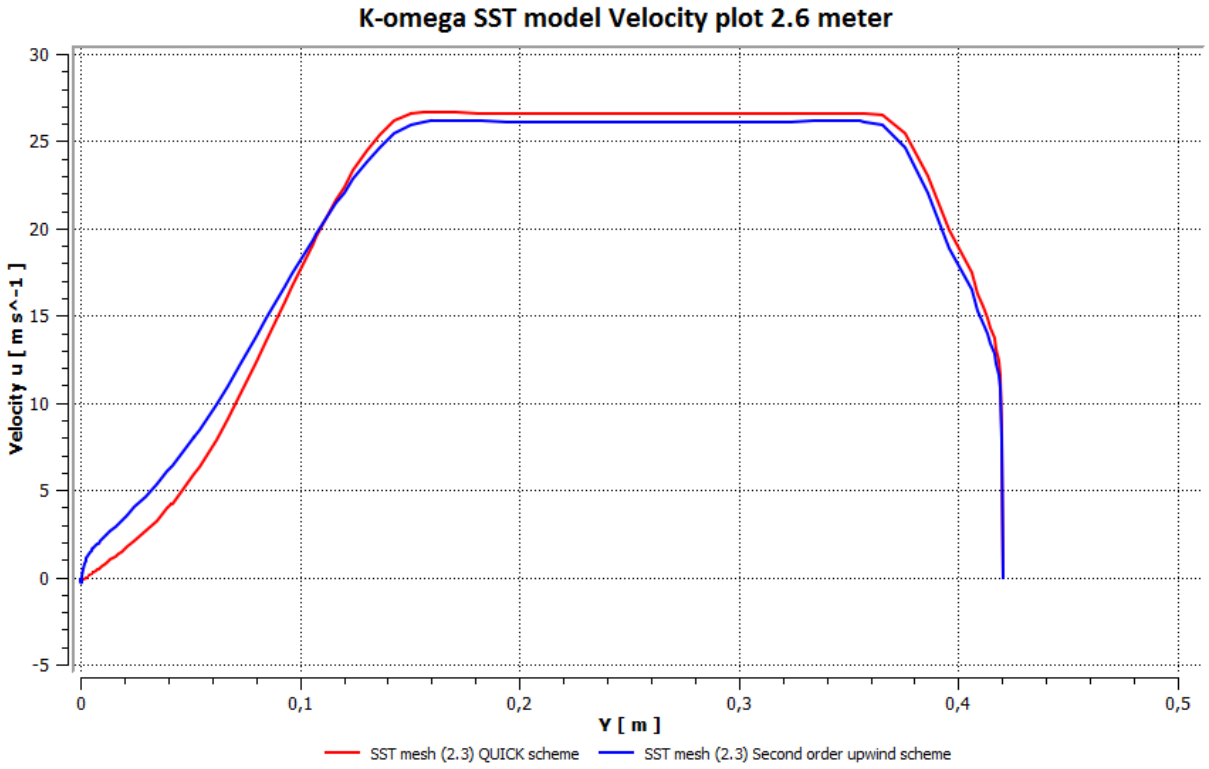

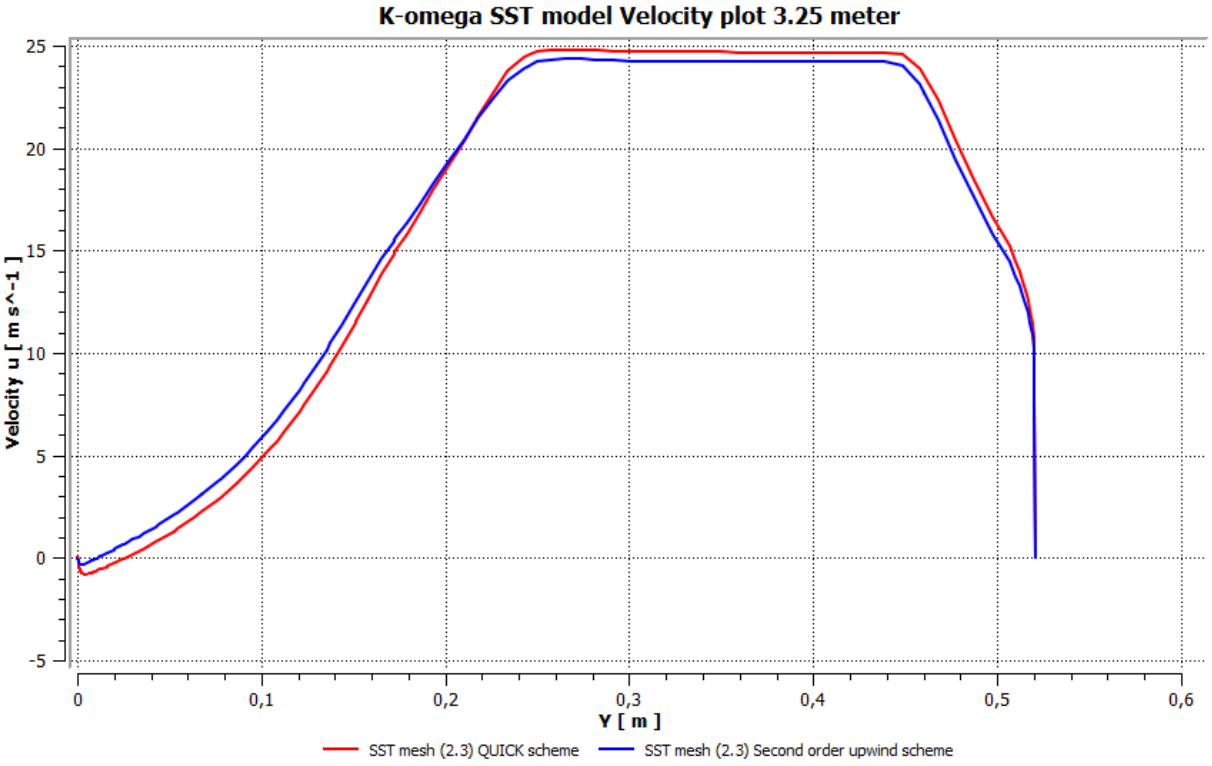
K-omega SST model Velocity plot 3.25 meter
Velocity u [m s^-1]
25
20
15
10
5
0
-5
0
0,1
0,2
0,3
0,4
0,5
0,6
Y [m]
SST mesh (2.3) QUICK scheme
SST mesh (2.3) Second order upwind scheme

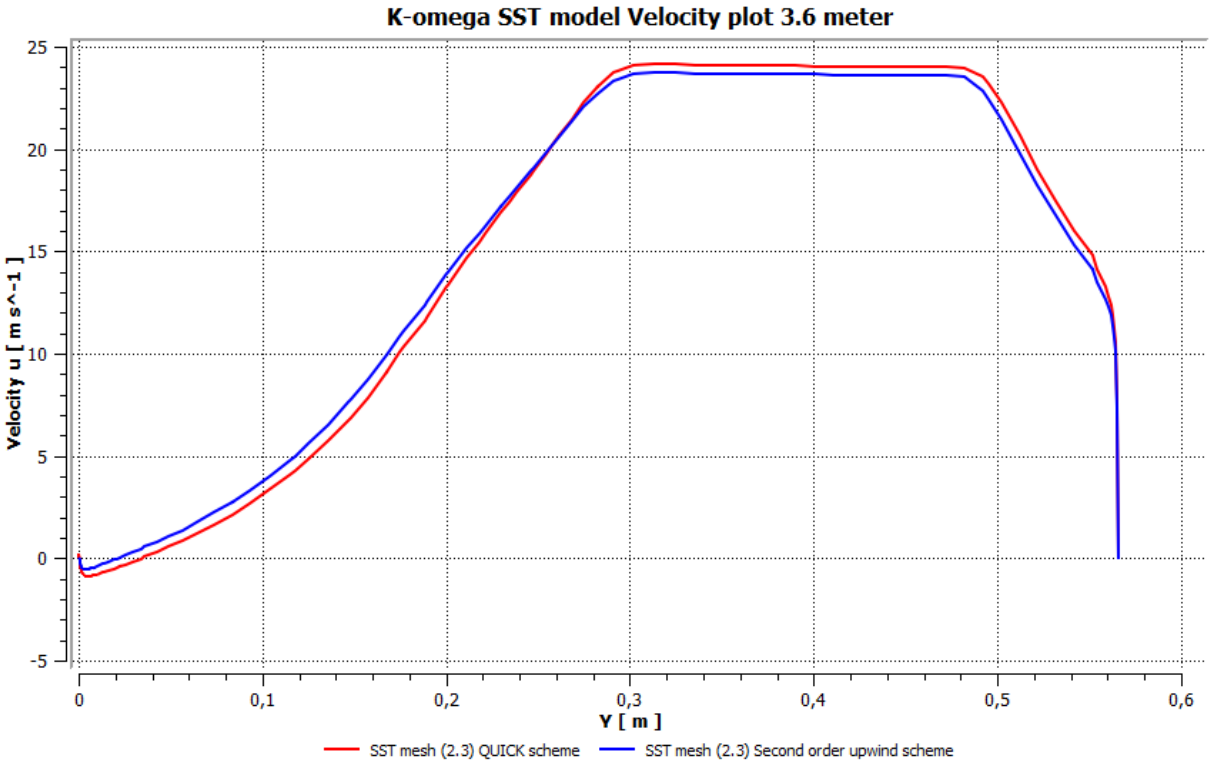
K-omega SST model Velocity plot 3.6 meter
Velocity u [m s^-1]
25
20
15
10
5
0
-5
0
0,1
0,2
0,3
0,4
0,5
0,6
Y [m]
SST mesh (2.3) QUICK scheme
SST mesh (2.3) Second order upwind scheme

Appendix I - Standard k-ε with wall functions

In this section some plots of the standard k-ε model employed with wall functions are presented.

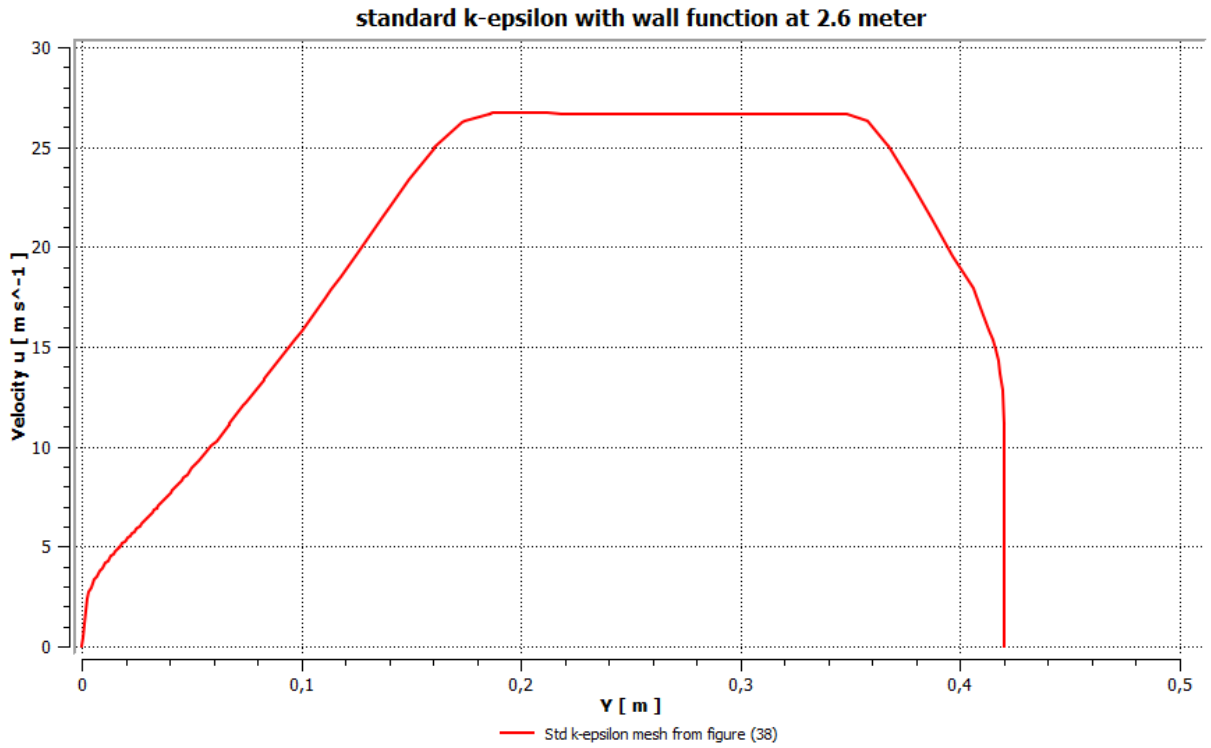

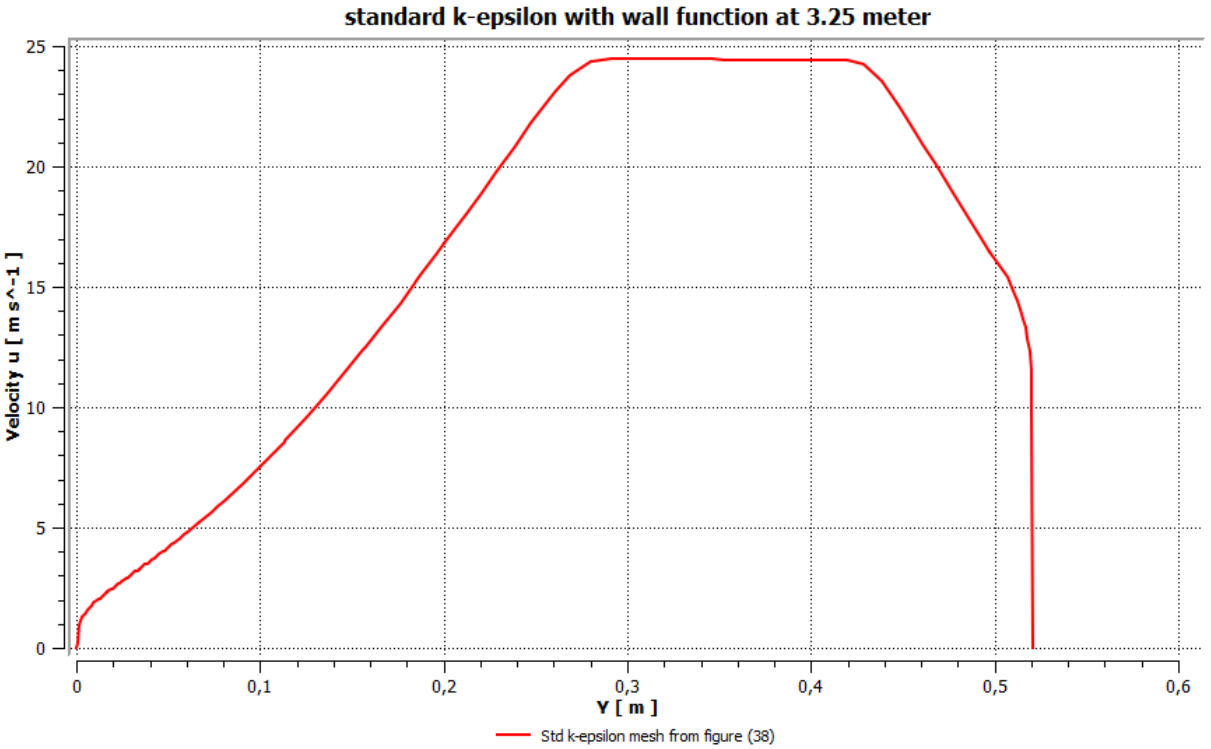

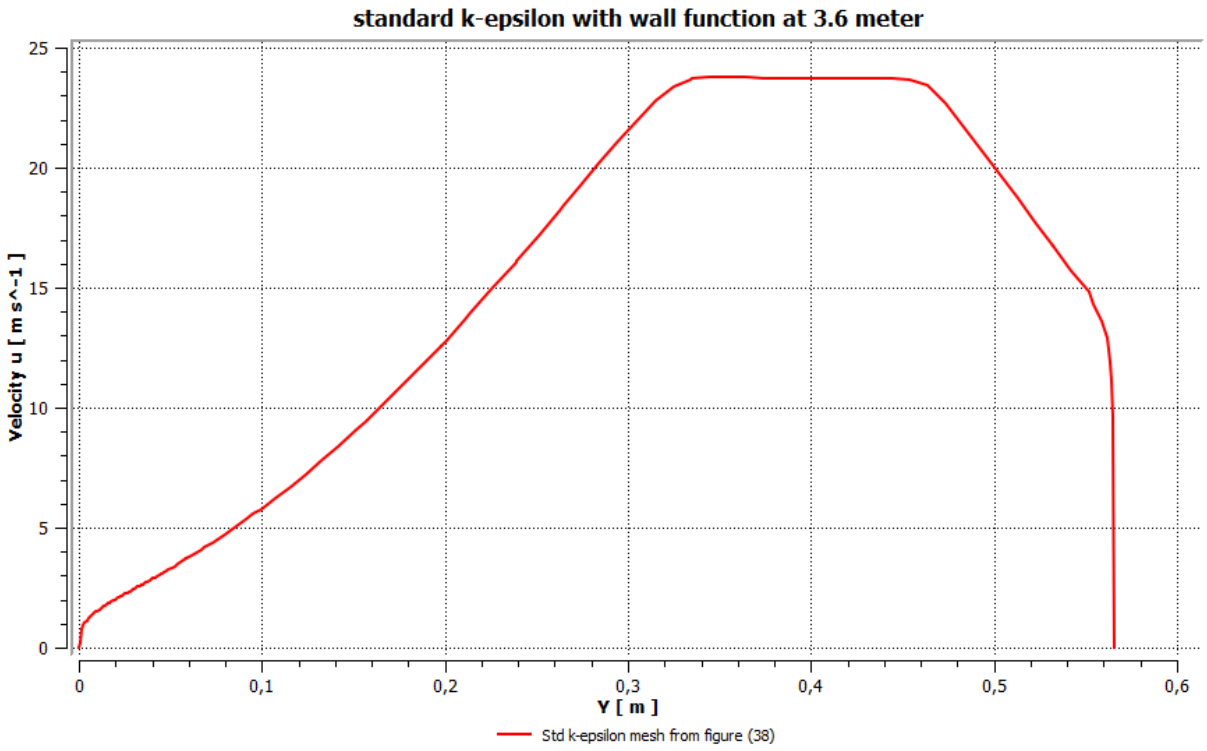
standard k-epsilon with wall function at 3.6 meter
Velocity u [m s^-1]
25
20
15
10
5
0
0
0,1
0,2
0,3
0,4
0,5
0,6
Y [m]
Std k-epsilon mesh from figure (38)

Appendix J - Residuals

In this section the residuals for each turbulence model and the associated mesh which the turbulence model where applied are presented. Note that iter is short for iterations.

Residuals Smooth diffuser simulations

- **K-ω SST model**

SST mesh 1.1:

iter	continuity	x-velocity	y-velocity	k	omega
2184	5.2964e-08	2.5960e-07	3.8425e-08	9.9799e-07	1.6063e-07

SST mesh 1.2:

iter	continuity	x-velocity	y-velocity	k	omega
52246	5.1649e-09	2.8078e-08	2.6765e-09	9.9876e-08	1.2832e-08

- **K-ε RNG model:**

RNG mesh 1.1:

iter	continuity	x-velocity	y-velocity	k	epsilon
2001	6.8562e-11	3.6184e-10	7.3664e-11	9.9885e-10	9.9627e-11

RNG mesh 1.2:

iter	continuity	x-velocity	y-velocity	k	epsilon
13683	2.5710e-09	1.8518e-10	4.7185e-11	8.0975e-09	3.4568e-09

- **Spalart-Allmaras model:**

Spalart-Allmaras 1.1:

iter	continuity	x-velocity	y-velocity	nut
2650	4.6731e-10	1.6864e-09	3.5474e-10	9.9978e-09

Spalart-Allmaras 1.2:

iter	continuity	x-velocity	y-velocity	nut
5878	3.2735e-11	1.3433e-10	2.2116e-11	9.8403e-10

Residuals rough diffuser simulations

- **K-ω SST model**

SST mesh 2.1:

iter	continuity	x-velocity	y-velocity	k	omega
13068	3.8882e-08	8.5053e-07	4.1812e-08	9.9970e-07	1.6984e-07

SST mesh 2.2:

iter	continuity	x-velocity	y-velocity	k	omega
13368	2.7851e-08	8.3988e-07	4.0075e-08	9.9972e-07	1.4501e-07

SST mesh 2.3:

iter	continuity	x-velocity	y-velocity	k	omega
11811	1.279e-09	6.2516e-08	6.6567e-09	5.5967e-08	1.3762e-10

SST mesh 2.4:

iter	continuity	x-velocity	y-velocity	k	omega
12471	3.4179e-09	6.5816e-08	5.4267e-09	9.9990e-08	1.3362e-10

- **Standard k-ω model**

Standard k-ω mesh 2.1:

iter	continuity	x-velocity	y-velocity	k	omega
20000	9.3158e-07	3.1696e-08	1.2840e-08	6.0274e-07	3.9040e-06

Standard k-ω mesh 2.2:

iter	continuity	x-velocity	y-velocity	k	omega
20000	4.2229e-07	2.5577e-08	7.0064e-09	4.6363e-07	1.7879e-0

Standard k-ω mesh 2.3:

iter	continuity	x-velocity	y-velocity	k	epsilon
20000	1.0484e-07	1.3841e-08	3.8675e-09	3.4709e-07	1.3752e-09

Standard k-ω mesh 2.4:

iter	continuity	x-velocity	y-velocity	k	omega
20000	9.1800e-05	5.6817e-05	5.8305e-05	2.1405e-04	2.5537e-05

- **K-ε RNG model:**

RNG mesh 2.1:

iter	continuity	x-velocity	y-velocity	k	epsilon
17224	6.3670e-09	6.1879e-08	3.6176e-09	9.9912e-08	3.1869e-08

RNG mesh 2.2:

iter	continuity	x-velocity	y-velocity	k	epsilon
17461	2.8009e-09	6.2087e-08	3.4431e-09	9.9998e-08	2.8169e-08

RNG mesh 2.3:

iter	continuity	x-velocity	y-velocity	k	epsilon
6231	6.5867e-08	4.1977e-07	1.8379e-08	9.9984e-07	2.3528e-07

RNG mesh 2.4:

iter	continuity	x-velocity	y-velocity	k	epsilon
10815	1.1633e-08	5.2866e-08	2.5269e-09	9.9919e-08	2.4125e-08

- **K-ε Realizable model:**

Realizable mesh 2.1:

iter	continuity	x-velocity	y-velocity	k	epsilon
20000	1.3932e-08	2.3536e-07	1.1320e-08	2.0747e-07	5.5003e-08

Realizable mesh 2.2:

iter	continuity	x-velocity	y-velocity	k	epsilon
20000	1.0684e-08	2.3474e-07	1.0960e-08	2.1318e-07	5.2449e-08

Realizable mesh 2.3:

iter	continuity	x-velocity	y-velocity	k	epsilon
9589	1.1291e-08	9.9926e-08	4.8063e-09	1.9033e-07	6.0158e-08

Realizable mesh 2.4:

iter	continuity	x-velocity	y-velocity	k	epsilon
30000	1.8273e-09	9.6434e-10	3.4308e-10	5.1255e-09	7.1619e-09

- **RSM model:**

RSM mesh 2.3:

Flow time : 2.999 seconds, time step 300000

```
iter continuity x-velocity y-velocity          k    epsilon
513805 1.6616e-11 9.9429e-11 6.5658e-11 5.0521e-09 7.3005e-10

uu-stress  vv-stress  ww-stress  uv-stress
9.1184e-10 9.0421e-10 7.1610e-10 1.0414e-09
```

- **Spalart-Allmaras model:**

Spalart-Allmaras mesh 2.1:

```
iter continuity x-velocity y-velocity        nut
12063 8.3564e-09 4.1172e-08 3.4489e-09 9.9949e-08
```

Spalart-Allmaras mesh 2.2:

```
iter continuity x-velocity y-velocity        nut
12245 7.0488e-09 4.0756e-08 3.3010e-09 9.9936e-08
```

Spalart-Allmaras mesh 2.3:

```
iter continuity x-velocity y-velocity        nut
7454 1.5431e-08 2.5892e-08 2.0762e-09 9.9949e-08
```

Spalart-Allmaras mesh 2.4:

```
iter continuity x-velocity y-velocity        nut
9447 5.2810e-09 2.7419e-08 2.1613e-09 9.9975e-08
```